MATERIALS FOR ADAPTIVE STRUCTURAL ACOUSTIC CONTROLS

Period February 1, 1993 to January 31, 1994

AD-A279 255

Annual Report

3   **VOLUME I**

OFFICE OF NAVAL RESEARCH
Contract No. N00014-92-J-1510

APPROVED FOR PUBLIC RELEASE -- DISTRIBUTION UNLIMITED

Reproduction in whole or in part is permitted for any purpose
of the United States Government

L. E. Cross

DTIC QUALITY INSPECTED 5

220750

PENNSTATE

94-14607

THE MATERIALS RESEARCH LABORATORY
UNIVERSITY PARK, PA

94 5 16 071

REPORT DOCUMENTATION PAGE

Public reporting burden for this collection of information is estimated to average 1 hour per response, including the time for reviewing instructions, searching existing data sources, gathering and maintaining the data needed, and completing and reviewing the collection of information. Send comments regarding this burden estimate or any other aspect of this collection of information, including suggestions for reducing this burden, to Washington Headquarters Services, Directorate for Information Operations and Reports, 1215 Jefferson Davis Highway, Suite 1204, Arlington, VA 22202-4302, and to the Office of Management and Budget, Paperwork Reduction Project (0704-0188), Washington, DC 20503

1. AGENCY USE ONLY (Leave blank)	2. REPORT DATE 4/11/94	3. REPORT TYPE AND DATES COVERED ANNUAL REPORT 02/01/93 TO 01/31/94

4. TITLE AND SUBTITLE

MATERIALS FOR ADAPTIVE STRUCTURAL ACOUSTIC CONTROL

5. FUNDING NUMBERS

6. AUTHOR(S)

L. ERIC CROSS

7. PERFORMING ORGANIZATION NAME(S) AND ADDRESS(ES)

MATERIALS RESEARCH LABORATORY
THE PENNSYLVANIA STATE UNIVERSITY
UNIVERSITY PARK, PA 16802

8. PERFORMING ORGANIZATION REPORT NUMBER

9. SPONSORING / MONITORING AGENCY NAME(S) AND ADDRESS(ES)

OFFICE OF NAVAL RESEARCH	GERALD T. SMITH
CODE 1513:NRJ	OFFICE NAVAL RESEARCH RES. REP
800 NORTH QUINCY STREET	536 SOUTH CLARK STREET, RM 286
ARLINGTON, VA 22217	CHICAGO, ILLINOIS 60606-1588

10. SPONSORING / MONITORING AGENCY REPORT NUMBER

11. SUPPLEMENTARY NOTES

12a. DISTRIBUTION / AVAILABILITY STATEMENT

12b. DISTRIBUTION CODE

13. ABSTRACT (Maximum 200 words)

SEE FOLLOWING PAGE

14. SUBJECT TERMS

15. NUMBER OF PAGES

16. PRICE CODE

17. SECURITY CLASSIFICATION OF REPORT	18. SECURITY CLASSIFICATION OF THIS PAGE	19. SECURITY CLASSIFICATION OF ABSTRACT	20. LIMITATION OF ABSTRACT

GENERAL INSTRUCTIONS FOR COMPLETING SF 298

The Report Documentation Page (RDP) is used in announcing and cataloging reports. It is important that this information be consistent with the rest of the report, particularly the cover and title page. Instructions for filling in each block of the form follow. It is important to *stay within the lines* to meet *optical scanning requirements*.

Block 1. Agency Use Only (Leave blank).

Block 2. Report Date. Full publication date including day, month, and year, if available (e.g. 1 Jan 88). Must cite at least the year.

Block 3. Type of Report and Dates Covered. State whether report is interim, final, etc. If applicable, enter inclusive report dates (e.g. 10 Jun 87 - 30 Jun 88).

Block 4. Title and Subtitle. A title is taken from the part of the report that provides the most meaningful and complete information. When a report is prepared in more than one volume, repeat the primary title, add volume number, and include subtitle for the specific volume. On classified documents enter the title classification in parentheses.

Block 5. Funding Numbers. To include contract and grant numbers; may include program element number(s), project number(s), task number(s), and work unit number(s). Use the following labels:

C	-	Contract	PR	- Project
G	-	Grant	TA	- Task
PE	-	Program Element	WU	- Work Unit Accession No.

Block 6. Author(s). Name(s) of person(s) responsible for writing the report, performing the research, or credited with the content of the report. If editor or compiler, this should follow the name(s).

Block 7. Performing Organization Name(s) and Address(es). Self-explanatory.

Block 8. Performing Organization Report Number. Enter the unique alphanumeric report number(s) assigned by the organization performing the report.

Block 9. Sponsoring/Monitoring Agency Name(s) and Address(es). Self-explanatory.

Block 10. Sponsoring/Monitoring Agency Report Number. (If known)

Block 11. Supplementary Notes. Enter information not included elsewhere such as: Prepared in cooperation with...; Trans. of...; To be published in.... When a report is revised, include a statement whether the new report supersedes or supplements the older report.

Block 12a. Distribution/Availability Statement. Denotes public availability or limitations. Cite any availability to the public. Enter additional limitations or special markings in all capitals (e.g. NOFORN, REL, ITAR).

DOD - See DoDD 5230.24, "Distribution Statements on Technical Documents."
DOE - See authorities.
NASA - See Handbook NHB 2200.2.
NTIS - Leave blank.

Block 12b. Distribution Code.

DOD - Leave blank.
DOE - Enter DOE distribution categories from the Standard Distribution for Unclassified Scientific and Technical Reports.
NASA - Leave blank.
NTIS - Leave blank.

Block 13. Abstract. Include a brief *(Maximum 200 words)* factual summary of the most significant information contained in the report.

Block 14. Subject Terms. Keywords or phrases identifying major subjects in the report.

Block 15. Number of Pages. Enter the total number of pages.

Block 16. Price Code. Enter appropriate price code *(NTIS only)*.

Blocks 17. - 19. Security Classifications. Self-explanatory. Enter U.S. Security Classification in accordance with U.S. Security Regulations (i.e., UNCLASSIFIED). If form contains classified information, stamp classification on the top and bottom of the page.

Block 20. Limitation of Abstract. This block must be completed to assign a limitation to the abstract. Enter either UL (unlimited) or SAR (same as report). An entry in this block is necessary if the abstract is to be limited. If blank, the abstract is assumed to be unlimited.

ABSTRACT

The research goals of this ONR sponsored University Research Initiative entitled "Materials for Adaptive Structural Acoustics Control" relate directly to the sensing and actuating material which must be integrated to function in adaptive control of acoustic structures. This report documents work in the second year of the program and for convenience the activities are grouped under the headings General Summary Papers, Materials Studies, Composite Sensors, Actuator Studies, Integration Issues, Processing Studies, and Thin Film Ferroelectrics.

The general papers cover a new comprehensive description of ferroelectric ceramics and their applications, analysis of high temperature piezoelectric sensors and the possible application of nonlinearity in enhancing the "smartness" of ceramics and composites. Scale effects on ferroics are of increasing interest and the manner in which nano-scale polar regions control the properties of relaxor ferroelectrics is again emphasized.

For material studies the detailed examination of the evolution of diffuse, then relaxor behavior in lanthanum modified lead titanate has been completed. Interest in the soft PZTs, relaxor and phase switching materials continues, with a new thrust developing towards a more complete description of domain walls and morphotropic phase boundaries in perovskites. Materials issues in the wear out and fatigue effects in polarization switching systems have been subjected to detailed evaluation and the precautions necessary to fabricate long lasting materials which will stand 10^9 switches without any fatigue are delineated.

Sensor studies have continued to focus on flextensional composites and have demonstrated both the very high hydrostatic sensitivity and the amplified actuation response of this configuration. Integration of sensors with the "moonie" actuators has been accomplished in individual cells. Actuator studies cover the gamut from highly reproducible micro positioning using electrostrictive compositions to high strain polarization switching shape memory ceramics capable of driving a latching relay device. Studies of the destruct mechanisms in practical MLA systems complement the earlier materials work and show the importance of internal electrodes and consequent stress concentrations for crack initiation. Integration studies have focused upon more detailed evaluation of 1:3, 2:2 and tabular 1:3 composites and upon the influence of the polymer characteristic and of face plates and edge guards upon sensing and actuation capabilities. In processing, the interest in dielectrophoretic forming of composites is continuing and assembly of interesting 1:3 composites is demonstrated. Guidelines for the transducer application of electrostrictive materials have been formulated and a useful classification scheme proposed. In fiber PZTs techniques for fabricating thin (30 μ) fibers are demonstrated, the first successful technique for poling fibers is described and it is shown that properly poled fibers have electro-elastic characteristics similar to bulk material. Film papers are selected to reflect the transducer capabilities of lead titanate and of phase switching lead zirconate titanate stannate antiferroelectric compositions.

MATERIALS FOR ADAPTIVE STRUCTURAL ACOUSTIC CONTROLS

Period February 1, 1993 to January 31, 1994

Annual Report

VOLUME I

OFFICE OF NAVAL RESEARCH
Contract No. N00014-92-J-1510

APPROVED FOR PUBLIC RELEASE – DISTRIBUTION UNLIMITED

L. E. Cross

Accesion For		
NTIS CRA&I		☒
DTIC TAB		☐
Unannounced		☐
Justification		
By		
Dist.ibution /		
Availability Codes		
Dist	Avail and / or Special	
A-1		

PENNSTATE

THE MATERIALS RESEARCH LABORATORY
UNIVERSITY PARK, PA

TABLE OF CONTENTS

APPENDICES

General Summary of Papers

1. Turner, R. C. , P. A. Fuierer, R. E. Newnham, and T. R. Materials for High Temperature Acoustic and Vibration Sensors: A Review. Applied Acoustics 41:1-26 (1993).

2. Uchino, K. Ferroelectric Ceramics. Materials Science and Technology, Edited by R.W. Cahn, P. Haasen, E.J. Kramer, Vol. I, VCH 1994.

3. Newnham, R. E. Smart, Very Smart and Intelligent Materials, MRS Bulletin XVIII(4), 24-26 (April 1993).

General Summary of Papers (continued)

4. Newnham, R. E. Size Effects and Nonlinear Phenomena in Ferroic Ceramics. 3rd European Ceramic Society Conference, Madrid (1993).

5. Cross, L. E. Relaxor Ferroelectrics: Useful Electron Nanocomposite Structures, Proc. IUMRS, Ikabakura, Tokyo (September 1993).

Materials Studies

6. Rossetti, G. A., Jr., W. Cao, and C. A. Randall. Microstructural Characterization and Diffuse Phase Transition Behavior of Lanthanum Modified Lead Titanate. Ferroelectrics: Proceedings of IMF8, Gaithersburg, Maryland (August 1993).

7. Cao, W. and L. E. Cross. Distribution Function of Coexisting Phases in a Complete Solid Solution System. J. Appl. Phys. 73(7), 3250 (1993).

8. Cao, W. Polarization Gradient Coefficients and the Dispersion Surface of the Soft Mode in Perovskite Ferroelectrics. J. Phys. Soc. Jpn. 63, 827 (1994).

9. Cao, W. and L. E. Cross. Nonlinear and Nonlocal Continuum Theory on Domain Walls in Ferroelectrics. Ferroelectrics: Proceedings of IMF8, Gaithersburg, Maryland (August 1993).

10. Cao, W. and C. Randall. Theory on the Fringe Patterns in the Study of Ferroelectric Domain Walls Using Electron Holograpy. Solid State Comm. 86, 435-439 (1993).

11. Zhang, Q. M., H. Wang, N. Kim, and L. E. Cross. Direct Evaluation of Domain Walls and Intrinsic Contributions to the Dielectric and Piezoelectric Constants and Their Temperature Dependence in Lead Zirconate Titanate Ceramics. J. Appl. Phys. 75 (1), 454 (1994).

12. Subbarao, E. C., V. Srikanth, W. Cao, and L. E. Cross. Domain Switching and Microcracking during Poling of Lead Zirconate Titanate Ceramics. Ferroelectrics 145, 271-281 (1993).

13. Li, S., W. Cao, R. E. Newnham, and L. E. Cross. Electromechanical Nonlinearity of Ferroelectric Ceramic and Related non 180° Domain Wall Motion. Ferroelectrics 139, 25-49 (1993).

14. Jiang, Q., W. Cao, and L. E. Cross. Electrical Fatigue in Lead Zirconate Titanate Ceramics. J. Am. Ceram. Soc. 77(1), 211-215 (1994).

15. Jiang, Q., E. C. Subbarao, and L. E. Cross. Grain Size Dependence of Electrical Fatigue Behavior in Hot Pressed PLZT Ferroelectric Ceramics. (Submitted to Acta. Met.)

16. Jiang, Q., E. C. Subbarao, and L. E. Cross. Effects of Composition and Temperature on electrical Fatigue of La Doped Lead Zirconate Titanate Ceramics. J. Appl. Phys. (in press).

17. Jiang, Q. and L. E. Cross. Effect of Porosity on Electrical Fatigue Behavior in PLZT and PZT Ceramics. J. Mat. Sci. 28, 4536-4543 (1993).

2

18. Jiang, Q., E. C. Subbarao, and L. E. Cross. Effects of Electrodes and Electroding Methods on Fatigue Behavior in Ferroelectric Materials. Ferroelectrics: Proceedings of IMF8, Gaithersburg, Maryland (August 1993).

19. Jiang, Q., E. C. Subbarao, and L. E. Cross. Fatigue in PLZT: Acoustic Emission as a Discriminator Between Microcracking and Domain Switching. Ferroelectrics: Proceedings of IMF8, Gaithersburg, Maryland (August 1993).

20. Jiang, Q., E. C. Subbarao, and L. E. Cross. Field Induced Stress Concentration and Electrical Fatigue in Ferroelectric Ceramics. IEEE Trans. on Ultrasonic Ferroelectrics and Frequency Control (submitted).

21. Jiang, Q., E. C. Subbarao, and L. E. Cross. Dielectric Properties of Single Grain in PLZT Ferroelectric Ceramics. Ferroelectric Letters (in press).

22. Li, S., A. S. Bhalla, R. E. Newnham, and L. E. Cross. Quantitative Evaluation of Extrinsic Contribution to Piezoelectric Constant $d33$ in Ferroelectric PZT Ceramics. Materials Letters 17, 21-26 (1993).

23. Wang, H., Q. Zhang, and L. E. Cross. A High Sensitivity Phase Sensitive $d33$ Meter for Complex Piezoelectric Constant Measurement. Jpn. J. Appl. Phys. 32(Pt. 2; No. 9A), L1281-83 (1993).

Composite Sensors

24. Newnham, R. E., Q. C. Xu, and S. Yoshikawa. Metal-Electroactive Ceramic Composite Actuator. U.S. Patent# 5,276, 657.

25. Onitsuka, K., A. Dogan, J. A. Tressler, Q. C. Xu, S. Yoshikawa, and R. E. Newnham. Metal-Ceramic Composite Transducer-The Moonie. Ferroelectrics: IMF8, Gaithersburg, Maryland (August 1993).

26. Tressler, J. F., Q. C. Xu, S. Yoshikawa, K. Uchino, and R. E. Newnham. Composite Flextensional Transducer for Sensing and Actuating. Ferroelectrics: IMF8, Gaithersburg, Maryland (August 1993).

27. Newnham, R. E., A. Dogan, Q. C. Xu, K. Onitsuka, J. Tressler, and S. Yoshikawa. Flextensional "Moonie" Actuators. IEEE 1993 Ultrasonics Symp. Proc., Baltimore, Maryalnd; Vol. 2, pp. 509-514 (1993).

28. Harshe, G., J. P. Dougherty, and R. E. Newnham. Theoretical Modeling of Multilayer Magnetoelectric Composites. Int. J. of Appl. Mag. in Mtls. 4, 145-159 (1993).

29. Newnham, R. E. and G. R. Ruschau. Electromechanical Properties of Smart Materials. J. Intelligent Mtls. Systems and Structures 4, 289 (1993).

30. Onitsuka, K., A. Dogan, Q. Xu, S. Yoshikawa, and R. E. Newnham. Design Optimization for Metal-Ceramic Composite Actuator, "Moonie." Ferroelectrics: IMF8, Gaithersburg, Maryland (August 1993).

Actuator Studies

31. Uchino, K. Relaxor Ferroelectric Devices. Ferroelectrics: Proceedings IMF8, Gaithersburg, Maryland (August 1993).

32. Uchino, K. Recent Development of Piezoelectric Actuators for Adaptive Structures. 3rd International Conference on Adaptive Structures (1991).

33. Furuta, A. and K. Uchino. Dynamic Observation of Crack Propagation in Piezoelectric Multilayer Actuators. J. Am. Ceram. Soc. 76(6), 1615 (1993).

34. Uchino, K. Ceramic Actuators Principles and Applications. MRS Bull. (April 1993).

35. Uchino, K. Applications of Piezoelectric Ceramics in Smart Actuator Systems. ADPA/AIAA/ASME/SPIE Cont. on Active Mtls. (1992).

36. Uchino, K. and A. Furuta. Destruction Mechanism of Multilayer Ceramic Actuators. ISAF92, South Carlonia (1992).

37. Furuta, A., K. Y. Oh, and K. Uchino. Shape Memory Ceramics and Their Application to Latching Relays. Sensors and Materials 3, 205 (1992).

38. Uchino, K. Piezoelectric Ceramics in Smart Actuators Systems. 1st European Conference on Smart Structures and Materials, Glasgow (1992).

39. Zhang, Q. M., J. Chen, and L. E. Cross. Electric Field Induced Piezoelectric Response in Ferroelectric Materials Near the Paraelectric-Ferroelectric Transition. Proceedings Ultrasonics Symposium, pp. 525 (1993).

Integration Issues

40. Zhang, Q. M., W. Cao, J. Zhao, and L. E. Cross. Piezoelectric Performance of Piezoelectric Polymer Composites with 2-2 Connectivity–A Combined Theoretical and Experimental Study. IEEE Transactions UFFC (accepted) (1993).

41. Chen, J., Q. M. Zhang, L. E. Cross, and C. M. Trottier. Modeling and Design of 1-3 Tubular Composites for Smart Transducer Applications. 1994 Proceedings International Conference on Intelligent Materials (submitted) (1994).

42. Wang, H., Zhang, and L. E. Cross. Piezoelectric Relaxation of P(VDF-TrFE) Copolymers. Ferroelectrics: IMF8, Gaithersburg, Maryland (August 1993).

43. Zhao, J., Q. M. Zhang, and W. Cao. Effects of Face Plates and Edge Strips on Hydrostatic Piezoelectric in 1-3 Composites. J. Mat. Sci. (submitted).

Processing Studies

44. Yoshikawa, S. and T. R. Shrout. Multilayer Piezoelectric Actuator Structures and Reliability. Proceedings Structural Dynamics, Materials Conference AIAA/ASM Adaptive Structures Forum, Pt. 6, 3581-3586 (1993).

Processing Studies (continued)

45. Bowen, C. P., T. R. Shrout, R. E. Newnham, and C. Randall. Intelligent Processing of Composite Materials. J. Intelligent and Smart Materials (submitted) (1993).

46. Shrout, T. R., C. A. Randall, B. P. Brodeur, and S. J. Jang. Classification of Electrostrictive Based Materials for Transducers. U.S. Japan Meeting on Dielectrics, Lahaina, Hawaii (November 1994).

47. Yoshikawa, S., U. Selvaraj, P. Moses, Q. Jiang, and T. R. Shrout. Pb(ZrTi)O$_3$ [PZT] Fibers—Fabrication and Properties. J. of Intelligent Material Systems and Structures (submitted) (1994).

48. Miller, D., C. A. Randall, A. S. Bhalla, R. E. Newnham, and J. Adair. Electrorheological Properties of BaTiO$_3$ Suspensions. Ferroelectric Letters 15, 141-151 (1993).

49. Randall, C. A., C. P. Bowen, T. R. Shrout, A. S. Bhalla, and R. E. Newnham. Dielectrophoresis: A Means to Assemble Novel Electroceramic Composite Materials. Proceedings of Electrorheological Fluids. Feldrick, Austria (1993).

Thin Film Ferroelectrics

50. Udayakumar, K. R., S. B. Krupanidhi, K. Kushida, and L. E. Cross. Origina of Orientation in Sol-Gel-Derived Lead Titanate Films. J. Am. Ceram. Soc. 76, 1345 (1993).

51. Brooks, K. G., J. Chen, K. R. Udayakumar, and L. E. Cross. Electric Field Forced Phase Switching in La Modified Lead Zirconate Titanate Stannate Films. J. Appl. Phys. 75, 1399 (1994).

52. Sheen, J., R. Guo, A. S. Bhalla, and L. E. Cross. Measurements of Dielectric Constant and Quality Factor of Ba(Mg$_{1/3}$Ta$_{2/3}$) O$_3$ at X Band Frequencies. Ferroelectric Letters 16, 33 (1993).

Graduating Students in the Program

53. Rossetti, George A., Jr. PhD Thesis (Abstract), Solid State Science. Structural and Thermodynamic Investigation of the Ferroelectric Phase Transition in Lanthona-Substitued Lead Titanate. May 1993.

54. Chen, Jaiyu. PhD Thesis (Abstract), Electrical Engineering. Electrical and Electromechanical Properties of Ferroelectric Thin Films for Microelectromechanical Applications. August 1993.

55. Alberta, Edward. MS Thesis (Abstract), Solid State Science. The Dielectric, Piezoelectric and Pyroelectric Properties of Lead Zirconate-Lead Zinc Niobate-Lead Titanate Ceramics. October 1993.

ABSTRACT

The research goals of this ONR sponsored University Research Initiative entitled "Materials for Adaptive Structural Acoustics Control" relate directly to the sensing and actuating material which must be integrated to function in adaptive control of acoustic structures. This report documents work in the second year of the program and for convenience the activities are grouped under the headings General Summary Papers, Materials Studies, Composite Sensors, Actuator Studies, Integration Issues, Processing Studies, and Thin Film Ferroelectrics.

The general papers cover a new comprehensive description of ferroelectric ceramics and their applications, analysis of high temperature piezoelectric sensors and the possible application of nonlinearity in enhancing the "smartness" of ceramics and composites. Scale effects on ferroics are of increasing interest and the manner in which nano-scale polar regions control the properties of relaxor ferroelectrics is again emphasized.

For material studies the detailed examination of the evolution of diffuse, then relaxor behavior in lanthanum modified lead titanate has been completed. Interest in the soft PZTs, relaxor and phase switching materials continues, with a new thrust developing towards a more complete description of domain walls and morphotropic phase boundaries in perovskites. Materials issues in the wear out and fatigue effects in polarization switching systems have been subjected to detailed evaluation and the precautions necessary to fabricate long lasting materials which will stand 10^9 switches without any fatigue are delineated.

Sensor studies have continued to focus on flextensional composites and have demonstrated both the very high hydrostatic sensitivity and the amplified actuation response of this configuration. Integration of sensors with the "moonie" actuators has been accomplished in individual cells. Actuator studies cover the gamut from highly reproducible micro positioning using electrostrictive compositions to high strain polarization switching shape memory ceramics capable of driving a latching relay device. Studies of the destruct mechanisms in practical MLA systems complement the earlier materials work and show the importance of internal electrodes and consequent stress concentrations for crack initiation. Integration studies have focused upon more detailed evaluation of 1:3, 2:2 and tubular 1:3 composites and upon the influence of the polymer characteristic and of face plates and edge guards upon sensing and actuation capabilities. In processing, the interest in dielectrophoretic forming of composites is continuing and assembly of interesting 1:3 composites is demonstrated. Guidelines for the transducer application of electrostrictive materials have been formulated and a useful classification scheme proposed. In fiber PZTs techniques for fabricating thin (30 μ) fibers are demonstrated, the first successful technique for poling fibers is described and it is shown that properly poled fibers have electro-elastic characteristics similar to bulk material. Film papers are selected to reflect the transducer

capabilities of lead titanate and of phase switching lead zirconate titanate stannate antiferroelectric compositions.

INTRODUCTION

This report summarizes work carried out in the Materials Research Laboratory of The Pennsylvania State University during the second year of an ONR sponsored University Research Initiative (URI) entitled "Materials for Adaptive Structural Acoustic Control." The program has a proposed five year duration and is being carried out largely in five sections each reporting to a senior faculty member.

These sections are:

Materials Studies	A. S. Bhalla
Composite Sensors	R. E. Newnham
Actuator Studies	K. Uchino
Integration Issues	J. Dougherty
Processing Studies	T. R. Shrout

There is of course a necessary and highly desirable overlap between many of these topic areas, the reciprocity of the piezoelectric effect which is at the base of many of our studies ensure that most acutators can also be used as excellent sensors. The composite approaches for which the laboratory is quite renowned fuzzy the edges of the integration issues and in fact most faculty practice in more than one topic area.

Following precedent established over more then seventeen earlier annual reports, this document presents a very brief narrative summary of the work which has been accomplished making reference for backup to the fifty-two published studies from the group which are included as the technical appendices which form the bulk of the report.

In this respect, for convenience in reference, the papers are grouped under the following topic headings.

1. GENERAL SUMMARY PAPERS
2. MATERIALS STUDIES
3. COMPOSITE SENSORS
4. ACTUATOR STUDIES
5. INTEGRATION ISSUES
6. PROCESSING STUDIES
7. THIN FILM FERROELECTRICS

In general discussion, a new generalization of the broad panoply of applications for ferroelectrics has been given, highlighting the mechanisms which contribute the important responses. A balanced analysis of high temperature stress/strain sensors is presented, and the

manner in which nonlinearity may enhance the "smartness" inherent in ferroelectric electroceramics and composites are emphasized. Scale effects are clearly becoming of increasing interest and the manner in which self assembling nanoscale heterogeneity on an coherent crystal lattice influences the phase behavior in relaxor ferroelectrics is again emphasized.

For materials studies interest in the soft PZTs and relaxor ferroelectrics continues, but a new developing thrust focuses upon a more complete theoretical description of domain walls and morphotropic phase boundaries. This is in preparation for the more complete experimental information which should come available from studies of domain walls and phase boundaries with the new coherent source TEM machines now coming into use. In considering wear out and fatigue mechanism in charge switching systems it is important to separate material issues from the ancillary problems imposed in the fabrication of practical actuators. A sequence of the papers presented wraps up a very comprehensive evaluation of phenomena contributing to polarization switching fatigue in PZT and PLZT ceramics. It is intriguing to see that from grain grown PLZTs it has been possible to extract some of the first single crystal data in this system. One notes also that the continuing refinement of approaches, highlights new experimental needs, such as refinement of the d_{33} meter to provide phase information and the full complex d^* constants.

For sensing and some actuation functions, the emphasis of the program has continued on the flextensional moonie systems. The patent has now been issued for this technology. The first integration of the moonie into a composite sensing and actuation couple is demonstrated and the ability to control vibration explored. Several more sophisticated systems which seek to exploit nonlinear properties for very smart composite behavior have also been reported.

In actuation, the strong electrostriction in the relaxor ferroelectric families provides highly reproducible strain which can be exploited in a wide family of micropositioners. The application of more conventional piezoelectric actuators in smart systems and adaptive structures is discussed and the limiting destruct mechanisms for the practical multilayer co-fired devices explored. Clear evidence of the cracking which occurs at high strain levels is obtained from simultaneous optical studies. The basic characteristics of phase switching shape memory ceramics are discussed and their application to a bistable latching relay structure examined.

For applications where a very limited temperature range can be tolerated the extremely high induced piezoelectric effects near the Curie temperature show very interesting application possibilities.

The complexities of integration, as exemplified by the piezoceramic polymer composites, have been explored using examples in 2:2 connectivity, classic 1:3 composite and a new family of tubular type 1:3 systems. For the tubular geometry significant advantage can be obtained by control of tube diameter and wall thickness. Economical modes for fabricating these structures are being actively explored with FMI and with Material Systems Inc. A detailed study of the P(VDF-

8

TrFe) copolymer system initiated under funding from Sykes Associates has now been completed and a model proposed which is in good agreement with the experimental results.

Processing related problems in co-fired multilayer actuators (MLAs) are discussed, and a newer configuration using interdigitated internal electrodes is highlighted. This configuration permits the fabrication of larger actuators with longer throws. The capability of electrophoretic and dielectrophoretic forces in permitting the intelligent assembly of pseudo 1:3 composites is examined and the rheological effects in high K suspensions explored. Criteria for selecting relaxor ferroelectric composition for transducer applications have also been formalized. Lead zirconate titantate fibers are of interest for many type of 'smart' structure, techniques for fabricating fibers are discussed and the first demonstration of poling and piezoelectric response have been effected.

In related thin film work, the nature and origin of the strong orientation effects in sol-gel lead titanate thin films has been explained. Using the sol-gel method thin films of PSnZT compositions have been fabricated and the phase switching behavior from antiferroelectric to ferroelectric states under electric fields evident in the bulk ceramics has been confirmed for the film system.

1.0   GENERAL SUMMARY PAPERS

Increasing interest in the topic of high temperature vibration sensing is reflected in the balanced discussion in Appendix 1. Commercially available techniques are first reviewed concentrating on sensors with operating temperatures in excess of 650°C. New piezoelectric options are underscored in the layer structure and complex pyrochlore ferroelectrics which have $T_c > 1000$°C and in new AlN thin film sensors which are piezoactive above 1150°C. In the series Materials Science and Technology, Vol. II, K. Uchino provides a comprehensive discussion of the fundamentals of ferroelectricity and a broad ranging discussion of the applications of ferroelectric ceramics to capacitor dielectrics, pyroelectric devices, piezoelectric sensors and actuators, electro-optic and PTC systems (Appendix 2). The topic of "smart" materials was covered in Volume 18 of the MRS Bulletin with the introduction discussing development in the field from smart, to very smart towards Intelligent Materials discussed by the guest editor R. E. Newnham (Appendix 3). The whole area of size effects in ferroic materials is of increasing interest, stimulated by the very fine scale microstructures which appear in thin film systems. Appendix 4 discusses scale effects reaching into the nanometer region and their importance for the control of nonlinear phenomena. A more detailed discussion of the unusual self-assembling self-limiting nanoscale heterogeneity which develops on the coherent crystal lattice of the relaxor ferroelectrics is given in Appendix 5. Lead magnesium niobate is the classic example exhibiting unusual glass like dielectric properties as the polar nanostructure attendant in limited ordering of the B site cations freezes in.

2.0 MATERIALS STUDIES

Examination of the properties of lanthanum modified lead titanate continues the interest in nanoscale sub-structures with evidence of a texturing in the domain structure of the ferroelectric phase as the system evolves toward diffuse then relaxor behavior with increasing lanthanum concentration (Appendix 6). A more comprehensive report will be given in the 1994 annual report as Dr. G. Rossetti writes up his excellent thesis work on the PLT system. Appendices 7-10 cover the initiation of more systematic in depth theoretical studies of two of the most important problems in piezoelectric ceramics, namely intrinsic boundary conditions on the co-existence of ferroelectric phases at the Morphotropic Phase Boundary (MPB) in PZT (Appendix 7), and that of the detailed description of domain walls by continuum theory (Appendix 9) and the light which this can throw upon the fundamentally important gradient terms in the Landau Ginsburg Devonshire Theory (Appendix 8). These approaches are particularly timely as the new coherent source Transmission Electron Microscopes promises a cornucopia of new data on internal fields in ferroics (Appendix 10).

New experimental information regarding domain wall contributions to dielectric and piezoelectric response are presented in Appendices 11-13. Since wall motion can produce no volumetric change at low field levels a separation between intrinsic and extrinsic (domain) contribution to response can be effected by considering the temperature dependence of hydrostatic versus linear piezoelectric responses. Using this method it is shown (Appendix 11) that domains make the major contribution to response in both doped and undoped PZTs at the 52:48 Zr:Ti ratio. The use of acoustic emission and concurrent current pulse measurement to separate domain switching and micro-cracking which can occur in the poling process is discussed in Appendix 12. An extension of current phenomenological theory to explore nonlinearities in response associated with domain wall motion is described in Appendix 13. New measurements of nonlinearity in PZT and PLZT compositions are used to support the theoretical conclusions. Full detail of earlier studies on fatigue effects associated with polarization switching in PZT and PLZT compositions are given in Appendices 14-20. These studies focus on material problems associated with electroding, grain size effects, composition and temperature influences, the effects of porosity and the vital importance of full density, electrodes and electroding methods, and field induced stress concentration.

It is shown that with proper precautions in these areas it is possible to achieve zero fatigue after ~10^9 cycles of field application. In PLZT at the 8:65:35 composition grain grown ceramics with single grains in the range 50-100 μ meter diameter, supplied from the Shanghai Institute of Ceramics have been used to measure the anisotropy of the single crystal dielectric response (Appendix 21). Using a highly simplified model a qualitative evaluation of the extrinsic domain contribution to d_{33} has also been given (Appendix 22).

10

For a number of polymer and composite piezoelectrics it is clear that all material constants are complex. In Appendix 23 a modification to the Berlincourt d_{33} meter is described which phase locks the charge detector to the AC force generator. In the phase locked mode the meter will measure d_{33} values down to 1 pC/N and phase angle to 0.05°.

3.0 COMPOSITE SENSORS

Sensor studies have focused upon the flextensional "moonie" type systems. A copy of United States Patent 5,276,657 detailing the several claims for the origination of this concept by Newnham, Xu, and Yoshikawa is given in Appendix 24 which covers mostly the actuation function. The design of the moonie type structure for a range of both sensing and actuation functions is discussed in Appendix 25. Resonant frequencies and finite element analysis of the stress distribution are considered and factors which affect the integration of both sensing and actuation in the same package are discussed. This theme is further developed in Appendix 26 which considers explicitly a vibration control element using a moonie actuator and separate piezoceramic sensor. The device has a dynamic range from 100 Hz to 2,500 Hz and is capable of sensing and suppressing small ~ 1μm displacements at small force levels. This topic is developed further in Appendix 27 which also considers multiple stacked flextensional structures.

The topic of composite multilayer piezoelectric:piezomagnetic structure is considered theoretically in Appendix 28 and expressions derived for the effective magneto-electric coupling in such structures are derived. Examples of electroceramic materials and composite structures which qualify for the adjective 'smart' are discussed in Appendix 29.

The final moonie flextensional paper (Appendix 30) discusses in more detail the design of highly reliable units using finite element methods to model shape, material and geometrical contributions to the response.

4.0 ACTUATOR STUDIES

The relaxor ferroelectric nanocomposites discussed in Appendix 5 are materials which have useful and important applications in actuator studies discussed in Appendix 31. The absence of classical stable domain structures in these materials leads to highly reproducible anhysteritic strain response for micro-positioning and optical applications. A more general discussion of conventional piezoelectric actuators and the very wide range of material systems and modes of operation is given in Appendix 32. Shape memory and semiconductor derived monomorphs are discussed along with more conventional piezoelectric stacked elements. A problem in the stacked actuators made by the co-fire process concerns the stress concentration at electrodes which terminate within the ceramic. In Appendix 33 the problem in graphically illustrated by optical observation of the cracks which initiate in the regions of tensile stress at these electrode edges. The

whole range of ceramic actuators is reviewed in Appendix 34 with examples of a wide range of practical capabilities for both simple and mechanical amplifier configurations.

The topics of actuation in smart systems is taken up briefly in Appendix 35 which is the outline of a paper presented at ADPA/AIAA/ASME/SPIE. Appendix 36 takes up in more detail the mechanical damage mechanisms which limit the performance of co-fired multilayer actuators and discusses an interesting acoustic emission test for diagnosing wear out in actuators used in highly critical applications like precision machining. It is interesting that the phase switching antiferroelectric PZT compositions show shape memory behavior and of particular importance as shown in Appendix 37 is the fact that shape recovery can be activated electrically without ·' energetically extravagant heating and cooling required in the metallic shape memory syste Appendix 37 discusses the phenomena in PZSnT and its application to a simple latching relay. Smart control of actuators is discussed in Appendix 38, and the very high values which can be achieved in compositions close to the ferroelectric Curie point in some solid solution systems is determined in Appendix 39.

5.0 INTEGRATION ISSUES

A much more detailed analysis of the piezoceramic:polymer composite in 2:2 connectivity is given in Appendix 40. The theoretical study shows that major stress transfer takes place near the surface so that it may be desirable to have a stiffer polymer in this location. Work on the 1:3 polymer ceramic composites has been going forward with FMI (Appendix 41) who have facilities for assembling these tubular systems. The results of analysis confirm the advantage of this tubular configuration and the very high values of d_h which can be achieved. The laboratory has been involved in a comprehensive experimental study of the piezoelectric PVDF copolymer (vinylidene fluoride:trifluoroethylene 75:25) and has demonstrated the complex nature of elastic, dielectric and piezoelectric constants. To explain the different observed dispersion regimes a two phase composite model is proposed (Appendix 42) and numerical calculations from the model are shown to be in good agreement with experiment.

In the final paper in this section (Appendix 43) the effects of surface face plates and edge strips on the hydrostatic response of 1:3 composite panels are considered. It is shown that the earlier shear-coupling model provides good guidelines for the design and permits the optimization of geometry and material properties.

6.0 PROCESSING STUDIES

For co-fired multilayer piezoelectric actuators it is essential to consider the processing parameters along with the design of the system (Appendix 44). For the very thin layer low voltage structures, stress concentrations at the electrode edges limit application of the simple MLC design

and it is necessary to go to slits or gaps in these locations to relieve stress. Full plate through electrodes can only be accomplished for thicker layers and suffer also from the problems of silver migration. A new type of interdigitated longitudinal mode which can use d_{33} is discussed and the performance achieved does permit longer actuators with larger throw. Manipulation of the microstructure in polymer/ceramic 0:3 composites using dielectrophoretic orientation and chaining techniques is discussed in Appendix 45. The paper highlights the use of in situ dielectric measurement to determine alignment, batch uniformity and as a general quality control technique.

Electrostriction in relaxor ferroelectric systems occurs with a number of distinct "flavors." Appendix 46 suggests a useful classification which separates the families into four major categories. There is a growing interest in the possible advantages of PZT fibers for both passive and active smart systems in vibration control. Techniques for the fabrication by sol-gel methods, the poling and testing of very fine fibers are discussed in Appendix 47. It is gratifying to note that even at 30 μ meter diameter the properties are similar to those of an equivalent bulk PZT. The properties of electrorheological fluids using fine $BaTiO_3$ powders in silicone oil are discussed in Appendix 48. Under 60 Hz AC fields strong fibril formation was observed optically and turbulent flow was not observed for fields up to more than 20 Kv/cm. The characteristics observed in yield stress suggest a dominant dipole:dipole interaction in chain formation. More details of the application and versatility of the dielectrophoretic assembly method are given in Appendix 49 which discusses pseudo 1:3 composite assemble and the conditions required for optimum alignment.

7.0 THIN FILMS FERROELECTRICS

Following earlier established practice, thin film studies which we believe are relevant to the objectives of this program are appended. Conditions which influence the orientation of sol-gel formed lead titanate films used for high frequency transduction are discussed in Appendix 50. It is shown that both the nature of the sol and the type and condition of the substrate can have a marked influence upon the nature and the degree of film orientation.

The phase switching high zirconia PSnZT composition are of strong interest in bulk form for high strain actuation. In Appendix 51 it is demonstrated that thin films in the same composition family can be fabricated by sol-gel spin on techniques. The films also exhibit phase switching under high electric field with fast switchover times (~300 n sec) and high induced elastic strain (~0.16%).

For all perovskite type thin films, and for films like the YBCO superconductors which are in closely similar structure types, substrates with appropriate matching crystallographic structure and unit cell dimensions are of major importance. An example of the materials of interest is $Ba(Mg_{1/3}Ta_{2/3})O_3$ (Appendix 52), a cubic perovskite which is shown to have exceedingly low

microwave dielectric loss. The laboratory has an extensive ONR/ARPA sponsored program on substrate materials which will be of interest to both ferroelectric and superconductor film fabricators.

8.0 HONORS AND AWARDS

Over the year 1993 the Ferroelectric Group in MRL has continued to receive excellent recognition from both Domestic and International Societies. In May 1993 Professor R. E. Newnham was awarded the Humboldt Research Award which will support his stay at the Max Plank Institute in Stuttgart during early 1994. Professor L. E. Cross and Dr. A. S. Bhalla were recipients of the Edward C. Henry Award from the Electronics Divisions of the American Ceramic Society. The award for the best paper in electroceramics published in the Journal over the period 1989-1993 and was for their paper with T. Takanaka and K. Sakata on "Dielectric Piezoelectric and Pyroelectric Properties of Lead Zirconate:Lead Zinc Niobate Ceramics."

The group has continued to be very active in the organization of both National and International Meetings. For IMF8 L. E. Cross was Vice Chairman, and orchestrated industrial support, S. J. Jang and R. E. Newnham were responsible for the Proceedings.

For ISAF9 which will be at Penn State in August 1994 A. S. Bhalla is General Chair. Dr. Bhalla was also responsible for ACerS Symposia on Materials for Smart/Intelligent Systems and for Ferroelectric Thin Films at the Fall 1993 PAC RIM Meeting in Hawaii.

9.0 APPRENTICE PROGRAM

The 1993 ONR Apprentices were:

Liza Rivera
A senior from State College High School. Her work was in the area of electrophoresis and dielectrophoretic assembly of composites.

Maria Teresa Defesdini
Maria was a graduating senior from Col. Senora Merced High School in Puerto Rico. Her studies were focused on the processing and fabrication of relaxor ferroelectric materials with a range of compositions directly relevant to work on the URI program.

10.0 GRADUATING STUDENTS ON THE PROGRAM

George A. Rossetti, Jr., PhD, Solid State Science, "Structural and Thermodynamic Investigation of the Ferroelectric Phase Transition in Lanthana-Substituted Lead Titanate," May 1993 (Abstract included as Appendix 53).

Jaiyu Chen, PhD, Electrical Engineering, "Electrical and Electromechanical Properties of Ferroelectric Thin Films for Microelectromechanical Applications," August 1993 (Abstract included at Appendix 54). *Only the electromechanical measurement part of this work was supported on URI funding.*

Edward Alberta, MS, Solid State Science, "The Dielectric, Piezoelectric and Pyroelectric Properties of Lead Zirconate-Lead Zinc Niobate-Lead Titanate Ceramics," October 1993 (Abstract included as Appendix 55).

11.0 PAPERS PUBLISHED IN REFERRED JOURNAL

1. Turner, R. C. , P. A. Fuierer, R. E. Newnham, and T. R. Materials for High Temperature Acoustic and Vibration Sensors: A Review. Applied Acoustics 41:1-26 (1993).

2. Uchino, K. Ferroelectric Ceramics. Materials Science and Technology, Edited by R.W. Cahn, P. Haasen, E.J. Kramer, Vol. I, VCH 1994.

3. Newnham, R. E. Smart, Very Smart and Intelligent Materials, MRS Bulletin XVIII(4), 24-26 (April 1993).

6. Rossetti, G. A., Jr., W. Cao, and C. A. Randall. Microstructural Characterization and Diffuse Phase Transition Behavior of Lanthanum Modified Lead Titanate. Ferroelectrics: Proceedings of IMF8, Gaithersburg, Maryland (August 1993).

7. Cao, W. and L. E. Cross. Distribution Function of Coexisting Phases in a Complete Solid Solution System. J. Appl. Phys. 73(7), 3250 (1993).

8. Cao, W. Polarization Gradient Coefficients and the Dispersion Surface of the Soft Mode in Perovskite Ferroelectrics. J. Phys. Soc. Jpn. 63, 827 (1994).

9. Cao, W. and L. E. Cross. Nonlinear and Nonlocal Continuum Theory on Domain Walls in Ferroelectrics. Ferroelectrics: Proceedings of IMF8, Gaithersburg, Maryland (August 1993).

10. Cao, W. and C. Randall. Theory on the Fringe Patterns in the Study of Ferroelectric Domain Walls Using Electron Holograpy. Solid State Comm. 86, 435-439 (1993).

11.0 PAPERS PUBLISHED IN REFERRED JOURNAL (continued)

11. Zhang, Q. M., H. Wang, N. Kim, and L. E. Cross. Direct Evaluation of Domain Walls and Intrinsic Contributions to the Dielectric and Piezoelectric Constants and Their Temperature Dependence in Lead Zirconate Titanate Ceramics. J. Appl. Phys. 75 (1), 454 (1994).

12. Subbarao, E. C., V. Srikanth, W. Cao, and L. E. Cross. Domain Switching and Microcracking during Poling of Lead Zirconate Titanate Ceramics. Ferroelectrics 145, 271-281 (1993).

13. Li, S., W. Cao, R. E. Newnham, and L. E. Cross. Electromechanical Nonlinearity of Ferroelectric Ceramic and Related non 180° Domain Wall Motion. Ferroelectrics 139, 25-49 (1993).

14. Jiang, Q., W. Cao, and L. E. Cross. Electrical Fatigue in Lead Zirconate Titanate Ceramics. J. Am. Ceram. Soc. 77(1), 211-215 (1994).

15. Jiang, Q. and L. E. Cross. Effect of Porosity on Electrical Fatigue Behavior in PLZT and PZT Ceramics. J. Mat. Sci. 28, 4536-4543 (1993).

16. Jiang, Q., E. C. Subbarao, and L. E. Cross. Effects of Electrodes and Electroding Methods on Fatigue Behavior in Ferroelectric Materials. Ferroelectrics: Proceedings of IMF8, Gaithersburg, Maryland (August 1993).

17. Jiang, Q., E. C. Subbarao, and L. E. Cross. Fatigue in PLZT: Acoustic Emission as a Discriminator Between Microcracking and Domain Switching. Ferroelectrics: Proceedings of IMF8, Gaithersburg, Maryland (August 1993).

18. Li, S., A. S. Bhalla, R. E. Newnham, and L. E. Cross. Quantitative Evaluation of Extrinsic Contribution to Piezoelectric Constant d33 in Ferroelectric PZT Ceramics. Materials Letters 17, 21-26 (1993)

19. Wang, H., Q. Zhang, and L. E. Cross. A High Sensitivity Phase Sensitive d33 Meter for Complex Piezoelectric Constant Measurement. Jpn. J. Appl. Phys. 32(Pt. 2; No. 9A), L1281-83 (1993).

20. Onitsuka, K., A. Dogan, J. A. Tressler, Q. C. Xu, S. Yoshikawa, and R. E. Newnham. Metal-Ceramic Composite Transducer–The Moonie. Ferroelectrics: IMF8, Gaithersburg, Maryland (August 1993).

21. Tressler, J. F., Q. C. Xu, S. Yoshikawa, K. Uchino, and R. E. Newnham. Composite Flextensional Transducer for Sensing and Actuating. Ferroelectrics: IMF8, Gaithersburg, Maryland (August 1993).

22. Newnham, R. E., A. Dogan, Q. C. Xu, K. Onitsuka, J. Tressler, and S. Yoshikawa. Flextensional "Moonie" Actuators. IEEE 1993 Ultrasonics Symp. Proc., Baltimore, Maryland; Vol. 2, pp. 509-514 (1993).

23. Harshe, G., J. P. Dougherty, and R. E. Newnham. Theoretical Modeling of Multilayer Magnetoelectric Composites. Int. J. of Appl. Mag. in Mtls. 4, 145-159 (1993).

24. Newnham, R. E. and G. R. Ruschau. Electromechanical Properties of Smart Materials. J. Intelligent Mtls. Systems and Structures 4, 289 (1993).

25. Onituka, K., A. Dogan, Q. Xu, S. Yoskikawa, and R. E. Newnham. Design Optimization for Metal-Ceramic Composite Actuator, "Moonies." Ferroelectrics: IMF8, Gaithersburg, Maryland (August 1993).

26. Uchino, K. Relaxor Ferroelectric Devices. Ferroelectrics: Proceedings IMF8, Gaithersburg, Maryland (August 1993).

27. Uchino, K. Recent Development of Piezoelectric Actuators for Adaptive Structures. 3rd International Conference on Adaptive Structures (1991).

28. Furuta, A. and K. Uchino. Dynamic Observation of Crack Propagation in Piezoelectric Multilayer Actuators. J. Am. Ceram. Soc. 76(6), 1615 (1993).

29. Uchino, K. Ceramic Actuators Principles and Applications. MRS Bull. (April 1993).

30. Uchino, K. Applications of Piezoelectric Ceramics in Smart Actuator Systems. ADPA/AIAA/ASME/SPIE Cont. on Active Mtls. (1992).

32. Furuta, A. , K. Y. Oh, and K. Uchino. Shape Memory Ceramics and Their Application to Latching Relays. Sensors and Materials 3, 205 (1992).

33. Wang, H., Zhang, and L. E. Cross. Piezoelectric Relaxation of P(VDF-TrFE) Copolymers. Ferroelectrics: IMF8, Gaithersburg, Maryland (August 1993).

34. Miller, D., C. A. Randall, A. S. Bhalla, R. E. Newnham, and J. Adair. Electrorheological Properties of $BaTiO_3$ Suspensions. Ferroelectric Letters 15, 141-151 (1993).

35. Udayakumar, K. R., S. B. Krupanidhi, K. Kushida, and L. E. Cross. Origina of Orientation in Sol-Gel-Derived Lead Titanate Films. J. Am. Ceram. Soc. 76, 1345 (1993).

36. Brooks, K. G., J. Chen, K. R. Udayakumar, and L. E. Cross. Electric Field Forced Phase Switching in La Modified Lead Zirconate Titanate Stannate Films. J. Appl. Phys. 75, 1399 (1994).

37. Sheen, J., R. Guo, A. S. Bhalla, and L. E. Cross. Measurements of Dielectric Constant and Quality Factor of $Ba(Mg_{1/3}Ta_{2/3})O_3$ at X Band Frequencies. Ferroelectric Letters 16, 33 (1993).

12.0 INVITED PRESENTATIONS AT NATIONAL AND INTERNATIONAL MEETINGS

1. Cross, L. E., High Strain Actuators and Agile Transducers, *SPIE Mtg. Smart Structures and Materials,* Albuquerque, New Mexico (January 31, 1993).

2. Cross, L. E., Relaxor Ferroelectrics: Current Problems and Opportunities for New Work, *ONR Workshop on Fundamental Experiments in Ferroelectrics,* Williamsburg, Virginia (February 7, 1993).

12.0 INVITED PRESENTATIONS AT NATIONAL AND INTERNATIONAL MEETINGS (continued)

3. Cross, L. E., Applications of Ferroelectric Thin Films to Microelectromechanical (MEMS) Systems, *Prospector V Conference*, Park City, Utah (March 22, 1993).

4. Cross, L. E., Ferroelectric Materials and Devices Current Issues and Future Prospects, *MRS Spring Meeting*, San Francisco, California (April 12, 1993).

5. Cross, L. E., MEMS Systems Based On Ferroelectric Films, *Am. Ceram. Soc. 95th Annual Mtg.*, Cincinnati, Ohio (April 18-22, 1993).

6. Cross, L. E., Relaxor Ferroelectrics: An Overview, *IMF8*, Gaithersburg, Maryland (August 8, 1993).

7. Cross, L. E., Electronic Ceramics: New Actuators and Transducers, *1st Okinaga Symposium*, Ikabakura, Tokyo, Japan (August 29, 1993).

8. Cross, L. E., Relaxor Ferroelectrics: Self Assembling Nanocomposites, *IMRS*, Tokyo, Japan (August 31, 1993).

9. Cross, L. E., Shape Memory in High Strain Polarization Switching Ferroelectric Actuators, *IUMRS-ICA Conference*, Wuhan, China (September 6, 1993).

10. Cross, L. E., Recent Developments in Piezoelectric and Electrostrictive Sensors and Actuators, *Am. Ceram. Soc. PAC RIM Meeting*, Oahu, Hawaii (November 7, 1993).

11. Cross, L. E., Shape Memory Ceramics: Status and Potential, *Sixth US:Japan Seminar on Dielectric and Piezoelectric Ceramics*, Lahaina, Hawaii (November 11, 1993).

12. Newnham, R. E., Structure-Property Relationships in Act ator Materials, Annual meeting of the American Ceramic Society, Cincinnati, Ohio (4/19-21/93).

13. Newnham, R. E., Structure-Property Relations in Actuator Materials, Seminar at the Industrial Technology Research Institute, Hsinchu, Taiwan (4/30/93).

14. Newnham, R. E., Ceramic Sensors and Actuators - Smart Materials, Material Research Society of Taiwan, Keynote address at annual meeting of Chinese Society of Materials Science, National Chiao-Tung University, Hsinchu, Taiwan, Republic of China (5/1/93).

15. Newnham, R. E., Electrostrictive Materials, Seminar at the National Tsing Hua University, Hsinchu, Taiwan, Republic of China (5/3/93).

16. Newnham, R. E., Composite Electroceramics, seminar at the National Cheng-Kung University, Tainan, Taiwan, Republic of China (5/5/93).

17. Bhalla, A. S., Ferroelectric Fiber Devices for Holographic Image Storage, *IMF8*, Gaithersburg, Maryland (August 8, 1993).

18. Uchino, K., Relaxor Ferroelectric Devices, *IMF8*, Gaithersburg, Maryland (August 8-13, 1993).

19. Uchino, K., Photostriction and Its Applications, *Am. Ceram. Soc. PAC RIM Meeting*, Oahu, Hawaii (November 7-10, 1993).

12.0 INVITED PRESENTATIONS AT NATIONAL AND INTERNATIONAL MEETINGS (continued)

20. Uchino, K., Optical Domain Studies, *ONR Transducer Materials Review*, State College, Pennsylvania (April 6-8, 1993).

21. Yoshikawa, S. and K. Uchino., Recent Development of Multilayer Actuators–Review of Materials and Structures, *95th Annual Meeting of the American Ceramic Society*, Cincinnati, Ohio (April 19-21, 1993).

22. Randall, C. A., C. P. Bowen, T. R. Shrout, and A. S. Bhalla. Smart Processing of Composite Materials by Electric Fields, *Am. Ceram. Soc. PAC RIM Meeting*, Oahu, Hawaii (November 7, 1993).

23. Uchino, K., Photo Striction and Its Applications, *Am. Ceram. Soc. PAC RIM Meeting*, Oahu, Hawaii (November 7, 1993).

24. Krupanidhi, S. B., H. Hu, and G. Fox, Study of DC Conduction Mechanisms in Ferroelectric $Ph(ZrTi)O_3$ and $(PbLa)TiO_3$ Thin Films, *Sixth US:Japan Seminar on Dielectric and Piezoelectric Ceramics*, Lahaina, Hawaii (November 11, 1993).

25. Dougherty, J. P. and R. Bacsa, Synthesis of $BaTiO_3$ Films on Titanium, *Sixth US:Japan Seminar on Dielectric and Piezoelectric Ceramics*, Lahaina, Hawaii (November 11, 1993).

26. Trolier-McKinstry, Susan, Microstructure Property Relations in Ferroelectric Films, *Sixth US:Japan Seminar on Dielectric and Piezoelectric Ceramics*, Lahaina, Hawaii (November 11, 1993).

27. Uchino, K., M. Mulvihill, Ki Young Oh, R. Brodeur, and L. E. Cross, Optical Studies of Domains in Ferroelectric Actuators, *Sixth US:Japan Seminar on Dielectric and Piezoelectric Ceramics*, Lahaina, Hawaii (November 11, 1993).

28. Randall, C. A., R. P. Brodeur, S. J. Jang, and T. R. Shrout, Classification of Electrostrictive–Based Materials for Transducers, *Sixth US:Japan Seminar on Dielectric and Piezoelectric Ceramics*, Lahaina, Hawaii (November 11, 1993).

29. Randall, C. A., C. P. Bowen, T. R. Shrout, A. S. Bhalla, and R. E. Newnham, Dielectrophoresis: A Means to Assemble Novel Electroceramic Composites, *Sixth US:Japan Seminar on Dielectric and Piezoelectric Ceramics*, Lahaina, Hawaii (November 11, 1993).

30. Guo, R., Electro-optic Properties of Ferroelectric Lead Barium Niobate (PBN) Single Crystals, *Sixth US:Japan Seminar on Dielectric and Piezoelectric Ceramics*, Lahaina, Hawaii (November 11, 1993).

31. Bhalla, A. S., New Pyro-optic Technique for Imaging Long Wave IR Radiation, *Sixth US:Japan Seminar on Dielectric and Piezoelectric Ceramics*, Lahaina, Hawaii (November 11, 1993).

32. Cao, W. and L. E. Cross, Phase Coexistence at the Morphotropic Phase Boundary in Lead Zirconate Titanate, *Sixth US:Japan Seminar on Dielectric and Piezoelectric Ceramics*, Lahaina, Hawaii (November 11, 1993).

12.0 INVITED PRESENTATIONS AT NATIONAL AND INTERNATIONAL MEETINGS (continued)

33. Yoshikawa, S., U. Selvaraj, P. Moses, and T. R. Shrout, Pb(ZrTi)O₃(PZT) Fibers: Formation and Property Measurement Methods, *Sixth US:Japan Seminar on Dielectric and Piezoelectric Ceramics*, Lahaina, Hawaii (November 11, 1993).

34. Cao, Wenwu, The Importance of Conventional and Holographic Electron Microscopy in the Fundament Understanding of Ferroelectrics, *The Second Williamsburg Workshop on Fundamental Experiments in Ferroelectrics (MIT/ONR)*, Williamsburg, Virginia (February 1993).

35. Bhalla, A. S., Photorefractive Fibers for Optical Holographic Storage, *Gordon Conference–Optical Processing and Holography* (June 28-July 2, 1993).

36. Bhalla, A. S., Photorefractive Materials: Sensors and Storage Devices, *SPIE Meeting–Photorefraction Materials: Effects and Applications*, San Diego, California (July 11-14, 1993).

37. Bhalla, A. S., Morphotropic Phase Boundaries and Relaxor Ferroelectrics, *Workshop on Optical Materials*, Tokyo, Japan (July 21, 1993).

38. Bhalla, A. S., Single Crystal Fibers for Sensors and Optoelectronic Applications, *International Meeting on Actuator/Sensors*, Japan (July 23, 1993).

39. Bhalla, A. S., Applications of Morphotropic Phase Boundary Compositions, *IUMRS–International Meeting on Advanced Materials: Relaxor Ferroelectrics*, Japan (August 31-September 3, 1993).

13.0 INVITED PAPERS PRESENTED AT UNIVERSITY, GOVERNMENT, AND INDUSTRIAL LABORATORIES

1. Newnham, R. E., Recent Trends in Multilayer Technology, Seminar at Vistatech Corp., San Diego, CA (5/13/93).

2. Newnham, R. E., Smart Ceramics, Seminar at Engineering College, University of California, Irvine, CA (5/14/93).

3. Newnham, R. E., S. Krupanidhi, and A. Trolier-McKinstry, Two-day short course at U.S. Army Research Laboratory, Electronics Technology and Power Sources Directorate, Fort Monmouth, NJ (5/17-28/93).

4. Newnham, R. E., Smart Ceramics, Lecture at the Ceramic Science and Technology Workshop supported by the U.S. Office of Naval Research European Office, Technical Council of Turkey and the Middle East Technical University, In Ankara, Turkey (7/21-22/93).

5. Newnham, R. E., Composite Electroceramics, Raychem Corporation Seminar, Chicago, IL (7/28/93).

6. Shrout, T., Processing of Ferroelectric and Related Materials, Cabot Co., Boyertown, PA (April 1993); ATC Co., Jacksonville, FL (October 1992); and Harris Co., Dundalk, Ireland (May 1993).

13.0 INVITED PAPERS PRESENTED AT UNIVERSITY, GOVERNMENT, AND INDUSTRIAL LABORATORIES (continued)

7. Shrout, T., Non-Linear Dielectrics, Hughes Aircraft Co., Los Angeles, CA (September 1993) and General Electric Co., Schenectady, NY (May 1993).

8. Shrout, T., Real Time Sintering Observations of 2LTJCC Substrate and Conductor Materials, Heraeus Co., Konshohocken, PA (April 1993).

9. Shrout, T., Lead Based $Pb(B_1B_2)O_3$ Relaxors vs $BaTiO_3$ Relaxors for Multilayer Capacitors, Storage Tek and AKZO-Amp.

10. Uchino, K., Piezoelectric/Electrostrictive Actuators - Tutorial Lecture, *Third Smart Actuator Symp.*, State College, Pennsylvania (October 22-23, 1992).

11. Uchino, K., "Fabrication Processes and Actuator Characteristics: Introduction," *Fourth Smart Actuator Symp.*, State College, Pennsylvania (January 21-22, 1993).

12. Uchino, K., Electrodes for Ceramic Actuators, *Fourth Smart Actuator Symp.*, State College, Pennsylvania (January 21-22, 1993).

13. Uchino, K., Fabrication of Multilayer Piezoelectric Actuators, *Fourth Smart Actuator Symp.*, State College, Pennsylvania (January 21-22, 1993).

14. Newnham, R. E., Electro Sensors and Actuators, Matsushita Central Research and Development Laboratory, Osaka, Japan (12/7/92).

15. Newnham, R. E., Electroceramic Sensors and Actuators, NEC Research and Development Laboratory, Kawasaki City, Japan (12/8/92).

16. Newnham, R. E., Electroceramic Composite Transducers, Toshiba Ceramics Research Laboratory, Hadano, Japan (12/9/92).

17. Newnham, R. E., Structure-Property Relations in Composite Electroceramics, Materials Science Dept. Seminar, Shonan Institute of Technology, Fujisawa, Japan (12/11/92).

18. Newnham, R. E., Structure-Property Relationships in High-Permittivity Ceramics, Murata Manufacturing Company Research Laboratories, Kyoto, Japan (12/12/92).

19. Newnham, R. E., Electrostriction, *Seminar at the Army Electronics Laboratory*, Fort Monmouth, New Jersey (2/16/93).

20. Newnham, R. E., Piezoelectric and Electrostrictive Materials, Seminar at the Metals and Ceramics Division of Oak Ridge National Laboratory, Oak Ridge, TN (4/15/93).

21. Newnham, R. E., Smart Ceramics, *ASM Symposium on "Smart Materials and Structures,"* Oak Ridge National Laboratory Seminar, Oak Ridge, TN (4/16/93).

22. Cao, Wenwu, Composite Electroceramics, *Fall Meeting of the Center for Dielectric Studies*, State College, Pennsylvania (September 22, 1993).

23. Cao, Wenwu, Statics and Dynamics of Ferroic Microstructures, Department of Physics, Pennsylvania State University, *Solid State Seminar* (September 13, 1993).

13.0 INVITED PAPERS PRESENTED AT UNIVERSITY, GOVERNMENT, AND INDUSTRIAL LABORATORIES (continued)

24. Bhalla, A. S., Single Crystal Fibers for Sensors, *International Center of Actuator/Sensors*, Penn State (January 22, 1993).

25. Bhalla, A. S., Electronic Materials, *Seminar at Cornell University* (April 29, 1993).

26. Bhalla, A. S., Pyro-optic Materials & IR Detectors, Invited speaker/co-organizer, *Special Army Workshop on Uncooled IR-Detectors*, Minneapolis, Minnesota (June 3, 1993).

27. Bhalla, A. S., AFM Studies of Ferroelastic Domains, *Army Workshop–Atomic Force Microscopy*, Matik, Maine (June 8, 1993).

28. Bhalla, A. S., Low and High k Materials, Murata, Japan (September 4, 1993).

29. Bhalla, A. S., AFM Studies of Ferroelectric Crystals, Invited Seminar, University of Puerto Rico (September 12, 1993).

14.0 CONTRIBUTED PAPERS AT NATIONAL AND INTERNATIONAL MEETINGS

1. Newnham, R. E., Structure Property Relationships in Composite Electroceramics, American Society for Composite Materials, Pennsylvania State University, University Park, October 13-15, 1992).

2. Aburatani, H., S. Harada, A. Furuta, Y. Fuda, and K. Uchino, Destruction Mechanisms of Multilayer Piezoelectric Actuators, Ultrasonic Electronics Symp., Yokohama, Japan (December 7-9, 1993).

95th Annual Meeting of the American Ceramic Society, Cincinnati, Ohio (April 19-21, 1993).
3. Subbarao, E. C., W. Cao, and V. Srikanth, Thermal Stress Driven Tetragonal-Monoclinic Transition in Zirconia.

4. Uchino, K and R. E. Newnham, Composite Flextensional Transducers for Sensing and Actuation.

5. Dogan, A., Q. C. Xu, S. Yoshikawa, K. Uchino, and R. E. Newnham, High Displacement Ceramic Composite Actuators "Moonies."

6. Meyer, R. J., M. Blaskiewicz, D. Smith, Q. C. Xu, U. Selveraj, and R. E. Newnham, Metal-Ceramic Composites for Sensors and Actuators.

7. Onitsuka, K., A. Dogan, J. F. Tressler, Q. C. Xu, S. Yoshikawa, K. Uchino, and R. E. Newnham, Design Optimization for Metal Ceramic Composite Actuators.

8. Dogan, A., S. Sentz, S. Yoshikawa, Q. C. Xu, B. R. Tittman, K. Uchino, and R. E. Newnham, Bonding in Metal-Ceramic Composite Actuators.

9. Chu, S. Y., K. Uchino, and Z. Ye, Photostriction Effect in Doped PLZT Ceramics.

10. Troiler-McKinstry, S., Microstructure-Property Relations in Ferroelectric Thin Films.

14.0 CONTRIBUTED PAPERS AT NATIONAL AND INTERNATIONAL MEETINGS (continued)

95th Annual Meeting of the American Ceramic Society, Cincinnati, Ohio (April 19-21, 1993).

11. Uchino, K., Novel Ceramic Actuator Materials.

12. Mulvihull, M. L., L. E. Cross, and K. Uchino, Low Temperature Domain Observation of Relaxor Ferroelectric Domains.

13. Oh, K. Y., K. Uchino, and L. E. Cross, Dynamical Observation of Domain Motion in Ferroelectric Polycrystalline Ceramics.

14. Gibbons, R. J., S. Troiler-McKinstry, J. Chen, and L. E. Cross, Electrical and Optical Studies of Fatigue in Ferroelectric Thin Films.

15. Fielding, J. P., S. J. Jang, T. R. Shrout, Electrostrictive Materials for Transducer Applications.

16. Bowen, C. P., A. S. Bhalla, R. E. Newnham, and C. A. Randall, Dielectrophoretic Assembly of Ceramic/Polymer Composite Materials.

17. Lee, N. Y., N. Usuki, K. Uchino, and Y. Ito, Pb/Ti Ratio in RF Magnetron Sputtered $PbTiO_3$ Films.

18. Brodeur, R. P., C. O. Ruud, and K. Uchino, Non Uniform Induced Strain in Semiconducting Lead Zirconate-Based Ceramics.

19. Aburatani, H. and K. Uchino, Destruction Mechanism of Multilayer Ceramic Actuators.

20. Ye, Z., S. Y. Chu, C. Gu, and K. Uchino, Spacial Light Modulator Using Photostrictive Ceramics.

International Meeting on Ferroelectrics (IMF 8), NIST, Gaithersburg, Maryland (August 8, 1993).

21. Dogan, A., Q. C. Xu, K. Onitsuka, S. Yoshikawa, K. Uchino, and R. E. Newnham, High-Displacement Ceramic Composite Actuators (Moonies).

22. Onitsuka, K., A. Dogan, Q. C. Xu, S. Yoshikawa, and R. E. Newnham, Design Optimization for Metal-Ceramic Composite Actuator "Moonie."

23. Tressler, J. F., Q. C. Xu, S. Yoshikawa, K. Uchino, and R. E. Newnham, Composite Flextensional Transducers for Sensing and Actuating.

24. Xu, Q. C., A Poling Technical for Piezoelectric Fibers and Fiber Property Characterization.

25. Trolier-McKinstry, S., Spectroscopic Ellipsometric Studies of Ferroelectric Thin Films.

26. Bhalla, A. S., G. Raina, and S. K. Sharma, Atomic Force Microscope (ATM) Study of Ferroelectric Domains.

14.0 CONTRIBUTED PAPERS AT NATIONAL AND INTERNATIONAL MEETINGS (continued)

International Meeting on Ferroelectrics (IMF 8), NIST, Gaithersburg, Maryland (August 8, 1993).

27. Cao, W., Domains As Nonlinear and Nonlocal Excitations.

28. Mathur, S. C., D. C. Dube, D. S. Rawat, and A. S. Bhalla, Microwave AC Conductivity and Dielectric Permittivity of TGS Doped with Urea.

29. Alberta, E., A. S. Bhalla, and T. Takenaka, Complex Piezoelectric Elastic and Dielectrics Coefficient of Lead Zirconate Based Ceramics Under Electric Bias.

30. Mathur, S. C., D. C. Dube, U. Sinha, H. Yadav, and A. S. Bhalla, Dielectric Properties of PbBiSrCaCuO Ceramics in Normal and Superconductivity States.

31. Guo, R., A. S. Bhalla, L. E. Cross, and R. Roy, Candidate Materials for High T_c Superconductor Substrates.

32. Mathur, S. C., D. C. Dube, U. Sinha, and A. S. Bhalla, Microstructure and Superconductivity in BiPbSrCaCuO Oxide Ceramics.

33. Jiang, Q. Y., E. C. Subbarao, and L. E. Cross, Fatigue in PLZT: Acoustic Emission as a Discriminator Between Microcracks and Domain Flips.

34. Jiang, Q. Y. and L. E. Cross, Effects of Electrode Materials and Electroding Methods on Fatigue and Behavior in Ferroelectric Materials.

35. Kumar, U., S. F. Wang, U. Selvaraj, and J. P. Dougherty, Densification and Dielectric Properties of Hydrothermal $BaTiO_3$ with Bi_2O_3.

36. Povoa, J. M., R. Guo, and A. S. Bhalla, Low Temperature Dielectric Relaxation Phenomena in Relaxor Ferroelectric Strontium Barium Niobate Single Crystal.

37. Rossetti, G. A., C. A. Randall, and W. Cao, Microstructural Characteristics of Perovskite Ferroelectrics with Diffuse Phase Transitions.

38. Wang, H., Q. M. Zhang, and L. E. Cross, Characteristics of Complex Piezoelectric d Coefficients of PVDF Copolymer.

39. Wang, S. F., U. Kumar, Y. S. Chou, P. Marsh, and H. Kunkel, Effect of Preparation Parameters on the Induced Piezoelectric and Mechanical Properties of 0.90 PMN 0.10 PT Ceramics.

40. Guo, R. and A. S. Bhalla, Crystal Fibers of Eulectic Compositions, *Am. Ceram. Soc. PAC RIM*, Oahu, Hawaii (November 7, 1993).

41. Cao, Wenwu, Theoretical Study on Domain Walls in $BaTiO_3$, *American Physical Society March Meeting*, Seattle, Washington (1993).

15.0 BOOKS (AND SECTIONS THEREOF).

1. Newnham, R. E. and T. R. Shrout, Electronic Ceramics, Kirk-Othmer Encyclopedia (Concise Edition) John Wiley and Sons, New York (1992).

2. Troiler-McKinstry, S., P. Chindaudom, K. Vedam, and R. E. Newnham, Characterization of Ferroelectric Films by Spectroscopic Ellipsometry, "Real-time Studies on Growth and Structure of Thin Films," Physics of Thin Films, K. Vedam, editor, Academic Press, Inc. (1993).

3. Uchino, K., "Ferroelectrics Ceramics," Materials Science and Technology, Vol. II, chapter 12, VCH, Germany (1993).

4. Uchino, K., "Ceramic Actuators," Encyclopedia of Advanced Materials, Pergamon Press, United Kingdom (1993).

5. Uchino, K., "Recent Development of Ceramic Actuators," Ceramic Data Book '92 Inst. Industrial Manufacturing Technology, Tokyo (1992).

6. Bhalla, A. S., W. R. Cooke, Jr., and S. T. Liu, Landolt Börnstein 1993, Group 3, Vol. 29, Solid State Physics, "Low Frequency Properties of Dielectric Crystals.

GENERAL SUMMARY PAPERS

APPENDIX 1

Materials for High Temperature Acoustic and Vibration Sensors: A Review

R. C. Turner, P. A. Fuierer, R. E. Newnham & T. R. Shrout

The Materials Research Laboratory, The Pennsylvania State University,
University Park, Pennsylvania 16802, USA

ABSTRACT

The industrial and scientific communities have expressed a real need for the capability of pressure, acoustic, and vibration sensing at elevated temperatures. This review compares the various commercial methods and materials for acoustic transduction, identifying their advantages and limitations. Techniques and devices include simple piezoelectric sensors, accelerometers, strain gauges, proximity sensors, fiber optics and buffer rods. Sensors with operating temperatures in excess of 650°C are readily available from commercial sources. Of the mechanisms investigated, the piezoelectric approach offers several advantages, including design cost and simplicity. Therefore, the bulk of this review concentrates on piezoelectric materials, both those that are already available commercially, and those that are presently under development. The new materials include perovskite layer structure ferroelectric ceramics, which possess the highest known Curie temperatures and thin film AlN, which has been reported to be piezoactive at 1150°C.

1 INTRODUCTION

High-temperature electronics is an area of research offering interesting materials and design challenges and one of significant industrial importance. The major impetus for the development of high-temperature electronic materials, devices, circuits, and systems can be credited to the energy crisis of 1974, when a commitment was made to the development of national energy resources by geothermal exploration.[1] At that time, geothermal and oil-well logging industries voiced their need for sensors and electronic

systems with higher operational temperatures for deep drilling in the earth's crust. The economic importance of world energy independence and reduced waste provided additional incentive for their development.

The aerospace and aircraft industries have especially difficult high-temperature requirements. With space and weight at a premium, engine designers and builders find it difficult to protect sensitive electronic systems in a cool, remote place. Electronic controls are to be placed directly inside jet engines because of reliability and noise requirements, so sensors need to be built that can withstand temperatures of 500–1000°C while allowing mission lifetimes up to 100 000 h.

In automotive electronics, the number of sensors and actuators continues to increase each year. Ceramic and semiconductor sensors which record temperature, oxygen pressure, and preignition knock are used in conjunction with microprocessor-based controls to improve the efficiency and reliability of internal combustion engines.[2] Further efficiency can be realized by operating combustion engines at higher temperatures. Research on the use of ceramic components in a diesel engine has led to higher operating temperatures, resulting in a potential increase in fuel efficiency up to 65%, along with a notable reduction in exhaust pollution.[3] Higher operating temperatures do, however, place additional requirements on the sensors. Environments of 150°C with repeated temperature cycles are at present considered the automotive norm, and higher temperatures are expected in the future.

Until the present, there has not been a review of the types of sensors commercially available for high-temperature acoustic sensing applications. The purpose of this paper is to provide such a review. Included in the discussion are the commercially available high-temperature piezoelectric materials used in many of the sensors described. In addition, new advances in materials that may permit the design of sensors which can operate at temperatures well above those currently available will be presented.

2 ACOUSTIC MEASUREMENT TECHNIQUES AND APPLICATIONS

Critical parameters for acoustic and vibration sensors involve the measurement of dynamic pressure pulses, vibrations (relative and absolute), acoustic emissions, strains, and the dynamic proximity of machine components. An example of a dynamic pulse is the rapid increase in pressure upon ignition of the air–fuel mixture in the cylinders of an internal combustion engine. The timing and the shape of the pulse have a large effect upon

engine efficiency. Transducers fitted into the cylinder head have been used for monitoring combustion pressure to optimize ignition timing.[4]

Dynamic monitoring is also employed in such machines as aircraft engines, gas turbines, and power generators, all of which have high speed rotors. Sensors strategically mounted on the machine detect destructive conditions of imbalance, or unequal loading of the rotor, enabling the possibility of corrective measures to be implemented. The sensors convert the associated mechanical energy of the vibration to electrical energy which can then be amplified and monitored. Computer coupling, allows real-time status reports of the condition of the machine while providing a comparison with an operating norm.

Non-destructive testing (NDT) is another widely used application of acoustic sensors that involves either passive sensing of 'acoustic emissions', or active 'ultrasonic testing' techniques. An application of the first method involves affixing a number of acoustic sensors in strategic locations on the wall of a vessel, such as a chemical storage tank, pressurizing the vessel to create strains, and examining the acoustic emissions which result from the Kaiser effect.[5] Cracks and poor joints can then be detected and logged so that repairs can be made. This method has also been successfully applied in the inspection of the fuselage of large aircraft to detect cracks resulting from fatigue. The ultrasonic method of NDT incorporates a transducer to generate an acoustic signal at ultrasonic frequencies that is transmitted through the test specimen. When the acoustic wave reaches an interface of the sample it is reflected back to the transmitter/sensor which, therefore, acts as a transceiver. If, however, the wave impinges upon a flaw, a portion of the wave is reflected and thus reaches the sensor ahead of the original wave. This, then, becomes a valuable tool for locating defects within a structure.[6] Figure 1 is a simple illustration of the technique. Acoustic sensors also find use in the hostile environments of deep oil wells for seismic data logging, and in nuclear power plants to monitor the condition of heat exchange pumps and pipes.[7]

An indirect way of sensing vibration is by measuring capacitive changes in an air gap. An air gap sensor placed in close proximity to a
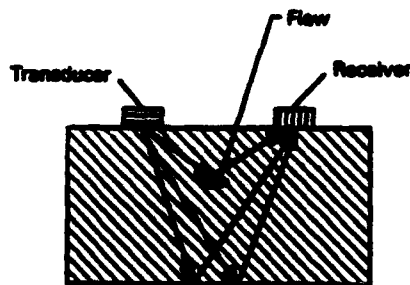
Fig. 1. Detection of a flaw in a solid by ultrasonic testing (NDT).

TABLE 1
Acoustic and Vibration Measurement: Industrial Applications

Aerospace	Measure rotational speed of jet turbine rotors
	Space vehicle acceleration
	Trajectory monitor
	In-flight vibration monitor
	Nozzle pressure
	NDT test of air frames
Automotive	Knock sensor
	Fluid level sensor
	Crash test
	Vibration control
Industrial	Dynamic pressure monitors
	Vibration detectors
	Flow detectors
	NDT testing
	Proximity detectors
	Noise 'fingerprinting'
Medical	Diagnostic imaging
	Impact sensors
Military	Hydrophones
	Range finders
	Noise detection in vehicles
	Security systems
Power generation	Leak detector
	Liquid sodium coolant pump monitor
	Nuclear reactor monitor
	Air gap monitoring between stator and rotor
	Fuel rod monitor
	Coal feeder monitor
	NDT of pressure vessels
Commercial	Fish finders
	Phonographs pick-up
	Microphones

high-speed rotor will detect dynamic changes in the spacing between the two which, in effect, is an indicator of an imbalance condition or some other malfunction. This type of sensor has found wide acceptance in hydroelectric power plants.[5]

Examples of pressure, acoustic and vibration measurement techniques described above serve to illustrate the wide variety of possible applications. Additional applications are listed by industry in Table 1. These are routinely employed in the range of −55°C to 125°C, however, several devices are needed to operate in much harsher thermal conditions. Sensor designs and their respective temperature limitations are described in the following section.

3 SENSOR DESIGNS

Listed in Table 2 are current commercial sensor designs. They include piezoelectric discs or plates, accelerometers, strain gauges, proximity sensors, fiber-optic sensors, and systems incorporating buffer rod extensions. Brief descriptions of these devices are as follows.

3.1 Simple disc

The most basic sensor incorporates a simple disc, or other simple shape, composed of a piezoelectric ceramic, which is attached directly to the wall or frame of an engineering structure, embedded in a recess, or mounted in a replaceable fixture. Figure 2 is a schematic construction of a piezoelectric knock sensor using a bending mode resonance to detect vibrations. The piezoelectric element 'generates' a voltage in response to stresses caused by the acoustic energy impinging upon it.[9] The magnitude of the voltage generated is directly related to the product of the applied stress and the piezoelectric voltage or 'g' constant of the material. The electrical signal is then amplified and fed to a microprocessor in the control system. This arrangement is capable of extremely high sensitivity on the order of pico (10^{-12}) strains. It is also self-generating, rugged, low-cost, and simple. The temperature limitations of these sensors arise from the loss of piezoelectric properties that occur as the material approaches its transition (Curie) temperature T_c, a topic which will be discussed later. For lead zirconate-titanate, (commonly called PZT), the most widely used piezoelectric ceramic material, the maximum use temperature is ~200°C. Other temperature limitations result from the failure of the adhesives used to mount the disk, and melting of the solder used to attach the leads.

3.2 Buffer rod extensions

For many high-temperature applications, buffer rod extensions are utilized to transmit and receive acoustic signals from very hot areas, effectively
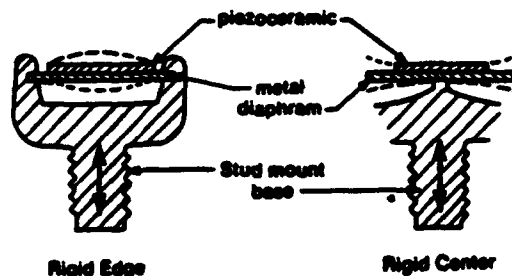
Fig. 2. Two methods of mounting a piezobender used in automotive knock sensors.[9]

TABLE 2
Comparison of Commercial Strain, Vibration, and Acoustic Sensors

Operation principle	Piezoelectric disc or plate	Accelerometer		Strain gauge	Proximity sensor		Buffer rod	Fiber-optic sensor
	Piezoelectric	Piezoelectric	Magnetic induction	Resistive metal	Capacitive	Eddy current	Piezoelectric	Laser/optic
Measured parameter	Acoustic waves vibration	Acceleration absolute dynamic	Vibration pressure	Load, force vibration absolute	Relative air gap displacement	Vibration	Acoustic waves	Strain vibration
Present maximum temperature (°C)	400	650	480	850	150	450	1100	300
Temperature stability	Good	Good	Good	Fair	Good	Fair	Good	Poor
Temperature sensitivity	Good	Good	Good	Fair	Good	Fair	Good	Poor
Resolution/ sensitivity	High	High	Fair	Low	Low	Low	Fair	High
Frequency range	0·05–1 MHz	0·05– MHz	0·015–2 kHz	DC–kHz	DC–kHz	DC–10 kHz	0·05 kHz–MHz	DC–10 kHz
Power consumption	Low	Low	Low	Medium	Medium	Medium	Low	High
Cost and complexity	Low	Medium	Medium	Low	Low	High	High	High
Durability	Good	Good	Good	Fair	Good	Fair	Good	Poor

isolating temperature-sensitive transducers from hostile environments. The rod serves as an acoustic wave guide to couple the hot test specimen with the sensitive piezoelectric transducer. The rods are generally constructed of stainless-steel and are cooled with water or air to prevent damage to the transducers. This arrangement permits the use of a conventional piezoelectric material, which would otherwise lose its piezoelectric properties at high temperatures. This technique is widely used on NDT probes in the metals industry to detect cracks and other defect in hot steel blooms and pipes at temperatures in the neighborhood of 1100°C.[10] A similar application employs hollow 'buffer pipes' to couple dynamic pressure sensors with jet and rocket engines.

3.3 Accelerometers

Accelerometers most often use a piezoelectric as the internal sensing element. The various designs exploit different mechanisms to translate mechanical energy to a measurable response, but all operate based on Newton's second law:

$$F = ma$$

The accelerometer shown in Fig. 3 differs from the simple disk piezoelectric sensor in that a seismic mass (m) is attached to the piezoelectric element and the assembly is hermetically sealed in a protective case.[11] As a response to acceleration (a), the mass imparts a force (F) on the element, which in turn generates a voltage in proportion to the magnitude of the stress. Depending upon the sensitivity and temperature range required for the application, transducer manufacturers utilize several different piezoelectric materials. Commercial accelerometers using lithium niobate ($LiNbO_3$) single crystal elements are rated for continuous use up to 650°C.[12,13]
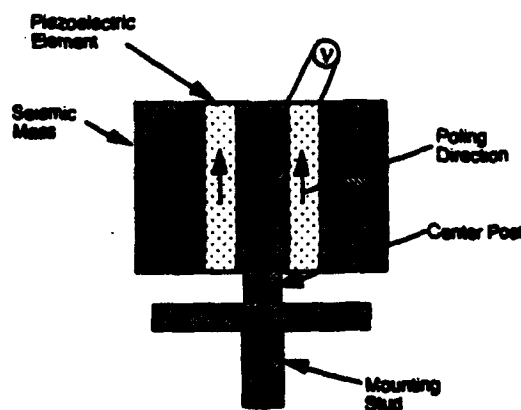
Fig. 3.   Cross-section of a tubular accelerometer element.[11]

Accelerometers based on magnetic induction, employ a permanent magnet as the seismic mass and a field coil for the active element. The mass is partially restrained by a spring, but when the mass is accelerated, it moves relative to the coil, thus inducing an electromotive force. As with the case of piezoelectric types, the resulting electric signal must be amplified and filtered before it is fed to the instrumentation. The upper temperature limit of this type of device is determined by the Curie temperature of the permanent magnet. Commercial units are rated for temperatures as high as 480°C.[14]

3.4 Strain gauges

Figure 4(a) is an illustration of a bonded metallic foil strain gauge.[15] Resistive strain gauges involve a change in electrical resistance (ΔR) resulting from the mechanical strain ($\Delta L/L$) of the sample to which the gauge is bonded. The sensitivity is determined by the gauge factor (GF):

$$GF = \frac{\Delta R/R}{\Delta L/L}$$

With a typical gauge factor of 2, and a nominal resistance $R = 100 \ \Omega$, these gauges require an ohmmeter with very high sensitivity to measure the ΔR accompanying a strain of 1×10^{-6}. A more accurate way of measuring small changes in resistance incorporates a Wheatstone bridge as shown in Fig. 4(b).

To compensate for the nonlinear character of the thermal coefficients of expansion of the alloys used, an unstrained reference gauge is installed in an adjacent bridge arm. This second gauge is subjected to the same temperature as the first, thereby effecting electrical cancellation of the apparent strain. Commercial metal gauges are typically limited in temperature range to about 300°C; however PtW wire gauges are available for

(a)   (b)
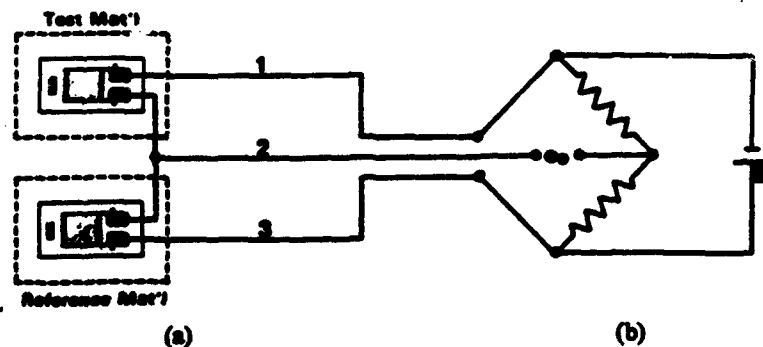
Fig. 4. Bonded grid resistance gauges including (a) the measurement and reference components, and (b) Wheatstone bridge circuit for measuring strain.[15]

use up to 850°C,[16] and other exotic metals such as PdCr are being studied for use up to 1000°C.[17]

Metal strain gauges are simple in design, low-cost, and can detect static strains. Even using the Wheatstone bridge configuration, however, strain sensitivity is low compared with piezoelectric transducers.

3.5 Proximity sensors

Proximity sensors are often used to monitor the degree of rotation of the armatures of electric generators as well as the clearance between the armature and the stator. This serves as an indirect method of measuring vibration if an unbalanced condition exists. The two types of proximity sensors available commercially are (i) air gap capacitors, and (ii) eddy current detectors. Both types require electronic conditioners to supply an input signal, and processors to analyze the signals modified by the sensors.

(i) An example of an air gap capacitor is illustrated in Fig. 5.[18] In this application on an electric power generator, the armature serves as one plate of the capacitor while the other plate is an integral part of the sensor and air is the dielectric. The plates are maintained at a close proximity with one another so that a small change in spacing results in significant changes in capacitance. The change in capacitance can then be detected by the control circuitry and acted upon accordingly. The detection of variations in air gap as small as one micron are possible in installations on hydroelectric power generators. At present, commercial units are constructed of fibreglass composites for use at temperatures up to 150°C,[12] but it seems reasonable that units could be constructed from more refractory materials for higher temperature applications.
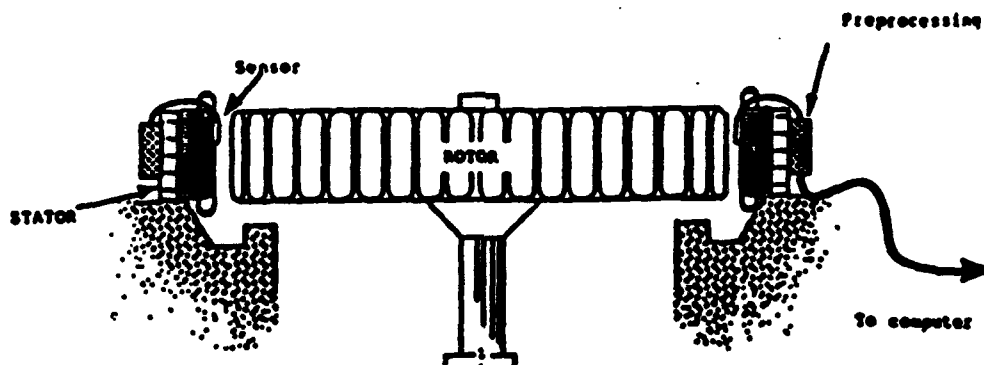
Fig. 5. Air gap sensors mounted on an AC generator.[18]

(ii) The second kind of proximity sensor is the eddy current type. It determines the relative position of a rotating shaft by detecting changes in magnetic field between the sensor and the target shaft. The eddy current sensor operates in a manner similar to that of an electrical transformer. The sensing coil resembles the primary winding, and the small eddy current loops induced in the target by the variable magnetic field of the sensing coil act like the secondary windings. The small eddy currents cause a change in phase and amplitude of the sensing coil signal. The target material must therefore be metallic. The sensing coil is mounted near the rotating shaft or moving component of a machine with lead cables attached to the exterior end. Commercial models are currently rated for use up to 450°C.[14] The temperature limitation is primarily due to the temperature coefficient of resistance of the wire used to wind the probe coil.[19]

3.6 Fiber optic sensor interferometers

Fiber optic sensor (FOS) interferometers or phase sensors are used to detect small strains, (in the order of 10^{-7}) or vibrations in a sample without making physical contact. This capability allows measurements to be made inside a hostile environment, such as a furnace. A simplified schematic of a system is shown in Fig. 6. There are several different designs, but all are based on measuring a phase change in the transmitted light signal resulting from a change in length of the optical fiber. Optical fibers are typically SiO_2 glass; however, fibers of more heat-resistant materials such as sapphire (Al_2O_3) are commercially available. Along with the fiber, a large number of additional components, such as a laser source, phase demodulator, filters, and microprocessors, etc., are needed for these systems. High cost, complexity and sensitivity to variations in temperature are disadvantages of this approach.
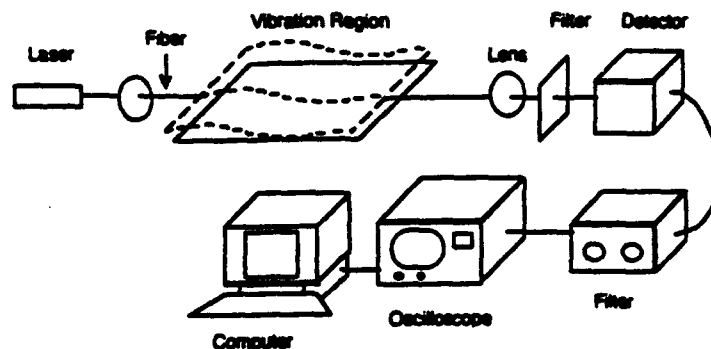
Fig. 6. Fiber-optic vibration sensor and associated electronics.

In summary, with respect to the operational parameters listed in Table 2, piezoelectric trandusers offer many advantages over the other types of acoustic sensors. Specifically, their compliment of sensitivity, stability over a wide temperature range, and simple design offers the lowest cost approach. Polycrystalline ceramics are often the material of choice because they can be readily manufactured into a variety of configurations. Therefore, the remainder of this paper concentrates on high-temperature piezoelectric materials, with a review of those currently available, and a discussion of future prospects.

4 PIEZOELECTRIC CERAMICS

4.1 Piezoelectricity

The phenomenon of piezoelectricity was first reported in 1880 by Pierre and Jacques Curie. Since that time, a number of crystalline materials have been found to exhibit piezoelectric activity, although only a few are of practical concern. The common feature of all piezoelectric crystals is that they have no center of symmetry along the piezoelectric axes. Ferroelectric ceramics possess a multitude of individual dipole domains which are distributed throughout the body in various crystallographic orientations, resulting, in a net dipole moment of zero. In a process, called poling, a relatively large electric field is applied through the body causing a common alignment of a large portion of the dipoles, thus rendering the material piezoelectric. These crystals develop an electric field when subjected to an applied stress (sensor), or conversely, exhibit a mechanical deformation with the application of an electric field (actuator). Since the details of piezoelectricity are covered in a number of excellent texts and review articles, the reader is advised to consult them for further information.[11,20-22]

4.2 Electromechanical properties

In order to describe the electromechanical properties of piezoelectric materials, a large number of interrelated coefficients are used, many of which have been standardized by the IEEE.[23] However, with regards to high-temperature materials, only the most important coefficients and properties will be presented in this section. (Note: where subscripts are used with coefficients, the first number refers to the axis of polarization, and the second refers to the axis of applied stress, or applied field.)

4.2.1 Ferroelectric Curie temperature

Most of the piezoelectric materials described in this paper are ferroelectric and capable of being polarized, with the polarization resulting from the asymmetry of its crystal structure. When the crystal is heated, its internal kinetic energy increases. At a certain temperature, called the Curie temperature (T_c), the crystal changes to a structure of a higher symmetry, the alignment of the dipoles is lost and all piezoelectric activity disappears. Upon cooling, the dipoles do not realign unless they are subjected to a strong electric field. Other consequences of increasing temperature are changes in the values of electromechanical coefficients, which become more pronounced as the T_c is neared. This can be particularly important in applications where the electrical properties of the sensor are closely matched to the instrumentation. In addition, dipoles that were polar oriented have a tendency to reverse back to their original position thus degrading the piezoelectric effect in a process known as 'thermally activated aging'. Generally, a maximum operating temperature of one-half the T_c is considered safe.

4.2.2 Resistivity and the RC time constant

High electrical resistivity is necessary so that a large field can be applied during poling without breakdown or excessive charge leakage. High insulation resistance 'R' is also required during operation of the device. The transducer must not only develop a charge for an applied stress or strain, but must also maintain the charge for a time long enough to be detected by the electronic system. The length of time the charge is maintained is proportional to the RC time constant (resistance × capacitance). The minimum useful frequency of a sensor, known as the lower limiting frequency (f_{LL}), is inversely proportional to the time constant:

$$f_{LL} = \frac{1}{2\pi RC}$$

where C is the device capacitance.

Below f_{LL}, the charge will drain off before it is detected because of conduction in the sensor. With low f_{LL} the dynamic bandwidth can be extended to sonic frequencies, and thus, a large RC constant is desirable for many applications.

4.2.3 Piezoelectric constants

The piezo strain 'd' constant gives the ratio of the strain developed in the specimen to the electric field applied at the electrodes, and conversely, the ratio of short circuit charge, per electrode area, to the applied stress. The stress can be applied to the body in different modes as illustrated in
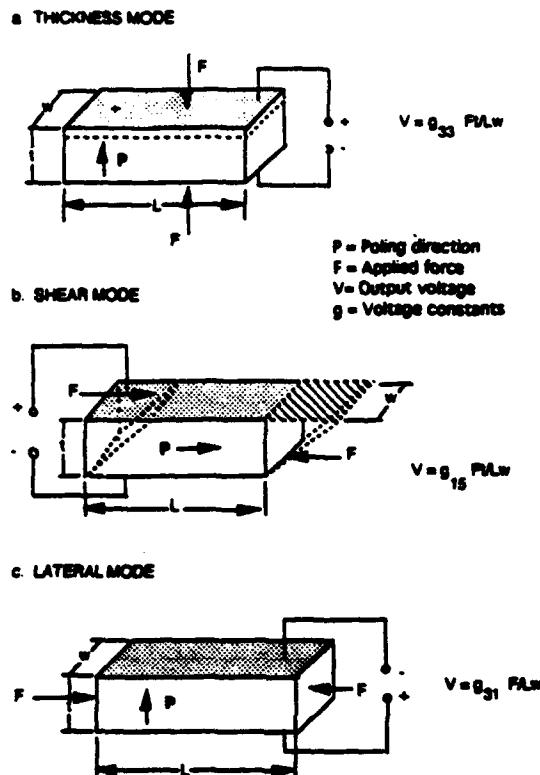
Fig. 7. (a) Thickness, (b) shear, and (c) lateral mode piezoelectric sensors. P indicates the poling direction. The output voltage (V) is proportional to the applied force (F) and piezoelectric voltage coefficient (g_{ij}) of the material.

Fig. 7. The piezoelectric voltage 'g' constant gives the ratio of the field developed to the stress applied, and conversely, the ratio of strain to the applied charge to the electrode area. The 'g' constant is related to the 'd' constant by the permittivity, $K\varepsilon_0$.

$$g = \frac{d}{K\varepsilon_0}$$

In comparing the properties of high-temperature piezoelectric materials, the 'g' constant tends to be the more meaningful coefficient.

4.2.4 Mechanical Q

The mechanical Q expresses the ratio of strain in phase with stress to strain out of phase with stress in the vibrating element, or in other words, the relative amount of input electrical energy that is converted to mechanical energy as opposed to that which is lost as heat. Piezoelectric materials with high 'Q_m' factors are characterized by having narrow

resonant peaks, whereas, those with low 'Q_m' factors have broader band-widths.

4.2.5 Sensitivity

For a given stress applied to the device, the output voltage generated by the piezoelectric 'generator' should be sufficiently high to be detected above background noise. The most sensitive devices produce the greatest output per unit of stress. Unfortunately, for high-temperature sensors, ferroelectric materials exhibit a considerable increase in permittivity, with increasing temperature, a condition which effectively reduces the voltage constant 'g'. Every piezoelectric material reaches some temperature at which its voltage constant 'g' and resistivity are diminished to the point where the output becomes undetectable. In practice, the relatively small output signals generated by high temperature accelerometers necessitate the use of electronic charge amplifiers for enhancement, but there is a practical limit to how small a signal that can be accurately detected.

5 COMMERCIAL PIEZOELECTRIC CERAMICS

Table 3 lists typical piezoelectric ceramic materials found in commercial accelerometers and vibration sensors, along with reported room temperature properties.[21,24-28] Owing to the lack of reliable published high-temperature data available for this work, samples were obtained, their electrical properties were measured at elevated temperatures, and the data reported in Table 4.[25-29] In addition, the resistivity of each material was measured over a wide range of temperatures as shown in Fig. 8.[25-28,30-34] Good agreement was found with values reported in the literature (as shown in Fig. 8).

A brief description of each of these piezoelectric materials, or related compositional families, is presented in this section. With the exception of quartz, all are ferroelectric.

5.1 Quartz

Quartz (SiO_2) is one of the earliest piezoelectric materials used in electronic devices. Originally, natural quartz crystals were used, but now have been widely replaced by hydrothermally-grown synthetic quartz. Because of its low mechanical loss (high Q_m), narrow bandwidth, and highly temperature-stable resonant frequency, quartz is the material of choice for timing standards and monolithic filters in communication equipment. However, as seen in Table 3, the piezo 'd' coefficient is relatively small and thus

TABLE 3

Reported Room Temperature Electrical Properties of Commercial High Temperature Piezoelectric Materials

Material	Structure	Curie point T_c (°C)	Dielectric constant K $(10^{-12}\ C/N)$	Piezoelectric strain constant $(10^{-3}\ Vm/N)$		Piezoelectric voltage constant		Electromechanical coupling		Mechanical quality Q_m	Resistivity 20°C $(10^{12}\ \Omega\text{-cm})$ ρ	Ref.
				d_{33}	d_{15}	g_{33}	g_{15}	k_{33}	k_{15}			
Pb(Zr, Ti)O$_3$ (Soft PZT)	Perovskite	330	1800	417	710	25	41	0·73	0·77	75	100	N-21[26]
(BaPb)Nb$_2$O$_6$ (BPN)	Tungsten bronze	400	300	85	100	32	46	0·30		15	1	K-81[25]
PbTiO$_3$ (PT)	Perovskite	470	190	56	68	33	32	0·45		1300	10	LTT-3[28]
Na$_{0.5}$Bi$_{4.5}$Ti$_4$O$_{15}$ (NBT)	Bismuth	~600	140	18		15		0·15		100	1000	K-15[25]
LiNbO$_3$ (LN)	Corundum	1150	25	6	69	23	91	0·23	0·60	NR	1	27
SiO$_2$ (α-Quartz)	α-Quartz	573	4·5	2(d_{11})		50		NR		10^5	1000	21,24

R. C. Turner et al.

TABLE 4
Selected High Temperature Properties of Piezoelectrics

Material[a]	T_c (°C)	Vibration mode (ij)	g (RT)[b] ($\times 10^{-3}$ Vm/N)	TCF (ppm/°C)	ρ (Ω-cm)	ε_r (10 kHz)	tan δ (10 kHz)	RC (s)	Ref.
PZT (DOD II) (200°C)	360	[33]	15 (25)	+200	10^{12}	3000		250	N-21[26]
(BaPb)Nb$_2$O$_6$ (300°C)	400	[33]	24 (30)	−135	10^7	530	0·036	0·0005	K-81[25]
PbTiO$_3$ (400°C)	450	[15]	21 (29)	−97	2×10^5	1000	0·35	0·00002	LTT-3[28]
Na$_{0.5}$Bi$_{4.5}$Ti$_4$O$_{15}$ (400°C)	600	[33]	10 (18)	−118	3×10^8	262	0·10	0·007	K-15[25]
LiNbO$_3$ (400°C)	1150	[15]	93 (99)	−76	3×10^7	100	0·001	0·0003	27
Sr$_2$NbTaO$_7$ (400°C)	823	[24]	5 (6)	−74	4×10^9	40	0·10	0·01	29

[a] PZT and BPN were evaluated at approximate maximum use temperature, the others at 400°C.
[b] Room temperature values (RT) also shown for the voltage constant (g).
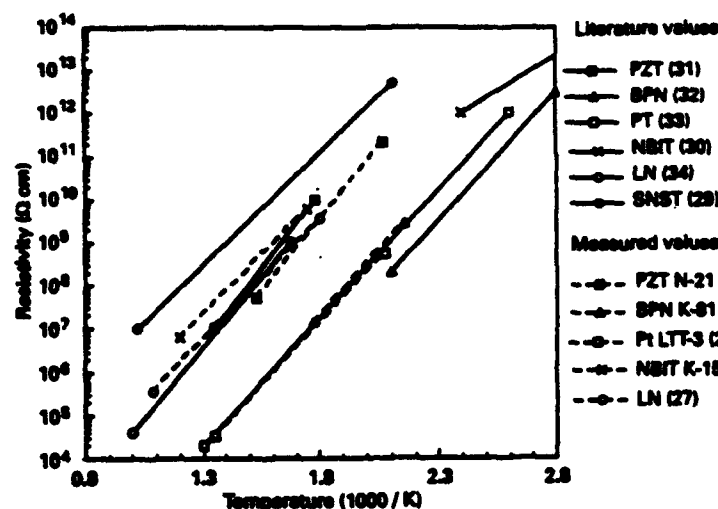
Fig. 8. Temperature dependence of resistivity for piezoelectric ceramics: 'soft' lead zir-
conate titanate (PZT), barium-doped lead metaniobate (BPN), sodium bismuth titanate
(NBIT), lead titanate (PT), lithium niobate (LN), and perovskite layer structure stron-
tium niobate tantalate (SNST). Solid lines represent data taken from literature, while
dashed lines represent data measured from commercial materials for this work. All are
polycrystalline ceramics except single crystal LN.

the amount of electric charge that can be generated is low. Although
piezoelectric α-quartz has a transition temperature of 573°C, its use
temperature is normally limited to 350°C. Above that temperature the
crystal structure is subject to twinning, destroying its piezoelectric
properties.[24]

5.2 Lead zirconate titanate

Lead zirconate titanate $(Pb(ZrTi)O_3(PZT))$ has the perovskite structure
and is a solid solution of tetragonal $PbTiO_3(PT)$ and orthorhombic
$PbZrO_3(PZ)$. Because of the large number of polarization directions
available, compositions near the morphotropic phase boundary at
approximately 53:47 PZ to PT are easily poled to high remanent
polarization and exhibit extremely high values of electromechanical
coupling coefficients and electrical permittivity. Because of its superior
piezoelectric properties and higher operating temperature, PZT has
largely replaced barium titanate (BT)—$T_c \sim 130°C$, the first widely used
ferroelectric, in all but the lowest cost commercial products. Useful varia-
tions in properties of PZT can be obtained by compositional additives.
Niobium-doped PZT (DOD Type II) is used extensively in accelerometers,
hydrophones (underwater microphones), and acoustic emission instruments.
Although its electrical resistivity and RC time constant remain quite high

up to a T_c of 360°C (Table 4 and Fig. 8), its use is kept well under 200°C because of its tendency to age very rapidly, leading to depoling.[11]

5.3 Lead titanate

Lead titanate ($PbTiO_3$(PT)) the solid solution end member of PZT family, has a T_c of about 490°C. As in the case of PZT, a large number of modifications have been developed to optimize specific electrical and mechanical characteristics. Many commercial compositions of PT are doped with samarium or calcium for use in hydrophones, but this has the effect of lowering the T_c to around 240°C. Compositions, doped with other elements, have T_c values near 490°C and have found applications in knock sensors for automobile engines. The higher operating temperature of PT allows it to be mounted closer to the combustion chamber, thus giving a faster response time as compared to PZT.[6] The data presented in Tables 3 and 4 and Fig. 8 reflects the latter composition. Evaluation at 400°C has shown it to have a resistivity of only about 10^5 Ω-cm. Such a low value would adversely affect the RC time constant.

5.4 Lead metaniobate

Lead metaniobate ($PbNb_2O_6$(PN)) belongs to the tungsten-bronze family. Because of its low Q_m (wide bandwidth) and relatively high d_{33} to d_{31} ratio (high degree of anisotropy), PN finds its greatest use in transducers in NDT and medical diagnostic imaging. Commercial PN compositions are modified to enhance specific electrical characteristics but at the expense of the T_c. A commonly used composition contains about 10% Ba(BPN) and has a T_c of about 400°C. Although BPN is reported to resist depoling up to its T_c, limitations are imposed by its high conductivity above 300°C.[35] Figure 8 reveals that BPN exhibits the lowest resistivity of the materials tested. Other problems associated with this material are its high level of porosity and relatively low mechanical strength.[21]

5.5 Bismuth titanate

Bismuth titanate ($Bi_4Ti_3O_{12}$) is the titular compound of bismuth layer structure ferroelectrics (BLSF). Modification by one or more of a large number of other elements, to enhance dielectric and piezoelectric properties, is also common. A member of the family, reported to have favorable piezoelectric properties, high resistivity and high T_c (>600°C), is $Na_{0.5}Bi_{4.5}Ti_4O_{15}$, (NBT). Commercially available,[25] it is used in accelerometers operated at temperatures up to 400°C.[36] The strongest mode of vibration in NBT is the [33] mode but d_{33} and g_{33} are somewhat lower

than many of the perovskite ferroelectrics previously discussed (see Table 3). Nevertheless, the high T_c and high resistivity make NBT an attractive, moderately high-temperature piezoelectric.

Although not commercially available, other complex variations of BLSF compounds have been reported to have Curie temperatures of over 800°C. Representative of this group is Bi_3TiNbO_9 for which room temperature values of d_{33}, and g_{33} were reported to be near those of NBT.[37] To date, little else has been reported about other properties, particularly at high temperature.

Unlike previously mentioned ferroelectric ceramics, BLSF materials can be made with grains having a plate-like structure. In ceramics formed and fired by conventional processes, these grains are oriented in a more or less random fashion, which leaves only a limited number of crystallographic orientation directions available for polarization due to the low symmetry of the structure. The achievement of an optimum degree of remnant polarization in polycrystalline ceramics necessitates the use of some mechanism to provide grain orientation. By employing hot forging techniques, researchers have prepared samples of several BLSF family members which display a high degree of texturing. The textured samples exhibited a twofold increase in coupling coefficient k_{33} and piezoelectric constant d_{33} over those from conventional sintering.[37]

5.6 Lithium niobate

Lithium niobate ($LiNbO_3$(LN)) has the corundum structure and a reported Curie point near 1150°C. Single crystals are grown from a melt using the Czochralski technique. Single crystals are preferred because of the higher piezoactivity, as well as difficulties encountered in conventional sintering of the polycrystalline form. As with polycrystalline ferroelectrics, single crystals of $LiNbO_3$ exhibit a multidomain structure, and must be polarized. This is accomplished by applying relatively small electric field (1 V/cm DC) at a temperature just below the T_c, thus converting the structure to single domain. The polarized crystal is then sliced along the desired axis indicated for the application, and the faces polished.[38] For accelerometers, electrodes are usually applied parallel to the poling axis to take advantage of the greater value of the d_{15} piezoelectric constant and to eliminate pyroelectric effects The voltage output of LN ($g_{15} = 91 \times 10^{-3}$ Vm/N) is significantly larger than those of the other piezoelectric materials listed in Table 3 due to the inherently low dielectric constant. Sensitivity remains high up to 400°C (Table 4) but resistivity is the limiting factor for use above 650°C (Fig. 8).

The tantalum analog, $LiTaO_3$, exhibits many of the same characteristics

of $LiNbO_3$; however, the T_c (720°C) and piezoelectric constants are somewhat lower, thus offers no apparent advantage for high-temperature acoustic sensors.

6 NEW HIGH-TEMPERATURE PIEZOELECTRIC MATERIALS

In general, the ferroelectric ceramics discussed thus far are limited to temperatures of approximately $T_c/2$. Therefore, applications requiring yet higher temperatures than those just presented, require other materials such as ferroelectrics with higher Curie temperatures, oriented polar non-ferroelectric materials, non-polar piezoelectric single crystals, or piezo-electric thin films. Several novel materials currently under investigation are presented below.

6.1 Perovskite layer structure (PLS) ferroelectrics

PLS ferroelectrics have the general formula $A_2B_2O_7$ and possess an anisotropic layered structure similar to the BLSF family. Single crystals of the two most recognized compounds, $Sr_2Nb_2O_7$ and $La_2Ti_2O_7$, possess the highest known ferroelectric Curie temperatures, 1342°C and 1500°C respectively.[39,40] Thus, PLS ferroelectrics have been proposed for use in transducers with high operating temperatures and good thermal stability. Unfortunately, the cost of growing good-quality single crystals is high due to the high melting points of these compounds (which is considerably higher than that of $LiNbO_3$).

In a manner similar to that used for BLSF compounds, previously described, hot-forging was used to synthesize PLS compounds. The resulting samples, shown in Fig. 9, were found to exhibit near theoretical density and high degree of orientation, and polarizability.[29,41] The use of solid solutions with $Sr_2Ta_2O_7(T_c = -107°C)$, to adjust T_c of the parent compound to <900°C, aided poling and the subsequent piezoactivity. One compound, $Sr_2(Nb_{0.5}Ta_{0.5})_2O_7$, had a T_c of 820°C and demonstrated the ability to resist depoling at temperatures as high as 650°C. The electromechanical properties for $Sr_2(Nb_{0.5}Ta_{0.5})_2O_7$ are listed in Table 4. Although the room temperature d-coefficient is low ($d_{24} = 2.6 \times 10^{-12}$ C/N), a value similar to that of quartz, the piezoelectric voltage constant at 400°C is significant ($g_{24} = 6.3 \times 10^{-3}$ Vm/N). From Fig. 8 is is also seen that the hot-forged PLS ceramics have the highest resistivity at elevated temperatures of any of the materials tested. By using compositions of $Sr_2(Nb_{1-x}Ta_{3x})_2O_7$ with a higher Nb content, the T_c can be increased to 1200°C with no loss of resistivity. Efforts to optimize the composition and processing variables are currently under way and may lead to improved properties.[42]
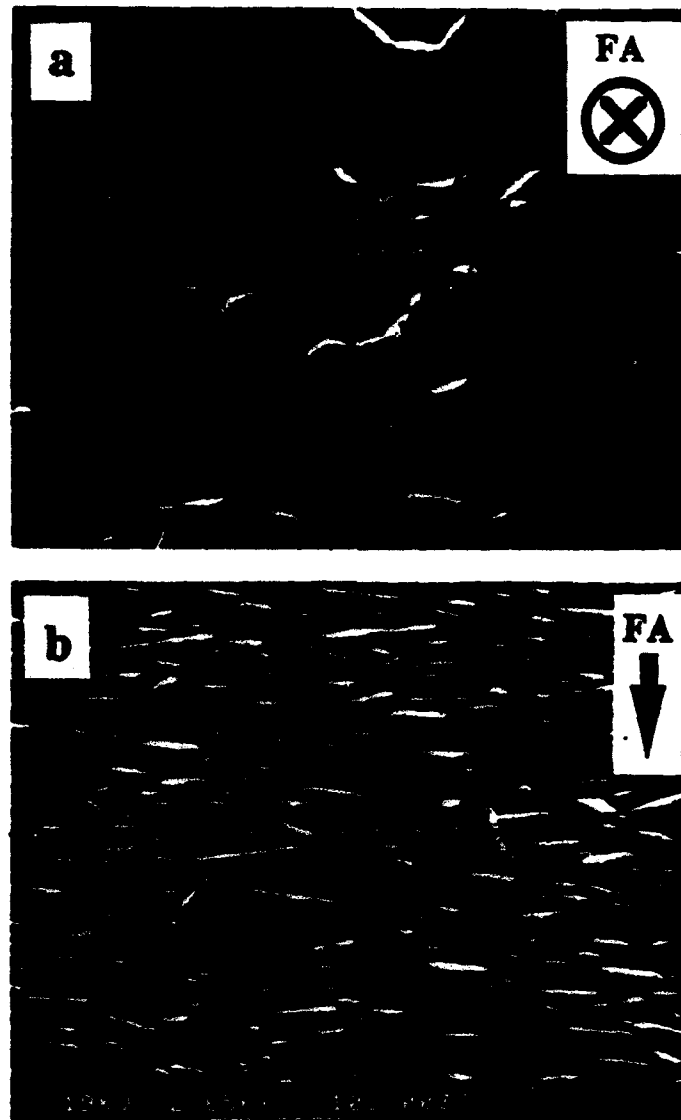
Fig. 9. Micrographs of hot forged $La_2Ti_2O_7$ ceramic. The plane perpendicular to the forging axis (FA) is shown in (a). The plane parallel to FA is shown in (b).

6.2 Polar glass ceramics

A classification of piezoelectric materials, totally diffrent from any previously discussed, exists in the form of polar glass ceramics. These non-ferroelectric compounds require single crystal growth or polar texturing for piezoactivity. One successful technique for obtaining oriented grains is the texturing of microscopic recrystallized polar crystals in an amorphous

glassy matrix. Using a controlled thermal gradient technique, the polar material $Ba_2TiSi_2O_8$ (fresonite) was recrystallized from a glass of the composition $2BaO \cdot 3SiO_2 \cdot TiO_2$ resulting microstructure that contained polar oriented grains. With room temperature values of d_{33} and g_{33} were 7×10^{-12} C/N and 88×10^{-3} Vm/N respectively, and relatively low density (4·01 g/cm^3), these composite materials may be of interest for hydrophone applications.[43]

It has been suggested that polar glass ceramics may also be useful for high temperature piezoelectric devices. Since they are polar, but not ferroelectric, poling is unnecessary and, consequently, there is no problem with depoling or aging effects. Foreseen problems do exist, though, including softening of the glassy phase and possible ferroelastic phase transitions that would restrict the high-temperature capabilities. Further evaluation of the electrical properties, including resistivity at high temperatures, is needed before these materials can be commercialized.

6.3 AlN thin films

In recent years, numerous studies have been made of the piezoelectric properties of thin films of several materials, including the ferroelectrics previously discussed.[21] Thin films of non-ferroelectric materials are also of great interest, including aluminium nitride (AlN). Because of its exceptionally high thermal conductivity and dielectric breakdown strength, polycrystalline (AlN) is an important ceramic material used in substrates for hybrid microelectronics, but in the bulk form exhibits no piezoelectric activity. However, when properly oriented on a compatible substrate, AlN thin films exhibit piezoelectric properties which have been studied for their potential use as pressure transducers, speakers, and SAW devices.[44]

Of most interest for this report are the high-temperature piezoelectric properties of AlN thin films. A recent paper[45] reported that an AlN SAW device deposited on a fused quartz substrate, operating at 60–100 MHz, exhibited piezoelectric responses at temperatures up to 1150°C. Other reports on chemical vapor deposited (MOCVD) AlN thin films have shown room temperature d_{33} values of $5·5 \times 10^{-12}$ Vm/N (about the same as LiNbO$_3$) and a dielectric constant K_{33} of 12.[46] Tsubouchi and Mikosheba[47] reported room temperature resistivity values of 10^{16} Ω-cm, a value higher than any other piezoelectric material discussed in this paper. With this combination of very high temperature operation, high resistivity, and reasonable piezoelectric coefficients, it seems that AlN thin films warrant further investigation.

7 SUMMARY

High-temperature technology is of major importance for chemical and material processing, automotive, aerospace, and power generating industries to name just a few. For many, the primary benefit of operating at higher temperatures is the direct cost savings associated with increased efficiency in fuel conversion. In a related matter, the development of advanced structural materials such as silicon nitride and carbon–carbon composites promotes a need for high-temperature electronic materials to monitor processing of these systems. This is exemplified by the recent organization of the First International High Temperature Electronics Conference by Sandia National Laboratory and Wright Laboratory.[46] Along with semiconductor, capacitor, magnetic, and packaging materials, electromechanical transducing materials are required to sense strains, vibrations, and noise under severe thermal conditions. Of the several different types of acoustic and strain sensors investigated, including accelerometers, strain gauge, air gap, eddy current, buffer rod, and fiber optic, piezoelectric types offer the best candidates when one considers sensitivity, cost, and design.

Figure 10 summarizes the maximum use temperature of widely commercial piezoelectric materials and the projected values of two experimental ones. If an operating temperature of 400°C or greater is required, the number of available sensor materials is clearly limited. If an operating
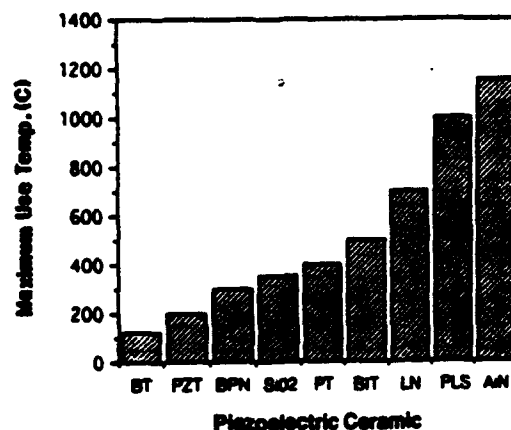
Fig. 10. Approximate maximum temperature of operation for piezoelectric ceramics. Most are estimated by combined consideration of the ferroelectric Curie temperature, sensitivity, and measured electrical resistivity. Others are known with a higher degree of certainty such as barium titanate (BT) limited by its T_c of 125°C, lead zirconate titanate (PZT) known to experience accelerated depoling at 200°C and quartz (SiO$_2$) with a maximum use temperature of 350°C.

temperature 750°C is chosen, there is no commercial material available. It is reasonable to assume that there now exists a need for vibration sensors that can function at 750°C, or even at 1000°C, and that the need will be even more pressing in the future. The design of such sensors presents a great challenge and will require the development of new materials and novel processing techniques.

This paper has discussed two options for very high temperature piezo-electric materials. The first was the family of PLS ferroelectrics, with the highest known T_c (some greater than 1500°C), The second was non-ferroelectric AlN thin film with a reported operating temperature of 1150°C. New ferroelectric compounds, also with very high T_c, have been predicted based on the Abrahams–Kurtz–Jameson relationship and an extensive inorganic crystal structure database.[49] This study, and other computer assisted studies of materials, may well identify the next generation of high-temperature vibration sensor materials.

ACKNOWLEDGMENT

REFERENCES

1. McCormick, B. J., Preface. In *High Temperature Electronics.* IEEE, Tucson, AZ, USA, 1981.
2. Naito, M., Recent sensors for automotive applications. *Ceram. Eng. Sci. Proc.,* 8(9–10) (1987) 1106–19.
3. Meetham, G. W., High temperature materials—a general review. *J. Mat. Sci.,* 26(4) (1991) 853–60.
4. Kusakabe, H., Okauchi, T. & Takigawa, M., *A Cylinder Pressure Sensor for Internal Combustion Engine.* SAE (Society of Automotive Engineers) paper 920701. SAE International, Warrendale, PA, USA, 1992.
5. Fowler, T. J., Acoustic emission testing of vessels. *Chem. Engng Prog.,* Sept. (1988) 59–70.
6. Helmshaw, R., *Non-Destructive Testing,* (2nd edn). Edward Arnold Publishing, London, UK, 1991.
7. Managan, W., Needs for high temperature electronics in fossil energy plants. In *Conference on High Temperature Electronics.* Tucson, AZ, USA, 1981.
8. Bissonnette, M. & Cloutier, M., Air gap measuring system. 1st International Machinery Monitoring and Diagnostic Conference. Las Vegas, NV, USA, 1989.
9. Guess, J. F., Analysis of piezoelectric benders used as knock sensors. In *Sensors and Actuators 1983.* Society of Automotive Engineers, Inc., Warrendale, PA, USA, 1983, p. 79.

10. Droner, B. E. & Pfeiffer, T. J., Ultrasonic inspection of hot steel blooms to detect internal pipe. *Mater. Evaluat.*, 36(6) (1980) 31–6.
11. Jaffe, B., Cook, Jr, W. R. & Jaffe, H., *Piezoelectric Ceramics.* Academic Press Ltd, London, 1971.
12. Endevco Div. Allied Signal, San Juan Capistrano, CA, USA, General Catalog (1989) 92675.
13. Vibrometer, Inc., Longveuil, Quebec, Canada, Product Catalog (1988).
14. CEC Instruments Division of IMO Industries, Inc., San Dimas, CA, USA, Product Literature.
15. Measurements Group, Inc., Tech-Note TN-513, Measurement of Thermal Expansion Coefficient Using Strain Gages. Measurements Group Inc., Raleigh, NC, USA, 1986.
16. Omega Engineering, Inc., *Pressure, Strain, and Force Measurement Handbook and Encyclopedia.* Omega Engineering, Inc., Stamford, CT, USA, 1987.
17. Lei, J. F., Mentor, J. & Van Horn, H. J., Influence of rare earth oxide addition on the oxidation behavior of PdCr strain gauge material. *1990 Meeting of the Electrochemical Society*, Montreal, Canada.
18. Ménard, P. & Bourgeois, J. M., Using capacitive sensors for AC generator monitoring. International Conference on Large High Voltage Electric Systems, Paris, France, 1990.
19. Car, W., Eddy current proximity sensors. *Sensors*, Nov. (1987) 21–5.
20. Cady, W. G., *Piezoelectricity*. McGraw Hill, New York, USA, 1946.
21. Herbert, J. M., *Ferroelectric Transducers and Sensors.* Gordon and Breach Science Publishers, New York, USA, 1982.
22. Swartz, S. L., Topics in electronic ceramics. *IEEE Trans. on Electrical Insulation*, 25(5) (1990) 935–87.
23. IEEE Standard on Piezoelectricity, *ANSI/IEEE Std 176-1978.* IEEE, New York, USA, 1978.
24. Kistler Instruments AG Winterthur, Switzerland, 1989, General Catalog.
25. Keramos, Inc., Indianapolis, IN, USA, General Catalog, 1991.
26. Token Corp. Tokyo, Japan, Piezoelectric Ceramic Catalog.
27. Crystal Technology, Inc., Palo Alto, CA, USA, Product Catalog.
28. Matsushita Electric Industrial Co., LTD, Osaka, Japan.
29. Fuierer, P. A., Grain-oriented perovskite layer ceramics for high temperature applications. PhD thesis, The Pennsylvania State University, Pennsylvania, USA, 1991.
30. Korzunova, L. V., Piezoelectric ceramics for high temperature transducers. *Ferroelectrics*, 134 (1992) 175–80.
31. Takahashi, M., Electrical resistivity of lead zirconate titanate ceramics containing impurities. *Jpn J. of Appl. Phys.*, 10(5) (1971) 643–51.
32. Gurevich, V. M., *Electronic Conductivity of Ferroelectrics.* English trans. from Russian (Israel Program for Scientific Translators, Jerusalem, 1971).
33. Ueda, I., Effects of additives on piezoelectric and related properties of $PbTiO_3$ ceramics. *Jpn J. Appl. Phys.*, 11(4) (1972) 450–61.
34. Bollman, W. & Gernand, M., In the disorder of $LiNbO_3$ crystals. *Phys. Stat. Sol.*, A9(1) (1972) 301–23.
35. Gurevich, V. M. & Rez, I. S., Possibility of controlling the conductivity of lead metaniobate by doping. *Isv. AN SSSR. Ser. Fiz.*, 24, No11 (Trans. Bulletin) (1960) p. 1258.

36. Angleton, P. A. & Hayer, J. R., Ceramic transducer elements and accelerometers using same. US Pat. No. 3,487,238 (1967).
37. Takenaka, T. & Sakata, K., Grain oriented and Mn-doped $(NaBi)_{(1-x)/2}$-$Ca_xBi_4Ti_4O_{15}$ ceramics for piezo- and pyrosensor materials. *Sensors and Materials*, 1 (1988) 35–46.
38. Fraser, M., Poling crystals of lithium niobate. *Properties of Lithium Niobate*. INSPEC, The Institute of Electrical Engineers, London, UK, 1989.
39. Nanamatsu, S., Kimura, M., Doi, K. & Takahashi, M., Ferroelectric properties of $Sr_2Nb_2O_7$ single crystals. *J. Phys. Soc. Japan*, 30 (1971) 300–4.
40. Nanamatsu, S., Kimura, M., Doi, K., Matsushita, S. and Yamada, N., A new ferroelectric, $LaTiO_3$. *Ferroelectrics*, 8 (1974) 511–13.
41. Fuierer, P. A. & Newnham, R. E., $La_2Ti_2O_7$ ceramics. *J. Am. Ceram. Soc.*, 75(11) (1991) 2876–81.
42. Turner, R. C., Work in progress.
43. Halliyal, A., Study of the piezoelectric and pyroelectric properties of polar glass ceramics. PhD thesis, The Pennsylvania State University, Pennsylvania, USA, 1991.
44. Mujasaka, Y., Hashino, S. & Takahashi, S., Advances in structure and fabrication process for thin film acoustic resonators. *1987 Ultrasonics Symposium*. IEEE, New York, USA, 1987, pp. 385–93.
45. Patel, N. D. & Nicholson, P. S., High frequency, high temperature ultrasonic transducers. *NDT International*, 23(5) (1990) 262–6.
46. Shiosaki, T., Hayoshi, M. & Kawabata, A., Audio-frequency characteristics of a piezoelectric speaker using an AlN film deposited on a polymer or metal membrane. *1982 Ultrasonics Symposium, Proc.* IEEE, New York, USA, 1982, pp. 529–32.
47. Tsubouchi, K. & Mikoshiba, N., Zero temperature coefficient saw delay line on AlN epitaxial films. *1983 Ultrasonics Symposium, Proc.* IEEE, New York, USA, 1980, pp. 299–310.
48. King, D. B. & Thome, F. V., *Transactions of the First International High Temperature Electronics Conference*. Sandia National Laboratory, Albuquerque, NM, USA, 1991.
49. Abrahams, S. C., Systematic prediction of new ferroelectrics on the basis of structure. *Ferroelectrics*, 104 (1990) 37–48.

APPENDIX 2

Materials Science and Technology

A Comprehensive Treatment

Edited by
R. W. Cahn, P. Haasen, E. J. Kramer

Volume 11
Structure and Properties
of Ceramics

Volume Editor: Michael V. Swain

VCH

12 Ferroelectric Ceramics

Kenji Uchino

Materials Research Laboratory, Pennsylvania State University, University Park, PA, U.S.A.

List of Symbols and Abbreviations

c_p	specific heat
C	Curie–Weiss constant
d	piezoelectric coefficient
D	electric displacement
E	electric field
f_A	antiresonance frequency
f_R	resonance frequency
F	Landau free energy
g	piezoelectric coefficient,
	secondary electrooptic coefficient
I	light intensity
k	electromechanical coupling factor
k, k'	force constants
L	optical pathlength
M	electrostrictive coefficient
n	refractive index
p	pyroelectric coefficient
P	dielectric polarization
P_s	spontaneous polarization
Q	electrostrictive coefficient
Q_M	mechanical quality factor
r	primary electrooptic coefficient,
	voltage rise ratio of a piezoelectric transformer
s	elastic compliance
T_0	Curie–Weiss temperature
T_C	Curie temperature
u	displacement of an ion from the equilibrium position
U	energy
v	sound velocity
W_{dip}	energy of the dipole moment
W_{elas}	elastic energy of displacement
x	strain
x_s	spontaneous strain
X	stress
α	ionic polarizability
γ	Lorentz factor
Γ	phase retardation
ε	relative permittivity
ε_0	vacuum permittivity
μ	dipole moment of the unit cell of a crystal
ϕ	barrier height of the Schottky barrier

D-TGS deuterated triglycine sulphate
GBL   grain boundary layer
MLC   multilayered capacitor
OA   office automation
PLZT $(Pb, La)(Zr, Ti)O_3$
PMN   lead magnesium niobate
PTC   positive temperature coefficient
PTCR   positive temperature coefficient of resistivity
PVFD   polyvinylidene fluoride
PZT   lead zirconate titanate
rpm   revolutions per minute
SAW   surface acoustic wave
VTR   video tape recorder

12.1 General View of Ferroelectrics

12.1.1 Crystal Structure and Ferroelectricity

In so-called dielectric materials, the constituent atoms are considered to be ionized to a certain degree and are either positively or negatively charged. In such ionic crystals, when an electric field is applied, cations are attracted to the cathode and anions to the anode due to electrostatic interaction. The electron clouds also deform, causing electric dipoles. This phenomenon is called the *electric polarization* of the dielectrics, and the polarization is expressed quantitatively as the sum of the electric dipoles per unit volume (C/m^2). Figure 12-1 shows schematically the origin of the electric polarization. There are three kinds; electron, ion and dipole reorientation-related polarizations.

Compared with vacuum capacitors, dielectric capacitors can store more electric charge due to the dielectric polarization P as shown in Fig. 12-2. The physical quantity corresponding to the stored electric charge per unit area is called the electric displacement D, and is related to the electric field by the following expression:

$$D = \varepsilon_0 E + P = \varepsilon \varepsilon_0 E \qquad (12\text{-}1)$$

Here, ε_0 is the vacuum permittivity ($= 8.854 \times 10^{-12}$ F/m), ε is the material's relative permittivity (also simply called permittivity or dielectric constant, and in general it is a tensor).

Depending on the crystal structure, in *some crystal lattices, the centers of the positive and negative charges do not coincide even without the application of external electric field. In this case, it is said that there exists *spontaneous polarization* in the crystal, and, especially when the polarization of the dielectric can be altered by an electric field, it is called *ferroelectric*.

Not every dielectric can be a ferroelectric. Crystals can be classified into 32 point groups according to their crystallographic symmetry, and these point groups can be divided largely into two classes, one with a center of symmetry and the other without. There are 21 point groups which do not have a center of symmetry. In crystals belonging to 20 of these point groups [except for the point group (432)], positive and negative charges appear on surfaces when stresses are applied. These materials are known as *piezoelectrics*. *Pyroelectricity* is the phenomenon in which, because of the temperature dependence of the spontaneous polarization, as the temperature of the crystal is changed, electric charges cor-
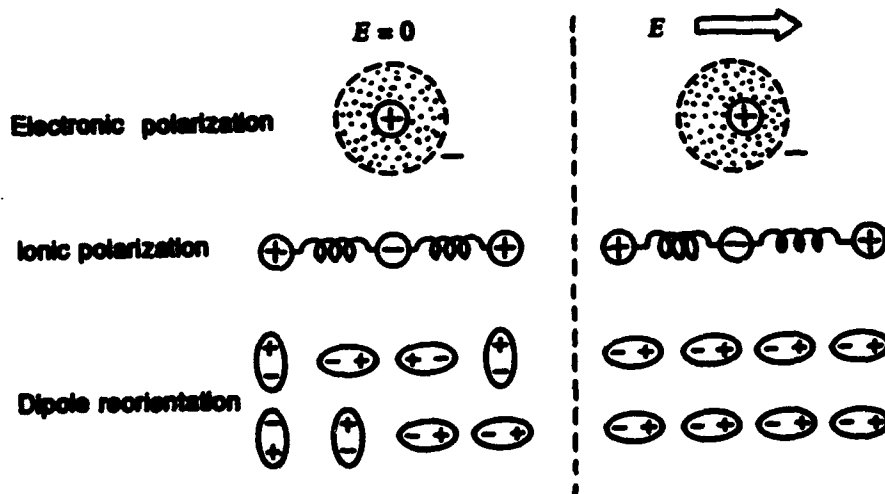
Figure 12-1. Microscopic origins of the electric polarization.

σ_f : Free charge
σ_b : Bound charge
σ_t : True charge
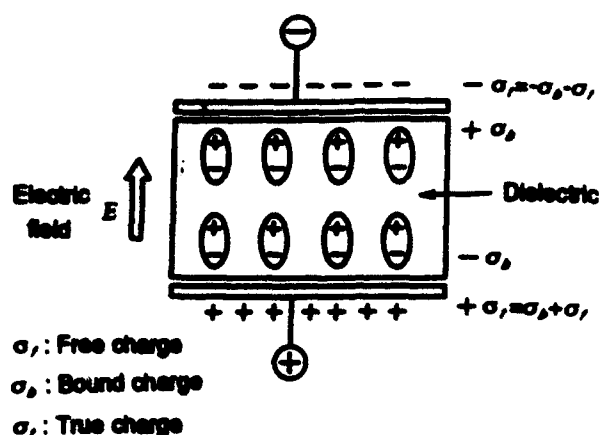
Figure 12-2. Electric charge accumulation in a dielectric capacitor.

responding to the change of the spontaneous polarization appear on the surface of the crystal. Among the pyroelectric crystals, those whose spontaneous polarization can be reversed by an electric field (not exceeding the breakdown limit of the crystal) are called ferroelectrics. There is some ambiguity in this definition. In order to establish ferroelectricity, it is necessary to apply an electric field on a pyroelectric material and experimentally ascertain the polarization reversal. Table 12-1 shows the classification of the point groups.

12.1.2 Origin of Spontaneous Polarization

Why is it that crystals which, from a consideration of the elastic energy, should be stable by being non-polar, still experience the shifting of cations and anions and become spontaneously polarized? The reason is briefly explained below. For simplicity, let us assume that dipole moments result from the displacement of one kind of ion A (electric charge q) relative to the crystal lattice. Consider the case in which the polarization is caused by all the A ions being displaced equally in a lattice. It follows that, on any individual A ion, there exists a local field from the surrounding polarization P, even if there is no external field. The concept of the local field is shown schematically in Fig. 12-3. It can be shown that:

$$E^{loc} = [\gamma/(3\,\varepsilon_0)]\,P \qquad (12\text{-}2)$$

Table 12-1. Crystallographic classification with respect to crystal centrosymmetry and polarity.[a]

Polarity	Centrosymmetry	Number of point groups	Crystal class						
			Cubic	Hexagonal	Tetragonal	Rhombohedral	Orthorhombic	Monoclinic	Triclinic
Non-polar (22)	O (11)	11	$m3m$ O_h $m3$ T_h	$6/mmm$ D_{6h} $6/m$ C_{6h}	$4/mmm$ D_{4h} $4/m$ C_{4h}	$\bar{3}m$ D_{3d} $\bar{3}$ C_{3i}	mmm D_{2h}	$2/m$ C_{2h}	$\bar{1}$ C_i
	× (21)	11	432 O 23 T $\bar{4}3m$ T_d	622 D_6 $\bar{6}$ C_{3h} $\bar{6}m2$ D_{3h}	422 D_4 $\bar{4}$ S_4 $\bar{4}2m$ D_{2d}	32 D_3	222 D_2		
Polar (pyro) (10)		10		$6mm$ C_{6v} 6 C_6	$4mm$ C_{4v} 4 C_4	$3m$ C_{3v} 3 C_3	$2mm$ C_{2v}	2 C_2 m C_s	1 C_1

[a] Piezoelectric crystals are those in the area enclosed by the thick line.
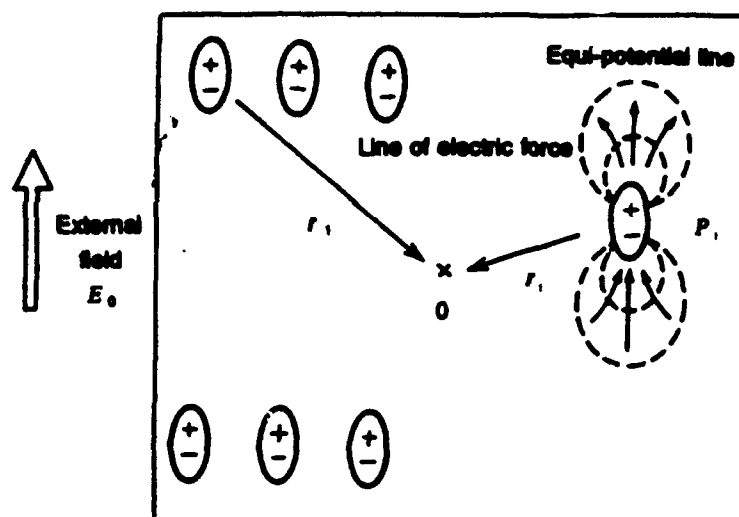
Figure 12-3. Concept of the local field. E^{loc} is given by

$$E^{loc} = E_0 + \sum_i \frac{3(P_i \cdot r_i)r_i - r_i^2 P_i}{4\pi\varepsilon_0 r_i^5}.$$

This is the driving force of the ion shift. Here γ is called the *Lorentz factor*. For an isotropic and a cubic system, it is known that $\gamma = 1$ (Kittel, 1966). ε_0 is the permittivity in vacuum and is equal to 8.854×10^{-12} F/m. If the *ionic polarizability* of ion A is α, then the dipole moment of the unit cell of this crystal is:

$$\mu = [\alpha\gamma/(3\varepsilon_0)]P \tag{12-3}$$

The energy of this dipole moment (dipole-dipole coupling) is

$$W_{dip} = -\mu \cdot E^{loc} = -[\alpha\gamma^2/(9\varepsilon_0^2)]P^2 \tag{12-4}$$

Per unit volume, it is:

$$W_{dip} = N w_{dip} = -[N\alpha\gamma^2/(9\varepsilon_0^2)]P^2 \tag{12-5}$$

On the other hand, when the A ions are displaced from their nonpolar equilibrium positions, the elastic energy also increases. If the displacement is u, and the force constants k and k', then the increase of the elastic energy per unit volume can be expressed as:

$$W_{elas} = N\left(\frac{k}{2}u^2 + \frac{k'}{4}u^4\right) \tag{12-6}$$

Here, k' (> 0) is the higher-order force constant. It should be noted that in pyroelec-

trics, k' plays an important role in determining the magnitude of the dipole moment. By rewriting Eq. (12-6) using:

$$P = Nqu \quad (q \text{ is the electric charge}) \tag{12-7}$$

Combining with Eq. (12-5), the total energy can be expressed as follows (see Fig. 12-4):

$$W_{tot} = W_{dip} + W_{elas} = \tag{12-8}$$

$$= \left(\frac{k}{2Nq^2} - \frac{N\alpha\gamma^2}{9\varepsilon_0^2}\right)P^2 + \frac{k'}{4N^3q^4}P^4$$

From this, one can see that if the coefficient of the harmonic term of the elastic energy is equal or greater than the coefficient of the dipole-dipole coupling, then $P = 0$, i.e., the A ions are stable and remain at their non-polar equilibrium positions. Otherwise, a shift from the equilibrium position $\{P^2 = [2N\alpha\gamma^2/(9\varepsilon_0^2) - k/(Nq^2)]/[k'/(N^3q^4)]\}$ is stable. In the perovskite-type crystal structure (as in barium titanate) as described in the next section, it is thought that because of the occurrence of a larger Lorentz factor γ (≈ 10) (Kinase et al., 1969) than found for other crystal structures, spontaneous polarization can occur more easily.

(a)

W_{dip}

P

Dipole interaction

(b)

W_{elas}

P

Elastic energy

(c)

W_{tot}

P
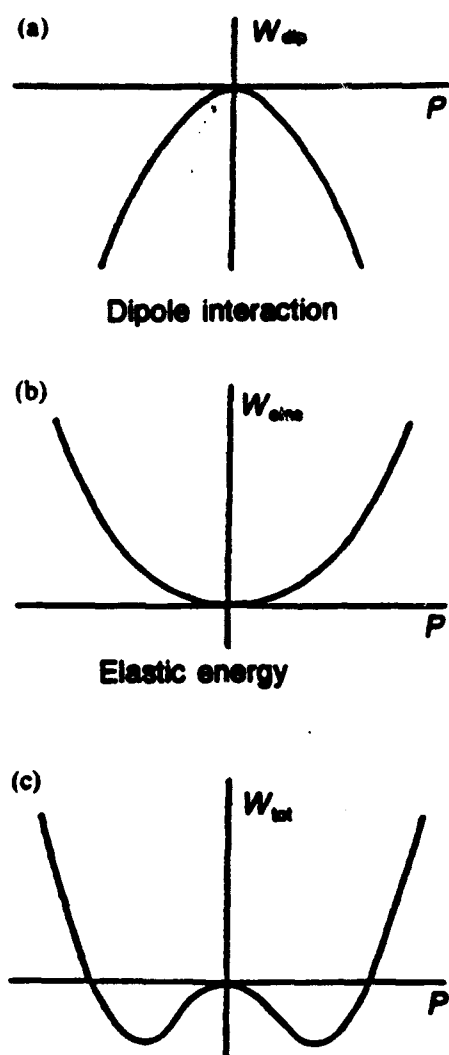
Figure 12-4. Energy explanation of the origin of spontaneous polarization.

(a) Dipole interaction

$$W_{dip} = -[N\alpha\gamma^2/(9\varepsilon_0^2)]P^2$$

(b) Elastic energy

$$W_{elas} = \frac{k}{2Nq^2}P^2 + \frac{k'}{4N^3q^4}P^4$$

(c) Total energy

$$W_{tot} = W_{dip} + W_{elas}$$

12.1.3 Origin of Field Induced Strain

With the application of an electric field, the dielectric material inevitably induces strain or crystal deformation. There are two types of *strain* (defined by the ratio $\Delta L/L$: the amount of deformation with respect to the original length) that may be induced by an electric field depending on the nature of the interaction "springs" between the ions which is, in turn, determined by the crystal structure (Uchino et al., 1983). As shown in Fig. 12-5a, in crystals where there is no centrosymmetry, strain, x, is generated in proportion to the electric field E. This is the *converse piezoelectric effect*, and the tensor quantity, **d**, defined by the relationship

$$x = \mathbf{d}E \tag{12-9}$$

is referred to as the *piezoelectric coefficient*. On the other hand, in centrosymmetric crystals, as shown in Fig. 12-5b, the expansion and contraction of the "spring" are such that the net response is nearly zero. However, the anharmonic nature of the "spring" motion will still bring about a small induced strain that is proportional to the square of the electric field E. This is referred to as the *electrostriction effect* which is expressed in terms of the strain, x, the applied electric field, E, and the *electrostriction coefficient*, M, as:

$$x = ME^2 \tag{12-10}$$

The system pictured in Fig. 12-5a also possesses a spontaneous bias of electrical charge, or a spontaneous polarization. When a large reverse bias electric field is applied to a crystal that has a spontaneous polarization in a particular polar direction, a transition "phase" is formed which is another stable crystal state in which the relative positions of the ions are reversed (in terms of an untwinned single crystal, this is equivalent to rotating the crystal 180° about an axis perpendicular to its polar axis). This transition, referred to as *polarization reversal*, also causes a remarkable change in strain. This particular class of
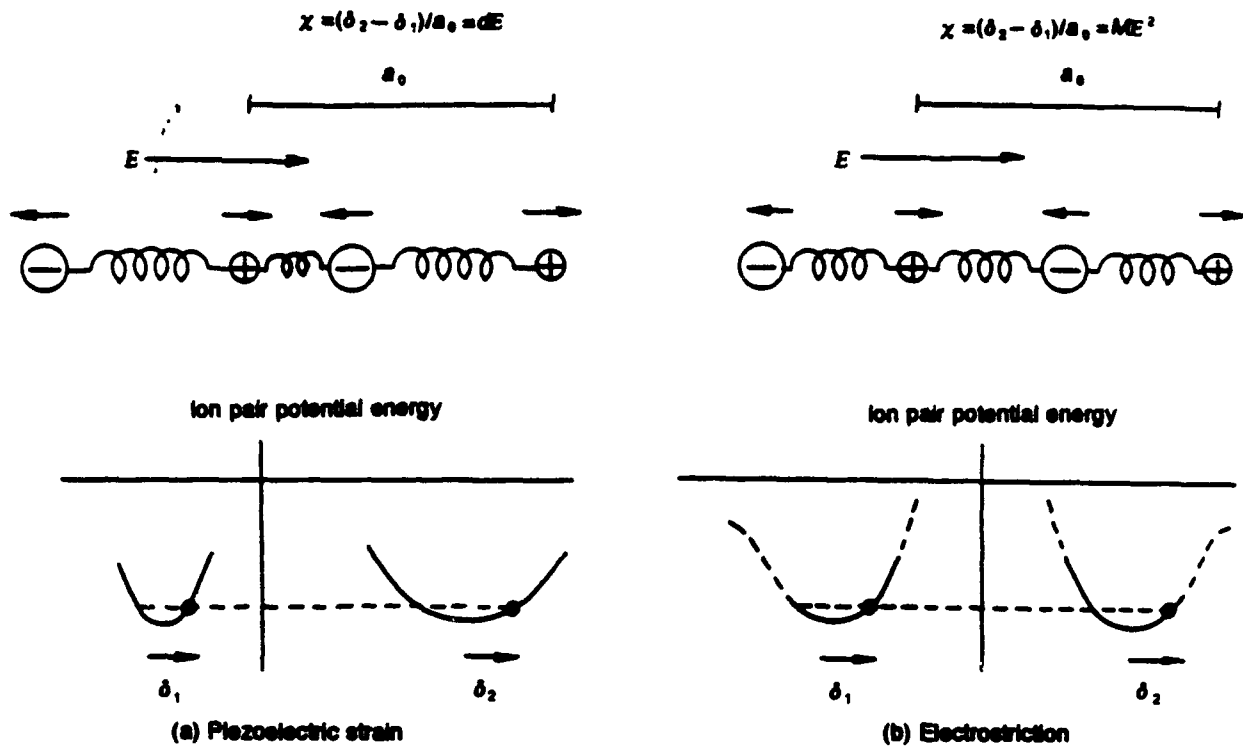
Figure 12-5. Diagrammatic explanation of the origins of piezoelectric strain (a) and electrostriction (b).

substances are referred to as ferroelectrics, as mentioned in Sec. 12.1.1. Generally, what is actually observed as a field-induced strain, is a complicated combination of the three basic effects just described.

12.1.4 Electrooptic Effect

Since light is an alternating electromagnetic wave with electric and magnetic field directions crossing each other, it induces electric polarization in a dielectric crystal and the light itself is influenced by the crystal. The alternating frequency of the light is so high ($\approx 10^{15}$ Hz) that only the electronic polarization should follow the field change, and the relative permittivity of the crystal is small, not exceeding 10. The permittivity ε at this high frequency is related to the refractive index n by the following equation:

$$\varepsilon = n^2 \qquad (12\text{-}11)$$

When an external electric field is applied to the crystal, ion shift is induced, deforming the shape of the electron cloud, and consequently the refractive index is changed. This phenomenon is called the *electrooptic effect*.

Generally, refractive indices are symmetrical 2-R tensor quantities and represented by using a *refractive indicatrix* (Eq. 12-12), where n_1, n_2 and n_3 are principal refractive indices.

$$\frac{x^2}{n_1^2} + \frac{y^2}{n_2^2} + \frac{z^2}{n_3^2} = 1 \qquad (12\text{-}12)$$

With the application of an electric field, the change in refractive index is given by an expansion expression:

$$1/n_{ij}^2(E) - 1/n_{ij}^2(0) =$$
$$= \sum r_{ijk} E_k + \tfrac{1}{2}\sum g_{ijkl} E_k E_l \qquad (12\text{-}13)$$

Here r_{ijk} is a primary electrooptic coefficient (*Pockel's effect*) and g_{ijkl} is a secondary coefficient (*Kerr effect*).

Considering a paraelectric phase of a perovskite crystal ($m3m$) as an example, the Kerr coefficients are represented in the following matrix:

$$
\begin{bmatrix}
g_{11} & g_{12} & g_{12} & 0 & 0 & 0 \\
g_{12} & g_{11} & g_{12} & 0 & 0 & 0 \\
g_{12} & g_{12} & g_{11} & 0 & 0 & 0 \\
0 & 0 & 0 & g_{44} & 0 & 0 \\
0 & 0 & 0 & 0 & g_{44} & 0 \\
0 & 0 & 0 & 0 & 0 & g_{44}
\end{bmatrix}
$$

Then, the refractive indicatrix under the electric field applied along z-direction can be expressed as:

$$
\frac{x^2 + y^2}{n_0^2[1 - (n_0^2/2)g_{12}E_z^2]^2} +
$$

$$
+ \frac{z^2}{n_0^2[1 - (n_0^2/2)g_{11}E_z^2]^2} = 1 \quad (12\text{-}14)
$$

When light is transmitted along the y-direction, the phase retardation Γ_y between an ordinary and an extraordinary light is given by:

$$
\Gamma_y = \frac{2\pi}{\lambda}\frac{n_0^3}{2}(g_{12} - g_{11})L\left(\frac{V_z}{d}\right)^2 \quad (12\text{-}15)
$$

d is the electrode gap and L is the optical path length (see Fig. 12-6). Putting a crystal between crossed polarizers arranged at the 45° direction with respect to z-axis, the output light intensity can be modulated as a function of applied voltage in the following way:

$$
I = I_0 \sin^2\left(\frac{\Gamma_y}{2}\right) = \frac{1}{2}I_0(1 - \cos\Gamma_y) \quad (12\text{-}16)
$$

This is the principle of a light shutter/valve, and the voltage required for the first intensity maximum (i.e., $\Gamma_y = \pi$) is essential and called the *half-wavelength voltage*.

12.1.5 Example of a Ferroelectric

A typical ceramic ferroelectric is barium titanate, which is used here as an example to illustrate some properties of the ferroelectrics.

As shown in Fig. 12-7, $BaTiO_3$ has a perovskite crystal structure. (See also Chap. 1, Secs. 1.3.3 and 1.6.2 of this Volume for a more complete description of the crystal structures of perovskites.) In the high-temperature paraelectric phase (nonpolar phase) there is no spontaneous polarization (the symmetry is $O_h - m3m$). Below the transition temperature T_C called the
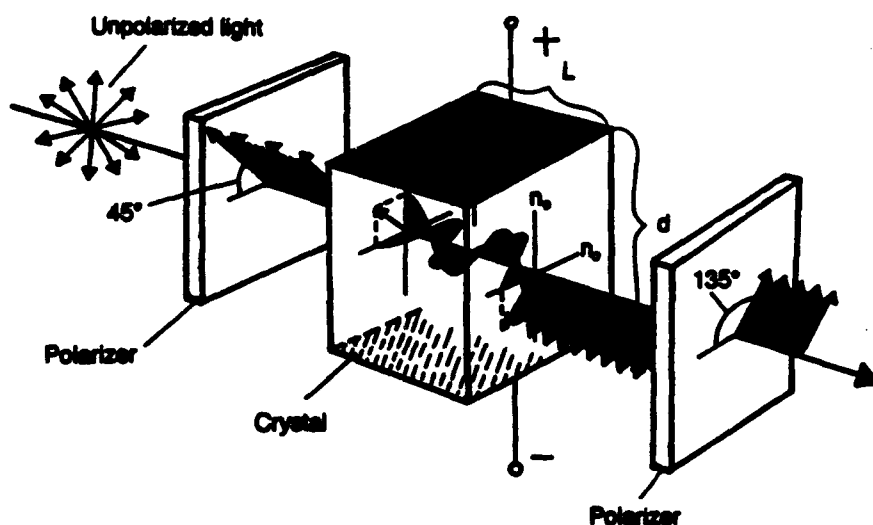
Figure 12-6. Optical phase retardation through an electrooptic crystal. Notice the crossed polarizer configuration.

(a)

$T > T_c$

(b)

Ba^{2+}

Ti^{4+}

$T < T_c$

● Ti^{4+} ● Ba^{2+} ○ O^{2-}

T_c : Curie temperature
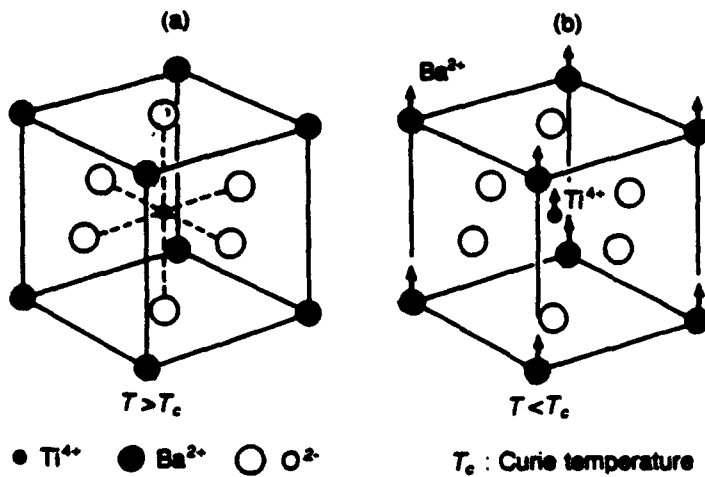
Figure 12-7. Structure of $BaTiO_3$.

Curie temperature (about 120 °C), spontaneous polarization occurs, and the crystal structure becomes slightly elongated, that is, tetragonal ($C_{4v} - 4mm$). Figure 12-8 shows schematically the temperature dependence of the spontaneous polarization P_s and permittivity ε. P_s decreases with increasing temperature and vanishes at the Curie point, while ε tends to diverge near T_C. Also, the reciprocal permittivity $1/\varepsilon$ is known to be linear with respect to the temperature in a wide range in the paraelectric phase (so-called Curie–Weiss law),

$$\varepsilon = C/(T - T_0) \qquad (12\text{-}17)$$

Here C is the Curie–Weiss constant and T_0 the Curie–Weiss temperature. T_0 is slightly lower than exact transition temperature T_C.

It is also known that the spontaneous polarization P_s and the spontaneous strain x_s follow the relationship:

$$x_s = Q P_s^2 \qquad (12\text{-}18)$$

x_s decreases almost linearly with increasing temperature. In the case of $BaTiO_3$, in the ferroelectric phase, it exhibits the piezoelectric effect, while in the paraelectric phase, it is non-piezoelectric and exhibits the electrostrictive effect.

12.1.6 Applications of Ferroelectrics

Ferroelectric materials, especially polycrystalline ceramics, are very promising for varieties of application fields such as *high-permittivity capacitors, pyroelectric sensors, piezoelectric/electrostrictive transducers, electrooptic devices* and *PTC thermistors.*

For capacitor dielectrics, the peak dielectric constant around the transition (Curie) temperature is utilized, while the strong temperature dependence of the spontaneous polarization below T_C is applied for pyroelectric sensors. Piezoelectric materials are applicable in sensors and actuators. Pressure and acceleration sensors
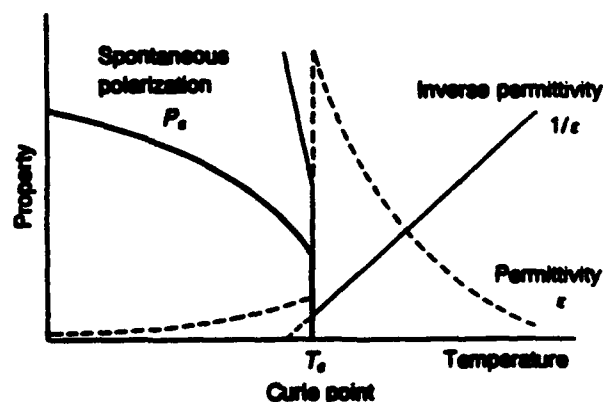
Figure 12-8. Temperature dependence of the spontaneous polarization P_s and permittivity ε.

are now commercially available in addition to conventional piezo-vibrators. Precision positioners and pulse drive linear motors have already been installed in precision lathe machines, semiconductor manufacturing apparatus and OA equipment etc. Recent topical development is found in ultrasonic motors. Electrooptic materials will become future key components in displays and optical-communication systems. For thermistor applications, semiconductive ferroelectric ceramics with a positive temperature coefficient (PTC) of resistivity due to a junction effect have been developed from barium-titanate-based materials.

12.2 High-Permittivity Dielectrics

12.2.1 Relaxor Ferroelectrics

There are two classes of ceramic capacitors: one is used for the thermal compensation of electrical circuits, using a TiO_2-based material, and the other is a high-permittivity capacitor with $BaTiO_3$- or $Pb(Zr,Ti)O_3$-based materials. Recently relaxor ferroelectrics such as $Pb(Mg_{1/3}Nb_{2/3})O_3$ and $Pb(Zn_{1/3}Nb_{2/3})O_3$ have been developed for very compact chip capacitors.

The reasons why these complex perovskites have been investigated intensively for capacitor applications are: (1) their very high permittivity, and (2) their temperature-insensitive characteristics (i.e., diffuse phase transition) in comparison with the normal perovskite solid solutions.

An intuitive crystallographic model has been proposed to explain the high permittivity of the disordered perovskites (Uchino, 1980). Figures 12-9a and 12-9b show the ordered and disordered structures for an $A(B_{11/2}B_{111/2})O_3$ perovskite crystal. As-

suming a rigid-ion model, a large "rattling" space is expected for the smaller B ions in the disordered structure because the large B ions prop open the lattice framework. Much less "rattling" space is expected in the ordered arrangement where neighboring atoms collapse systematically around the small B ions.

When an electric field is applied to a disordered perovskite, the B ions with a large rattling space can shift easily without distorting the oxygen framework. A larger polarization can be expected per unit magnitude of electric field. In other words, larger dielectric constants and larger Curie–Weiss constants. On the other hand, in ordered perovskites with a very small rattling space, the B ions cannot move easily without distorting the octahedron. A smaller permittivity and Curie–Weiss constant are expected.

The reason why the phase transition becomes diffuse in the relaxor ferroelectrics has not yet been clarified, although the "microscopic composition fluctuation" model is the most widely accepted (Kanzig, 1951; Rolov, 1963, Uchino et al., 1981). Considering the Känzig region (the minimum size region in order to cause a cooperative phenomenon, ferroelectricity) to be in the range of $100-1000 Å$, disordered perovskites such as $Pb(Mg_{1/3}Nb_{2/3})O_3$ reveal a local fluctuation of the distribution
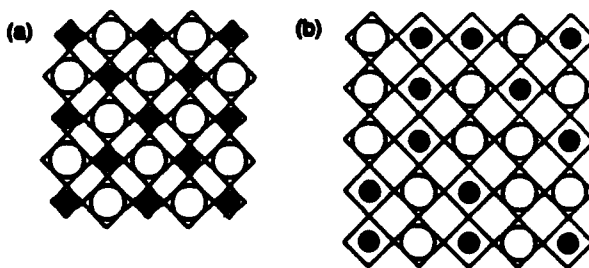
Figure 12-9. Crystal structure models of the $A(B_{11/2}B_{111/2})O_3$ type perovskite: (a) ordered structure with a small rattling space and (b) disordered structure with a large rattling space ($O = B_1$ and $\bullet = B_{11}$).

Ordered

Disordered
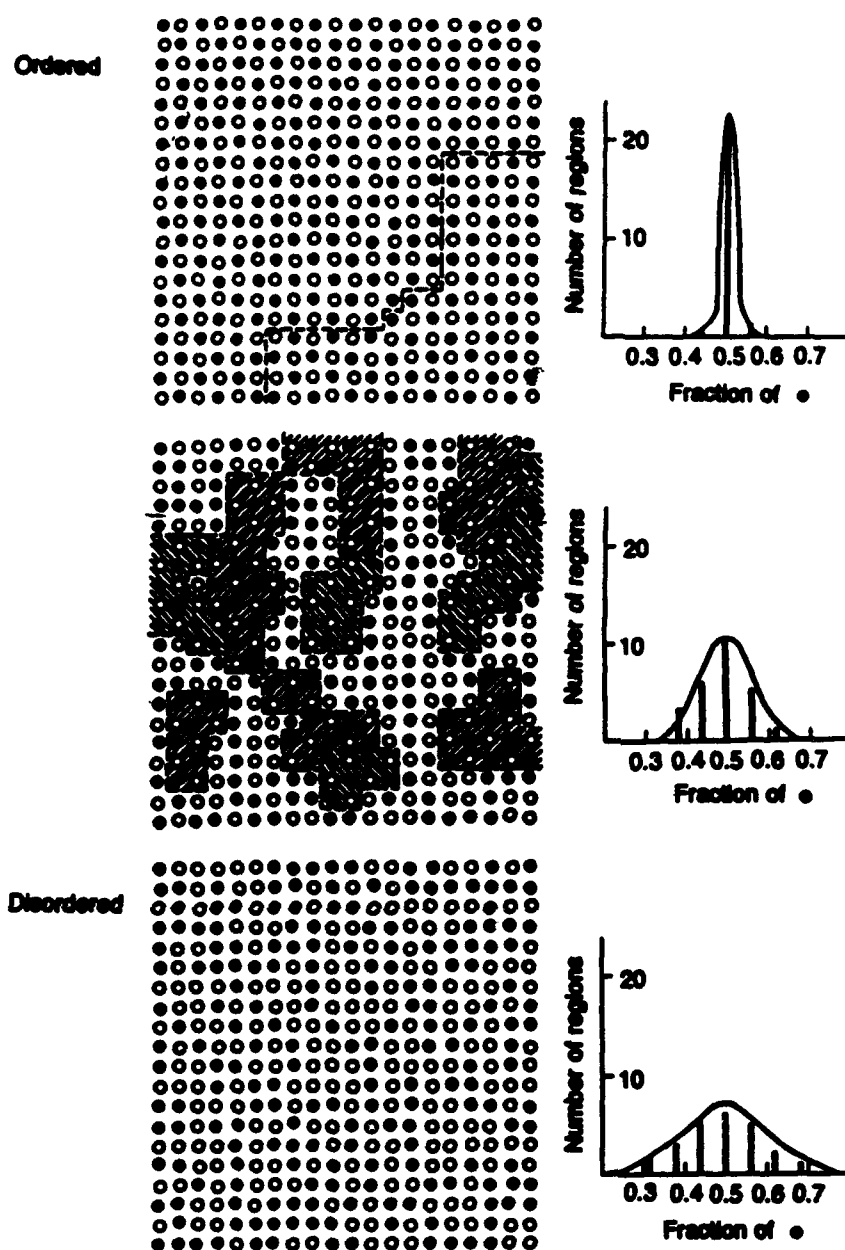
Figure 12-10. Computer simulation of the composition fluctuation in the $A(B_{I1/2}B_{II1/2})O_3$-type calculated for the varying degrees of the ionic ordering (Känzig region size: 4×4).

of Mg^{2+} and Nb^{5+} ions. Figure 12-10 shows a computer simulation of the composition fluctuation in the $A(B_{I1/2}B_{II1/2})O_3$-type crystal calculated for various degrees of the ionic ordering. The fluctuation of the B_I/B_{II} fraction x obeys a Gaussian error distribution. H. B. Krause reported observing the short-range ionic ordering of $Pb(Mg_{1/3}Nb_{2/3})O_3$ by electron microscopy (Krause et al., 1979). The high-resolution image in Fig. 12-11 reveals somewhat

ordered (ion-ordered) islands in the range of 20–50 Å, each of which may have a slightly different transition temperature.

Another significant characteristic of these "relaxor" ferroelectrics is *dielectric relaxation* (frequency dependence of permittivity) from which their name originates. Temperature dependence of the permittivity in $Pb(Mg_{1/3}Nb_{2/3})O_3$ is plotted in Fig. 12-12 for various measuring frequencies (Smolensky et al., 1961). With in-

Figure 12-11. High resolution electron-microscope image of the $Pb(Mg_{1/3}Nb_{2/3})O_3$ single crystal ((110) plane). Note ion-ordered islands in the range c' 20–50 Å.

creasing measuring frequency, the permittivity in the low-temperature (ferroelectric) phase decreases and the peak temperature shifts towards the higher frequency; this contrasts with normal ferroelectrics such as $BaTiO_3$ where the peak temperature hardly changes with frequency. This is probably caused by shallow multipotential-wells in a locally distorted perovskite cell due to the disordered ionic arrangement (*Skanavi-type dielectric relaxation*) (Skanavi et al., 1958), in addition to a ferroelectric phase transition phenomenon.

12.2.2 Multilayered Capacitors (MLC)

Multilayer structures have been developed as part of capacitor manufacturing aimed at the integration of electrical circuit components. Figure 12-13 schematically shows a multilayer capacitor chip. Thin sheets made by the *tape casting technique*, starting from a slurry of the dielectric powder and organic solvents, are coated with Pt or Ag-Pd paste to form electrodes, then several tens of sheets are stacked together and sintered. Finally, external electrodes, used to connect the chip with the circuit, are painted on.

Figure 12-12. Temperature dependence of the permittivity and $\tan\delta$ in $Pb(Mg_{1/3}Nb_{2/3})O_3$ for the various measuring frequencies (kHz): (1) 0.4, (2) 1, (3) 45, (4) 450, (5) 1500, (6) 4500.
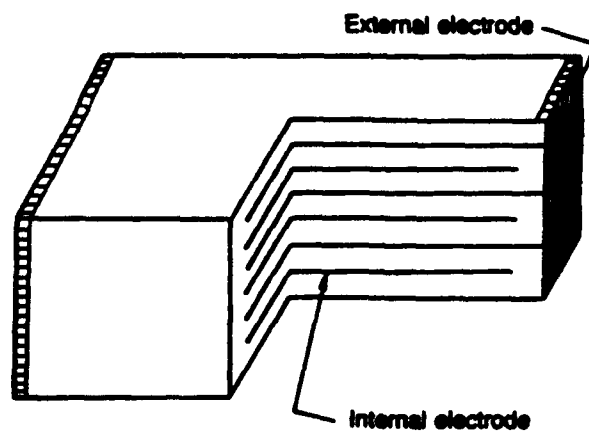
Figure 12-   cture of a multilayer capacitor chip.

12.3 Pyroelectric Devices

12.3.1 Temperature/Infrared-Light Sensors

Practical applications of the pyroelectric effect in temperature sensors and infrared-light detectors have gradually been promoted, providing, together with uses in piezoelectric resonators, of the commercial market for dielectric ceramics.

Figure 12-14. Typical geometric configurations for pyroelectric detectors: (a) face electrodes; (b) edge electrodes.

The merits of pyrosensors compared to other infrared-sensor materials such as semiconductors are summarized as follows:

(a) Wide range of response frequency

(b) Use at room temperature

(c) Quick response in comparison with other temperature sensors

(d) High-grade quality (optical-grade homogeneity etc.) of ceramic pyrosensors is unnecessary.

The principle on which the pyroelectric effect is based is the measurement of the charge generation associated with the spontaneous polarization change with temperature:

$$j = \partial P_s/\partial t = (\partial P_s/\partial T)(\partial T/\partial t) = p(? \quad) \qquad (12\text{-}19)$$

Here, p is denoted as a *pyroelectric coefficient*. Two typical electrode arrangements for pyrosensors are illustrated in Fig. 12-14: (a) face electrodes with the polarization direction parallel to the infrared irradiation,

and (b) edge electrodes with the polarization direction perpendicular to the irradiation. The former type has higher efficiency, but requires a sophisticated fabrication process of transparent uniform electrodes for infrared light.

The pyroelectric sensor is a device transducing optical/thermal energy to electrical energy, and its efficiency or figure of merit is evaluated in several ways; p, p/c_p, or $p/(c_p \varepsilon)$ (c_p: specific heat). This is because the temperature change of the sample is larger for the smaller c_p material under constant heating, and the voltage generated by a certain amount of pyrocharge becomes larger for the smaller ε (permittivity) material.

Table 12-2 lists the figures of merit of several pyroelectric materials.

Improvement of the characteristics has been attempted by using composites of

Table 12-2. Room-temperature properties of various pyroelectric detector materials and some "figures of merit" for their detector operation.

Material	p ($nC\,cm^{-2}\,K^{-1}$)	$\varepsilon/\varepsilon_0$	c_p ($J\,cm^{-3}\,K^{-1}$)	p/c_p ($nA\,cm\,W^{-1}$)	$p/(c_p\varepsilon)$ ($V\,cm^{-2}\,J^{-1}$)
TGS	30	50	1·7	17·8	4000
LiTaO$_3$	19	46	3·19	6·0	1470
Sr$_{1/2}$Ba$_{1/2}$Nb$_2$O$_6$	60	400	2·34	25·6	720
PLZT (6/80/20)	76	1000	2·57	29·9	340
PVF$_2$	3	11	2·4	1·3	1290

pyro-ceramics and polymers (Bhalla et al., 1981). In addition to the primary pyroelectric effect, a secondary effect is superimposed, i.e., the stress due to the thermal expansion d difference between the ceramic and polymer generates electric charge through the piezoelectric effect.

Figure 12-15 shows a typical structure of a polymer used in pyroelectric infrared sensors. In practical usage, a pyro-sensor requires an infrared-light (thermal-ray) chop-

per, because the electrical signal can be detected only at the transient stage of light illumination or shut off. An electromagnetic motor was conventionally used as a light-chopper mechanism, and recently a piezoelectric bimorph chopper has been developed by Y. Kuwano et al. (Shibata et al., 1985), which prompted miniaturization of the pyrosensors (Fig. 12-16).

12.3.2 Infrared Image Sensors

In Fig. 12-17 the visualization of a thermal-distribution image is exemplified by a pyro-vidicon tube (Taylor et al., 1973). The light emitted from an object is filtered with a germanium lens producing an infrared beam which is focused onto the pyroelectric target through an optical chopper. The temperature distribution of the object is represented on the target as a voltage distribution. This is monitored from the back surface of the target by electron-beam scanning using a conventional TV tube.

One of disadvantages of the pyro-vidicon is the degradation of the image over a long period of usage due to thermal diffusion on the target. Pedder et al. proposed a segmented target design in order to solve the diffusion problem (Warner et al., 1981). Figure 12-18 shows the microscopic struc-
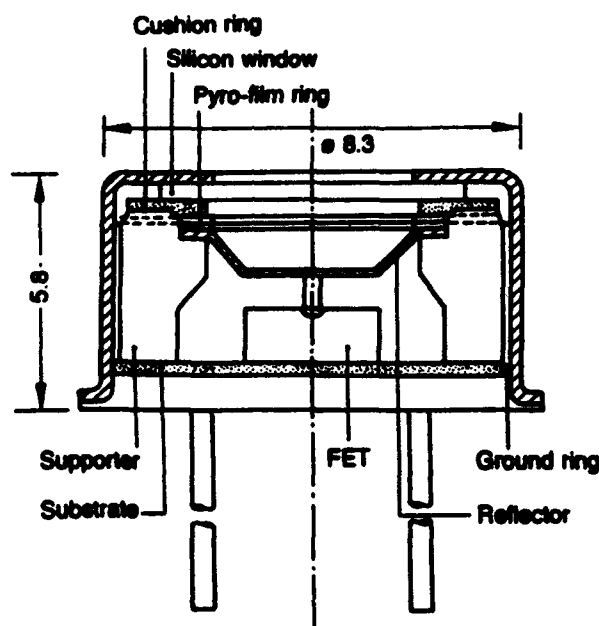
Figure 12-15. A polymer-based pyroelectric infrared sensor.
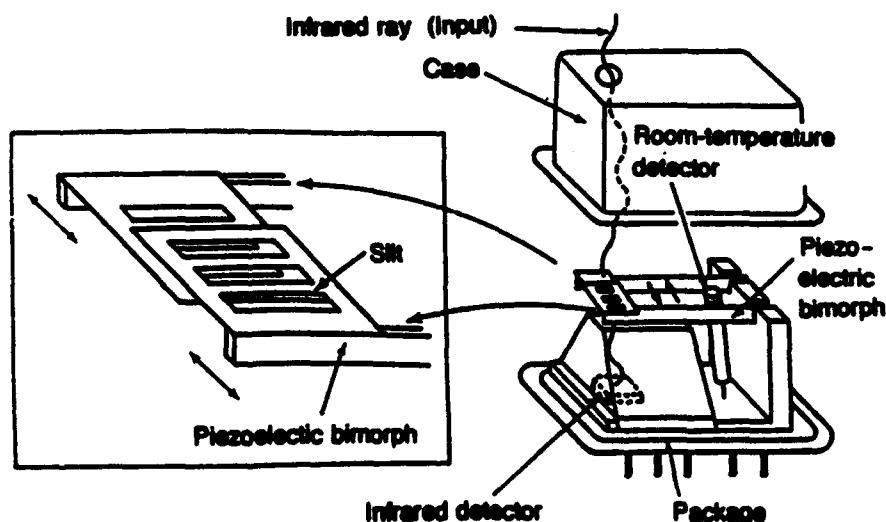
Figure 12-16. Swing-type pyroelectric temperature sensor.
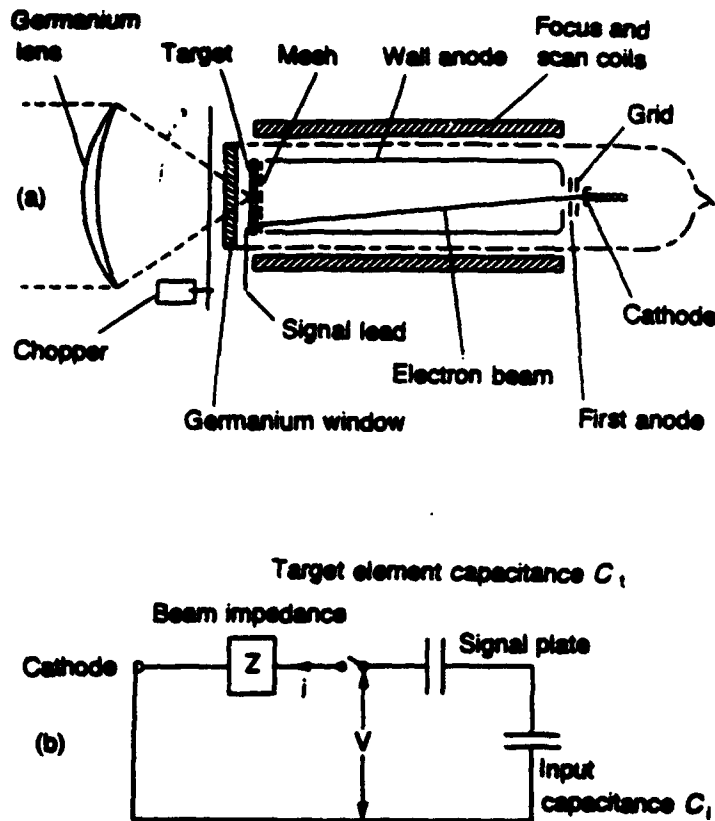
Figure 12-17. Pyro-vidicon tube (a) and its equivalent circuit (b).

ture of a D-TGS (deuterated triglycine sulphate, $(ND_2CD_2COOD)_3D_2SO_4$) target, and Fig. 12-19 is an example of a picture taken in darkness.

ples of these ternary compositions are; $Pb(Mg_{1/3}Nb_{2/3})O_3$, $Pb(Mn_{1/3}Sb_{2/3})O_3$, $Pb(Co_{1/3}Nb_{2/3})O_3$, $Pb(Mn_{1/3}Nb_{2/3})O_3$, $Pb(Ni_{1/3}Nb_{2/3})O_3$, $Pb(Sb_{1/2}Sn_{1/2})O_3$, $Pb(Co_{1/2}W_{1/2})O_3$, $Pb(Mg_{1/2}W_{1/2})O_3$.

12.4 Piezoelectric Devices

12.4.1 Piezoelectric Materials

In the early 1950s, barium titanate ($BaTiO_3$) began to be utilized in *Langevin-type* piezoelectric vibrators. Later, at the National Bureau of Standards (NBS) in the USA (now NIST), PZT ($Pb(Zr, Ti)O_3$) was found to exhibit piezoelectric constants twice as large as those of $BaTiO_3$ around the *morphotropic phase boundary* between the rhombohedral–tetragonal phases (Fig. 12-20); (Jaffe et al., 1955). Subsequently, PZT modified by doping, and a ternary solid solution with a different perovskite have been intensively investigated. Exam-

Figure 12-18. Infrared image target with divided fine segments (19 μm width, 16 μm depth, 25 μm pitch).

Piezoelectric data for PZT ceramics are summarized in Table 12-3.

In polycrystalline piezoelectric ceramics, a poling process (applying a strong DC electric field) is required to rearrange the spontaneous polarization. After being poled, the ceramic can exhibit the piezoelectric effect just as single crystals do (Fig. 12-21).

Piezoelectricity is also found in polymers (Kawai, 1969). Figure 12-22 shows an example polyvinylidenefluoride (PVDF).

Figure 12-19. Images taken by a pyro-vidicon on a dark night.
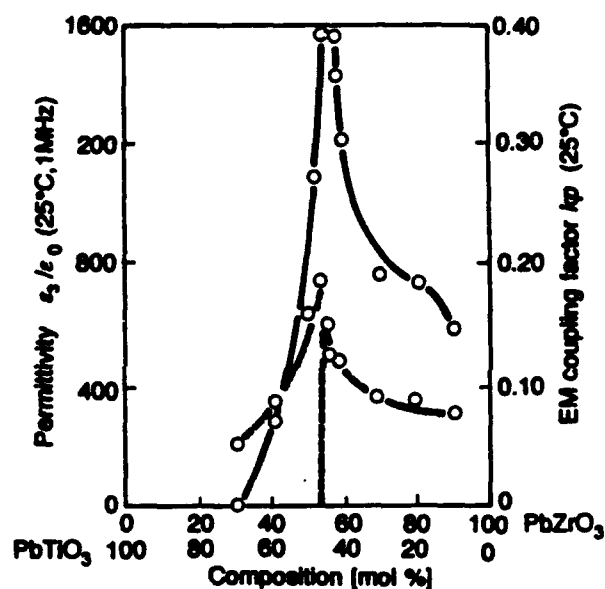
Figure 12-20. Permittivity and the planar coupling factor in PbZrO$_3$-PbTiO$_3$ ceramics.
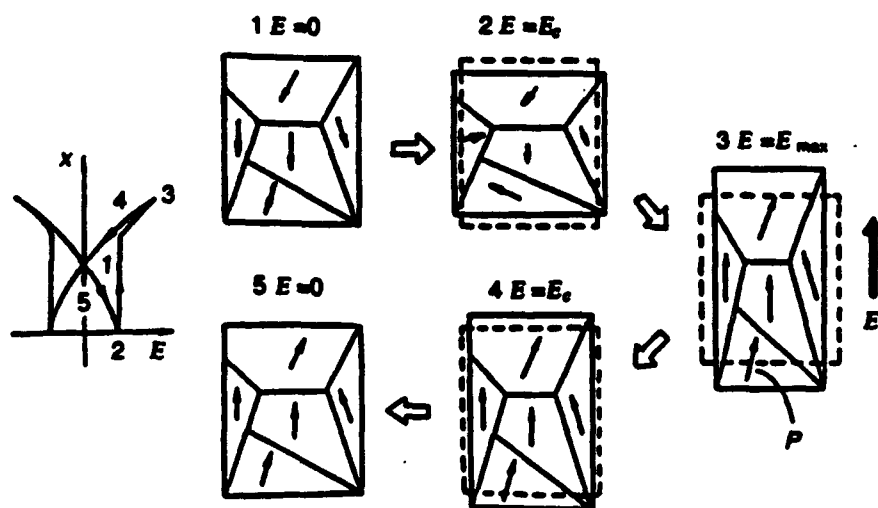
Figure 12-21. Illustration of the strain change associated with the domain reversal in a ferroelectric ceramic.

Piezoelectric polymers have the following characteristics:

(a) small piezoelectric d constants (for actuators) and large g constants (for sensors).

(b) Lightweight and high elasticity, leading to good acoustic impedance matching to water or the human body.

(c) Low mechanical quality factor Q_M, giving a wide frequency band resonance.
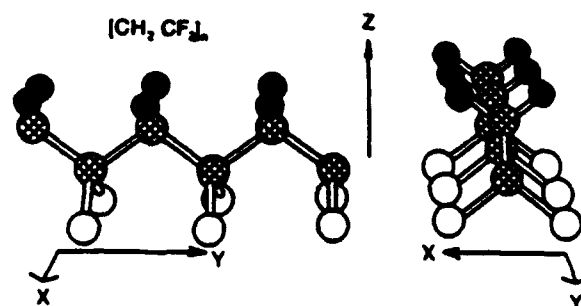
Figure 12-22. Structure of polyvinylidene difluoride (PVDF); O: fluorine, ●: carbon, ●: hydrogen.

Table 12-3. Electromechanical parameters in PZT–PMN ceramics.[a]

	PCM-5A	PCM-33	PCM-4B	PCM-67	PCM-80
Electro-mechanical coupling factors					
k_p	0.65	0.65	0.70	0.32	0.58
k_{31}	0.38	0.39	0.43	0.19	0.35
k_{33}	0.71	0.74	0.72	0.48	0.69
k_{15}	0.70		0.63	0.37	0.64
k_t	0.50	0.50	0.50	0.40	0.47
Piezoelectric constants					
d_{31}	-186×10^{-12}	-263×10^{-12}	-247×10^{-12}	-42×10^{-12}	-122×10^{-12}
d_{33}	375×10^{-12}	575×10^{-12}	490×10^{-12}	109×10^{-12}	273×10^{-12}
d_{15}	579×10^{-12}		599×10^{-12}	131×10^{-12}	412×10^{-12}
g_{31}	-12.3×10^{-3}	-8.4×10^{-3}	-11.8×10^{-3}	-7.7×10^{-3}	-11.3×10^{-3}
g_{33}	-25.7×10^{-3}	18.4×10^{-3}	20.6×10^{-3}	19.8×10^{-3}	25.5×10^{-3}
g_{15}	33.9×10^{-3}		29.7×10^{-3}	24.7×10^{-3}	31.9×10^{-3}
Permittivity					
$\varepsilon_{33}^X/\varepsilon_0$	1710	3530	2380	620	1210
$\varepsilon_{11}^X/\varepsilon_0$	1830	2740	2280	600	1460
Loss tangent D	1.50	2.30	1.40	0.64	0.64
Elastic constants					
$1/s_{11}^E$	6.2×10^{10}	6.9×10^{10}	6.3×10^{10}	11.0×10^{10}	8.8×10^{10}
$1/s_{22}^E$	5.5×10^{10}	5.2×10^{10}	5.1×10^{10}	10.8×10^{10}	6.8×10^{10}
$1/s_{44}^E$	2.0×10^{10}		2.2×10^{10}	4.2×10^{10}	3.1×10^{10}
Density ϱ	7.7	7.7	7.8	7.7	7.9
Mechanical quality factor Q_M	60	50	64	3130	2080
Curie temperature (°C)	326	182	264	340	283

[a] Elastic constant $1/s$: N/m^2; piezoelectric constants d: m/V, g: $V \cdot m/N$; loss tangent D: %; density ϱ: 10^3 kg/m³.

Recent development in the field of composites of piezoceramics and polymers is remarkable (Klicker, 1981), superior piezoelectric response being achieved while still maintaining the mechanical flexibility of the polymers.

12.4.2 Piezoelectric Resonance

When an electric field is applied to a piezoelectric material, deformation (ΔL) or strain ($\Delta L/L$) arises. When the field is alternating, mechanical vibration is caused, and if the drive frequency is adjusted to a mechanical resonance frequency of the device, large resonating strain is generated. This phenomenon can be understood as a strain magnification due to accumulating input energy, and is called *piezoelectric resonance*. The piezoelectric resonance is very useful for realizing energy trap devices, actuators etc. The theoretical treatment is described in the following.

If the applied electric field and the generated stress are not large, the stress x and the dielectric displacement D can be represented by the following equation:

$$x_i = s_{ij}^E X_j + d_{mi} E_m$$

$$(i,j = 1,2,\ldots,6; \quad m,k = 1,2,3) \quad (12\text{-}20)$$

$$D_m = d_{mi} X_i + \varepsilon_{mk}^X E_k \quad (12\text{-}21)$$

These are called *piezoelectric equations*. The numbers of independent parameters for a lowest symmetry trigonal crystal are 21 for s_{ij}^E, 18 for d_{mi} and 6 for ε_{mk}^X. The number of independent parameters decreases with increasing crystallographic symmetry. Concerning the polycrystalline ceramics, the poled axis is usually denoted as the z-axis and the ceramic is isotropic with respect to this z-axis (point group $C_{\infty v}(\infty m)$). The number of non-zero matrix elements is 10 (s_{11}^E, s_{12}^E, s_{13}^E, s_{33}^E, s_{44}^E, d_{31}, d_{33}, d_{15}, ε_{11}^X, and ε_{33}^X).

Next, let us introduce an *electromechanical coupling factor* k, which corresponds to the efficiency of an electro-mechanical transducer. The internal energy of a piezoelectric vibrator is given by summation of the mechanical energy $U_M (= \int x\,dX)$ and the electrical energy $U_E (= \int D\,dE)$. U is calculated as follows, when linear relations Eqs. (12-20) and (12-21) are applicable:

$$U = U_M + U_E = \quad (12\text{-}22)$$

$$= \left(\frac{1}{2}\sum_{i,j} s_{ij}^E X_j X_i + \frac{1}{2}\sum_{m,i} d_{mi} E_m X_i\right)$$

$$+ \left(\frac{1}{2}\sum_{i,j} d_{mi} X_i E_m + \frac{1}{2}\sum_{k,m} \varepsilon_{mk}^X E_k E_m\right)$$

The s and ε terms represent purely mechanical and electrical energies (U_{MM} and U_{EE}), respectively, and the d term denotes the energy transducer from electrical to mechanical energy or vice versa through the piezoelectric effect. The coupling factor k is defined by:

$$k = U_{ME}/\sqrt{U_{MM} \cdot U_{EE}} \quad (12\text{-}23)$$

The k value varies with the vibrational mode (even in the same ceramic sample), and can have a positive or negative value (see Table 12-4).

Let us consider the transverse mechanical vibration of a piezo-ceramic plate as shown in Fig. 12-23. If the polarization is
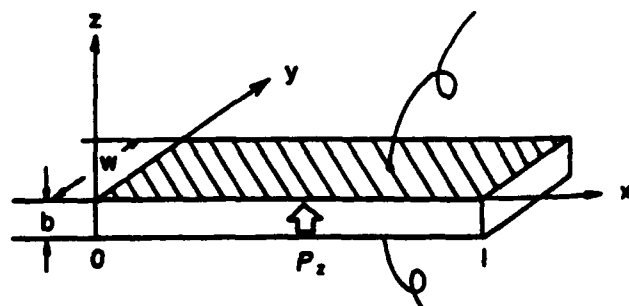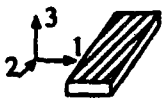

Figure 12-23. Transverse vibration in a rectangular plate.

Table 12-4. Several shapes of the resonator and their electromechanical coupling factors.

Coupling factor	Elastic conditions	Shape of the resonator	Definition
a k_{31}	$X_1 \neq 0,\ X_2 = X_3 = 0$ $x_1 \neq 0,\ x_2 \neq 0,\ x_3 \neq 0$		$\dfrac{d_{31}}{\sqrt{s_{11}^E\,\epsilon_{33}^X}}$
b k_{33}	$X_1 = X_2 = 0,\ X_3 \neq 0$ $x_1 = x_2 \neq 0,\ x_3 \neq 0$		$\dfrac{d_{33}}{\sqrt{\epsilon_{33}^X\,s_{33}^E}}$
c k_p	$X_1 = X_2 \neq 0,\ X_3 = 0$ $x_1 = x_2 \neq 0,\ x_3 \neq 0$		$k_{31}\sqrt{\dfrac{2}{1-\sigma}}$
d k_t	$X_1 = X_2 \neq 0,\ X_3 \neq 0$ $x_1,\ x_2 = 0,\ x_3 \neq 0$		$k_{33}\sqrt{\dfrac{\epsilon_{33}^X}{c_{33}^D}}$
e k_p'	$X_1 = X_2 \neq 0,\ X_3 \neq 0$ $x_1 = x_2 \neq 0,\ x_3 = 0$		$\dfrac{k_p - A k_{33}}{\sqrt{1-A^2}\,\sqrt{1-k_{33}^2}}$
f k_{31}'	$X_1 \neq 0,\ X_2 \neq 0,\ X_3 = 0$ $x_1 \neq 0,\ x_2 = 0,\ x_3 \neq 0$		$\dfrac{k_{31}}{\sqrt{1-k_{31}^2}}\sqrt{\dfrac{1+\sigma}{1-\sigma}}$
g k_{31}''	$X_1 \neq 0,\ X_2 = 0,\ X_3 \neq 0$ $x_1 \neq 0,\ x_2 \neq 0,\ x_3 = 0$		$\dfrac{k_{31} - B k_{33}}{\sqrt{1-k_{33}^2}}$
h k_{33}'''	$X_1 \neq 0,\ X_2 \neq 0,\ X_3 \neq 0$ $x_1 \neq 0,\ x_2 = 0,\ x_3 = 0$		$\dfrac{\sqrt{\dfrac{(k_p - A k_{33})^2}{1-A^2} - (k_{31} - B k_{33})^2}}{1 - k_{31}^2 - (k_{31} - B k_{33})^2}$
i k_{33}'	$X_1 \neq 0,\ X_2 = 0,\ X_3 \neq 0$ $x_1 = 0,\ x_2 \neq 0,\ x_3 \neq 0$		$\dfrac{k_{33} - B k_{31}}{\sqrt{(1-B^2)(1-k_{31}^2)}}$
j $k_{24} = k_{15}$	$X_1 = X_2 = X_3 = 0,\ X_4 \neq 0$ $x_1 = x_2 = x_3 = 0,\ x_4 \neq 0$		$\dfrac{d_{15}}{\sqrt{\epsilon_{11}^X\,s_{44}^E}}$

$$A = \frac{\sqrt{2}\,s_{13}^E}{\sqrt{s_{33}^E(s_{11}^E + s_{12}^E)}}, \quad B = \frac{s_{13}^E}{\sqrt{s_{11}^E\,s_{33}^E}}.$$

in the z-direction and the x-y planes are the planes of the electrodes, the extentional vibration in the x-direction is represented by the following dynamic equation:

$$(\partial^2 u/\partial t^2) = F = (\partial X_{11}/\partial x) + (\partial X_{12}/\partial y) + (\partial X_{13}/\partial z), \quad (12\text{-}24)$$

u is the displacement of the small volume element in the ceramic plate in the x-direction. The relations between stress, electric field (only E_z exists) and the induced strain are given by:

$$x_1 = s_{11}^E X_1 + s_{12}^E X_2 + s_{13}^E X_3 + d_{31} E_z$$

$$x_2 = s_{12}^E X_1 + s_{11}^E X_2 + s_{13}^E X_3 + d_{31} E_z$$

$$x_3 = s_{13}^E X_1 + s_{13}^E X_2 + s_{33}^E X_3 + d_{33} E_z$$

$$x_4 = s_{44}^E X_4 \qquad\qquad (12\text{-}25)$$

$$x_5 = s_{44}^E X_5$$

$$x_6 = 2(s_{11}^E - s_{12}^E) X_6$$

When the plate is very long and thin, X_2 and X_3 may be set equal to zero through the plate. Since shear stress will not be generated by the electric field E_z, Eq. (12-25) is reduced to:

$$X_1 = x_1/s_{11}^E - (d_{31}/s_{11}^E) E_z \qquad (12\text{-}26)$$

Introducing Eq. (12-26) into Eq. (12-24), and allowing for $x_1 = \partial u/\partial x$ and $\partial E_z/\partial x = 0$ (due to the equal potential on each electrode), leads to a harmonic vibration equation:

$$-\omega^2 \varrho s_{11}^E u = \partial^2 u/\partial x^2 \qquad (12\text{-}27)$$

ω is the angular frequency of the drive field, and ϱ is the density. Substituting a general solution $u = u_1(x) e^{j\omega t} + u_2(x) e^{-j\omega t}$ into Eq. (12-26), and with the boundary condition $X_1 = 0$ at $x = 0$ and L (sample length), the following solution can be obtained:

$$\partial u/\partial x = x_1 = d_{31} E_z [\sin \omega (L - x)/v +$$

$$+ \sin (\omega x/v)]/\sin (\omega L/v) \qquad (12\text{-}28)$$

Here, v is the sound velocity in the piezoceramics and is given by

$$v = 1/\sqrt{\varrho s_{11}^E} \qquad (12\text{-}29)$$

When the specimen is utilized as an electrical component such as a filter or a vibrator, the electrical impedance [(applied voltage/induced current) ratio] plays an important role. The current flow into the specimen is described by the surface charge increment, i.e., $\partial D_3/\partial t$, and the total current is given by:

$$i = j\omega w \int_0^L D_3 \, dx = j\omega w \int_0^L \left[\left(\varepsilon_{33}^X - \frac{d_{31}^2}{s_{11}^E} \right) E_z + \frac{d_{31}}{s_{11}^E} x_1 \right] dx \qquad (12\text{-}30)$$

Using Eq. (12-28), the admittance for the mechanically free sample is calculated as:

$$\frac{1}{z} = \frac{i}{V} = \frac{i}{E_z t} =$$

$$= \frac{j\omega w L}{t} \varepsilon_{33}^{LC} \left[1 + \frac{d_{31}^2}{\varepsilon_{33}^{LC} s_{11}^E} \left(\frac{\tan [\omega L/(2 v)]}{\omega L/(2 v)} \right) \right] \qquad (12\text{-}31)$$

w is the width, L the length, t the thickness of the sample, and V is the applied voltage. ε_{33}^{LC} is the permittivity in a longitudinally clamped sample, and is given by:

$$\varepsilon_{33}^{LC} = \varepsilon_{33}^X - (d_{31}^2/s_{11}^E) \qquad (12\text{-}32)$$

The piezoelectric resonance is achieved where the admittance becomes infinite or the impedance is zero. The resonance frequency f_R is calculated from Eq. (12-31), and the fundamental frequency is given by:

$$f_R = v/(2 L) = 1/(2 L \sqrt{\varrho s_{11}^E}) \qquad (12\text{-}33)$$

On the other hand, the antiresonance state is generated for zero admittance or infinite impedance:

$$\qquad\qquad (12\text{-}34)$$

$$\frac{\omega_A L}{2 v} \cot \frac{\omega_A L}{2 v} = -\frac{d_{31}^2}{\varepsilon_{33}^{LC} s_{11}^E} = -\frac{k_{31}^2}{1 - k_{31}^2}$$

The final transformation is provided by the definition:

$$k_{31} = \tfrac{1}{2} d_{31} E_z X_1/(\tfrac{1}{2} \sqrt{s_{11}^E X_1^2 \varepsilon_{33}^X E_z^2}) =$$

$$= d_{31}/\sqrt{s_{11}^E \varepsilon_{33}^X} \qquad (12\text{-}35)$$

The resonance and antiresonance states are described by the following intuitive model. In a high electromechanical coupling material with $k \approx 1$, the resonance or antiresonance states appear for $\tan [\omega L/(2 v)] = \infty$ or 0, i.e., $\omega L/(2 v) = (m - 1/2) \pi$ or $m \pi$ (m: integer), respectively. The strain amplitude x_1 distribution for each state [calculated using Eq. (12-28)] is

Resonance   Antiresonance
                        Low coupling   High coupling

m=1   m=1

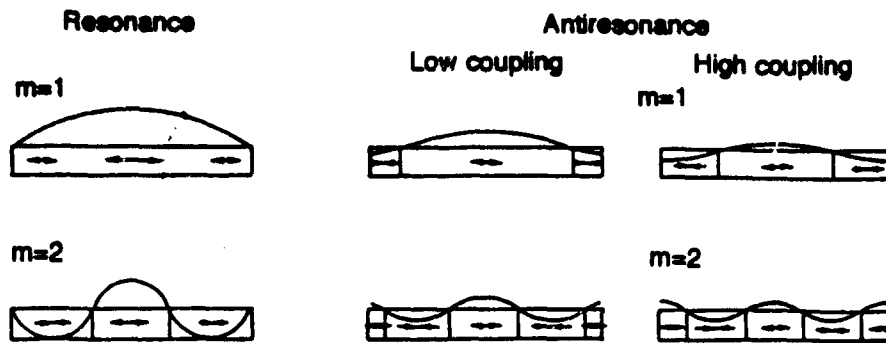m=2   m=2

Figure 12-24. Strain generation in the resonant or antiresonant state.

illustrated in Fig. 12-24. In the resonance state, large strain amplitudes and large capacitance changes are induced, and the current can easily flow into the device. On the contrary, at the antiresonance, the strain induced in the device compensates in total, not causing the capacitance change, and the current can not flow easily into the sample.

In the usual case, where $k_{31} \approx 0.3$, the antiresonance state varies from the above-mentioned mode and becomes closer to the resonance mode. The low-coupling material exhibits an antiresonance mode where capacitance change due to the size change is compensated completely by the current required to charge up the static capacitance.

In general, the sound velocity v of the specimen is first obtained from the resonance frequency f_R, then the electromechanical coupling factor k_{31} is calculated from the v value and the antiresonance frequency f_A using Eq. (12-34). Especially in low-coupling piezoelectric materials, the following approximate equation is available:

$$k_{31}/(1 - k_{31}^2) = \frac{\pi^2}{4}(\Delta f/f_R) \quad (\Delta f = f_A - f_R)$$
$$(12\text{-}36)$$

12.4.3 Piezoelectric Transformers

One of the very basic applications of piezoelectric ceramics is a gas igniter. The

very high voltage generated in a piezoelectric ceramic under applied mechanical stress can cause sparking and ignite the gas (Fig. 12-25). There are two means to apply the mechanical force; sudden application and continuous increase.

When input and output terminals are fabricated on a piezo-device and input/output voltage is changed through the vibration energy transfer, the device is called a *piezoelectric transformer*. Proposed by C. A. Rosen et al. (Rosen, 1957), there have been a variety of such transformers investigated: Fig. 12-26 shows a fundamental structure where two differently-poled parts coexist in one piezoelectric plate. A standing wave with a wavelength equal to the sample length is generated, a half wavelength portion of the wave existing on both
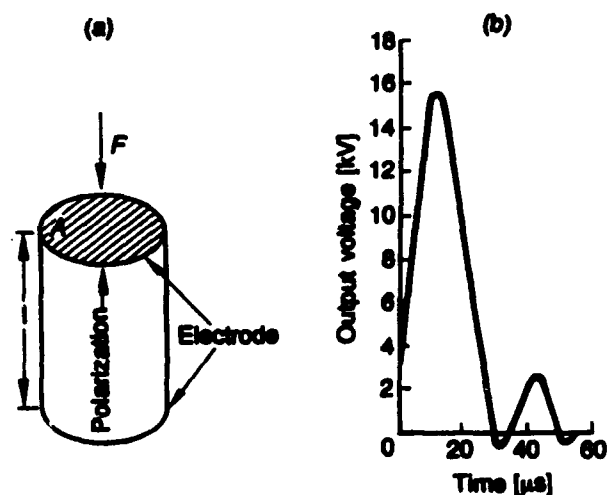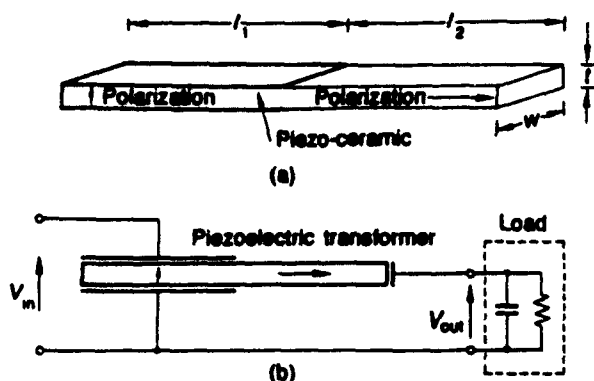
Figure 12-25. (a) Gas igniter and (b) output voltage.

Figure 12-26. Piezoelectric transformer.

the input (l_1) and output (l_2) parts of the sample. The voltage rise ratio r is given for the unloaded condition by Eq. (12-37). The r ratio is increased with an increase of (l_2/t).

$$r = \frac{4}{\pi^2} k_{31} k_{33} Q_m \frac{l_2}{t} \frac{2\sqrt{s_{33}^E/s_{11}^E}}{1 + \sqrt{s_{33}^D/s_{11}^E}} \quad (12\text{-}37)$$

Piezoelectric transformers were previously used in color TVs because of their compact size in comparison with the conventional electromagnetic coil-type transformers.

12.4.4 Piezoelectric Vibrators

In the use of mechanical vibration devices such as filters or oscillators, the size and shape of a device is very important, and both the vibration mode and the ceramic material must be considered. The resonance frequency of the bending mode in a cm-size sample ranges from 100–1000 Hz, which is much lower than that of the thickness mode (100 kHz). For these vibrator applications the piezo-ceramic should have a high mechanical quality factor (Q_M) rather than a large piezoelectric coefficient d; i.e., hard-type piezoelectric ceramics are preferable.

For speakers or buzzers, audible for humans, devices with a rather low resonance frequency are used (kHz range): Examples

are a bimorph consisting of two piezo-ceramic plates bonded together, and a piezoelectric fork consisting of a piezo-device and a metal fork. A piezoelectric buzzer is shown in Fig. 12-27, which has merits such as high electric power efficiency, compact size and long life.

12.4.5 Ultrasonic Transducers

Ultrasonic waves are now used in various fields. The sound source is made of piezoelectric ceramics as well as of magnetostrictive materials. Piezoceramics are generally superior in efficiency and in size to magnetostrictive materials. Especially hard-type piezoelectric materials with a high Q_M are preferable. A liquid medium is usually used for sound energy transfer. Ultrasonic washers and ultrasonic microphones for short-distance remote control are widely used in factories, and ultrasonic scanning detectors are useful in medical electronics.

12.4.6 Surface Acoustic Wave Devices

Surface acoustic wave (SAW) filters have been widely used for the intermediate frequency image transfer signal in color TVs, because of their excellent time delay characteristics. The fundamental structure of the SAW filter is illustrated in Fig. 12-28, where a pair of interdigital electrodes are fabricated on the piezoelectric crystal. A
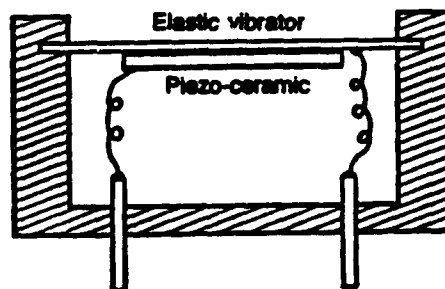
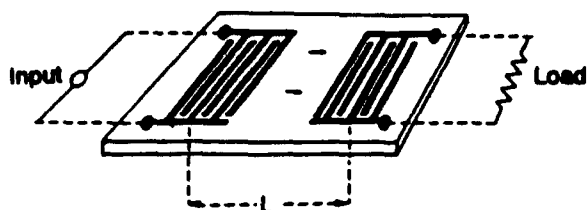

Figure 12-27. Piezoelectric buzzer.

Figure 12-28. Fundamental structure of a SAW filter.

surface wave generated at the input-side electrode is transferred and picked up at the output-side as an electric signal. The device is very useful as a high-frequency filter.

There are four materials at present used for SAW devices, $Pb(Zr,Ti)O_3$ (PZT)-based ceramics, ZnO thin films, $LiNbO_3$ and $LiTaO_3$ single crystals, whose characteristics are summarized in Table 12-5. A small temperature coefficient of the frequency is preferable, which is determined by the summation of the temperature coefficient of the sound velocity and the thermal expansion coefficient of the ceramic.

When a polycrystalline material is used, it must be pore-free and homogeneous. Samples must be highly reproducible, and require advanced fine ceramic preparation technology.

12.4.7 Piezoelectric Actuators

In recent years, the need for new displacement elements, in particular, in such fields as optics, precision machinery and small motors, has been rapidly increasing. The requirements for the processing accuracy of optical devices such as lasers and cameras, along with the positioning accuracy required in the processing of semiconductor chips are now typically of the order of micron and submicron levels. The need for a reliable micro-scale positioner has motivated a new surge of activity in the development of ceramic actuators which operate on the principle of electric-field-induced strain.

For actuator applications, large electric fields (≈ 1 kV/mm) are applied to the material, thereby generating large stresses (≈ 10 MPa) and strains ($\Delta l/l \approx 10^{-3}$). Therefore, in addition to an adequate electrostrictive response, electrical insulation strength and mechanical toughness are necessary material characteristics.

Lead zirconate titanate (PZT)-based ceramics are currently the primary materials for piezoelectric applications (Furuta et al., 1986). The $(Pb, La)(Zr, Ti)O_3$ (PLZT) (7/62/38) compound is one such material. The strain curves for this composition are shown in Fig. 12-29 a. When the applied electric field is small, the induced strain is nearly proportional to the electric field. As the field becomes larger (i.e., greater than about 100 V/mm), however, the strain curve deviates from this linear trend and a significant hysteresis is exhibited due to polarization reversal. This limits the use of

Table 12-5. Characteristics of SAW filter substrate materials.

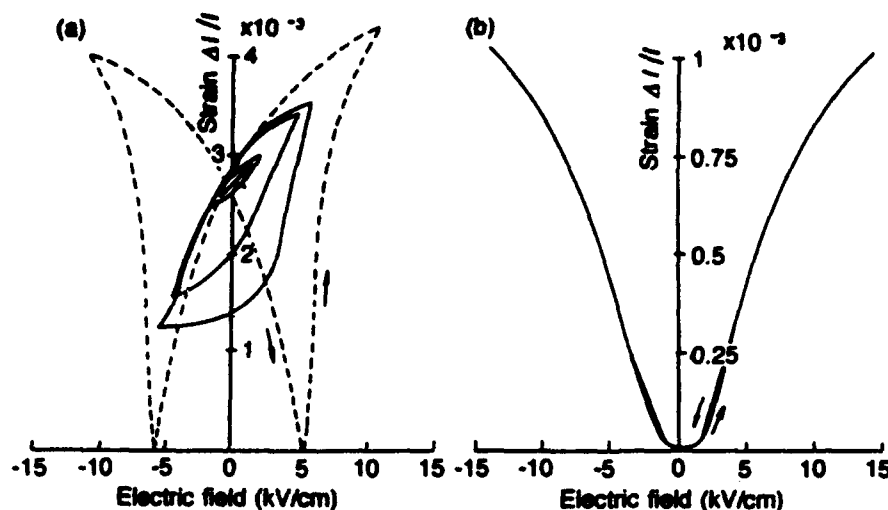|	$LiTaO_3$ (X-112°Y)	$LiNbO_3$ (128°Y)	PZT[a]	ZnO
SAW velocity (m/s)	3295	3960	2430	3150
Coupling factor (k^2, %)	0.7	6.0	2.9	0.6
Temperature coefficient of frequency (ppm/°C)	−31	−78	−17	−15
Permittivity (ε_s)	47.9	67.2	350	8.84
Curie point (T_C, °C)	618	1210	300	1200

[a] $Pb(Mn_{1/3}Nb_{2/3})O_3-PbZrO_3-PbTiO_3$.

Figure 12-29. Field-induced strain in ceramics. (a) Piezo-electric material PLZT(7/62/38). (b) Electro-strictive material $0.9\,Pb(Mg_{1/3}Nb_{2/3})O_3 - 0.1\,PbTiO_3$.

the material in actuator applications that require a linear, non-hysteresis response.

Previously, electrostriction, a second-order phenomenon of electromechanical coupling, was considered to be a negligible effect and, therefore, was not studied from a practical point of view. Recent research and development on PMN [lead magnesium niobate, $Pb(Mg_{1/3}Nb_{2/3})O_3$]-based ceramics (Cross et al., 1980), however, have kindled new interest in the use of such electrostrictive materials in this area. PMN-based ceramics exhibit significant strains up to 0.1% (i.e., a 1 cm sample can elongate

by as much as 10 μm). Another attractive feature of these materials is the near absence of hysteresis (Fig. 12-29 b).

Piezoelectric/electrostrictive actuators may be classified into two categories based on the type of driving field applied to the device and the nature of the strain induced by that field (Fig. 12-30): (1) Rigid displacement devices for which the strain is induced unidirectionally by an applied DC field, and (2) resonating strain devices for which the mechanical resonance is excited by an AC field. The first can be further divided into two categories: (1) Servo dis-
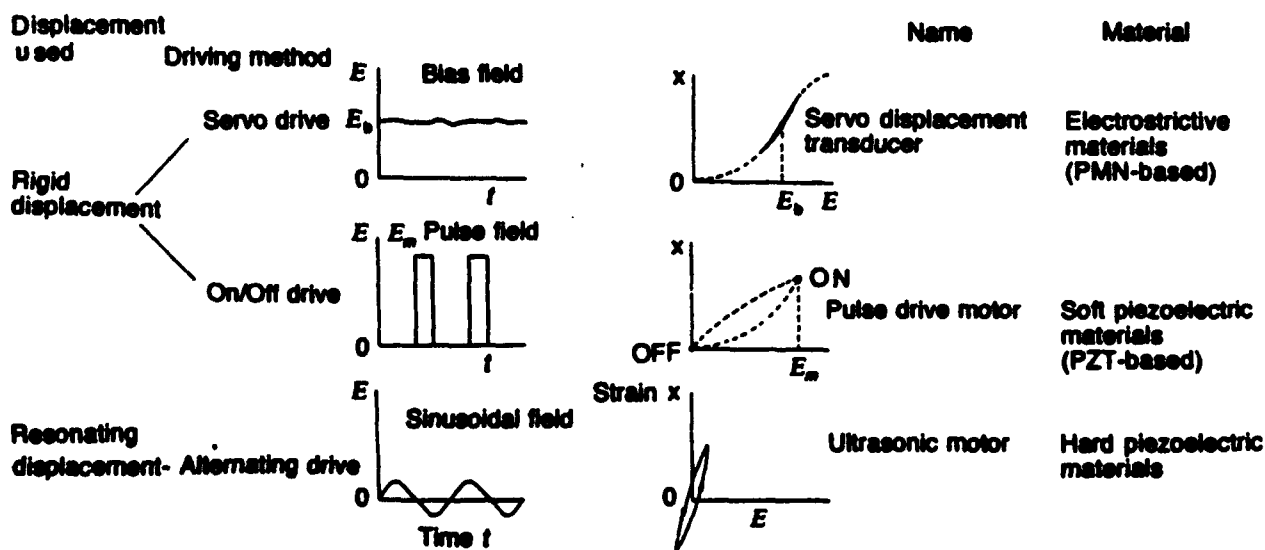
Figure 12-30. Classification of piezoelectric/electrostrictive actuators; E: electric field, x: strain.

placement transducers controlled by a feed-back system through a position-detection signal, and (2) pulse-drive motors that operate in a simple ON/OFF switching mode (Uchino, 1986). Very recently, an actuator referred to as a flight actuator has been proposed which hits a steel ball strongly by means of an ON/OFF piezoelectric unit similar to that found in a pinball machine (Ota et al., 1985).

The material requirements for the three classes of devices are somewhat different and hence, certain compounds will be better suited to particular applications. The ultrasonic motor, for instance, requires almost the conventional hard-type piezoelectric with a high mechanical Q. The servodisplacement transducer suffers most from strain hysteresis and, therefore, a PMN electrostrictor is used for this device. The pulse-drive motor requires a low-permittivity material aiming at a quick response rather than a small hysteresis so that soft-PZT piezoelectrics are most suitable for this application.

In the sections to follow, three typical application examples will be taken up for examination and discussion.

12.4.7.1 Deformable Mirrors

In the field of optical information processing, deformable mirrors have been proposed to control the phase of the incident light wave. The deformable mirror can be made more convex or concave as necessary. This type of mirror, which finds application as an accessory device on observatory telescopes, effectively corrects for image distortions resulting from fluctuating airflow.

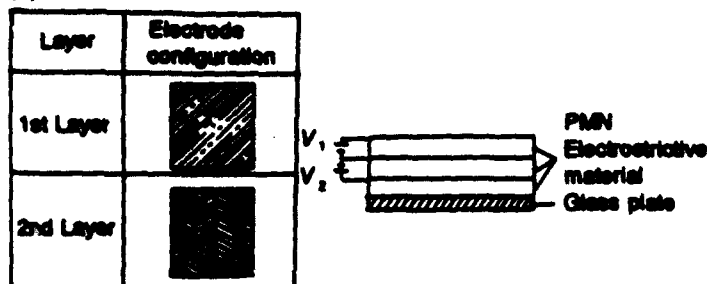An example of a deformable mirror is a multilayered two-dimensional bimorph type like that shown in Fig. 12-31 (Sato et al., 1982). The operation of this mirror is similar in principle to a "bi-metal" device which consists of two metal plates, with different thermal expansion coefficients, bonded together. The plates will bend with a change in temperature. When three layers of thin electrostrictive ceramic (PMN) plates are bonded to the elastic plate of a glass mirror, the mirror surface is deformed in various ways corresponding to the strain induced in the PMN-layer. The nature of the deformation is determined by the electrode configuration and the distribution of the applied electric field. Trial units have been designed such that the first layer, with a uniform electrode pattern, produces a spherical deformation (i.e., refocusing), while the second layer with an electrode pattern of six minute divisions corrects for coma aberration.

12.4.7.2 Impact Dot-Matrix Printers

Among the various types of printing devices currently in use, dot-matrix printers are routinely employed. Each character formed by such a printer is initially composed of a 9 × 9 dot matrix. A printing ribbon is subsequently impacted by a multi-wire array. A sketch of the printer appears in Fig. 12-32a (Yano et al., 1984).

The basic actuator assumes a multilayer configuration in which roughly 100 thin piezoelectric ceramic sheets are stacked. The advantages of using a multilayer-type actuator for this particular application include a low driving voltage, large displacement, and a high electromechanical conversion efficiency. This actuator is installed in a specially designed displacement magnification unit (Fig. 12-32b) to drive the top printer pins. This unique magnification unit is based on a *monolithic hinge* lever with a magnification of 30 and realizes an amplified displacement of 300 μm and an energy transfer efficiency greater than 50%.

(a)

Layer	Electrode configuration
1st Layer	
2nd Layer	

V_1
V_2

PMN
Electrostrictive
material
Glass plate

(b)

Aberration	Interference fringe pattern of desired wavefront	Interference fringe pattern of generated wavefront
Refocusing $x^2 + y^2$		
Coma aberration $x^3 + xy^2$		
Refocusing + coma aberration $C_p(x^2 + xy^2) + C_c(x^3 + xy^2)$		

Figure 12-31. (a) Structure of a multi-layer bimorph deformable mirror. (b) The actual control of wavefront.

The merits of the piezoelectric impact printer compared with the conventional electromagnetic type are: (1) higher printing speed by an order of magnitude, (2) lower energy consumption by an order of magnitude, and (3) reduced printing noise since a complete sound shield may be employed with the heatless drive.

12.4.7.3 Ultrasonic Motors

Efforts have been made to develop high-power ultrasonic vibrators as replacements for conventional electromagnetic motors. Two actuators, in particular, are currently being investigated for this application: A vibratory-coupler type and a surface-wave type (Akiyama, 1986).

The basic design of the vibratory coupler is pictured in Fig. 12-33. The Langevin-type piezoelectric vibrator generates a flat-elliptical movement at the tip of the vibratory piece. When contacting a rotor at a slight angle, the vibratory piece generates a rotational torque.

This simple design, however, has several drawbacks. Defacement of the rotor caused by mechanical friction at the contact point and lack of control in both the clockwise and counter-clockwise directions are two of the most serious problems associated with this unit. The problem of
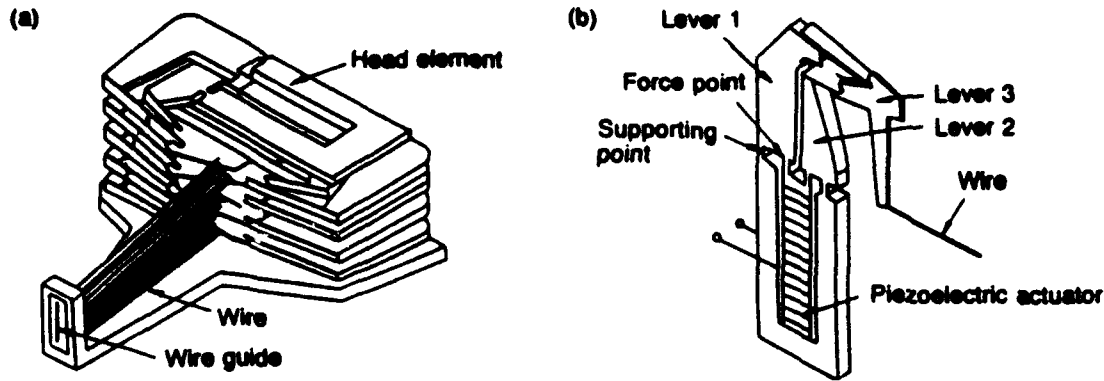
Figure 12-32. (a) Structure of printer head and (b) differential type piezoelectric printer head element.
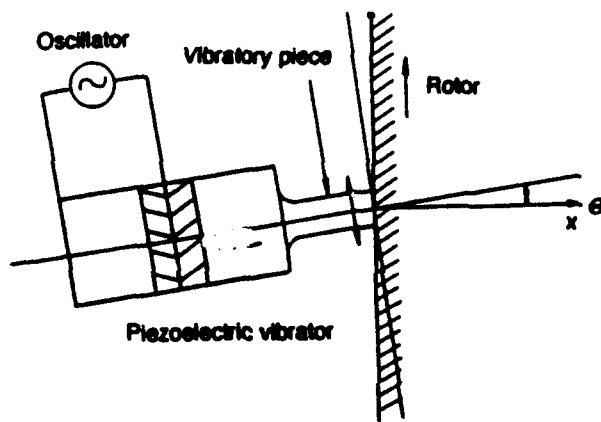

Figure 12-33. Basic structure of a vibratory coupler-type ultrasonic motor.

friction is alleviated by securely pressure-fitting the vibratory reed and rotor together in order to restrict, as much as possible, sliding during operation. The model picture in Fig. 12-34 is one such modified unit (Kumada, 1985). At a rotational speed of 600 rpm, this motor has performance characteristics that surpass normal electro-magnetic motors with a rotational torque of 13 kgf · cm (≈ 1.3 Nm) and an energy conversion efficiency of 80%.

The other type of motor utilizes surface wave vibrations. The operating principle of
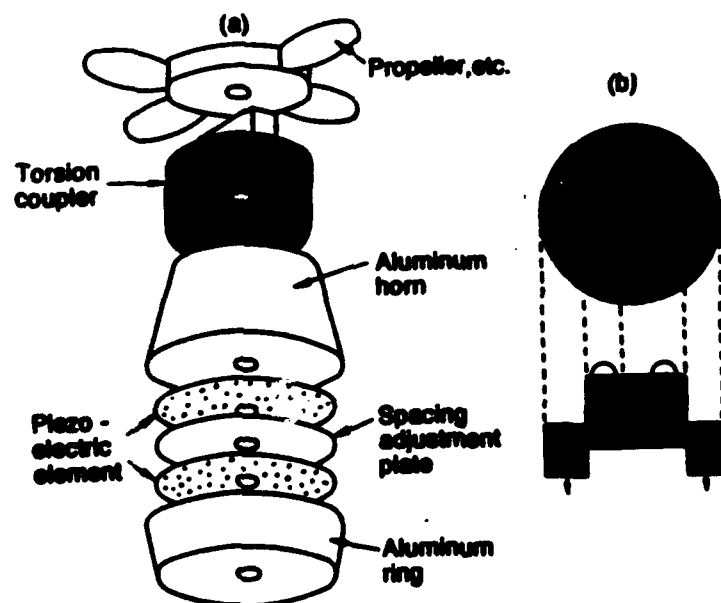
Figure 12-34. Ultrasonic motor using a torsion coupler (a) and rough sketch of the torsion vibration coupler (b).
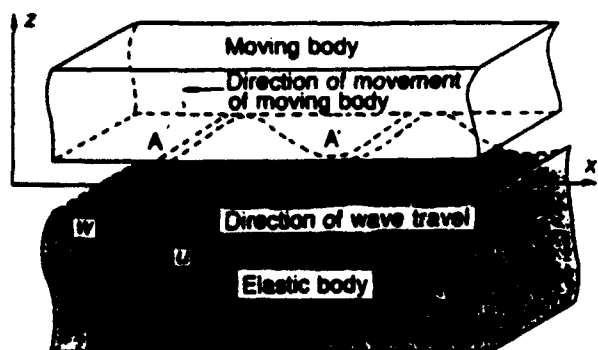
Figure 12-35. Operating principle of a surface wave linear motor (transverse propagating wave being excited on an elastic body).

this device is illustrated in Fig. 12-35. By means of the traveling elastic wave induced by the piezoelectric, a slider in contact with the "rippled" surface of the elastic body is driven in the direction indicated. Both linear and rotational-type motors of this type are possible. The structure of a surface-wave rotational-type motor is pictured in Fig. 12-36. Although the energy transformation efficiency (30%) and rotational torque (0.5 kgf · cm) of the surface wave device are rather low as compared to the vibratory-coupler type, its merit lies in its

ability to rotate in both directions and its thin design which makes it suitable for installation in video (VTR) or movie cameras as an automatic focusing device.

12.5 Electrooptic Devices

In the 1960s the nonlinear polarizability of ferroelectrics was discovered and various electrooptic and optical parametric devices have been investigated. However, problems still remaining are the difficulty of preparing high-grade optically-homogeneous single crystals, and the correspondingly high cost for a given level of performance.

12.5.1 Transparent Electrooptic Ceramics

Even with a polycrystalline microstructure, a ferroelectric ceramic can exhibit the electrooptic effect if it is sintered to a pore-free state to make it transparent. The best-known material is the $(Pb, La)(Zr, Ti)O_3$ system (PLZT), which has good transparency in a wavelength range from visual to infrared, and exhibits an optical anisotropy
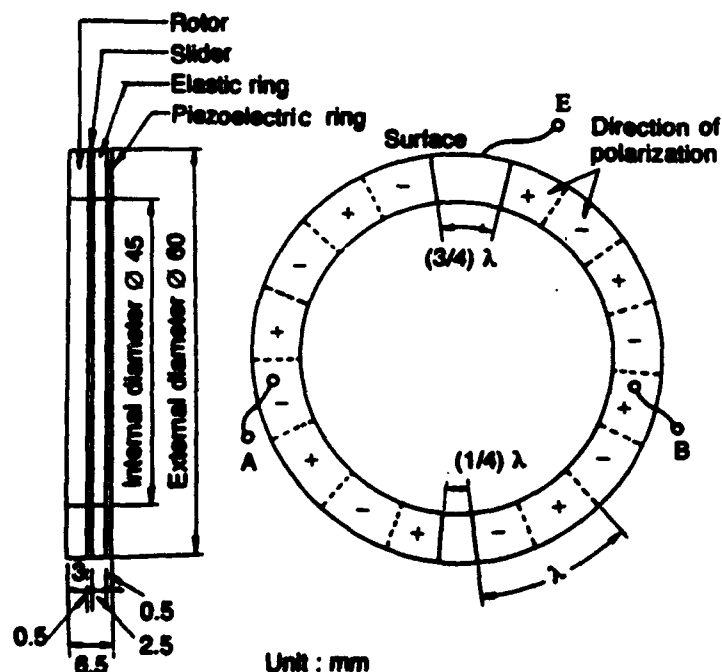

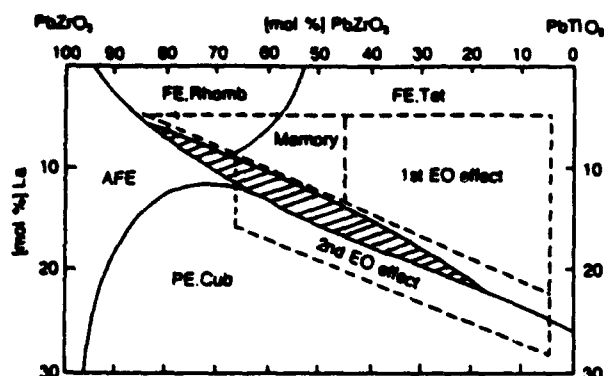**Figure 12-36.** Structural example of a surface wave rotational motor.

Figure 12-37. Relation between PLZT composition and structure and electrooptic application.

Figure 12-38. Polarization P and birefringence Δn as a function of electric field E in PLZT ceramics.

under applied electric voltage. Displays and light valves are promising applications. Figure 12-37 shows the phase diagram of the $(Pb_{1-x}La_x)(Zr_{1-y}Ti_y)_{1-x/4}O_3$ system and the corresponding possible applications.

The PLZT solid solution exhibits both the Pockels' and Kerr electrooptic effects, depending on the composition. Some examples are shown in Fig. 12-38. The electrooptic coefficients of the PLZT system are much larger than the values in conventional crystals such as $LiNbO_3$ and $(Sr, Ba)Nb_2O_6$ (SBN) (see Table 12-6), which means that the voltage required for the electrooptic shutter is much less in the PLZT.

12.5.2 Bulk Electrooptic Devices

PLZT eye glasses for stereo TV have been fabricated using the light shutter function (Kumada et al., 1977). Lenses consist of a pair of optically isotropic PLZT (9/65/35) discs sandwiched by two crossed polarizers. When zero voltage is applied on the electrode, the light will not be transmitted. The transmitted light intensity in-

Table 12-6. Pockels' (1st) and Kerr (2nd) electrooptic coefficients for various materials.

Materials		$r\,(\times 10^{-10}\ \mathrm{m/V})$
1st electrooptic coefficient	$LiNbO_3$	0.17
	$Ba_2(K_{0.9}Na_{0.1})Nb_5O_{15}$	0.52
	KH_2PO_4	0.52
	$(Sr_{0.5}Ba_{0.5})Nb_2O_6$	2.10
	PLZT 8/65/35 (GS = 10 μm)	5.23
	PLZT 8/65/35 (GS = 3 μm)	6.12
		$R\,(\times 10^{-16}\ \mathrm{m^2/V^2})$
2nd electrooptic coefficient	$KTa_{0.65}Nb_{0.35}O_3$	5.30
	PLZT 9/65/35 (GS = 2 μm)	9.12
	PLZT 10/65/35 (GS = 2 μm)	1.07

creases with increasing applied voltage, and reaches a maximum when the phase difference (retardation) of 180° is induced in the PLZT disc. The voltage required for the maximum intensity is denoted as a half-wavelength voltage.

The stereo TV image of an object is taken by two video cameras corresponding to the two eyes and the signal from each camera is mixed alternately to make a frame for the right- and left eyes. When viewing, the right and left PLZT shutters are triggered synchronously for each image frame, resulting in a stereo image.

Recent progress with high-definition TVs is remarkable, and several systems have been proposed. One of the promising devices is a projection-type TV utilizing two-dimensional PLZT displays (Ohmura, 1989). Electrooptic characteristics in PLZT ceramics are generally much superior in response speed and contrast ratio to those in liquid crystals. Moreover, the durability of ceramics under strong light illumination is excellent. However, the most significant problems in PLZT devices, which have prohibited their actual commercialization, are the high driving voltage and the cost. Therefore the development of a simple, mass-production process and the design of

electrode configurations with a narrow gap are the key factors for PLZT displays.

A recently developed design for a 2-dimensional display as shown in Fig. 12-39 presents a very bright image with no cross-talk-related problems and is easy to produce. The fabrication process of the 2-dimensional PLZT light valve array is outlined in Fig. 12-40. Wet-chemically prepared (coprecipitated) PLZT 9/65/35 powders were mixed with organic solvent and binder and formed into a green sheet. The sheets were printed with electrodes and then laminated and sintered in an atmosphere with a controlled oxygen content. A transmittance of 62% could be obtained by atmosphere-controlled sintering, comparing well with a value of 63% for the ideal sample prepared by hot-pressing. Finally, the external connecting electrodes were applied to make vertical and horizontal addressing possible.

The construction of the PLZT color image projector is shown in Fig. 12-41. Three light fluxes, red, green and blue, are obtained by separating light from a xenon lamp with dichroic mirrors, and passing each through identical PLZT shutter. Then, the fluxes are superimposed to make a color image.

12.5.3 Waveguide Modulators

Light waveguides can be fabricated by depositing a high-refractive-index layer on a substrate. The principle of the waveguide is shown schematically in Fig. 12-42. Nb-diffused $LiNbO_3$ single crystals are commonly used; Fig. 12-43a and 12-43b show typical planar- and ridge-type electrooptic waveguides (Kaminow, 1975). The transmitted light intensity is easily modulated by applying a relatively low voltage. Phase modulation by 1 radian can be achieved by applying a voltage of 0.3 V with power consumption of several μW/MHz.

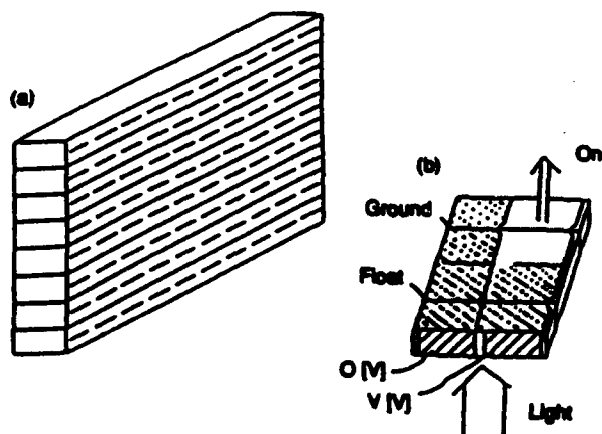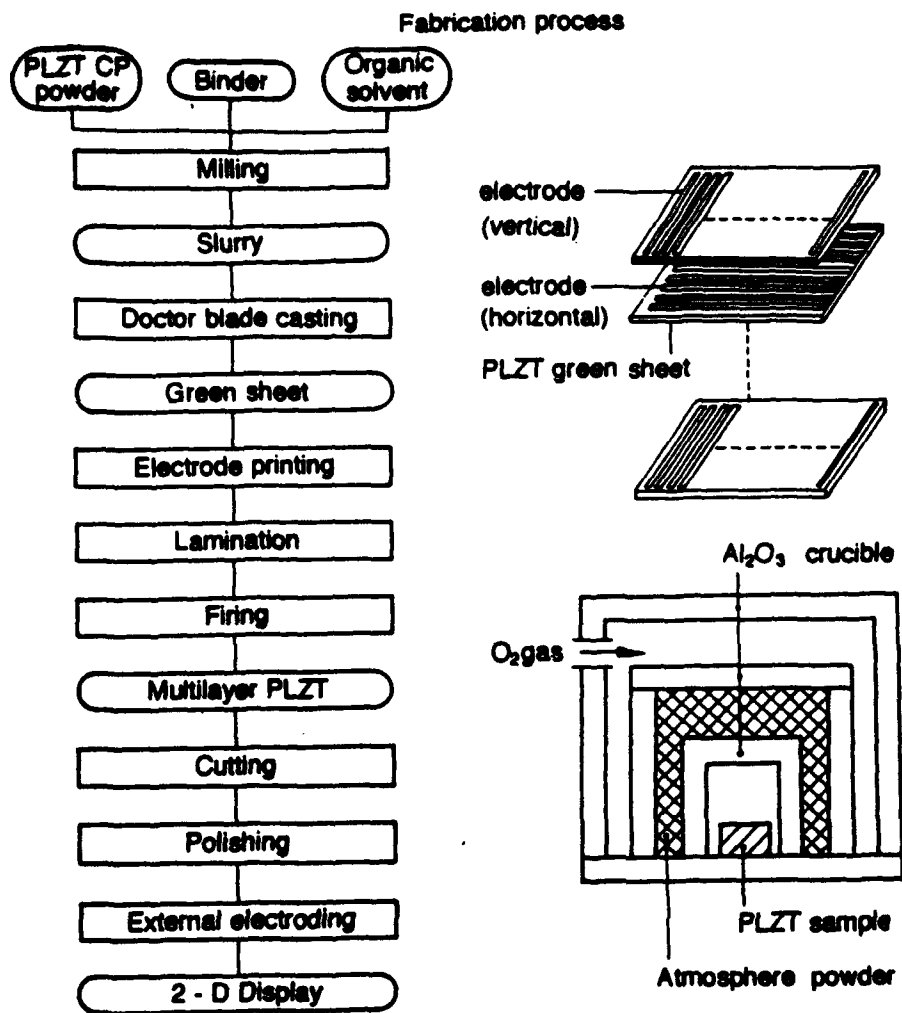Figure 12-39. Newly developed design of a 2-dimensional display.

Fabrication process

PLZT CP powder | Binder | Organic solvent
→
Milling
↓
Slurry
↓
Doctor blade casting
↓
Green sheet
↓
Electrode printing
↓
Lamination
↓
Firing
↓
Multilayer PLZT
↓
Cutting
↓
Polishing
↓
External electroding
↓
2 - D Display

electrode (vertical)
electrode (horizontal)
PLZT green sheet

Al_2O_3 crucible

O_2 gas

PLZT sample

Atmosphere powder

Figure 12-40. Fabrication process of the newly developed 2-D display.

Mirror
Red
Screen
PLZT light valve
Dichroic mirror (Green Ref.)
Green
Dichroic mirror (Blue Ref.)
Blue
Projection lens
Xenon lamp
Dichroic mirror (Red Ref.)
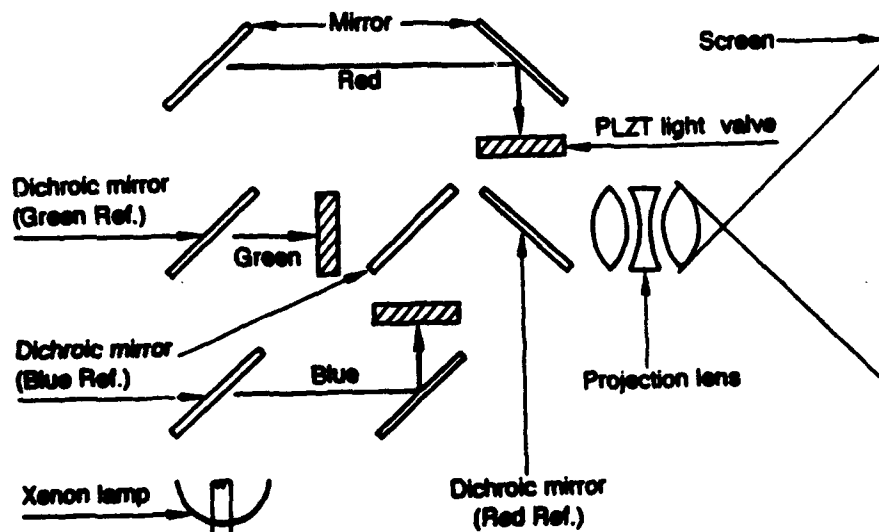
Figure 12-41. Construction of the PLZT color image projector.
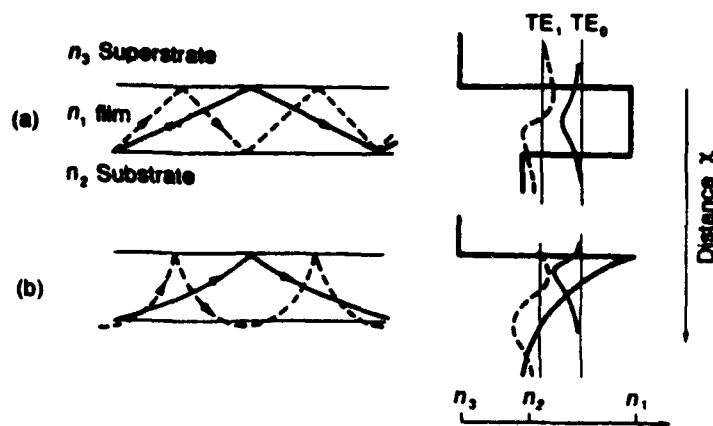
Figure 12-42. Diagrams of (a) slab and (b) graded-index waveguides. The wavefunctions for the TE_0 and TE_1 modes are shown in the refractive-index profiles.

12.6 Positive Temperature Coefficient (PTC) Materials

12.6.1 The PTC Phenomenon

When barium titanate ($BaTiO_3$) is doped with a low concentration of lanthanide ions (0.3 at.%) the ceramic becomes semiconductive with a resistivity in the range of $10-10^3 \, \Omega \cdot cm$. Moreover, the resistivity is

Figure 12-43. Electrooptic waveguides. (a) Planar-type and (b) ridge-type.

drastically increased by 3-5 orders of magnitude with increasing temperature around the Curie point. This phenomenon was discovered in 1954, and denoted as the PTC (positive temperature coefficient of resistivity) effect, since then it has been investigated intensively by many researchers (Andrich, 1965; Heywang, 1964).

The PTC dopant is an ionic species with a larger ionic valence such as La, Sm, Ce or Gd, and replaces the Ba ions and Nb, Ta, Bi in the Ti sites. Since the temperature at which the resistivity anomaly occurs is closely related with the Curie point, the temperature coefficient can easily be designed by choosing the solid solution on the basis of $BaTiO_3$. Fig. 12-44 shows some varieties of the PTCR curves.

The theory for the PTC effect has not been established completely. The most acceptable model is illustrated in Fig. 12-45, which was initially proposed by H. Heywang et al. (Heywang, 1964). When the two semiconductive (n-type) ceramic particles are in contact through a grain boundary, an electron energy barrier (Schottky barrier) is generated and the barrier height is given by the following equation:

$$\phi = e \, N_s^2 / (2 \, \varepsilon_0 \, \varepsilon \, N_d) \qquad (12-38)$$

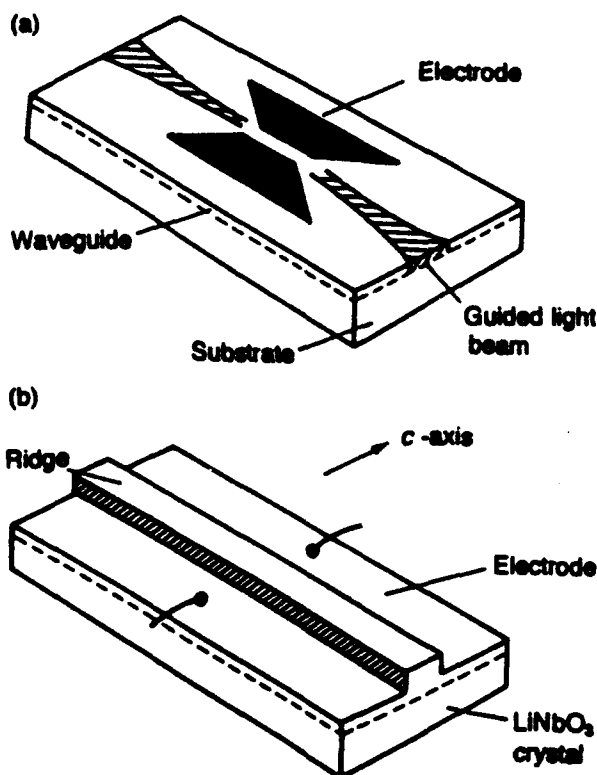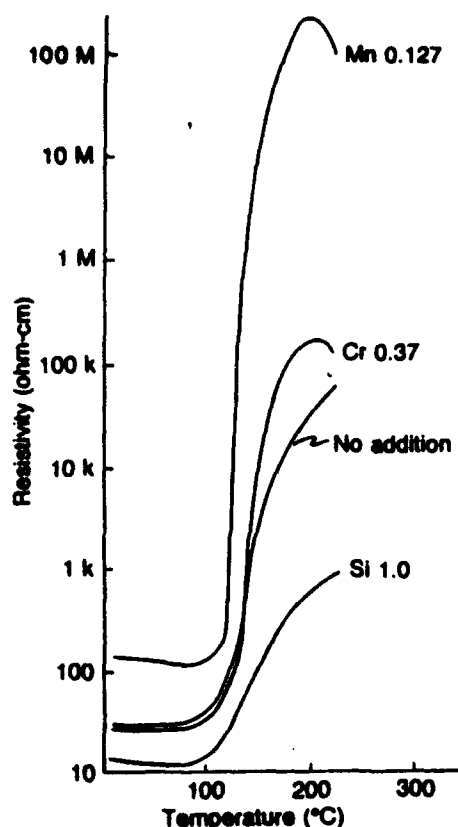N_d is the concentration of donor atoms and N_s is the surface density of negatively

Figure 12-44. Resistivity vs. temperature behavior of PTCR BaTiO$_3$ ceramics. Modifiers and additive concentrations are indicated.

tial barrier due to the increase in permittivity as the temperature falls to T_C.

$$\varepsilon = C/(T - T_0) \tag{12-39}$$

Below T_C the permittivity falls, but the spontaneous polarization appears and controls the electron concentration to reduce the barrier height. This keeps the resistivity in a rather low range.

12.6.2 PTC Thermistors

PTC thermistors are applicable not only for temperature-change detection but also for active current controllers. The thermistor, when self-heated, causes a decrease in the current owing to the drastic increase of resistivity. Practical applications are found in over-current/voltage protectors, starting switches for motors and automatic demagnetization circuits for color TVs.

"Ceramic heaters" have also been widely commercialized in panel heaters, electronic thermos bottles and hair dryers.

charged acceptors (here assumed to be confined to the surface due to Ba vacancies). Note that the permittivity ε obeys the Curie–Weiss law (Eq. (12-39)) above T_C, and that the low resistance at T_C is thus accounted for by the lowering of the poten-

12.6.3 Grain Boundary Layer Capacitors

When a semiconductive BaTiO$_3$ ceramic is oxidized to make a resistive surface layer, it can be used as a high-capacitance condenser. The capacitance is adjustable in the range of $0.4-0.5 \, \mu F/cm^2$.
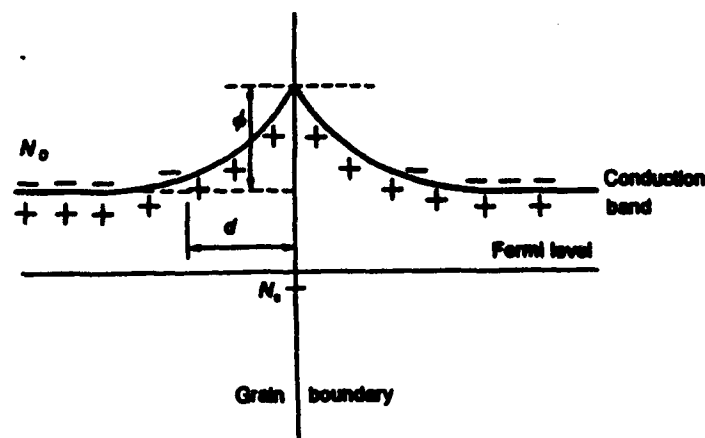

Figure 12-45. Energy-level diagram near a grain boundary of the PTCR BaTiO$_3$.
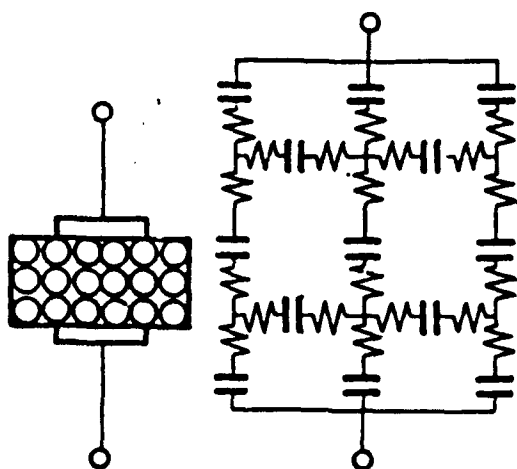
Figure 12-46. Model of the grain boundary layer condensers.

A new type of grain boundary layer (GBL) condensers has been developed by using electrically resistive grain boundaries. The model is illustrated in Fig. 12-46. (See also Chap. 14 of this Volume for a more detailed analysis of grain boundary semi-conducting effects.) In practice, CeO_2 or Bi_2O_3 is coated on a semiconductive ceramic and diffused into the grain boundaries by thermal treatment so as to make the boundary layer highly-resistive. The resistive grain boundary layers of 1 μm thickness are fully connected in the ceramics with grains of 10 μm in size. This type exhibit excellent frequency characteristics and can be used as wide-band pass condensers up to several GHz.

12.7 Conclusions

We have described the fundamentals and applications of ferroelectrics, including:

high-permittivity dielectrics
pyroelectric devices
piezoelectric devices
electrooptic devices
PTC materials

From a viewpoint of commercialization, capacitor dielectrics account for most of the sales at present, and piezoelectric vibrators such as buzzers and speakers hold the second position. The sales concerned with the other applications are negligibly small.

What does the future hold for ferroelectric devices? Ferroelectrics can be utilized in various devices but until now have failed to reach commercialization in most cases. In the light sensor, for example, semiconductive materials are superior to ferroelectrics in response speed and sensitivity. Magnetic devices are much more popular in the memory field, and liquid crystals are typically used for optical displays. Ferroelectric devices often fail to be developed in the cases where competitive materials exist. Therefore, it can be said that ferroelectrics are strong candidates for application only in those fields where no viable alternative materials exists. It is the author's opinion that the following will be promising areas:

electromechanical devices (piezoelectric actuators, ultrasonic motors)
thin-film hybrid sensors (pyro-, pressure, acceleration sensors)
electrooptic devices (light waveguides, thin-film hybrid displays)

12.8 Appendix 1: Tensor Representation of Physical Properties

12.8.1 Tensor Representation

Let us first consider an example of tensor conductivity. The conductivity is defined so as to correlate an applied electric field E and the induced current density j as follows:

$$j = \sigma E \tag{A1}$$

Since both the electric field and the current density are first rank tensors (i.e., vector) quantities, the conductivity should have a second rank tensor representation (i.e., with two suffixes); this is described as

$$\begin{pmatrix} j_1 \\ j_2 \\ j_3 \end{pmatrix} = \begin{pmatrix} \sigma_{11} & \sigma_{12} & \sigma_{13} \\ \sigma_{21} & \sigma_{22} & \sigma_{23} \\ \sigma_{31} & \sigma_{32} & \sigma_{33} \end{pmatrix} \begin{pmatrix} E_1 \\ E_2 \\ E_3 \end{pmatrix} \quad \text{(A 2)}$$

or

$$j_i = \sum_j \sigma_{ij} E_j \quad \text{(A 3)}$$

A third-rank tensor is exemplified by piezoelectric coefficients, providing a relation between the applied field and the induced strain x:

$$x = dE \quad \text{(A 4)}$$

Since the E and x are first-rank and second-rank tensors, respectively, the **d** should have a third-rank tensor form represented as

$$x_{jk} = \sum_i d_{ijk} E_i \quad \text{(A 5)}$$

The **d** tensor is composed of three layers of the symmetrical matrices.

1st layer $(i = 1)$ $\begin{pmatrix} d_{111} & d_{112} & d_{113} \\ d_{121} & d_{122} & d_{123} \\ d_{131} & d_{132} & d_{133} \end{pmatrix}$

2nd layer $(i = 2)$ $\begin{pmatrix} d_{211} & d_{212} & d_{213} \\ d_{221} & d_{222} & d_{223} \\ d_{231} & d_{232} & d_{233} \end{pmatrix}$ (A 6)

3rd layer $(i = 3)$ $\begin{pmatrix} d_{311} & d_{312} & d_{313} \\ d_{321} & d_{322} & d_{323} \\ d_{331} & d_{332} & d_{333} \end{pmatrix}$

Generally speaking, if two physical properties are represented using tensors of p-rank and q-rank, the quantity which combines the two properties in a linear relation is also represented by a tensor of $(p + q)$-rank.

12.8.2 Crystal Symmetry and Tensor Form

When we measure a physical property along two different directions, the two values measured must be equal if these two directions are crystallographically equivalent to each other. This consideration sometimes reduces the number of the independent tensor components representing the above property.

Let us again take conductivity as an example of a second-rank tensor. If the current density j in an (x, y, z) coordinate system is described in an (x', y', z') system as j', j and j' are related using a unitary matrix [1] as follows:

$$\begin{pmatrix} j'_1 \\ j'_2 \\ j'_3 \end{pmatrix} = \begin{pmatrix} a_{11} & a_{12} & a_{13} \\ a_{21} & a_{22} & a_{23} \\ a_{31} & a_{32} & a_{33} \end{pmatrix} \begin{pmatrix} j_1 \\ j_2 \\ j_3 \end{pmatrix} \quad \text{(A 7)}$$

The electric field is transformed in the same way:

$$\begin{pmatrix} E'_1 \\ E'_2 \\ E'_3 \end{pmatrix} = \begin{pmatrix} a_{11} & a_{12} & a_{13} \\ a_{21} & a_{22} & a_{23} \\ a_{31} & a_{32} & a_{33} \end{pmatrix} \begin{pmatrix} E_1 \\ E_2 \\ E_3 \end{pmatrix} \quad \text{(A 8)}$$

or

$$E'_i = \sum_j a_{ij} E_j \quad \text{(A 9)}$$

---

[1] A unitary matrix without an imaginary part has the following relation:

$$\begin{pmatrix} a_{11} & a_{12} & a_{13} \\ a_{21} & a_{22} & a_{23} \\ a_{31} & a_{32} & a_{33} \end{pmatrix}^{-1} = \begin{pmatrix} a_{11} & a_{21} & a_{31} \\ a_{12} & a_{22} & a_{32} \\ a_{13} & a_{23} & a_{33} \end{pmatrix}$$

For centro-symmetry, the transformation matrix is written as

$$\begin{pmatrix} -1 & 0 & 0 \\ 0 & -1 & 0 \\ 0 & 0 & -1 \end{pmatrix}$$

and for rotation about a principal axis,

$$\begin{pmatrix} \cos\theta & \sin\theta & 0 \\ -\sin\theta & \cos\theta & 0 \\ 0 & 0 & 1 \end{pmatrix}$$

Then, we can calculate the corresponding σ' tensor defined by

$$
\begin{pmatrix} j''_1 \\ j''_2 \\ j''_3 \end{pmatrix} = \sigma' \begin{pmatrix} E'_1 \\ E'_2 \\ E'_3 \end{pmatrix} \tag{A 10}
$$

$$
\begin{pmatrix} \sigma'_{11} & \sigma'_{12} & \sigma'_{13} \\ \sigma'_{21} & \sigma'_{22} & \sigma'_{23} \\ \sigma'_{31} & \sigma'_{32} & \sigma'_{33} \end{pmatrix} = \begin{pmatrix} a_{11} & a_{12} & a_{13} \\ a_{21} & a_{22} & a_{23} \\ a_{31} & a_{32} & a_{33} \end{pmatrix} .
$$

$$
\cdot \begin{pmatrix} \sigma_{11} & \sigma_{12} & \sigma_{13} \\ \sigma_{21} & \sigma_{22} & \sigma_{23} \\ \sigma_{31} & \sigma_{32} & \sigma_{33} \end{pmatrix} \begin{pmatrix} a_{11} & a_{21} & a_{31} \\ a_{12} & a_{22} & a_{32} \\ a_{13} & a_{23} & a_{33} \end{pmatrix}
$$

$$
\tag{A 11}
$$

$$
\sigma'_{ij} = \sum_{k,l} a_{ik} a_{jl} \sigma_{kl} \tag{A 12}
$$

When the crystal has a 2-fold axis along the z-axis, the conductivity tensor should have the same components for the transformation of

$$
\begin{pmatrix} -1 & 0 & 0 \\ 0 & -1 & 0 \\ 0 & 0 & 1 \end{pmatrix}
$$

From the condition

$$
\begin{pmatrix} \sigma_{11} & \sigma_{12} & \sigma_{13} \\ \sigma_{21} & \sigma_{22} & \sigma_{23} \\ \sigma_{31} & \sigma_{32} & \sigma_{33} \end{pmatrix} = \begin{pmatrix} -1 & 0 & 0 \\ 0 & -1 & 0 \\ 0 & 0 & 1 \end{pmatrix} .
$$

$$
\cdot \begin{pmatrix} \sigma_{11} & \sigma_{12} & \sigma_{13} \\ \sigma_{21} & \sigma_{22} & \sigma_{23} \\ \sigma_{31} & \sigma_{32} & \sigma_{33} \end{pmatrix} \begin{pmatrix} -1 & 0 & 0 \\ 0 & -1 & 0 \\ 0 & 0 & 1 \end{pmatrix} \tag{A 13}
$$

we can induce the relations:

$$
\sigma_{31} = \sigma_{13} = \sigma_{32} = \sigma_{23} = 0
$$

$$
\sigma_{11}, \sigma_{22}, \sigma_{33} \neq 0 \tag{A 14}
$$

$$
\sigma_{12} = \sigma_{21}
$$

It is very important to note that most of the physical constants have a symmetric tensor form (the proof involves thermodynamical considerations and is beyond the scope of this article).

As far as a third-rank tensor such as piezoelectric tensor is concerned, the transformation on change of the coordinate system is represented as

$$
d'_{ijk} = \sum_{l,m,n} a_{il} a_{jm} a_{kn} d_{lmn} \tag{A 15}
$$

When the crystal has a 4-fold axis along the z-axis, the transformation matrix is given by

$$
\begin{pmatrix} 0 & 1 & 0 \\ -1 & 0 & 0 \\ 0 & 0 & 1 \end{pmatrix}
$$

In consideration of the tensor symmetry with m and n such as $d_{123} = d_{132}$ and $d_{213} = d_{231}$ (each matrix of the ith layer of the d tensor is symmetrical), we can obtain the relations:

$$
d_{111} = d_{222} = d_{112} = d_{121} = d_{211}
$$

$$
= d_{221} = d_{212} = d_{122} = d_{331}
$$

$$
= d_{313} = d_{133} = d_{332} = d_{323}
$$

$$
= d_{233} = d_{312} = d_{321} = 0
$$

$$
\tag{A 16}
$$

$$
d_{333} \neq 0
$$

$$
d_{311} = d_{322}
$$

$$
d_{113} = d_{131} = d_{223} = d_{232}
$$

$$
d_{123} = d_{132} = -d_{213} = -d_{231}
$$

1st layer

$$
\begin{pmatrix} 0 & 0 & d_{131} \\ 0 & 0 & d_{123} \\ d_{131} & d_{123} & 0 \end{pmatrix}
$$

2nd layer

$$
\begin{pmatrix} 0 & 0 & -d_{123} \\ 0 & 0 & d_{131} \\ -d_{123} & d_{131} & 0 \end{pmatrix} \tag{A 17}
$$

3rd layer

$$
\begin{pmatrix} d_{311} & 0 & 0 \\ 0 & d_{311} & 0 \\ 0 & 0 & d_{333} \end{pmatrix}
$$

12.8.3 Reduction of the Tensor (Matrix Notation)

A general third-rank tensor has $3^3 = 27$ independent components. Since d_{ijk} is symmetrical in j and k some of the coefficients can be eliminated, leaving 18 independent d_{ijk}; it also facilitates the use of the matrix notation.

So far all the equations have been developed in full tensor notation. But when calculating actual properties, it is advantageous to reduce the number of suffixes as much as possible. This is done by defining new symbols, for instance, $d_{21} = d_{211}$ and $d_{14} = 2d_{123}$: The second and third suffixes in the full tensor notation are replaced by a single suffix 1 to 6 in matrix notation, as follows:

tensor notation	11	22	33	23,32	31,13	12,21
matrix notation	1	2	3	4	5	6

In terms of these new symbols the array (A 6) is rewritten as:

$$
\begin{pmatrix} d_{11} & \tfrac{1}{2}d_{16} & \tfrac{1}{2}d_{15} \\ \tfrac{1}{2}d_{16} & d_{12} & \tfrac{1}{2}d_{14} \\ \tfrac{1}{2}d_{15} & \tfrac{1}{2}d_{14} & d_{13} \end{pmatrix} \cdot
$$

$$
\cdot \begin{pmatrix} d_{21} & \tfrac{1}{2}d_{26} & \tfrac{1}{2}d_{25} \\ \tfrac{1}{2}d_{26} & d_{22} & \tfrac{1}{2}d_{24} \\ \tfrac{1}{2}d_{25} & \tfrac{1}{2}d_{24} & d_{23} \end{pmatrix} \cdot
$$

$$
\cdot \begin{pmatrix} d_{31} & \tfrac{1}{2}d_{36} & \tfrac{1}{2}d_{35} \\ \tfrac{1}{2}d_{36} & d_{32} & \tfrac{1}{2}d_{34} \\ \tfrac{1}{2}d_{35} & \tfrac{1}{2}d_{34} & d_{33} \end{pmatrix} \qquad \text{(A 18)}
$$

The last two suffixes in the tensor notation correspond to those of the strain components; therefore, for consistency, we make

the following change in the notation for the strain components

$$
\begin{pmatrix} x_{11} & x_{12} & x_{31} \\ x_{12} & x_{22} & x_{23} \\ x_{31} & x_{23} & x_{33} \end{pmatrix} \rightarrow \begin{pmatrix} x_1 & \tfrac{1}{2}x_6 & \tfrac{1}{2}x_5 \\ \tfrac{1}{2}x_6 & x_2 & \tfrac{1}{2}x_4 \\ \tfrac{1}{2}x_5 & \tfrac{1}{2}x_4 & x_3 \end{pmatrix} \qquad \text{(A 19)}
$$

The reason for the $\tfrac{1}{2}$s in the substitution (A 19) is due to the cancellation with $\tfrac{1}{2}$s in (A 18). Then, we have

$$
x_j = \sum_i d_{ij} E_i \quad (i = 1, 2, 3; j = 1, 2, \ldots, 6) \qquad \text{(A 20)}
$$

or

$$
\begin{bmatrix} x_1 \\ x_2 \\ x_3 \\ x_4 \\ x_5 \\ x_6 \end{bmatrix} = \begin{bmatrix} d_{11} & d_{21} & d_{31} \\ d_{12} & d_{22} & d_{32} \\ d_{13} & d_{23} & d_{33} \\ d_{14} & d_{24} & d_{34} \\ d_{15} & d_{25} & d_{35} \\ d_{16} & d_{26} & d_{36} \end{bmatrix} \begin{pmatrix} E_1 \\ E_2 \\ E_3 \end{pmatrix} \qquad \text{(A 21)}
$$

Concerning the stress components, the $\tfrac{1}{2}$s are unnecessary.

$$
\begin{pmatrix} X_{11} & X_{12} & X_{31} \\ X_{12} & X_{22} & X_{23} \\ X_{31} & X_{23} & X_{33} \end{pmatrix} \rightarrow \begin{pmatrix} X_1 & X_6 & X_5 \\ X_6 & X_2 & X_4 \\ X_5 & X_4 & X_3 \end{pmatrix} \qquad \text{(A 22)}
$$

The matrix notation has the advantage of compactness over the tensor notation, and it makes it easy to display the coefficients on a plane diagram. However, it must be remembered that in spite of their form, the d_{ij}s do not transform like the components of a second-rank tensor.

An example of a piezoelectric matrix for the point group 4 is written as

$$
\begin{pmatrix} 0 & 0 & 0 & d_{14} & d_{15} & 0 \\ 0 & 0 & 0 & d_{15} & -d_{14} & 0 \\ d_{31} & d_{31} & d_{33} & 0 & 0 & 0 \end{pmatrix} \qquad \text{(A 23)}
$$

12.9 Appendix 2:
Phenomenology of Ferroelectricity

12.9.1 Landau Theory of the Phase Transition

A thermodynamical theory explaining the behavior of a ferroelectric crystal can be obtained by considering the form of the expansion of the energy as a function of the polarization P. We assume that the Landau free energy F in one dimension should be represented formally as:

$$F(P, T) = \tfrac{1}{2}\alpha P^2 + \tfrac{1}{4}\beta P^4 + \tfrac{1}{6}\gamma P^6 + \ldots \tag{A24}$$

The coefficients α, β, γ depend on the temperature in general. Note that the series does not contain terms in odd powers of P because the free energy of the crystal will not change by the polarization reversal $(P \rightarrow -P)$. The phenomenological formulation should be applied for all the temperature range through paraelectric and ferroelectric states.

The equilibrium polarization in an electric field E satisfies:

$$\frac{\partial F}{\partial P} = E = \alpha P + \beta P^3 + \gamma P^5 \tag{A25}$$

To obtain the ferroelectric state, the coefficient of the term in P^2 must be negative, in which the polarized state is stable, while in a paraelectric state it must be positive passing through zero at some temperature T_0 (Curie–Weiss temperature):

$$\alpha = (T - T_0)/(\varepsilon_0 \cdot C) \tag{A26}$$

C is taken as a positive constant and T_0 is equal to or lower than the actual transition temperature T_C (Curie temperature). The variation of α with temperature is explained microscopically by thermal expansion and other effects of anharmonic lattice interactions.

12.9.1.1 Second-Order Transition

When β is positive, the γ is often neglected because nothing special is added by this term. The polarization for zero applied field (A27) is obtained from (A25) so that either $P_s = 0$ or $P_s^2 = (T_0 - T)/(\beta \varepsilon_0 C)$.

$$\frac{T - T_0}{\varepsilon_0 C} P_s + \beta P_s^3 = 0 \tag{A27}$$

For $T \geq T_0$, the unique solution $P_s = 0$ is obtained. For $T < T_0$ the minimum of the Landau free energy is obtained at:

$$P_s = \sqrt{(T_0 - T)/(\beta \varepsilon_0 C)} \tag{A28}$$

The phase transition occurs at $T_C = T_0$ and the polarization goes continuously to zero at this temperature; this is called a second-order transition.

Relative permittivity ε is calculated as:

$$1/\varepsilon = \varepsilon_0/(\partial P/\partial E) = \varepsilon_0(\alpha + 3\beta P^2) \tag{A29}$$

Then,

$$\varepsilon = \begin{cases} C/(T - T_0) & (T > T_0) \\ C/[2(T_0 - T)] & (T_0 < T) \end{cases} \tag{A30}$$

Figure 12-A1 shows the variations of P_s and ε with temperature. It is notable that the permittivity becomes infinite at the transition temperature. Triglycine sulphate is an example exhibiting the second-order transition.

12.9.1.2 First-Order Transition

When β is negative in Eq. (A24) and γ is taken positive, the transition becomes first order. The equilibrium condition for $E = 0$ (A31) leads to either $P_s = 0$ or (A32).

$$\frac{(T - T_0)}{\varepsilon_0 C} P_s + \beta P_s^3 + \gamma P_s^5 = 0 \tag{A31}$$

$$P_s^2 = \left[-\beta + \sqrt{\beta^2 - \frac{4\gamma(T - T_0)}{\varepsilon_0 C}} \right] \Big/ (2\gamma) \tag{A32}$$
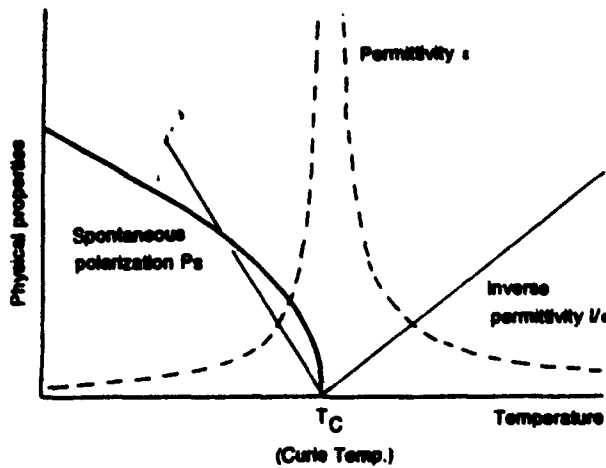
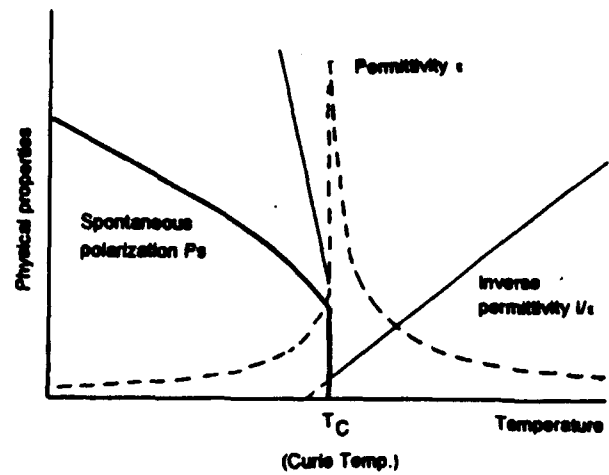**Figure 12-A 1.** Second-order transition in a ferroelectric.

Figure 12-A 2. First-order transition in a ferroelectric.

The transition temperature T_C is obtained from the condition that the free energies of the paraelectric and ferroelectric phases are equal: i.e., $F = 0$, or:

$$\frac{T - T_0}{\varepsilon_0 \varepsilon} + \frac{1}{2}\beta P_s^2 + \frac{1}{3}\gamma P_s^4 = 0 \qquad (A\,33)$$

Therefore:

$$T_C = T_0 + \frac{3}{16}(\beta^2 \varepsilon_0 C/\gamma) \qquad (A\,34)$$

Note that the Curie Temperature T_C is slightly higher than the Curie–Weiss temperature T_0, and that the discrete jump of the P_s appears at T_C. Also, the permittivity exhibits a finite maximum at T_C for a first-order transition (Fig. 12-A 2). Barium titanate is a good example.

12.9.2 Phenomenology of Electrostriction

Let us assume that the elastic Gibbs energy should be expanded in a one-dimensional form:
$$\qquad (A\,35)$$

$$G_1(P, X, T) = \tfrac{1}{2}\alpha P^2 + \tfrac{1}{4}\beta P^4 + \tfrac{1}{6}\gamma P^6 - \tfrac{1}{2}s X^2 - Q P^2 X, \quad [\alpha = (T - T_0)/(\varepsilon_0 C)]$$

P, X, T are polarization, stress and temperature, respectively, and s and Q are called

the elastic compliance and the electrostrictive coefficient. Note that the piezoelectric coupling term $P X$ is omitted and the electrostrictive coupling term $P^2 X$ is introduced when the paraelectric phase has centrosymmetry (non-piezoelectric). This leads to Eq. (A 36) and (A 37).

$$E = (\partial G_1/\partial P) = \alpha P + \beta P^3 + \gamma P^5 -$$
$$- 2 Q P X \qquad (A\,36)$$
$$x = -(\partial G_1/\partial X) = s X + Q P^2. \qquad (A\,37)$$

12.9.2.1 Case I: $X = 0$

When an external stress is zero, the following equations are derived:

$$E = \alpha P + \beta P^3 + \gamma P^5 \qquad (A\,38)$$
$$x = Q P^2 \qquad (A\,39)$$
$$1/\varepsilon_0 \varepsilon = \alpha + 3\beta P^2 + 5\gamma P^4 \qquad (A\,40)$$

If the external electric field is equal to zero $(E = 0)$, two different states are derived; $P = 0$ and $P^2 = (\sqrt{\beta^2 - 4\alpha\gamma} - \beta)/(2\gamma)$.

(I) Paraelectric phase: $P_s = 0$ or $P = \varepsilon_0 \varepsilon E$ (under small E)

Permittivity:

$$\varepsilon = C/(T - T_0) \text{ (Curie–Weiss law)} \qquad (A\,41)$$

Electrostriction:

$$x = Q \varepsilon_0^2 \varepsilon^2 E^2 \qquad \text{(A 42)}$$

(II) Ferroelectric phase:
$$P_s^2 = (\sqrt{\beta^2 - 4\alpha\gamma} - \beta)/(2\gamma) \text{ or } P = P_s + \varepsilon_0 \varepsilon E$$
(under small E)

$$x = Q(P_s + \varepsilon_0 \varepsilon E)^2 = Q P_s^2 +$$
$$+ 2\varepsilon_0 \varepsilon Q P_s E + Q \varepsilon_0^2 \varepsilon^2 E^2 \qquad \text{(A 43)}$$

Spontaneous strain:

$$x_s = Q P_s^2 \qquad \text{(A 44)}$$

Piezoelectric constant:

$$d = 2\varepsilon_0 \varepsilon Q P_s \qquad \text{(A 45)}$$

Piezoelectricity is equivalent to the electrostrictive phenomenon biased by the spontaneous polarization. Temperature dependence of the spontaneous strain and the piezoelectric constant is plotted in Fig. 12-A 3.
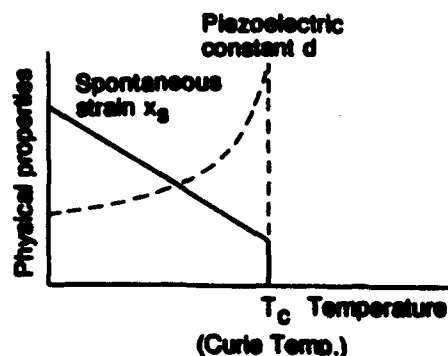
Figure 12-A 3. Temperature dependence of spontaneous strain and piezoelectric constant.

12.9.2.2 Case II: $X \neq 0$

When a hydrostatic pressure p ($X = -p$) is applied, the inverse permittivity is changed in proportion to p:

$$1/\varepsilon_0, \varepsilon = \begin{cases} \alpha + 3\beta P^2 + 5\gamma P^4 + 2Q p & \text{(Ferroelectric)} \qquad \text{(A 46)} \\ \alpha + 2Q p = (T - T_0 + 2Q\varepsilon_0 C p)/(\varepsilon_0 C) & \text{(Paraelectric)} \qquad \text{(A 47)} \end{cases}$$

Therefore, the pressure dependence of the Curie–Weiss temperature T_0 or the transition temperature T_C is derived as follows:

$$(\partial T_0/\partial p) = (\partial T_C/\partial p) = -2Q\varepsilon_0 C \qquad \text{(A 48)}$$

In general, the ferroelectric Curie temperature is decreased with increasing hydrostatic pressure.

12.10 References

Akiyama, Y. (1986), *Ultrasonic Motors/Actuators.* Tokyo: Triceps.

Andrich, E. (1965–66), *Electr. Appl. 26,* 123.

Bhalla, A. S., Newnham, R. E., Cross, L. E., Schulze, W. A., Dongherty, J. P., Smith, W. A. (1981), *Ferroelectrics 33,* 139.

Cross, L. E., Jang, S. J., Newnham, R. E., Nomura, S., Uchino, K. (1980), *Ferroelectrics 23,* 187.

Furuta, K., Uchino, K. (1986), *Advanced Ceram. Mater. 1,* 61.

Heywang, W. (1964), *J. Am. Ceram. Soc. 47,* 484.

Jaffe, B., Roth, R. S., Marzullo, S. (1955), *J. Res. Nat. Bur. Stds. 55,* 239.

Kaminow, I. P. (1975), *Trans. IEEE, M.T.T. 23,* 57.

Kanzig, W. (1951), *Helv. Phys. Acta 24,* 175.

Kawai, H. (1969), *Jpn. J. Appl. Phys. 8,* 975.

Kinase, W., Uemura, Y., Kikuchi, M. (1969), *J. Phys. Chem. Solids 30,* 441.

Kittel, C. (1966), *Introduction to Solid State Physics.* New York: John Wiley & Sons, Inc.

Klicker, K. A., Biggers, J. V., Newnham, R. E. (1981), *J. Amer. Ceram. Soc. 64,* 5.

Krause, H. B., Cowley, J. M., Wheatley, J. (1979), *Acta Cryst. A 35,* 1015.

Kumada, A. (1985), *Jpn. J. Appl. Phys. 24, Suppl. 24-2,* 739.

Kumada, A., Kitta, K., Kato, K., Komata, T. (1977), *Proc. Ferroelectric Mater. & Appl. -2,* p. 205.

Nikkei Mechanical (1983), Feb. 28 Ed., p. 44.

Ohmura, K., Murai, Y., Uchino, K., Giniewitcz, J. (1989), *Interaction. Display Research Confer., Proc., IEEE,* p. 138.

Ota, T., Uchikawa, T., Mizutani, T. (1985), *Jpn. J. Appl. Phys. 24, Suppl. 24-3,* 193.

Rolov, B. N. (1963), *Fiz. Twerdogo Tela 6,* 2128.

Rosen, C. A. (1957), *Proc. Electronic Component Symp.,* p. 205.

Sato, T., Ichikawa, H., Ikeda, O., Nomura, S., Uchino, K. (1982), *Appl. Optics 21,* 3669.

Shibata, K., Takeuchi, K., Tanaka, T., Yokoo, S., Nakano, S., Kuwano, Y. (1985), *Jpn. J. Appl. Phys. 24, suppl. 24-3,* 181.

Skanavi, G. I., Ksendzov, I. M., Trigubenko, V. A., Prokhvatilov, V. G. (1958), *Soviet Phys. – JETP 6,* 250.

Smolensky, G. A., Isupov, V. A., Agranovskaya, A. I., Popov, S. N. (1961), *Sov. Phys. – Solid State 2,* 2584.

Taylor, R. G. F., Boot, H. A. H. (1973), *Contemporary Phys. 14,* 55.

Uchino, K. (1986), *Bull. Amer. Ceram. Soc. 65,* 647.

Uchino, K., Cross, L. E., Newnham, R. E., Nomura, S. (1980), *J. Phase Transition 1,* 333.

Uchino, K., Kuwata, J., Nomura, S., Cross, L. E., Newnham, R. E. (1981), *Jpn. J. Appl. Phys. 20, Suppl. 20-4,* 171.

Uchino, K., Nomura, S. (1983), *Oyo Butsuri 52,* 575.

Warner, D. J., Pedder, D. J., Moody, I. S., Burrage, J. (1981), *Ferroelectrics 33,* 249.

Yano, T., Fukui, I., Sato, E., Inui, O., Miyazaki, Y. (1984), *Electr. & Commun. Soc., Proc. 1-156.*

General Reading

Herbert, J. M. (1982), *Ferroelectric Transducers and Sensors.* New York: Gordon and Breach.

Jaffe, B., Cook, W. R., Jaffe, H. (1971), *Piezoelectric Ceramics.* New York: Academic Press.

Jona, F., Shirane, G. (1962), *Ferroelectric Crystals.* Oxford: Pergamon Press.

Levinson, L. M. (1988), *Electronic Ceramics.* New York: Dekker.

Nowotny, J. (1992), *Electronic Ceramic Materials.* Brookfield: TransTech Publ.

Nye, J. F. (1969), *Physical Properties of Crystals.* Oxford: Oxford University Press.

Smolenskii, G. A. (1984), *Ferroelectrics and Related Materials.* New York: Gordon and Breach.

Uchino, K. (1986), *Piezoelectric/Electrostrictive Actuators.* Tokyo: Morikita Publ.

Uchino, K. (1991), *Piezoelectric Actuators – Problem Solving.* Tokyo: Morikita Publ.
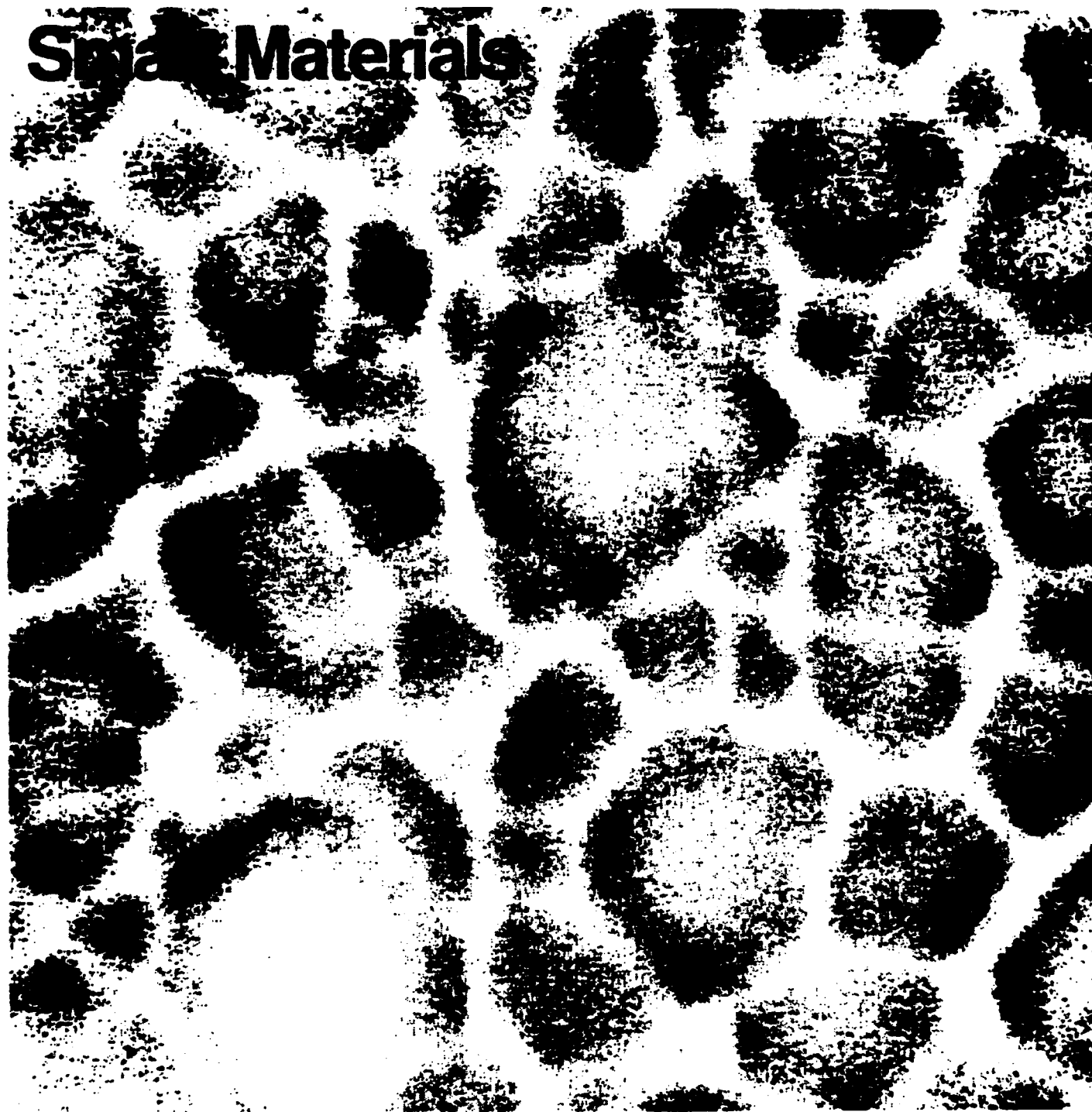
APPENDIX 3

MRS
BULLETIN

Smart Materials

Smart, Very Smart, and Intelligent Materials

Robert E. Newnham, Guest Editor

One of the qualities that distinguishes living systems from inanimate matter is the ability to adapt to changes in the environment. *Smart materials have the ability to perform both sensing and actuating functions* and are, therefore, capable of imitating this rudimentary aspect of life. Poled piezoelectric ceramics, for instance, are capable of acting as both sensor and actuator. External forces are detected through the direct piezoelectric effect, and a response is elicited through the converse piezoelectric effect, in which a voltage of suitable phase, frequency, and amplitude is applied to the same ceramic.

In this special issue, emphasis is placed on actuators, with articles on piezoelectric, electrostrictive, magnetostrictive, and shape memory materials. This is not to say that sensor materials are any less important; it is simply a matter of space. Optical fiber sensors, chemical sensors, thermistors, micromachined semiconductors, and other smart materials deserve special issues of their own.

Smart materials can be conveniently subdivided into *passively smart materials* that respond to external change without assistance, and *actively smart materials* that utilize a feedback loop enabling them to both recognize the change and initiate an appropriate response through an actuator circuit.

Zinc oxide varistors are passively smart materials capable of self-protection against high voltage breakdown. When struck by lightning, the ceramic varistor loses most of its electrical resistance, and the current is bypassed to ground. The resistance change is reversible, and acts as a standby protection phenomenon. Varistors also have a self-repair mechanism through which the highly nonlinear I-V relationship can be restored by repeated voltage pulses.

Actively smart materials include vibration-damping systems for outer-space platforms and electrically-controlled automobile suspension systems. Piezoelectric video tape head positioners operate on a similar principle. The positioners contain a bilaminate bender made from tape-cast PZT ceramic with a segmented electrode pattern dividing the sensing and actuating functions of the positioner. Signals appearing across the sensing electrode are analyzed and processed in the feedback circuit, resulting in a voltage across the positioning electrodes. This causes the cantilevered bimorph to bend, following the video tape track path.

These two examples illustrate how smart materials operate. Both sensing and actuating functions are involved in their performance—but are they really smart? Webster's Dictionary gives several definitions for the word "smart," including "alert, clever, capable," "stylish," and "to feel mental distress or irritation." All three definitions are appropriate for the currently fashionable subject "smart materials." They are "stylish," but are, in some cases, "clever," and it does cause some of us "mental distress" to think that a ceramic might somehow possess intelligence, even in rudimentary form.

How smart is "smart?" There are many words in the English language denoting various levels of intelligence. Beginning at the bottom, an intelligence scale might look like this: stupid - ignorant - trivial - sensible - smart - clever - intelligent - wise. Many modern-day materials have been cleverly designed to perform useful functions and we are, it seems to us, justified in calling them "smart." They are decidedly better than "sensible" materials, but calling them "intelligent" seems rather presumptuous and self-serving.

A number of research groups are looking for ways to raise the level of "intelligence" in materials by integrating the sensing and actuating functions with information processing systems, memories and learning mechanisms, power supplies, and various

forms of self-protection. In a crude way, these materials mimic the brain, metabolism, and protective reflex reactions of the human body that augment muscle motion and the five senses.

Materials with a built-in learning function are smarter than those without. A *very smart material* senses a change in the environment and responds by altering one or more of its property coefficients. In this way, it can tune its sensing and actuating capabilities in time or space to optimize behavior. With the help of a feedback system, a very smart material becomes smarter with age. The distinction between smart and very smart materials is essentially one between linear and nonlinear properties. The physical properties of nonlinear materials can be adjusted by bias fields or forces to control response.

The tunable transducer developed in our laboratory illustrates the concept of a very smart material. Two of the important properties of the ultrasonic transducers used in biomedical scanners and in nondestructive testing are the resonant frequency and the electromechanical coupling coefficient. The resonant frequency is controlled by the elastic constants of the transducer, and the electromechanical coupling coefficient by its piezoelectric constants. Tunable transducers are made by sandwiching together two highly nonlinear materials: rubber and relaxor ferroelectric ceramics. Rubber, like most elastomers, is elastically nonlinear. In its unstressed compliant state, the molecules are coiled and tangled, but under stress, the molecules align and the material stiffens noticeably. Relaxor ferroelectrics, such as lead magnesium niobate, are electrically nonlinear, and exhibit huge electrostriction effects. Under electric bias, the piezoelectric coefficient increases dramatically from zero to a value far higher than lead zirconate titanate. Both the resonant frequency and electromechanical coupling coefficient can be tuned when electric fields and mechanical stress are applied simultaneously.

Integration and miniaturization of electroceramic sensors and actuators is an ongoing process in the automotive and consumer electronics areas. Today's mid-range vehicles have about 50 sensors and actuators, and even more sophisticated functional materials are under development for exhaust gas monitoring, active suspensions, and integrated traffic guidance systems. Multilayer packages containing signal processing layers made up of low-permittivity dielectrics and printed metal interconnections are in widespread production. Further integration with imbedded resistors and capacitors is under development and it seems likely that intelligent

systems will make use of this processing technology. Tape casting and screen printing are the processes used most often, and varistors, chemical sensors, thermistors, and piezoelectric transducers can all be fabricated in this way, opening up the possibility of multicomponent multifunction ceramics with both sensor and actuator capabilities. Silicon chips can be mounted on these multifunctional packages to provide all or part of the control network.

The next logical step is to combine the sensor and actuator functions with the control system. This can be done by depositing electroceramic coatings on integrated circuit silicon chips—currently an active area for materials research. In the near future, when the information processing system, feedback circuitry, and power supply are integrated with the sensors and actuators, we will then perhaps be justified in calling our materials *intelligent*. The next goal will be to develop *wise materials*, that make the correct moral decision! ☐

Robert E. Newnham, Guest Editor for this issue of the *MRS Bulletin*, is Alcoa Professor of Solid State Science at Pennsylvania State University's Materials Research Laboratory. He also teaches courses in the Ceramic Science Section of the Materials Science and Engineering Department. Newnham, whose research interests are in structure-property relations, electroceramics, and composite materials for electronic applications, holds a PhD degree from Penn State in physics and mineralogy, and a PhD degree from Cambridge University in crystallography. Prior to joining the Penn State faculty, he taught at MIT, where he was a staff member of the Laboratory for Insulation Research. Newnham has authored four books and more than 300 papers, is co-editor of the *Journal of the American Ceramic Society*, and is a member of the National Academy of Engineering. Newnham was elected Ceramic Educator of the Year by the Ceramic Education Council and is a recipient of the John Jeppson Medal for "Distinguished, creative, and inspiring contributions to ceramic science, technology, and education in the area of electronic ceramic materials." He is also the recipient of the First International Ceramics Prize from the Academy of Ceramics.

Arthur E. Clark, Navy Distinguished Scientist, has been head of the magnetics group at the Naval Surface

Robert E. Newnham

Arthur E. Clark

Kristl B. Hathaway

Susan Trolier-McKinstry

Kenji Uchino

C.M. Wayman

Warfare Center, White Oak Laboratory, for 18 years. Since receiving his PhD in physics from Catholic University of America in 1960, he has been engaged in research on the elastic and magnetic properties of solids, particularly on the magnetorestrictive properties of rare-earth ions in metals and insulators. Clark holds patents in the areas of magnetic refrigeration, magnetostrictive materials, and magnetomechanical transduction.

Kristl B. Hathaway, research physicist at the Naval Surface Warfare Center, White Oak Laboratory, and a scientific officer in the Materials Division of the Office of Naval Research, manages basic research programs in magnetic materials. Her research interests include the magnetoelastic behavior of rare-earth transition metal alloys and amorphous metallic glasses, the electronic structure of transition metals, and the magnetic properties of

thin films and multilayers. Hathaway received her PhD degree in physics from Cornell University in 1976.

Susan Trolier-McKinstry is an assistant professor of ceramic science at Pennsylvania State University, where she researches ferroelectric and piezoelectric films and the optical characterization of bulk and thin-film ceramic materials. Trolier-McKinstry received her PhD degree in ceramic science from Penn

State, where she also earned her BS and MS degrees. A recipient of an MRS Graduate Student Award in spring 1992, she spent six months at the Hitachi Central Research Laboratory in Tokyo during her doctoral program, studying the development of graphoepitaxial alignment in platinum on sawtooth-profiled Si wafers for use as substrates for piezoelectric films.

Kenji Uchino is a professor of electrical and computer engineering, a professor of materials, and director of the International Center for Actuators and Transducers at Pennsylvania State University. He is also an associate professor of physics at Sophia University, Japan. Uchino received his MS and DSc degrees in physical electronics from the Tokyo Institute of Technology. His research interests cover dielectrics, ferroelectrics, and piezoelectrics, and include basic research on materials, as well as device designing and fabrication processes. An inventor holding 30 patents and the author of 24 books on piezoelectric actuators, Uchino is vice president of NF Electronic Instruments, Inc., a company formed to develop products relating to piezoelectric actuators. He is also the founder and chairman of the Society of Solid State Actuators, Japan Technology Transfer Association. Uchino has authored more than 150 publications and received the Best Paper Award of the Japanese Society of Oil/Air Pressure Control.

C.M. Wayman, professor of materials science and engineering at the University of Illinois, is a researcher in the field of martensitic transformations. He has published over 400 papers and edited numerous books. His textbook, *Crystallography of Martensitic Transformations*, has been translated into Japanese and Chinese. Wayman has received the AIME Mathewson Gold Medal, The Buehler Award from the International Metallographic Society, and the Eminent Faculty Award of the College of Engineering at the University of Illinois. He is also the recipient of honorary professorships at Harbin and Balian Universities in China, and fellowships in ASM International, the Metallurgical Society of AIME, the Institution of Metallurgists, the Japan Society for the Promotion of Science, the Guggenheim Foundation, and Churchill College at the University of Cambridge. □

APPENDIX 4

SIZE EFFECTS AND NONLINEAR PHENOMENA
IN FERROIC CERAMICS

R. E. Newnham, Materials Research Laboratory, Pennsylvania State University, University Park, PA 16802, USA

ABSTRACT

Recent developments in the field of electroceramic nanocomposites are described, placing particular emphasis on the role of the ferroic materials now utilized as soft ferrite transformers, barium titanate multilayer capacitors, toughened zirconia engine parts, lead zirconate-titanate transducers, and doped barium titanate PTC thermistors. The effect of nano-scale on both the material property coefficients of these systems and on their phase transitions is also discussed.

The concept of a fully tunable transducer is developed as an example of a nonlinear material whose sensing and actuating functions can be tuned to optimize behavior. By constructing the composite transducer from an elastically nonlinear material (rubber) and an electrically nonlinear material (relaxor ferroelectric), most of its key properties can be adjusted over wide ranges by applying DC bias fields or mechanical prestress. These properties include resonant frequency, acoustic and electric impedance, damping factors, and electromechanical coupling coefficients.

The origins of nonlinear properties are considered briefly using electrostriction as an example. The nonlinearities often involve phase transformations and size-dependent phenomena on the nanometer scale.

INTRODUCTION

Ferroic crystals have movable domain walls which impart useful properties to a number of electroceramic materials. The properties of these materials are usually largest near the phase transformation temperature where the ferroic domain structure is destabilized as the crystalline structure alters to a high-temperature, high-symmetry form. It is for this reason that the dielectric permittivity of ferroelectric capacitors is the largest near the Curie temperature, and the magnetic susceptibility of ferrite transformers peaks near T_c. PTC thermistors and toughened zirconia engine parts also exhibit ferroic behavior (Table 1).

Table 1: Primary and Secondary Ferroic Crystals (1)

<u>Primary Ferroics</u>

Ferromagnetism	Iron (Fe)
Ferroelectricity	Barium Titanate ($BaTiO_3$)
Ferroelasticity	Zirconia (ZrO_2)

<u>Secondary Ferroics</u>

Ferroelastoelectricity	Ammonium Chloride (NH_4Cl)
Ferromagnetoelectricity	Chromium Oxide (Cr_2O_3)
Ferromagnetoelasticity	Iron Carbonate ($FeCO_3$)
Ferrobielasticity	Quartz (SiO_2)
Ferrobimagnetism	Nickel Oxide (NiO)
Ferrobielectricity	Strontium Titanate ($SrTiO_3$)

Ferroelastic solids have domains which differ in spontaneous strain. The domain walls separating these domains can be shifted with mechanical stress, leading to hysteresis between stress and strain. Analogous behavior between the polarization and the electric field is observed in ferroelectric crystals, and between magnetization and magnetic field in ferromagnetic materials.

In addition to the three types of primary ferroics, there are six types of secondaries which also have movable domain walls. Some, like ferromagnetoelectric chromium oxide, require that two fields (E and H) be applied simultaneously, while others such as ferrobielastic quartz, are higher order primary effects in which the energy difference between domain states is proportional to the square of the applied stress.

PARTICLE SIZE EFFECTS

It is anticipated that many ferroic materials undergo changes in the phase transformations as the particle size is reduced. While ferromagnetic materials are still by far the best studied, new experimental evidence is accumulating that small ferroelastic, ferroelectric and secondary ferroic particles will show similar behavior.

When prepared as large grain size ceramics (typically microns or larger), ferroelectric and ferromagnetic oxides exhibit complex domain structures, often with several different types of domain walls. As the grain size is reduced, however, the surface area grows in comparison with volume and it becomes increasingly difficult to recover the wall energy from the volume term. Consequently, the number of domains decreases as first one and then the other types of walls are eliminated. The transition from polydomain to single domain behavior is well-documented in a number of ferromagnets, occurring near 30 nm for many spherical metallic particles. For example, pure iron suspended in mercury shows a critical size for conversion to single domain behavior at ~23 nm and $Fe_{0.4}Co_{0.6}$ a critical size of ~28 nm (2). This is in good agreement with calculations by Kittel, who suggested a 20 nm minimum size for the appearance of ferromagnetism in particles (3). Results for acicular agglomerates of γ-Fe_2O_3 particles separated by non-magnetic grain boundaries are also consistent with these estimates: Berkowitz et al. (4) report that the stable single domain range at room temperature is centered at ~40 nm.

Studies on $BaTiO_3$ ceramics (which contain ferroelectric 180° walls and 90° walls which are both ferroelectric and ferroelastic) also show fewer 90° domains in small-grained samples than are observed for large grain sizes (5-7). An intermediate regime, centered at a grain size of 0.7 mm, with an increased density of small 90° domains has also been reported by Arlt et al. (8,9). Explanation for the changes in the equilibrium number of domains as a function of grain size (and in particular the effect of this on

the dielectric properties) is complicated by the fact that in a ceramic where individual grains do not possess cubic symmetry, each grain is subjected to a complex set of stresses which arise when the body is cooled through the transition temperature after firing (7). Because 90° walls are ferroelastic as well as ferroelectric, large stresses should be expected to greatly affect the number and type of domains.

For free $BaTiO_3$ powders, however, the boundary conditions on each particle are much simpler than those existing in a ceramic. Consequently, the changes in properties as the particle size is decreased are expected to follow the magnetic analog more closely. As far as we are aware, however, critical sizes for the disappearance of 90° domains and the transition to single domain in unconstrained ferroelectric powders have not been reported in the literature.

At still smaller sizes, ferroic particles undergo a phase change to the high temperature symmetry group and sometimes show the enhanced responsiveness characteristic of a superparamagnetic, superparaelectric, or superparaelastic solid. For example, iron exhibits superparamagnetic behavior at particle sizes near 7 nm, (2), γ-Fe_2O_3 at about 30 nm (4) and $BaFe_{12-2x}Ti_xCo_xO_{19}$ at 15 - 35 nm depending on the stoichiometry and the degree of particle shape anisotropy (10). This state is characterized by a zero net magnetization, the disappearance of a magnetic hysteresis loop, and extremely high magnetic susceptibilities. These properties can be explained by assuming that the sample behaves as an unmagnetized but highly orientable single domain. Fine particle magnets are used in high frequency transformers where eddy current losses are a problem.

Although the transitions from polydomain to 180° domains and thence to single domain are not well documented for ferroelectrics, an electric analog to superparamagnetism may be found in the family of relaxor ferroelectrics (11). Compositions including many of the $A(B'_{1/2}.B''_{1/2})O_3$ and $A(B'_{2/3}.B''_{1/3})O_3$ perovskites exhibit microdomains (typically 20 - 300Å in size) of 1:1 ordering on the B sublattice dispersed in a disordered matrix (12,13). It has been suggested that as a result of this local nonstoichiometry the spontaneous polarization in these materials is also disordered on a very fine scale (14). Thus a lead magnesium niobate ceramic can be regarded as a collection of disordered, but highly orientable, dipoles. The result, much like the case of superparamagnetism, is a high dielectric permittivity over a broad temperature range even though the net spontaneous polarization is zero.

Once the ordered microdomains in a relaxor grow beyond a certain size, however, the material reverts to ordinary ferroelectric (or antiferroelectric) behavior with a well defined transition temperature and a non-dispersive dielectric response. For lead indium niobate the critical domain size at which antiferroelectric ordering appears is 80 nm (12). This size may also serve as a guideline for the dimension at which a ferroelectric particle might be expected to show superparaelectric behavior.

As yet, direct observations of superparaelectric behavior in particulate ordinary ferroelectrics has not been documented. Recently, however, many investigators have attempted to determine the critical size for reversion to the high temperature prototype symmetry. Their results indicate that unconstrained $BaTiO_3$ particles show the transition to cubic at room temperature near 1200Å (15,16) whereas $PbTiO_3$ is stable in the tetragonal form to ~20 nm (17-18). However, it should be noted that it is possible to shift the observed critical size with changes in the preparation. Residual strain in particular has been shown to drastically affect the properties of $BaTiO_3$ (19, 20). Thus it is not surprising that milled $BaTiO_3$ powders with an average radius of ~10 nm have been shown to possess permanent dipole moments (21).

Saegusa et al. examined the solid solution between $BaTiO_3$ and $PbTiO_3$ to determine the critical size for stabilization of the cubic phase at room temperature as a function of composition. Assuming that crystallinity and stoichiometry were maintained for the smallest sizes, their data suggests that the critical size is not a linear function of composition. Thus, at a 1:1 Ba:Ti ratio, the ferroelectric phase was stable at least to 40 nm (16). It would be tremendously interesting to follow the magnitude of the polarization as a function of temperature in such powders to see how

its magnitude is affected by the particle size. As research of this type is pursued, it may be possible that a transition to superparaelectric behavior will be observed at still smaller sizes.

We are not aware of any reports in the literature on superparaelasticity in ceramic compositions. However, this field is potentially interesting as it holds the promise of imparting large elastic compliance to ceramics and other brittle materials.

Because ferromagnetism is a cooperative phenomenon, it is intuitively appealing to suppose that the system will be forced to revert to paramagnetic at some size at which there are simply too few atoms to sustain the cooperative interactions. Thus, at still smaller sizes, approaching atomic dimensions, superparamagnetism reverts to ordinary paramagnetism in which the magnetic susceptibility follows a Curie law with temperature. Analogous behavior is not documented for ferroelectric or ferroelastic solids.

In summary, then, we expect four regions in the size dependence of ferroic properties (Fig. 1). In large crystallites, multidomain effects accompanied by hysteresis take place. Reductions in size lead to single domain particles, and at yet smaller sizes to destabilized ferroics with large property coefficients, and finally to normal behavior as the particle size approaches the atomic scale. Similar transitions with size are expected in secondary ferroics.

Figure 1. Transitions in ferroic behavior as a function of size

SMART AND VERY SMART MATERIALS

Much of the recent interest in nanoscale size effects stems from the desire to build "smart materials" for intelligent systems, utilizing nonlinear physical phenomena. The words "smart materials" have different meanings for different people, and can be smart in either a passive sense or an active sense. Passively smart materials incorporate self-repair mechanisms or stand-by phenomena which enable the material to withstand sudden changes in the surroundings.

Ceramic varistors and PTC thermistors [22] are passively smart materials. When struck by lightning or otherwise subjected to high voltage, a zinc oxide varistor loses its electrical resistance and the current is bypassed to ground. The resistance change is reversible and acts as a stand-by protection phenomenon. Barium titanate

PTC thermistors show a large increase in electrical resistance at the ferroelectric phase transformation near 130°C. The jump in resistance enables the thermistor to arrest current surges, again acting as a protection element. The R(V) behavior of the varistor and the R(T) behavior of the PTC thermistor are both highly nonlinear effects which act as standby protection phenomena, and make the ceramics smart in a passive mode.

A smart ceramic can also be defined with reference to sensing and actuating functions, in analogy to the human body. A smart ceramic senses a change in the environment, and using a feedback system, makes a useful response (23). It is both a sensor and an acutator. Examples include vibration damping systems for space structures and energy-saving windows for homes and factories. The new electronically-controlled automobile suspension systems using piezoelectric ceramic sensors and actuators constitutes an actively smart material.

By building in a learning function, the definition can be extended to a higher level of intelligence: A very smart ceramic senses a change in the environment and responds by changing one or more of its property coefficients. Such a material can tune its sensor and actuator functions in time and space to optimize behavior. The distinction between smart and very smart materials is essentially one between linear and nonlinear properties. The physical properties of nonlinear materials can be adjusted by bias fields or forces to control response.

TUNABLE TRANSDUCER

To illustrate the concept of a very smart material, we describe the tunable transducer recently developed in our laboratory (24). Electromechanical transducers are used as fish finders, gas igniters, ink jets, micropositioners, biomedical scanners, piezoelectric transformers and filters, accelerometers, and motors.

Four important properties of a transducer are the resonant frequency f, the acoustic impedance Z_A, the mechanical damping coefficient Q, the electromechanical coupling factor k, and the electrical impedance Zg. The resonant frequency and acoustic impedance are controlled by the elastic constants and density, as discussed in the next section. The mechanical Q is governed by the damping coefficient and is important because it controls "ringing" in the transducer. Electromechanical coupling coefficients are controlled by the piezoelectric coefficient which, in turn, can be controlled and fine-tuned using relaxor ferroelectrics with large electrostrictive effects. The dielectric "constant" of relaxor ferroelectrics depends markedly on DC bias fields, allowing the electrical impedance to be tuned over a wide range as well. In the following sections we describe the nature of nonlinearity and how it controls the properties of a tunable transducer.

ELASTIC NONLINEARITY: TUNING THE RESONANT FREQUENCY

Information is transmitted on electromagnetic waves in two ways: amplitude modulation (AM) and frequency modulation (FM). There are a number of advantages to FM signal processing, especially where lower noise levels are important.

Signal-to-noise ratios are also important in the ultrasonic systems used in biomedical and nondestructive testing systems, but FM-modulation is difficult because resonant frequencies are controlled by stiffness (c) and sample dimensions (t):

$$f = \frac{1}{2t}\sqrt{c/\rho}$$

Neither c, t, or the density ρ can be tuned significantly in most materials, but rubber is an exception. To tune the resonant frequency of a piezoelectric transducer, we have designed and built a composite transducer incorporating thin rubber layers exhibiting nonlinear elasticity.

Rubber is a highly nonlinear elastic medium. In the unstressed compliant state, the molecules are coiled and tangled, but under stress the molecules align and the material stiffens noticeably. Experiments carried out on rubber-metal laminates demonstrate the size of the nonlinearity. Young's modulus ($E = 1/s_{1111}$) was measured for a multilayer laminate consisting of alternating steel shim and soft rubber layers each 0.1 mm thick. Under compressive stresses of 200 MN/m^2, the stiffness is quadrupled from about 600 to 2400 MN/m^2. The resonant frequency f is therefore double, and can be modulated by applied stress (25).

Rubber, like most elastomers, is not piezoelectric. To take advantage of the elastic nonlinearity, it is therefore necessary to construct a composite transducer consisting of a piezoelectric ceramic (PZT) transducer, thin rubber layers, and metal head and tail masses, all held together by a stress bolt.

The resonant frequency and mechanical Q of such a triple sandwich structure was measured as a function of stress bias. Stresses ranged from 20 to 100 MPa in the experiments. Under these conditions the radial resonant frequency changed from 19 to 37 kHz, approximately doubling in frequency as predicted from the elastic nonlinearity. At the same time the mechanical Q increases from about 11 to 34 as the rubber stiffens under stress (25).

The changes in resonance and Q can be modeled with an equivalent circuit in which the compliance of the thin, rubber layers are represented as capacitors coupling together the larger masses (represented as inductors) of the PZT transducer and the metal head and tail masses. Under low stress bias, the rubber is very compliant and effectively isolates the PZT transducer from the head and tail masses. At very high stress, the rubber stiffens and tightly couples the metal end pieces to the resonating PZT ceramic. For intermediate stresses the rubber acts as an impedance transformer giving parallel resonance of the PZT - rubber - metal -radiation load.

It is interesting to compare the change in frequency of the tunable transducer with the transceiver systems used in the biological world. The biosonar system of the flying bat is similar in frequency and tunability to our tunable transducer. The bat emits chirps at 30 kHz and listens for the return signal to locate flying insects. To help it differentiate the return signal from the outgoing chirp, and to help in timing the echo, the bat puts an FM signature on the pulse. This causes the resonant frequency to decrease from 30 to 20 kHz near the end of each chirp. Return signals from the insect target are detected in the ears of the bat where neural cavities tuned to this frequency range measure the time delay and flutter needed to locate and identify its prey. Extension of the bat biosonar principle to automotive, industrial, medical and entertainment systems is readily apparent.

PIEZOELECTRIC NONLINEARITY: TUNING THE ELECTROMECHANICAL COUPLING COEFFICIENT

The difference between a smart and a very smart material can be illustrated with piezoelectric and electrostrictive ceramics. PZT (lead zirconate titanate) is a piezoelectric ceramic in which the ferroelectric domains are aligned in a poling field. Strain is linearly proportional to electric field in a piezoelectric material which means that the piezoelectric coefficient is a constant and cannot be electrically tuned with a bias field. Nevertheless it is a smart material because it can be used both as a sensor and an actuator.

PMN (lead magnesium niobate) is not piezoelectric at room temperature because its Curie temperature lies near O°C. Because of the proximity of the ferroelectric phase transformation, and because of its diffuse nature, PMN ceramics exhibit very large electrostrictive effects. The nature of this large nonlinear relationship between strain and electric field, and of its underlying atomistic origin, has already been discussed in terms of a nanoscale ordering phenomenon (26).

Electromechanical strains comparable to PZT can be obtained with electrostrictive ceramics like PMN, and without the troubling hysteretic behavior

shown by PZT under high fields. The nonlinear relation between strain and electric field in electrostrictive transducers can be used to tune the piezoelectric coefficient and the dielectric constant.

The piezoelectric d_{33} coefficient is the slope of the strain-electric field curve when strain is measured in the same direction as the applied field. Its value for Pb $(Mg_{0.3}Nb_{0.6}Ti_{0.1})O_3$ ceramics is zero at zero field and increases to a maximum value of 1300 pC/N (about twice as large as PZT) under a bias field of 3.7 kV/cm (27).

This means that the electromechanical coupling coefficient can be tuned over a very wide range, changing the transducer from inactive to extremely active. The dielectric constant also depends on DC bias. The polarization saturates under high fields causing decreases of 100% or more in the capacitance. In this way the electrical impedance can be controlled as well.

ORIGINS OF NONLINEARITY

What do nonlinear materials have in common? The passively-smart PTC thermistor and ZnO varistor described earlier have grain boundaries a few nm thick. These insulating barriers that can be obliterated by the polarization charge accompanying a ferroelectric phase transformation, or, in the case of the varistor, the insulating boundaries so thin they can be penetrated by quantum mechanical tunneling.

Small size is also key factor in the nonlinear behavior of semiconductors. The thin gate region in a transistor allows charge carriers to diffuse through unimpeded. The p-region in an n-p-n transistor is thin compared to the diffusion length in single crystal silicon. Similar size-related phenomena are observed in quantum well structures made from GaAs and $Ga_{1-x}Al_xAs$. Planar structures with nm-thick layers show channeling behavior of hot electrons in clear violation of Ohm's law. Current - voltage relationships are highly nonlinear in many submicron semiconductor structures. Ohm's law is a statistical law which relies upon the assumption that the charge carriers make a sufficiently large number of collisions to enable them to reach a terminal velocity characteristic of the material. When the size of the conduction path is sufficiently small, compared to the mean free path between collisions, the statistical assumption breaks down, and Ohm's law is violated.

Nonlinear behavior is also observed in thin film insulators where even a modest voltage of 1-10 volts can result in huge electric fields of 100 MV/m or more. This means that thin film dielectrics experience a far larger field than do normal insulators, and causing the polarization to saturate and electric permittivity to decline. Because of the high fields, electric breakdown becomes a greater hazard, but this is partly counteracted by an increase in breakdown strength with decreasing thickness. This comes about because the electrode equipotential surfaces on a thin film dielectric are extremely close together, thereby eliminating the asperities that lead to field concentration and breakdown.

The influence of nanometer-scale domains on the properties of relaxor ferroelectrics has already been made plain. Here the critical size parameter is the size of the polarization fluctuations arising from thermal motions near the broad ferroelectric phase transformation in PMN and similar oxides. The ordering of Mg and Nb ions in the octahedral site of the PMN structure results in a chemically inhomogeneous structure on a nm-scale, and this, in turn, influences the size of the polarization fluctuations. Tightly coupled dipoles within each Nb-rich portion of this self-assembling nanocomposite behave like a superparaelectric solid. The dipoles are strongly coupled to one another but not to the crystal lattice, and thus they reorient together under the influence of temperature or electric field. This in turn causes the large electric permittivities and large electrostrictive effects found in relaxor ferroelectrics.

The importance of nanometer-scale fluctuations and the instabilities associated with phase transformations is also apparent in the nonlinear elasticity of rubber and

other polymeric materials. The thermally-assisted movement of the randomly oriented polymer chains under tensional stress results in large compliance coefficients, but rubber gradually stiffens as the chains align with the stress into pseudo-crystalline regions. The increase in stiffness with stress gives rise to sizeable third order elastic constants in many amorphous polymers. The effect depends markedly on temperature. On cooling, to lower temperatures rubber and other amorphous polymers transform from a compliant rubber-like material to a brittle glass-like phase which is of little use in nonlinear devices.

Nonlinear behavior is also observed in magnetic and optical systems. Superparamagnetic behavior, analogous to the superparaelectric behavior of relaxor ferroelectrics, is found in spin glasses, fine powder magnets, and magnetic cluster materials. As in PMN, the magnetic dipoles are strongly coupled to one another in nanometer-size complexes, but are not strongly coupled to the lattice. Superparamagnetic solids display nonlinear magnetic susceptibilities and unusual "ΔE" effects in which Young's modulus E can be controlled by magnetic field. The effect is especially large in metallic glasses made from Fe-Si-B-C alloys. The cluster size in spin glasses is in the nanometer range like those in PMN.

Lead lanthanum zirconate titanate (PLZT) perovskites can be prepared as transparent ceramics for electrooptic modulators. Quadratic nonlinear optic behavior are observed in pseudocubic regions of the phase diagram which show relaxor-like properties.

In summary, the nonlinear properties of materials are often associated with nanometer-scale structure and diffuse phase transformations. Under these circumstances the structure is poised on the verge of an instability and responds readily to external influences such as electric or magnetic fields, or mechanical stress.

The ready response of nonlinear ceramics allows the properties to be tuned in space or time to optimize the behavior of the sensor-actuator systems referred to by some as "very smart ceramics."

REFERENCES

1. R. E. Newnham, "Domains in minerals", Amer. Mineral. 59 906-918 (1974).
2. E.F. Kneller and F.E. Luborsky, "Particle size dependence of coercivity and remanence of xingle- domain particles," J. Appl. Phys. 34(3) 656-656 (1963).
3. C. Kittel, "Theory of the structure of ferromagnetic domains in films and small particles," Phys. Rev 70(11,12) 965-971 (1946).
4. A.E. Berkowitz, W.J. Schuele, and P.J. Flanders, "Influence of crystallite size on the magnetic properties of acicular γ-Fe$_2$O$_3$ Particles," J. Appl. Phys. 39(2) 1261-1263 (1968).
5. J.M. Herbert, Ceramic dielectrics and capacitors, Gordon and Breach Science Publishers, New York pp.126-167 (1985).
6. K. Kinoshita and A. Yamaji, "Grain-size effects on dielectric properties in barium titanate ceramics," J. Appl Phys. 47(1) 371-373 (1976).
7. R.C. Pohanka, R.W. Rice, and B.E. Walker, Jr., "Effect of internal stress on the strength of BaTiO$_3$," J. Am. Ceram. Soc. 59(1-2) 71-74 (1976).
8. G. Arlt, D. Hennings, and G. De With, "Dielectric Properties of fine-grained barium titanate ceramics," J. Appl. Phys. 58(4) 1619-1625 (1985).
9. D. Hennings, "Grain size and grain boundary effects in passive electronic components," from Surface and near surface chemistry of oxide materials. J. Nowotny and L.-C. Dufour, eds. Elsevier Science Publishers, Amsterdam (1988).
10. O. Kubo, T. Ido, H. Yokoyama, and Y. Koike, "Particle size effects on magnetic properties of BaFe$_{12-2x}$Ti$_x$Co$_x$O$_{19}$ fine particles," J. Appl. Phys. 57(1) 4280-4282 (1985).
11. L.E. Cross "Relaxor ferroelectrics," Ferroelectrics 76(3-4) 241-267 (1987).

12. C.A. Randall, D.J. Barber, P. Groves, and R.W. Whatmore. "TEM study of the disorder-order perovskite, $Pb(In_{1/2}Nb_{1/2})O_3$." J. Mat. Sci. 23(10) 3678 - 3682 (1988).

13. J. Chen, H. M. Chan, and M.P. Harmer, "Ordering structure and dielectric properties of undoped and La/Na-doped $Pb(Mg_{1/3}Nb_{2/3})O_3$." J. Am. Ceram. Soc. 72(4) 593-96 (1989).

14. G.A. Smolensky, "Physical phenomena in ferroelectrics with diffused phase transition." J. Phys. Soc. Jpn 28 suppl. 26-37 (1970).

15. K. Uchino, E. Sadanaga, K. Oonishi, T. Morohashi, and H. Yamamura, "Particle/grain size dependence of ferroelectricity," Proceedings of the 91st Annual Meeting of the American Ceramic Society, (1989).

16. K. Saegusa, W. E. Rhine and H. K. Bowen, "Preparation of $Pb_xBa_{1-x}TiO_3$ and the effect of the composition and the size of the crystallite on the crystal phase," Proceedings of the 1989 American Ceramic Society Meeting.

17. K. Ishikawa, K. Yoshikawa and N. Okada, "Size effect on the ferroelectric phase transition in $PbTiO_3$ ultrafine particles," Phys. Rev. B37(10) 5852-5855 (1988).

18. M. Lee, A. Halliyal, and R. E. Newnham, "Poling Studies of Piezoelectric Composites Prepared by Coprecipitated $PbTiO_3$ Powder," Ferroelectrics 87 71-80 (1988).

19. E.H. Bogardus and R. Roy, "Effects of strain induced by pressing and grinding $BaTiO_3$ and SiO_2," J. Am. Ceram. Soc. 48 205 (1965).

20. S. Jyomura, I. Matsuyama, and G. Toda, "Effects of the lapped surface layers on the dielectric properties of ferroelectric ceramics," J. Appl. Phys. 51(11) 5838-5844 (1980).

21. R. Bachmann and K. Barner, "Stable suspensions of ferroelectric $BaTiO_3$ particles," Sol. State Comm. 68(9) 865-869 (1988).

22. A.J. Moulson and J.M. Herbert, Electroceramics, Chapman and Hall Publishers, London, pp. 117-180 (1992).

23. R.E. Newnham and G.R. Ruschau, "Smart electroceramics", J. Amer. Ceram. Soc. 74 (3) 463-480 (1991).

24. R.E. Newnham, "Tunable transducers: nonlinear phenomena in electroceramics", N.I.S.T. Special Publication 804. Chemistry of Electronic Materials, pp. 39-52 (1991).

25. M. Blaszkiewicz, Tunable Transducers, Ph.D. Thesis in Materials, Pennsylvania State University, 1992.

26. V. Sundar and R.E. Newnham, "Electrostriction and polarization", Ferroelectrics 135, pp. 431-446 (1992).

27. K. Uchino, S. Nomura, L.E. Cross and R.E. Newnham, "Electrostriction in perovskite crystals and its applications to transducers", J. Phys. Soc. Japan 49B, pp. 45-48 (1980.)

APPENDIX 5

RELAXOR FERROELECTRICS: USEFUL ELECTRONIC NANOCOMPOSITE STRUCTURES

L. ERIC CROSS
Materials Research Laboratory, The Pennsylvania State University, University Park, PA 16802-4800 USA.

Abstract The paper will discuss the current status of understanding of the ferroelectric relaxors which are a sub group of the larger family of ferroelectrics with diffuse phase transitions. In the lead magnesium niobate (PMN) and lead scandium tantalate (PST) systems limited B site cation ordering appears to break the long range translational symmetry giving rise to the glass like behavior associated with the freeze out of polar fluctuations. In PMN and PST of major interest is the extent to which the spin glass models can describe the full range of elasto dielectric properties.

In the lead lanthanum zirconate titanate (PLZT) family the symmetry breaking phenomenon is not so clear and new work on the break up of conventional ferroelectricity in the lead lanthanum titanate (PLT) system will be discussed. A wide range of tungsten bronze family materials also exhibit relaxor ferroelectric behavior with unusual freezing behavior and switching capability.

In practical application the use of relaxor compositions in capacitor and electrostrictive actuator systems will be highlighted. New used in surface deformable mirrors and in a tilt mirror corrector for the Hubble Space Telescope will be presented.

INTRODUCTION

It is perhaps useful to begin the discussion of the interesting sub group of relaxor ferroelectrics by considering in a more general way the nature of the Curie point transition which heralds the onset of proper ferroelectric behavior. In figure 1a is illustrated first the behavior in a rather perfect single crystal which goes through an abrupt second order phase transition into the ferroelectric phase. Above T_c, the permittivity follows a Curie Weiss law $\varepsilon^1 = C(T - T_c)^{-1}$, at T_c there is an abrupt but continuous onset of spontaneous polarization which evolves into the domain structure of the ferroelectric form. In some crystals the transition at T_c is first order, there is a finite maximum of ε at T_c and the Curie Weiss temperature θ in the relation $\varepsilon = C(T - \theta)^{-1}$ occurs some degrees below T_c e.g. 11°C in $BaTiO_3$. Again there is an abrupt loss of polarization at T_c now in a discontinuous step but ε_{max} and $Ps \to O$ occur at the same temperature T_c.

For many practical applications it is desired to use the very large property maxima in the vicinity of the ferroelectric phase transition, to move the transition into the temperature range of interest and to broaden and diffuse the very large sharp peak values. In solid solution systems this is accomplished by trimming the mean composition to move the Curie point and at the same time

making the sample (often a ceramic) deliberately inhomogeneous. In these diffuse transition systems the dielectric maximum is now much 'rounder' and polarization persists for a short range of temperature above Tm (figure 1b). Almost all practical Z5U and Y5V capacitor dielectrics use such diffuse transitions.

In the relaxor ferroelectrics, three features of the dielectric response are qualitatively different. The transition is clearly diffuse and rounded, but the response is now markedly dispersive below T_m and T_m is a function of frequency (figure 1c). The response at weak fields above T_m is no longer Curie Weiss. In the polarization the RMS value persists to temperature (T_D) 200 to 300°C above T_m but the mean polarization $\bar{P}$ decays to zero at a temperature T_F which is well below T_m.

The weak field dielectric behavior for a typical relaxor ferroelectric in the perovskite structure family, lead magnesium niobate, is shown in more detail in figure 2a, taken from the pioneer work of Smolensky,[1] the dispersion over the frequency range 10 Hz to 10^7 Hz is clearly evident. That the material is ferroelectric is evident from figure 2b which traces the evolution of dielectric hysteresis under high field as a function of temperature. Unlike the sharp transition materials there are not abrupt changes and non linearity persists to temperature well above T_m. Perhaps the most puzzling feature is the absence of evidence for any macroscopic phase change below T_m either in the X-rays spectra, or the optical birefringence (figure 2c), yet clearly spontaneous polarization is impossible in cubic symmetry.

The original explanation offered by Bokov and Mylnikova[2] for this behavior was that the diffuseness was again due to heterogeneity, giving a range of Curie points, but that now the scale was very small and therefore below the resolution of X-ray and optical probes (figure 3a). Considering this model of nano-scale polar regions, it appeared probable to us that since the energy barriers to reorientation in any ferroelectric are linearly related to the volume, at these very fine scales the electrocrystalline anisotropy energy ΔHr might become comparable to kT leading to super-paraelectric behavior at higher temperature.
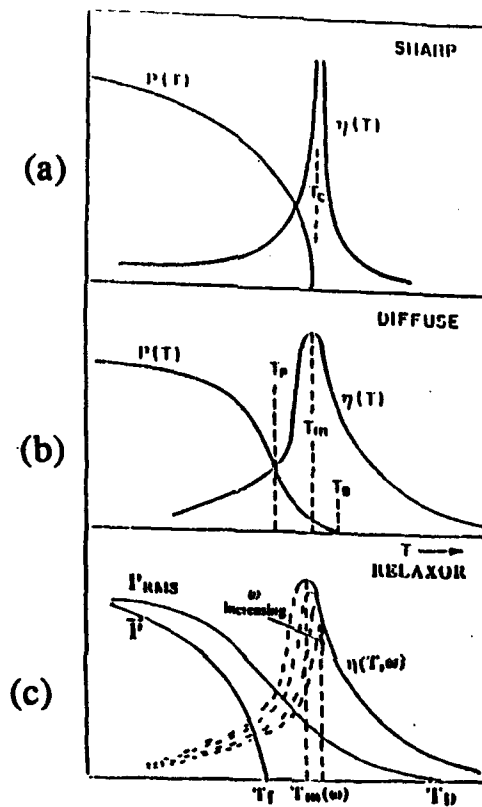
FIGURE 1   Types of Ferroelectric Phase Transitions
(a)   Simple proper ferroelectric:shape second order phase change in highly perfect single crystal.
(b)   Diffuse phase transition associated with macroscopic heterogeneity as in practical capacitor dielectrics.
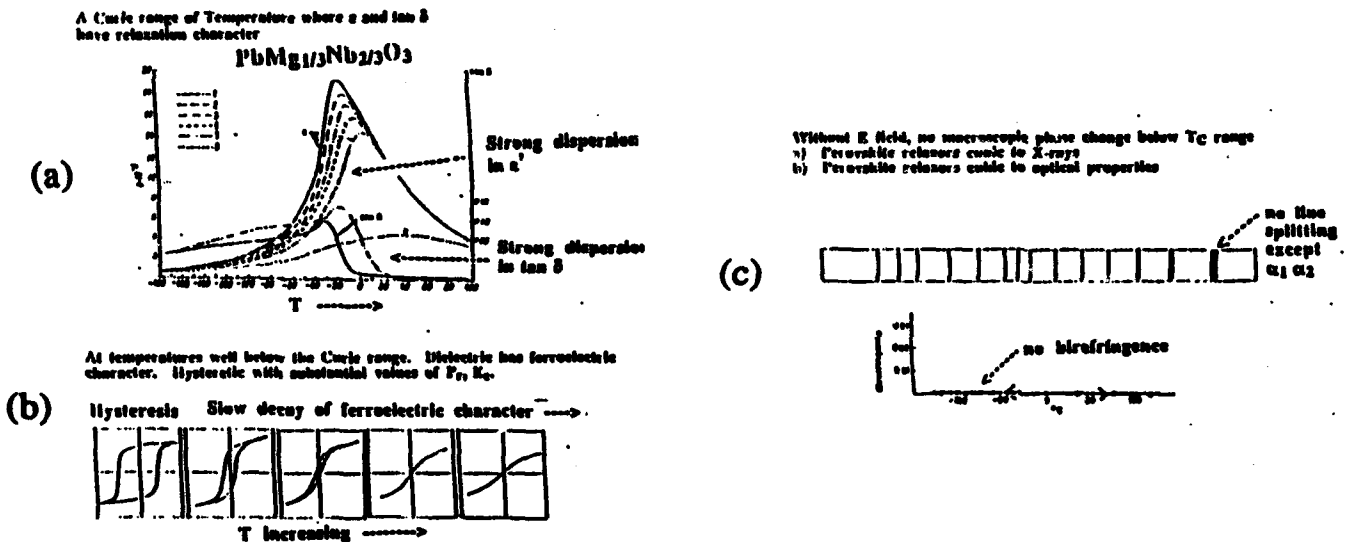(c)   Relaxor ferroelectric defining $T_m(\omega)$, T_D, T_F.

FIGURE 2 (a)   Dispersion around T_m is Lead Magnesium niobate PMN, a typical relaxor ferroelectric.
(b)   Slow decay of polarization with temperature.
(c)   Absence of a macroscopic symmetry change.

3

$Pb(Mg_{1/3}Nb_{2/3})O_3$
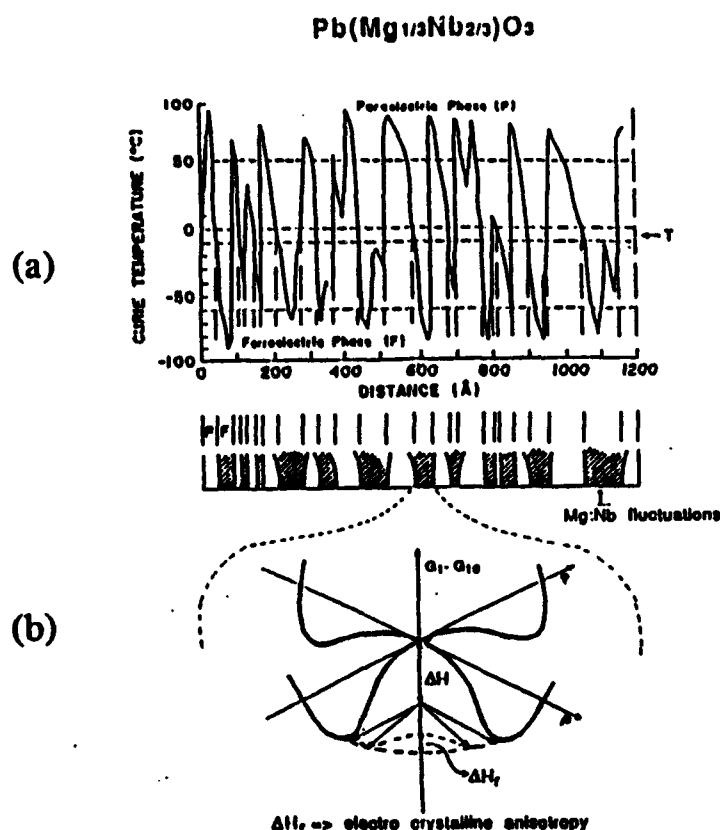
FIGURE 3 (a)   Suggested compositional heterogeneity model after Smolensky.
         (b)   Loss of stability with scale for very small micropolar regions.

A range of perovskite structure compounds with complex composition and a number of Tungsten bronze structure materials (Table I) show relaxor ferroelectric behavior. In perovskites the behavior occurs dominantly in lead based compositions and in both perovskites and bronzes there is always more than one type of ion occupying crystallographically equivalent sites.

For this brief review we will discuss first the origin of the symmetry breaking which occurs in the pre-cursors chemistry of these systems. It is reasonably well understood in $A(B_1B_2)O_3$ compositions but is less clear in the PLZTs and bronze family materials. Then the detail of the dielectric response which points towards a spin glass model for the freeze out of polar fluctuations as the origin of the dispersion will be considered. We then touch on some new evidence for unusual relaxor behavior in the low temperature polar phase of the tungsten bronze systems.

4

TABLE I Systems Which Exhibit Relaxor Ferroelectric Behavior

PEROVSKITES OF COMPLEX COMPOSITIONS

B-site complex	Lead magnesium niobate (PMN)	$PbMg_{1/3}Nb_{2/3}O_3$
	Lead scandium tantalate (PST)	$PbSc_{1/2}Ta_{1/2}O_3$
	Lead zinc niobate (PZN)	$PbZn_{1/2}Nb_{1/2}O_3$
	Lead indium niobate (PIN)	$PbIn_{1/2}Nb_{1/2}O_3$
A-site	Lead lanthanum zirconate titanate (PLZT)	$Pb_{1/x}La_{2x/3}TiO_3$
	Lead lanthanum titanate (PLT)	$Pb_{1-x}La_{2x/3}TiO_3$
Both sites complex	Potassium lead zinc niobate	$K_{1/3}Pb_{2/3}Zn_{2/9}Nb_{7/9}O_3$

TUNGSTEN BRONZE STRUCTURE COMPOSITIONS

| Strontium barium niobate (SBN) | $Sr_{1-x}Ba_xNb_2O_6$ |
| Lead barium niobate (PBN) | $Pb_{1-x}Ba_xNb_2O_6$ |

PERCURSON CHEMISTRY

In the lead based perovskite $A(B_1B_2)O_3$ relaxors it is clear from very extensive TEM studies[3,4,5] that in $Pb(Mg_{1/3}Nb_{2/3})O_3$ the origin of the nanoscale heterogeneity is in a strictly limited 1:1 non stoichiometric ordering of the Mg and Nb. A crude two dimensional picture is given in figure 4a showing the scale of the region's which are of the order 5 n meters. The dark field TEM image confirming the ordering and the scale is shown in figure 4b.

This 1:1 ordering must give rise to a significant charge imbalance and it has been suggested[6] that the developing electric field limits the scale. In $PbSc_{1/2}Ta_{1/2}O_3$ the ordering which is again 1:1 may be carried through to a highly ordered form by controlled thermal annealing, recovering full translational symmetry.[7] It is important to note that the nano scale ordered PST exhibits relaxor behavior whilst the highly ordered crystal shows a first order ferroelectric phase change.

Our picture of relaxor behavior in the $A(B_1B_2)O_3$ systems is suggested schematically in figure 5. Either complete disorder, or full long range order appears to give rise to normal ferroelectric behavior. It is the limited nano-scale ordering which appears to favor the development of small scale polar regions. The fascinating feature in the PMN type compounds is that the non stoichiometry inherent in the ordering process appears to make it a self limiting nano-composite which cannot be changed by

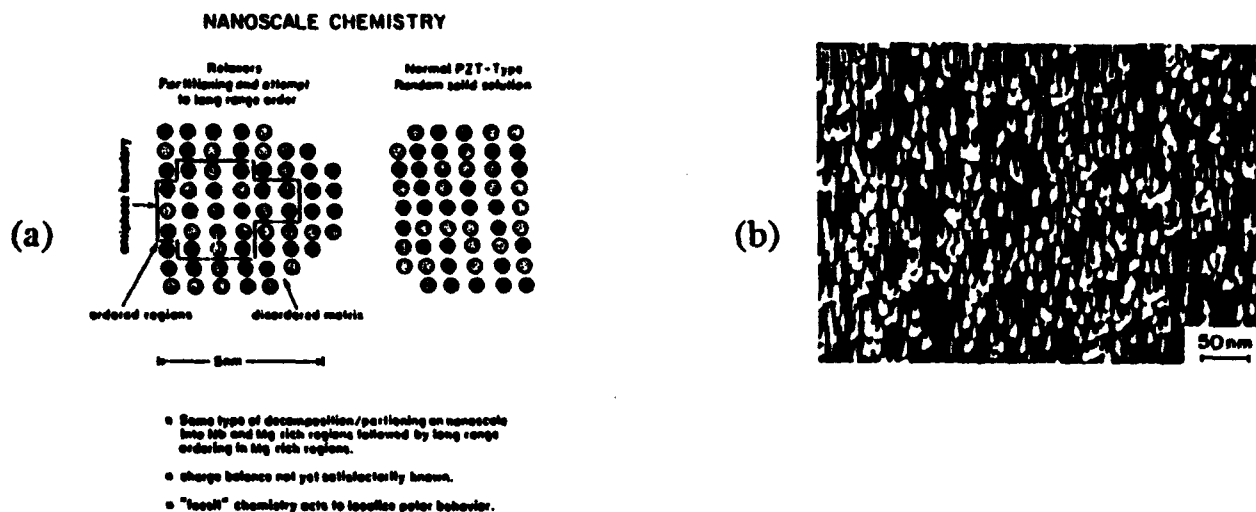NANOSCALE CHEMISTRY

(a)

(b)

FIGURE 4 (a)   Two dimensional sketch of observed 1:1 ordering of Mg:Nb cations in PMN.
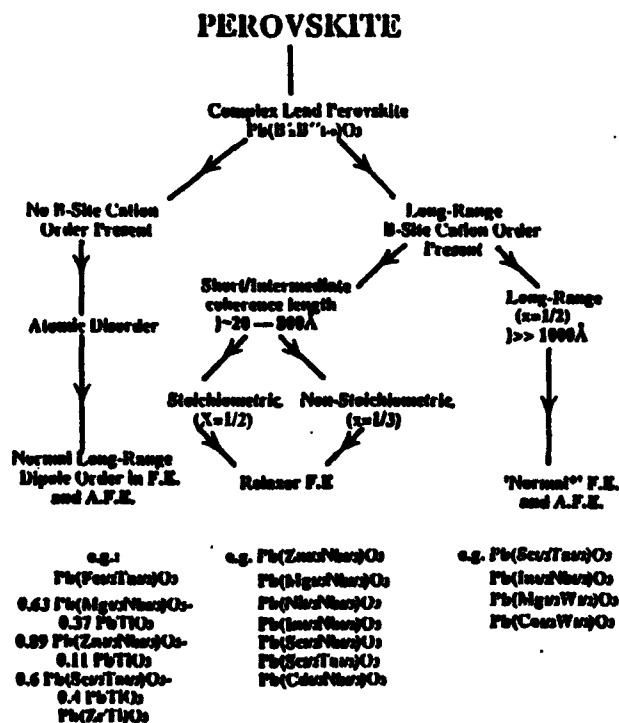   (b)   Dark field TEM and PMN showing the scale of the ordered regions.

FIGURE 5   Suggested dependence of relaxor behavior in perovskite $Pb(B_1B_2)O_3$
         compositions on limited $B_1:B_2$ ordering.

6

annealing. It should be emphasized that this is a most unusual nano-composite as the oxygen lattice is continuous and coherent through both ordered and disordered regions.

In the mixed A site relaxors such as the PLZTs with compositions along the 65:35 Zr:Ti mole ratio and Lanthanum concentration of more than 2 mole% (figure 6) the dielectric response is similar in many respects to the PMN system, however the symmetry breaking nanostructure is not so clear. Very careful TEM studies have revealed direct evidence of nano scale polar regions at low temperature[8] but the precursor chemistry which forces their formation is not yet clear. Very recently Rossetti[9] has explored the Lead lanthanum titanate system with high resolution X-ray techniques. It is clear that quite low levels of Lanthanum concentration rapidly reduce the strongly first order nature of the pure $PbTiO_3$ Curie point transition and begin to lead to a sub domain modulation of the magnitude of P_s in the domain, although there is no strong evidence for ordering of the lanthanum or the associated lead site vacancies at the higher concentrations. The necessary high defect concentration in the PLZT does however lead to an aging phenomenon[10] which modifies the relaxation response markedly making longer time measurements of response impossible to interpret unequivocally.

(a)

(b)
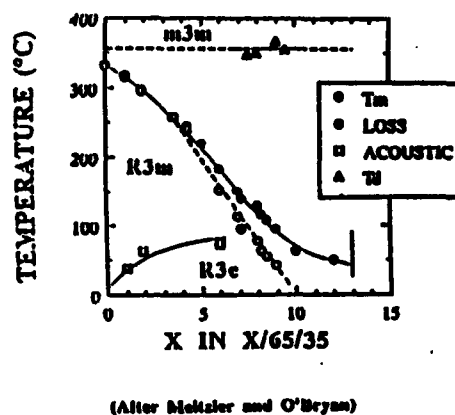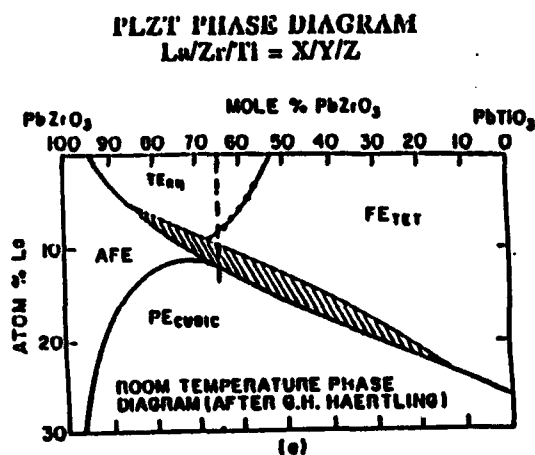
FIGURE 6 (a)   PLZT phase diagram showing the trace of the x:65:35 compositions studied.
         (b)   Evidence of the separation of T_m and T_d in these relaxor compositions.

7

In the tungsten bronze family, Barium strontium niobate $Ba_xSr_{1-x}Nb_2O_6$ is a prototypic relaxor here the structure is much more complex than the perovskite and more open. Again it is built on corner linked oxygen octahedra, but the sheet normal to the c axis of the tetragonal paraelectric form figure 7 is markedly crumpled. Here Nb ions occupy the centers of the oxygen octahedra, Ba ions the larger 5 fold channels and strontium are distributed between 4 fold and 5 fold channels. X-ray studies using the Rietveld method[11] suggest that Ba is always in the 5 fold channel but that annealing can change the Sr occupancy between 4 fold and 5 fold sites. Changing Sr occupancy has a marked effect upon the dielectric peak position T_m and it is suggested that variations in distribution throughout the crystal may be responsible for a wide distribution of local Curie points. It is interesting to note that the relaxation phenomenon becomes steadily stronger with increasing Sr concentration.

Much more work is however needed to pin down the symmetry breaking nonstructures in both the PLZTs and the bronze compositions.

Ferroelectric Tungsten Bronze Crystallographic Structure

$(A1)_2^{III}(A2)_4^{IV}(C)_4^{IX}(B1)_2^{VI}(B2)_8^{VI}O_{30}^{VI}$
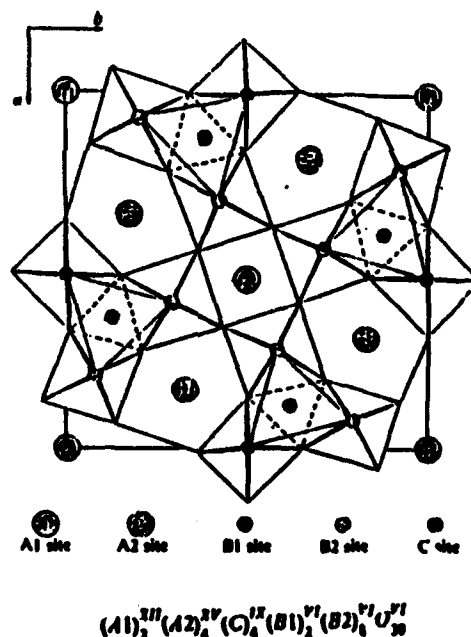
FIGURE 7   Projection of the Tungsten Bronze ferroelectric structure normal to the 4 fold c axis showing the sites for cation occupancy.

ELASTO-DIELECTRIC RESPONSE

Earlier studies have shown that the relaxor ferroelectric retain large values of RMS polarization to temperature some 100s of degrees above the dielectric maximum. In PMN, PLZT and SBN types measurement of lattice strain (thermal expansion) and optical refractive index[12,13,14] show very good agreement in the prediction of the decay of RMS polization. The question as to whether the residual polarization is static or dynamic has been more difficult to decide. Measurement of electrostriction in SBN above T_m strongly suggested the dynamical model,[15] but it is only very recently that careful neutron spectroscopy has completely confirmed the super-paraelectric behavior at higher temperature in PMN.

PMN-10PT AGE FREE

(a) χ'

$$\omega = \frac{1}{\tau} = \frac{1}{\tau_0} \exp\left[\frac{-B_a}{k(T-T_f)}\right]$$

activation energy of 0.0407 eV,

pre-exponential factor of 10^{12} Hz

freezing temperature of 291 K.

(b)

(c)

• Vogel-Fulcher type freezing of polar fluctuations.
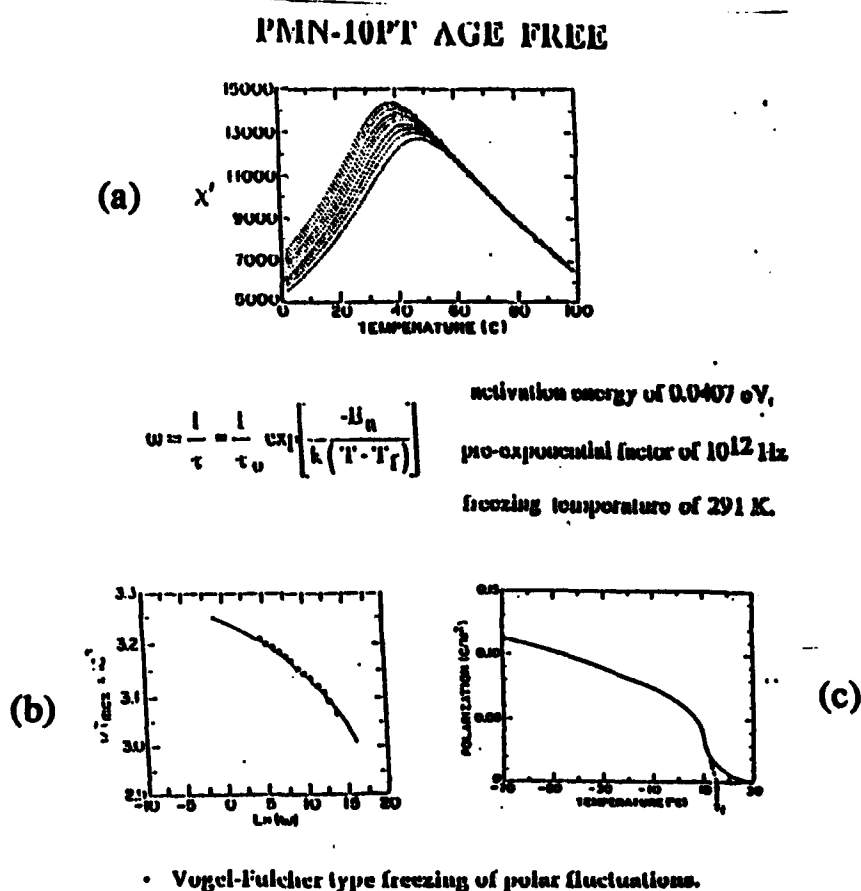
FIGURE 8 (a, b) Evidence for a glass like freezing of the dielectric response in PMN:PT solid solution lead in to Vogel:Fulcher type behavior with freezing temperature T_F.
(c) Field cooled poled sample show "thawing" temperature T_F.

9

A key feature of the dielectric response is the strong dispersion in the weak field permittivity. Studies by Viehland et al[16] have shown that the frequency/temperature characteristics are nicely described by the Vogel:Fulcher relation (figure 8a) and that the freezing temperature T_f deduced from this relation agrees closely with the thawing temperature where remanent polarization is lost on heating a field cooled sample (figure 8b). Vogel:Fulcher suggests a slowing down and freezing into a glass like ensemble of nano-domains, such a behavior would also suggest that the weakly cooperating nano-polar regions should begin to depart markedly from Debye like response towards a very long flat tail upon an ε^{11} corresponding to the freezing process and this is indeed observed (figure 9).[17]

For any precise dielectric studies it is essential to recognize and eliminate the aging process. As discussed earlier it is impossible to eliminate defects which couple to the polarization system in PLZT, since the La^{3+} doping necessitates that the sample have equivalent lead vacancies. In $Pb(Mg_{1/3}Nb_{2/3})O_3$ however the crystal is a compound, and if it is made with care from very high purity starting materials, macroscopic stoichiometry can be preserved in a fully stuffed structure. For this type of material aging can be eliminated (figure 10a), and the phenomenon can be reintroduced by a low level MnO doping. Figure 10b shows a MnO doped sample which has been aged at room temperature (20°C) then cooled to low temperature and reheated. Note the manner in which the relaxor response has been eliminated for all temperatures above the aging temperature, but is reintroduced at lower temperature. A full explanation is given in references 18 and 19 but is beyond the scope of this review. The data are emphasized however as it is clearly essential to 'uncouple' aging if time dependent properties of the relaxor are to be studied without gross perturbation.
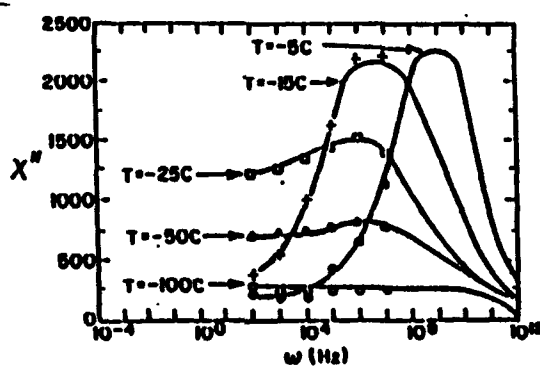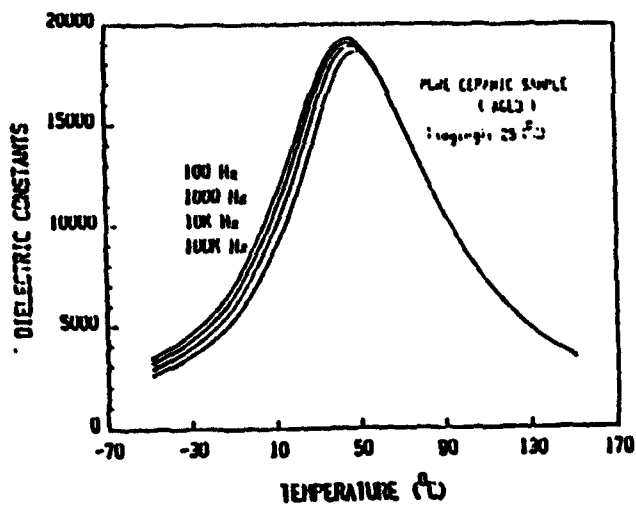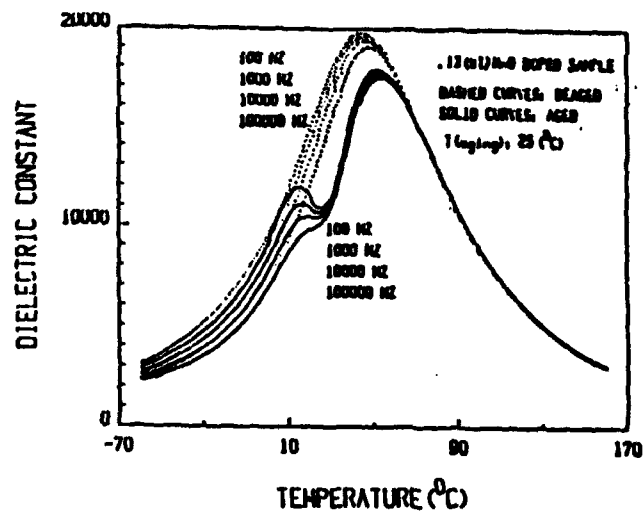

FIGURE 9   Glass like behavior of dielectric susceptibility x^{11}.

FIGURE 10 (a) "Clean" PMN:PT sample showing the absence of aging in ε^1 after 1,000 hours at room temperature.

(b) Aging behavior in PMN:PT reintroduced by low lever doping with MnO.

FIGURE 11 (a) Structure of nano-scale polar domains revealed in PLZT at the 8.2:65:35 composition by dark field TEM.

(b) Modification

To explore the high field response it is necessary to turn to the PLZTs and to take care to always study freshly de-aged samples. For an 8:2:70:30 PLZT composition Randall[20] has imaged using TEM the nano domain structure at low temperature (figure 11a) and by using charging from the beam current the evolution of nano-domains towards more normal continuous ferroelectric domains (figure 11b). Consequences of the application of static fields to PLZT samples which have been cooled in the zero field state have been explored by Yao Xi et al.[21] Typical curves of switch over to a macro polar state on heating under bias are shown in figure 12a,b. If the system behaves as a spin glass the switch over should be modeled by the deAlmeida-Thouless relation[22] and data taken from the measurements of Yao Xi et al are modeled in this manner in figures 13.[23]

In deducing the RMS polarization it was tacitly assumed that the polarization related electrostriction constants Q_{11}, Q_{12} are independent of temperature in fact his has been proven by direct measurement (figure 14).[24] Clearly then in this circumstance one must expect that all the dielectric (Polarization) behavior will be reflected into the elastic response. The close relation between elastic and dielectric responses is evident in figure 15. For the high field response, it is to be expected that the high polarization values which can be induced anhysterically near T_m will give rise to large elastic strains. Values of x_{33} the strain in the field direction for a PMN:PT solid solution are shown in figure 16. The slope of this curve at any point is the effective d constant (d_{33}) which goes to very large values at relatively modest E fields.[25]
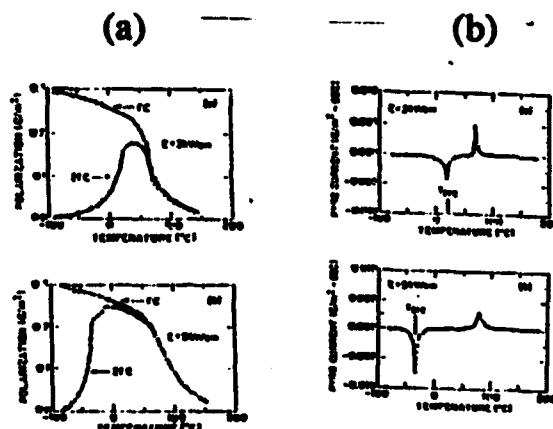

FIGURE 12 (a,b)   Polarization and depolarization of PLZT 8:65:35 under field cooled and zero field cooled conditions as determined by integration of the pyroelectric response.

$$u = A\left[\frac{T_f(0) - T_{zfc}(E)}{T_f(0)}\right]^{\frac{3}{2}}$$

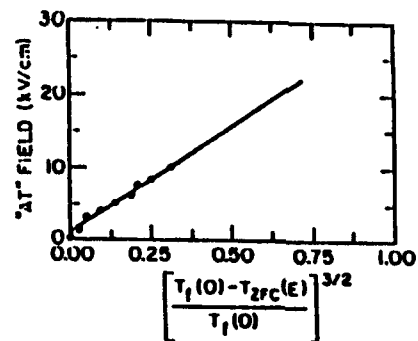deAlmeida-Thouless relationship

FIGURE 13 Data of 12(a) and similar studies at different field levels fitted to the deAlmedia-Thouless relation.
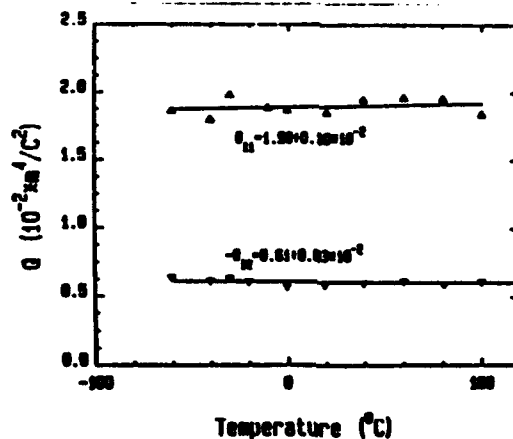

FIGURE 14 Ultradilatometer measurements of the electrostrictive constants Q_{11}, Q_{12} as a function of temperature in PMN:10 PT.
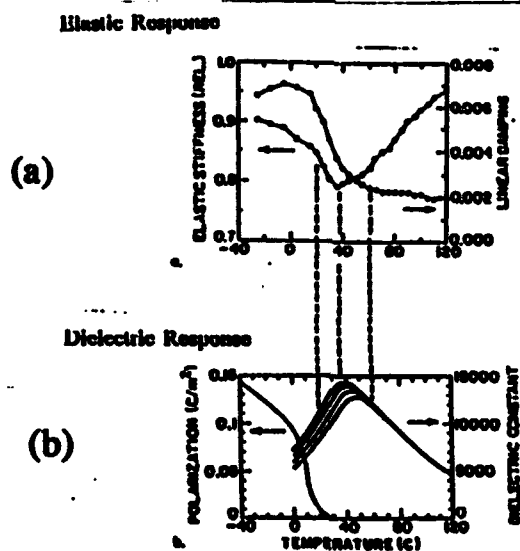

(a)

(b)

FIGURE 15 (a) Elastic stiffness and damping in ceramic PMN:10 PT.
(b) Comparison to dielectric softening associated with micro-polar behavior.

13
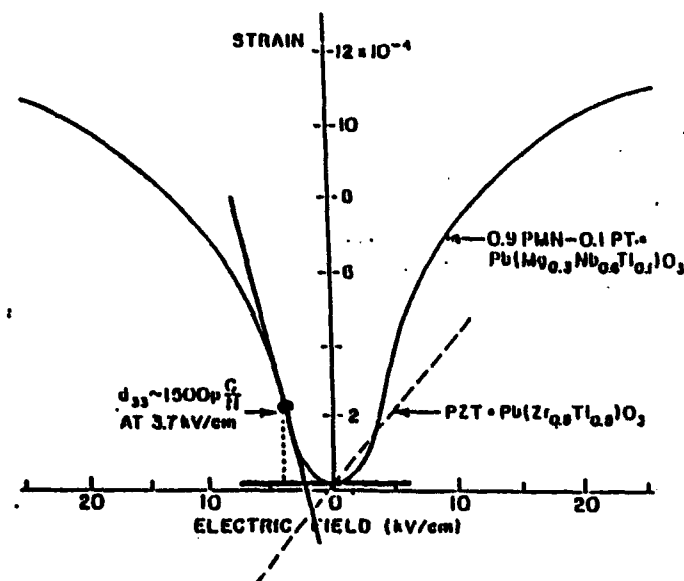
FIGURE 16 Strain vs. Field curve for PMN:10 PT illustrating the large values of induced piezoelectric d_{33} under DC field control.

TUNGSTEN BRONZE STRUCTURE RELAXOR FERROELECTRICS

In the solid solution system Sr Nb_2O_6:$BaNb_2O_6$ the end member compositions are not in the bronze structure, however in the range between $Sr_{0.8}Ba_{0.2}Nb_2O_6$ and $Sr_{0.3}Ba_{0.7}Nb_2O_6$ stable SBN bronzes form.[26] Across this range the prototypic structure is tetragonal and for fields in the 001 (c) axis direction the characteristics are these of a relaxor ferroelectric with polarization along (001). Both optical[27] and elastic[28] studies confirm that large values of RMS polarization persist to temperatures well above T_m and there is clear evidence of ferroelectric behavior at low temperature.[29] Dispersion near T_m becomes steadily more pronounced in compositions with increasing Strontium content.[30] For the congruently melting $Sr_{0.6}Ba_{0.4}Nb_2O_6$ excellent quality single crystals have been grown[31] and the crystal is widely used in photorefractive applications.[32]

The bronze system Lead barium niobate $Pb_{1-x}Ba_xNb_2O_6$ (PBN) is of special interest as in the vicinity of the $Pb_{0.6}Ba_{0.4}Nb_2O_6$ composition there is a pseudo morphotropic phase boundary between orthrhombic and tetragonal ferroelectric forms (figure 17).[33] For the tetragonal form at the 57:43 composition the permittivity for fields along (001) shows a transition with only very weak dispersion and large thermal hysteresis (figure 18a), however for fields along (100) there is now a pronounced dispersion at lower temperature (figure 18b).

In compositions on the orthorhombic side of the MPB again the upper transition exhibited for fields along 100 is reasonably sharp, however, now there is a lower temperature relaxation for field in the 001 c axis direction. There are no evidences of phase transitions in either crystal in the
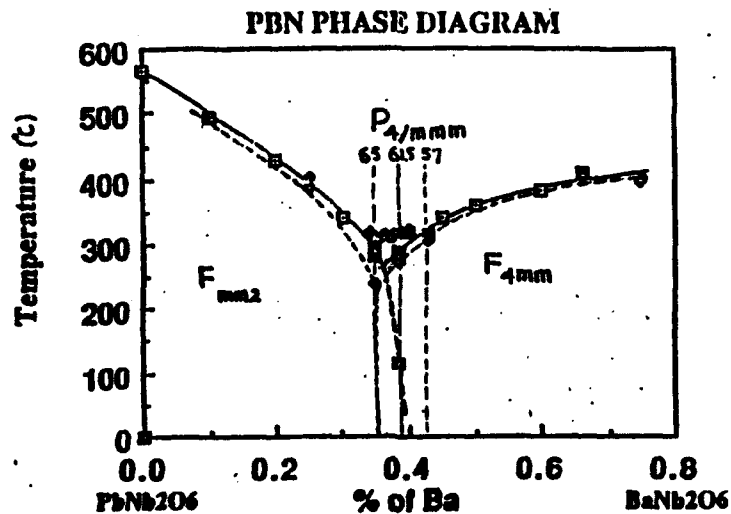
14

PBN PHASE DIAGRAM

FIGURE 17   Phase diagram for the lead niobate:barium niobate system (PBN) showing the pseudo-morphotorpic phase boundary near the 60:40 composition.

region of the dispersion, but cooling the crystal under a poling field orthogonal to the main polarization direction produces a clear remanence of order less than $1/20^{th}$ of the major polarization.[34] It is interesting to note that for compositions close to the MPB large orthogonal electric fields will switch the major component of P changing the symmetry from tetragonal to orthorhombic or vice versa. With symmetry change the lower frequency dispersion also changes axial direction always appearing normal to the major component of P.

Clearly at low temperature, the field forced symmetry must be truly monoclinic in each case, as the P_s is tilted away from the primary axis (4 fold or 2 fold). Our suggestion is that in each case the micro polar regions which make up the mean polarization have P_s vectors which are slightly tilted away from the major axis. At the higher temperature transitions the energy barriers against polarization inversion are large and the dispersion weak, however the tilts perpendicular to P are random and dynamical, freezing out at the lower temperature dispersion. Crudely the energies envisaged are shown schematically for the "orthorhombic" and "tetragonal" macro symmetries in figure 19. The situation could be envisaged as that of a spin glass with two freezing temperatures for the orthogonal components of P. Magnetic systems which exhibit such phenomena have been studies.[35]

15
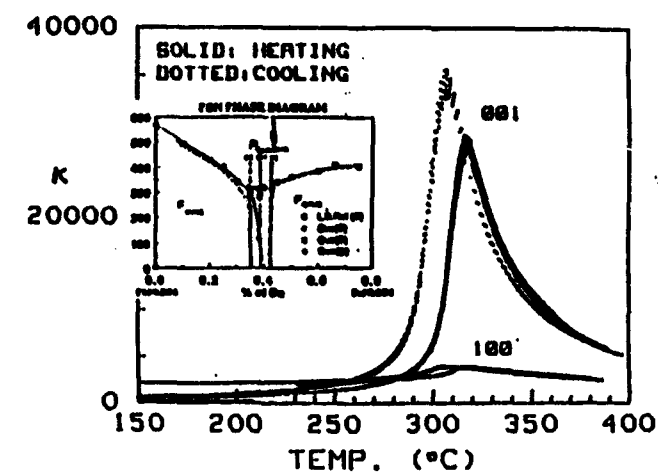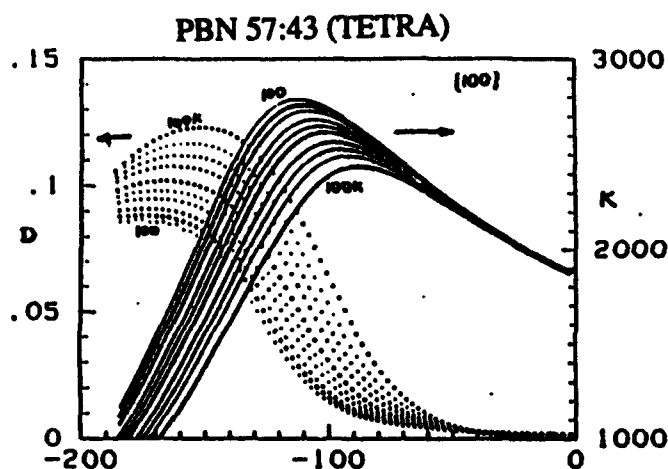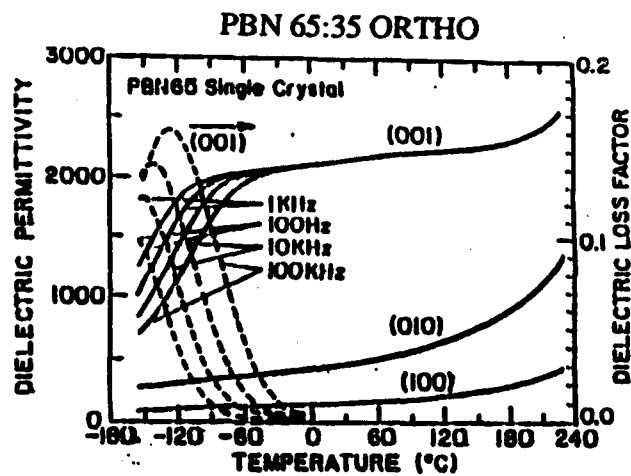
FIGURE 18 (a) Dielectric response for fields along 001 and 100 directions for a composition in the tetragonal ferroelectric phse field (57:43) of PBN.
(b) Low temperature dispersive dielectric response for fields orthogonal to the major polar direction
(c) Dielectric response at low temperature in the orthorhombic phase for dields along 001.
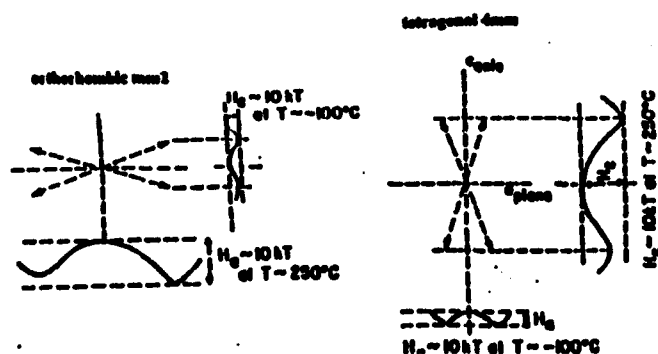

FIGURE 19 Proposed simple model for the anisotropic energetics of polar regions in the 'orthorhombic' and tetragonal relaxor phase fields of PBN.

16

THEORETICAL UNDERSTANDING

The relaxor ferroelectrics in the oxygen octahedron families are very complex solids so that it is certainly not surprising that in spite of some thirty years of continuous effort there is no comprehensive quantitative theory. It does appear that there is reasonably general agreement of the superparaelectric character at temperatures will above T_m but the detail of the kinetics of these regions and their mutual interaction as the temperature decreases is not clear.

An appealing simple model from A. Bell at EPFL[36] treats the micro region as a simple Devonshire ferroelectric, to calculate the activation energy ΔH as a function of size (assuming a simple spherical region). The distribution of activation energies then comes from a specific distribution of sizes, however to get good agreement with experiment (figure 20) it is still necessary to put in weak interaction between regions.

In a more general vein, Viehland et al have pointed up the many behavior features of the relaxors which suggest spin glass like features. Table II list many of these features, the small Y suggests a yes to the nature of the common feature in each case.

An alternative model which can again explain quatitatively most features of the relaxor appeals to random electric fields associated with the composition fluctuations as the origin of the break up of normal domain structure and the tremendous slowing down of the dynamics in PMN. For large non zero electric fields, it becomes difficult to explain the aging phenomena which occur in PLZT and in suitably doped PMN. For such crystals aging under a field as little as 3KV/cm is sufficient to wipe out the relaxation at room temperature and to lead to a poled ferroelectric structure on cooling under short circuit conditions. Evidently the kinetics is very sensitive to small fields generated by defect dipole systems. Perhaps a way out of this dilemma would be the suggestion that the random field is of elastic rather than electric origin.

Recent measurements of the poling of zero field cooled PMN does suggest[37] the presence of barkhausen pulses which could occur from the switching of ferroelectric micro-domains in concert with the random field model however it is not clear whether these measurements were carried out on aging free material.

In summary, many features of the chemo-elasto-dielectric behavior of relaxors are becoming more clear, even though there is not yet a comprehensive qualitative theory to explain the responses.

17

TABLE II   Comparative list of physical properties of relaxors to spin and orientational glasses.

PROPERTY	RELAXOR	SPIN GLASS
Dispersion of Susceptibility	Y	Y
Dispersion of Tmax	Y	Y
Freezing Temperature (Tf)	Y	Y
Imaginary Component Frequency Independent below Tf	Y	Y
Strong Nonlinear Response	Y	Y
Maximum Nonlinearities near Tf	Y	Y
Frustration	Y	Y
Susceptibility "Diffuse"	Y	Y
Deviations from Curie-Weiss Behavior	Y	Y
Analysis of Deviation for Local Order Parameter	Y	Y
Broadening of Relaxation Time Distribution on Cooling	Y	Y
Hysteresis, Irreversibility, and Remanence below Tf	Y	Y
Local polarization or magnetization	Y	Y
Local correlations between moments	Y	Y
Long range ordering in the Field Cooled State	Y	Y
Lack of anisotropy in the Zero Field Cooled State	Y	Y
De-Almeda Thouless Analysis	Y	Y
Polarization or Magnetization Viscosity	Y	Y
Chemical or Structural Inhomogeneity	Y	Y

18

PRACTICAL APPLICATION

One may judge the most likely areas of application for the relaxor ferroelectrics by considering the very unusual property combinations afforded in these systems. Table III outlines these properties. The very high dielectric permittivity is properly exploited in new multilayer ceramic capacitors. The very strong electrostrictive response does not depend on a domain contribution to the strain and is thus very largely reversible, a vital feature for precise actuators which cannot be servo controlled. The slope of the electrostrictive response as a function of field is the piezoelectric constant and d_{33} values much larger than those in conventional PZTs can be achieved under modest fields, giving a whole new family of potential agile transducers for sensing and actuation. Similarly under DC bias exceedingly large pyroelectric coefficients can be induced so for the bolometric long wavelength IR sensing and imaging the relaxors are of major interest.

In the following brief description we confine attention to just the capacitor and actuator potential. For capacitor dielectrics, three features of the lead based relaxors are exceedingly attractive.

TABLE III   Relaxor Properties which are of Interest for Practical Application.

PROPERTIES OF INTEREST

- **HIGH DIELECTRIC PERMITTIVITY.**
  Multilayer Ceramic Capacitors.
  Co-Fires with Copper Electrodes.

- **VERY STRONG ELECTROSTRICTION.**
  Multilayer Electrostrictive Actuators.
  Optical Telescope Adaptive Optics: Hubble Corrector.

- **SWITCHABLE PIEZOELECTRIC RESPONSE.**
  Agile Transducers for Electromedical Applications.

- **SWITCHABLE STRONG PYROELECTRICITY.**
  Long Wavelength Infra-red Pyroelectric Imaging Systems.

The dielectric permittivity for a typical PMN:10 PT relaxor (figure 20a) is significantly higher than equivalent Y5V type modified $BaTiO_3$ compositions. The loss level is also higher (figure 20b), but decays rapidly under bias field where MLC type capacitors are largely used. The bias behavior is also most attractive as the material retains high permittivity to higher fields than the

19
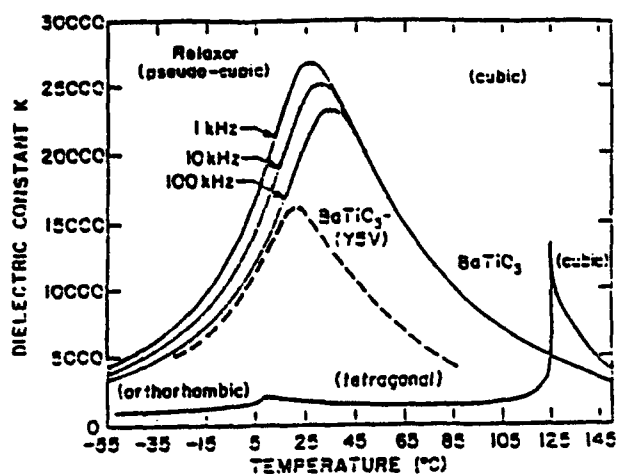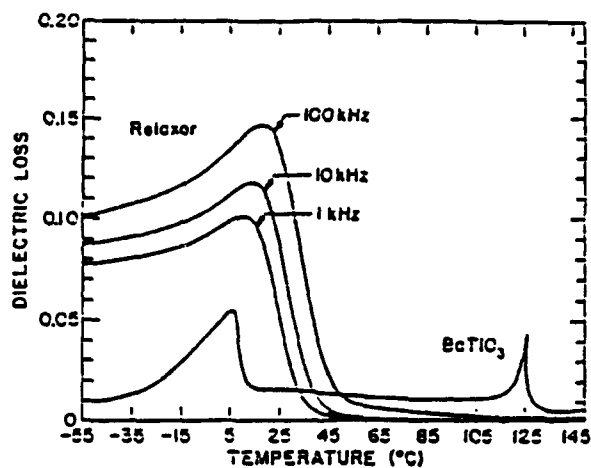
(a)   (b)

Relaxor: $(PbMg_{1/3}Nb_{2/3}O_3)_{0.9}(PbTiO_3)_{0.1}$

FIGURE 20 (a) Dielectric permittivity as function of temperature and frequency in relaxor
                $(PbMg_{1/3}Nb_{2/3}O_3)_{0.9}$ $(PbTiO_3)_{0.1}$ compared with a modified $BaTiO_3$ Y5V
                commercial composition and with pure $BaTiO_3$.
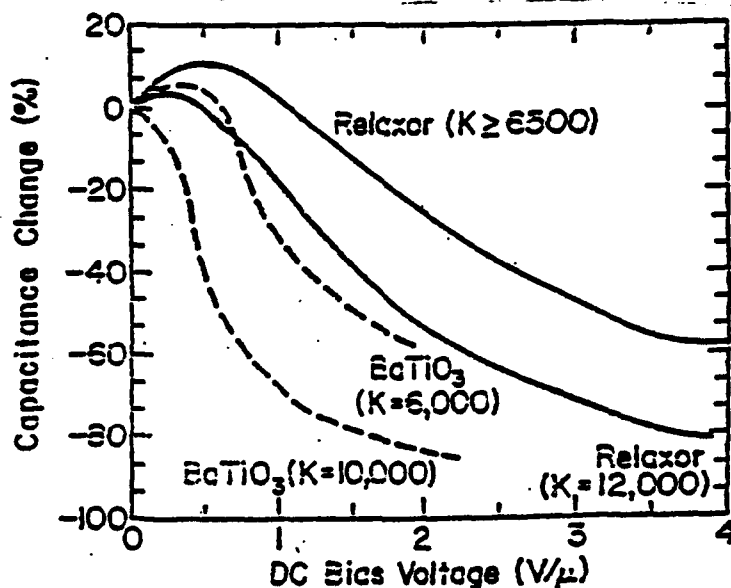   (b) Dielectric loss in PMN:PT compared to the loss in pure $BatiO_3$.

FIGURE 21   Dielectric saturation in the relaxor composition as compared to a $BaTiO_3$ based
            dielectric of similar permittivity.

conventional $BaTiO_3$ based materials (figure 21) and also the RC time constant is longer for the full
range of working temperatures (figures 22). A further signal advantage for the tape case
monomlitic MLC structures is that the PMN type compositions can be co-fired with copper
electrodes which is impossible with the $BaTiO_3$ based systems.
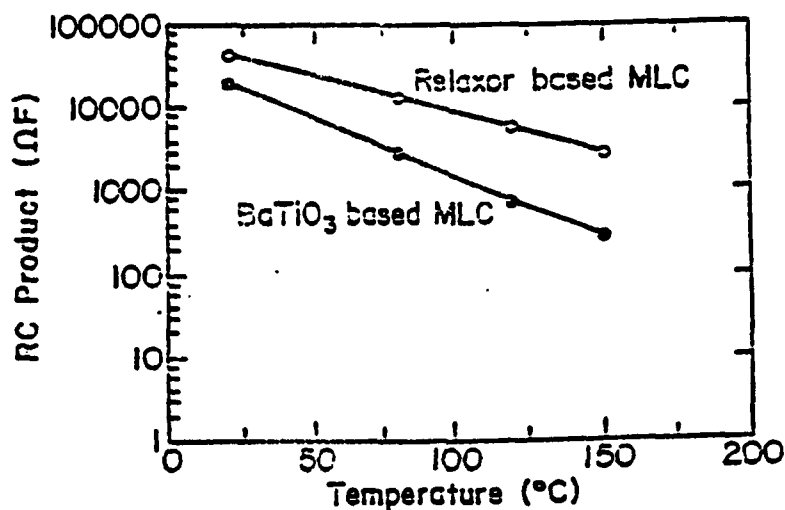
20

FIGURE 22   RC time constant as a function of temperature for the relaxor as compared to the
BaTiO₃ based dielectric.

It is thus not surprising that the World's major capacitor companies are exploring a very
wide range of these lead based relaxor compositions (Table IV).

In actuator application, the cardinal advantage of the PMN based relaxors is the very low
hysteresis which can be obtained in the strain:voltage characteristic (figures 23a) in comparison to
comparable soft PZT systems (figures 23b). A summary table fo commercial actuator performance
between PMN and PZT compositions is given in Table V. It is natural then to expect that
electrostrictive relaxor actuators will be of most value where precise positioning is required and
servo feedback control is not realizable. Such situations occur in a number of optical systems.
One such system of very high visibility is a corrector for the troubled Hubble Space Telescope.
This device is a tilt mirror (figure 24) which can be fully controlled from the ground by three PMN
actuators. The function of a mirror is to permit precise alignment of a new optical train in the wide
field camera which will contain elements configured to fully correct for the original improper figure
of the primary mirror. The actuators are small multilayer PMN:PT stacks, figure 25
 shows the dimension in comparison with the smallest American coin, the dime. The tilt mirror is
just one of a range of optical components which begin to incorporate PMN active control and field
in clearly ripe form any new products using these precise electro mechanical control elements.

21

TABLE IV

Composition families and associated companies involved in the application of relaxor type dielectrics to multilayer capacitors (Survey by the Penn State Dielectric Center).

Commonly Employed Perovskite End Members for Relaxor-Based

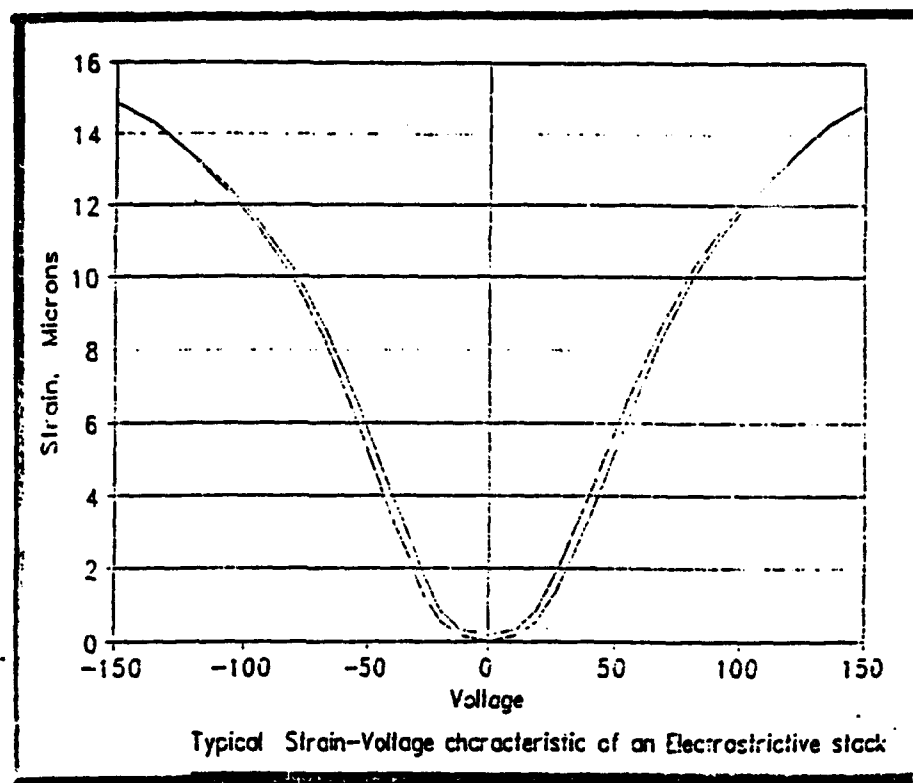| Complex Perovskites	+T_C(°C)	++Behavior	Simple Peroviskites	T_C(°C)	Behavior
[PMN]	-10	Relaxor-FE	PbTiO$_3$	490	FE
[PZN]	140	Relaxor-FE	PbZrO$_3$	230	AF
[PNN]	-120	Relaxor-Fe	BaTiO$_3$	—	Para
[PFN]	110	Normal-FE	SrTiO$_3$		
[PFW]	-95	Relaxor-FE			
[PMW]	38	AF			
[PNW]	17	AF			

+ Transition temperatures for relaxors are averages or at 1 kHz.
++ FE-Ferroelectric, AF-Antiferroelectric, Para-Paraelectric.

[PMN]:	Pb(Mg$_{1/3}$Nb$_{2/3}$)O$_3$	[PFW]:	Pb(Fe$_{2/3}$W$_{1/3}$)O$_3$
[PZN]:	Pb(Zn$_{1/3}$Nb$_{2/3}$)O$_3$	[PMW]:	Pb(Mg$_{1/2}$W$_{1/2}$)O$_3$
[PNN]:	Pb(Ni$_{1/3}$Nb$_{2/3}$)O$_3$	[PNW]:	Pb(Ni$_{1/2}$W$_{1/2}$)O$_3$
[PFN]:	Pb(Fe$_{1/2}$Nb$_{1/2}$)O$_3$		

Composition Families for Relaxor-Based MLCs

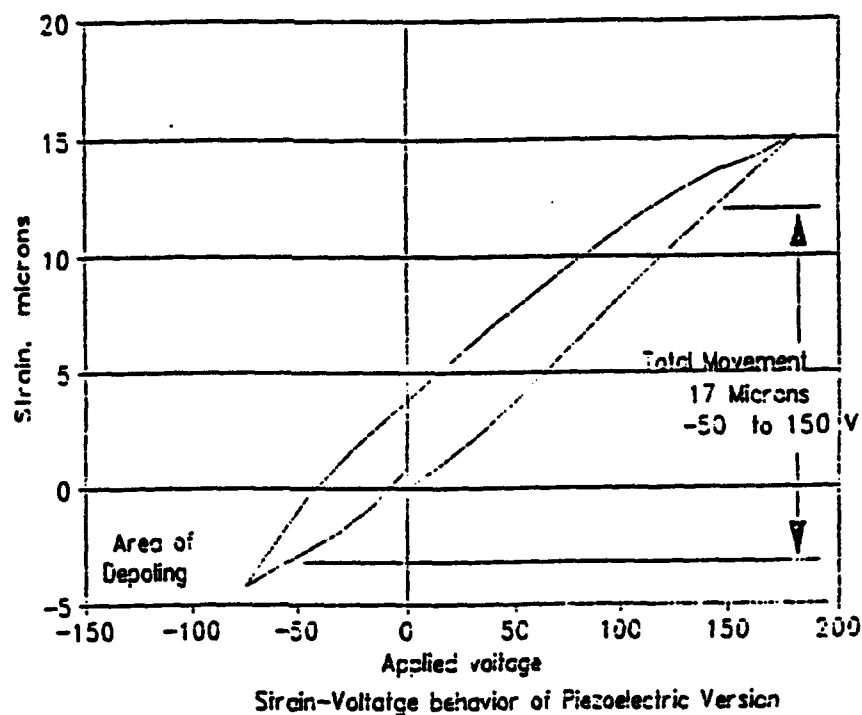| Composition	EIA Temp Specification	Manufacturer (Assignee)	Patents and Refs.
PLZT-Ag	X7R	Sprague	U.S. Pat. 4,027,209 (1973) Ref. 9
MPW-PT-ST	X7R	DuPont	U.S. Pat. 4,048,546 (1973)
PFN-PFW	Y5V	NEC	U.S. Pat. 4,078,938 (1978)
PFN-PFW-PZN	Y5V	NEC	U.S. Pat. 4,236,928 (1980)
PFN-PMT	—	TDK	U.S. Pat. 4,216,103 (1980)
PMN-PT	Y5V	TDK	U.S. Pat. 4,265,668 (1981)
PMN-PFN	Y5V	TDK	U.S. Pat. 4,216,102 (1980)
PMN-PFN-PMW	Y5V	TDK	U.S. Pat. 4,287,075 (1981)
PFW-PZ	Z5U	TDK	U.S. Pat. 4,235,635 (1980)
PFW-PT-MN	Z5U	Hitachi	U.S. Pat. 4,308,571 (1981)
PMN-PZN-PT	Z5U	Murata	U.S. Pat. 4,339,544 (1982)
PFN-PFW-PbGe (MSC)	X7R		Ref. 10
PFN-PFM-PNN	Z5U, Y5V	Ferro	U.S. Pat. 4,379,319 (1983)
PMW-PT-PNN	Z5U	NEC	U.S. Pat. 4,450,240 (1984) Ref. 11
PFN-BaCa(CuW)-PFW	Y5V	Toshiba	U.S. Pat. 4,544,644 (1985) Ref. 12
PMN-PZN	Z5U	STL	U.K. Pat. 2,127,187A (1984)
PMN-PFN-PT	Z5U	STL	U.K. Pat. 2,126,575 (1984)
PMN-PZN-PFN	Z5U	Matsushita	Japan Pat. 59-107959 (1984)
PMN-PFW-PT	—	Matsushita	Japan Pat. 59-203759 (1984)
PNN-PFN-PFW	Y5V	Matsushita	Japan Pat. 59-111201 (1984)
PZN-PT-ST	—	Toshiba	Ref. 13
PMN-PFN-PbGe	Z5U	Union Carbide	U.S. Pat. 4,550,088 (1985)
PFN-PNN	Y5V		Ref. 14
PFW-PFN (MSC)		NTT	Refs. 15-17
PMN-PT-PNW	Z5U	Matsushita	Ref. 18
PMW-PT-PZ	X7R	NEC	Ref. 19
PZN-PMN-PT-BT_ST	Z5U	Toshiba	Japan Pat. 61-155245 (1986)
PZN-PT-BT-ST	X7R	Toshiba	Japan Pat. 61-250904 (1986)
PZN-PMN-BT	Y5U, Y5S	Toshiba	Ref. 20
PMN-PLZT	Z5U	MMC	U.S. Pat. 4,716,134 (1987)
PMN-CT, ST, BT	Z5U	Matsushita	Japan Pat. 62-115817 (1986)
PFW-PFN-PT	Y5V		Ref. 21
PT-PMN-PZN (MSC)	X7R, X7S	Toshiba	U.S. Pat. 4,767, 732 (1988)
PMN-PS-PNW-Ca (Base Metal)	Z5U	Matsushita	Refs. 22-23

(a)

Strain, Microns

16
14
12
10
8
6
4
2
0
-150 -100 -50 0 50 100 150

Voltage

Typical Strain-Voltage characteristic of an Electrostrictive stack

(b)

Strain, microns

20
15
10
5
0
-5
-150 -100 -50 0 50 100 150 200

Applied voltage

Total Movement
17 Microns
-50 to 150 V

Area of
Depoling

Strain-Voltage behavior of Piezoelectric Version

FIGURE 23 (a) Anhysteritic nonlinear strain (x_3) versus field cure for PMN:PT relaxor
multilayer actuator.
(b) Strongly hysteritic response of a comparable multilayer soft PZT piezoelectric
actuator.

23

TABLE V   Comparison of the salient features of the relaxor based actuator as compared to the more conventional soft PLZT system.

Comparative Parameters of Piezoelectric vs Electrostrictive Stacks
(Both 20mm long, 6mm diam, 150 V Rated)

Parameter	Condition	Electro	Piezo	Units
Capacitance	25°C	4	1	μ-F
Diss. Factor	25°C	8	3	%
Frequency	Lose <10% strain	100	1000	Hz
Force	Lose <10% strain	700	450	Newtons
Extension	at 150 VDC	16.5	15	Microns
Hysteresis	25°C	<2	>15	%
Creep	After 24 hours	<2	~5	%
Temp Range	Keep 75% strain	±20	0-100	°C
TCE	25 - 125°C	<1	1.6	ppm/°C
Youngs Modulus	25°C	16	4	10^6 PSI
Response Time	25°C	<100	<5	μ-sec

JPL WF/PC-2 ARTICULATING FOLD MIRROR
(AFM)
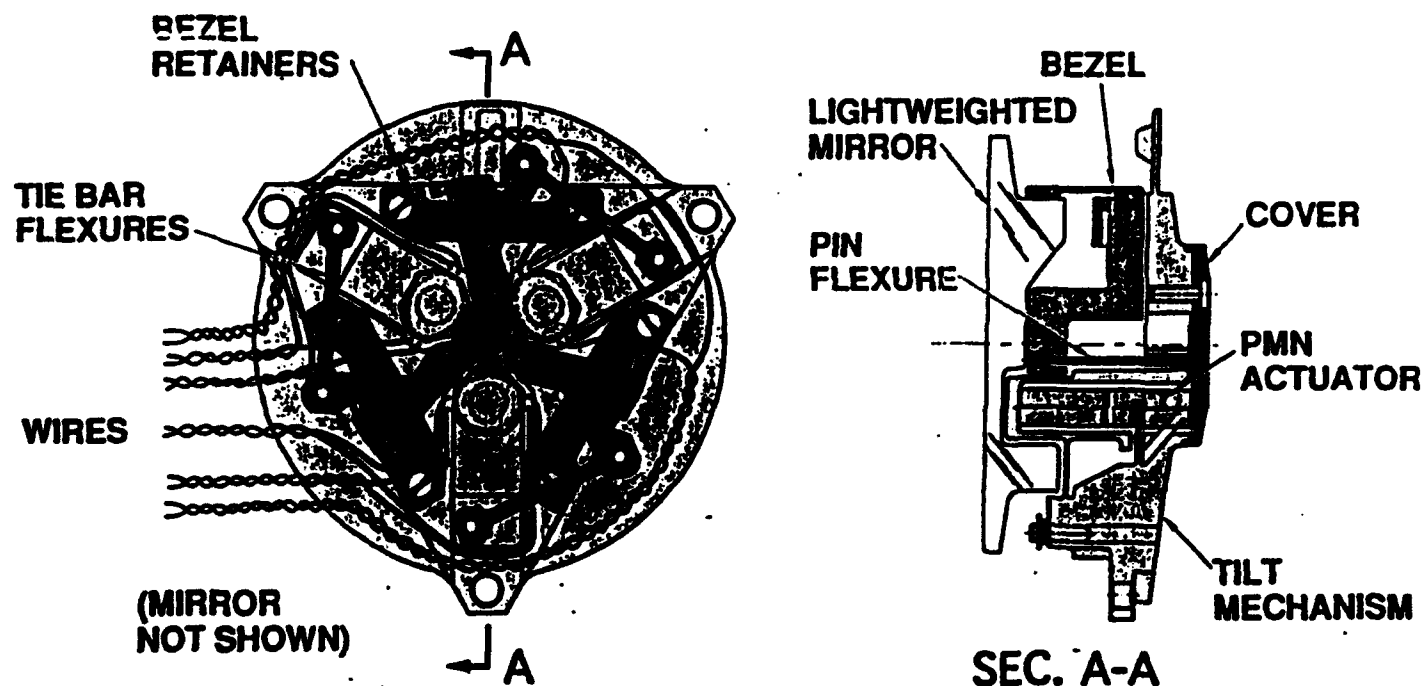
FIGURE 24   Plan and elevation views of the JPL Articulated fold mirror driven by PMN:PT actuators (Corrector to be flown December 1993).
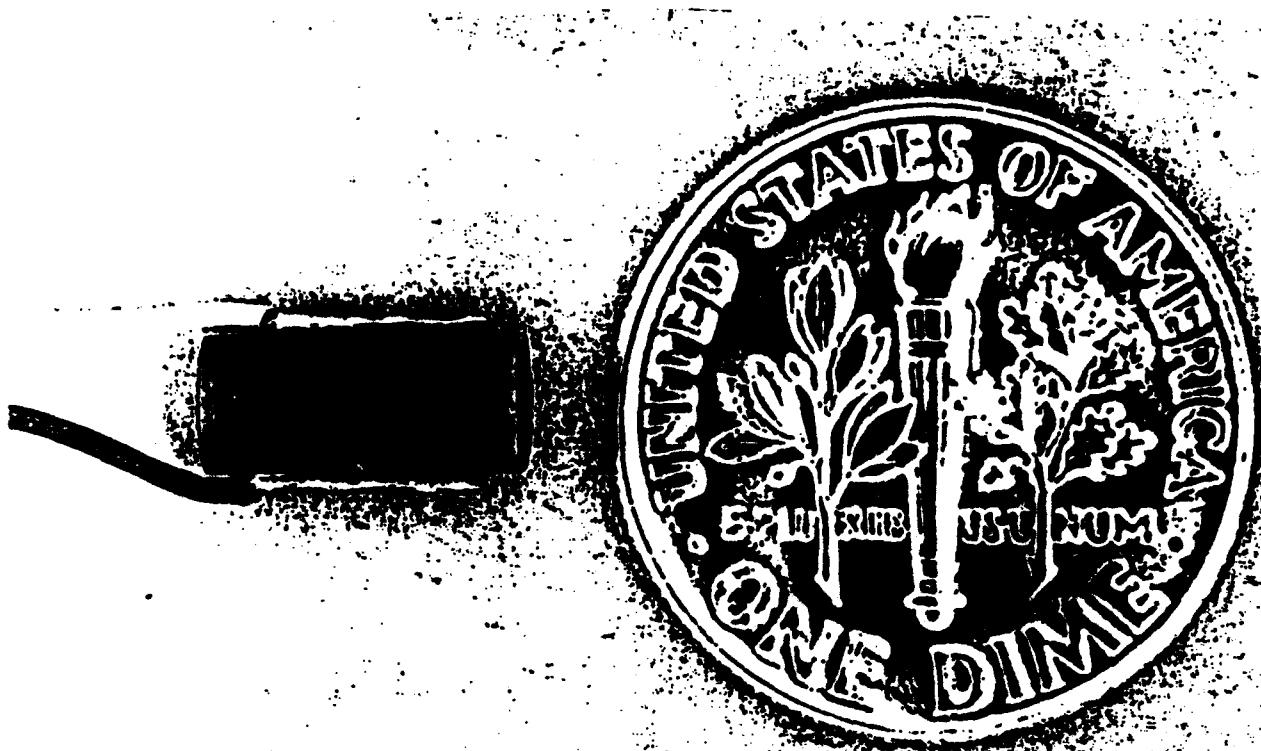
24

FIGURE 25 Scale of the multilayer PMN:PT actuator as compared to an American dime coil.

25

REFERENCES

1. G. S. Smolensky, A. Agronovskaya, Soviet Physics Solid State 1, 1429 (1960).

2. V. Bokov and I. Mylnikova, Soviet Physics Solid State 3, 3 (1960).

3. C. Randall and A. Bhalla, J. Mat. Sci. 29, 5 (1990).

4. J. Chen and M. Harmer, J. Am. Ceram. Soc. 72, 593 (1989).

5. C. Randall, PhD Thesis, University of Essex, Colchester, England (1987).

6. A. Katchaturyan, Private Communication.

7. N. Setter, PhD Theis, Pennsylvania State University (1980).

8. C. Randall, D. J. Barber, and R. W. Whatmore, Journal of Microscopy 145 (3), 275 (1987).

9. G. Rossetti, PhD Thesis, Pennsylvania State University (1993).

10. W. A. Schulze, J. V. Biggers, and L. E. Cross, J. Am. Ceram. Soc. 61, 749 (1980).

11. M. P. Leffler, MS Thesis, Pennsylvania State University (1989).

12. G. Burns and F. Dracol, Solid State Commun. 48, 853 (1983).

13. P. Asadipour, U. Kumar, S. J. Jang, A. S. Bhalla, and L. E. Cross, Jpn. J. Appl. Phys. 24 (2), 742 (1985).

14. A. S. Bhalla, R. Guo, L. E. Cross, and G. Burns, Phys. Rev. B. 36 (4), 2030 (1987).

15. P. Asadipour, MS Thesis, Pennsylvania State University (1986).

16. D. Viehland, S. J. Jang, L. E. Cross, and M. Wuttig, J. Appl. Phys. 66, 2916 (1990).

17. D. Viehland, M. Wuttig, and L. E. Cross, Ferroelectrics 120, 71 (1991).

18. W. Pan, E. Furman, G. O. Dayton, and L. E. Cross, J. Mat. Sci. Letters 5, 647 (1986).

19. W. Pan, Q. Zhang, and L. E. Cross, J. Am. Ceram. Soc. 71, C17 (1988).

20. C. Randall, D. Barbes, and P. Groves, J. Mat. Sci. 21, 4456 (1986).

21. Y. Xi, C. Zhilli, and L. E. Cross, J. Appl. Phys. 54, 3399 (1983).

22. J. deAlmedia and D. Thouless, J. Phys A 11, 983 (1978).

23. R. Chamberlin, M. Hardiman, L. Turkevich, and R. Orbach, Phys. Rev. B 25, 6720 (1982).

24. W. Pan and L. E. Cross, ONR Annual Report for 1985 on contract N00014-82-KO339 (July 1986).

25. W. Pay, W. Y. Gu, D. J. Taylor, and L. E. Cross, Jpn. J. Appl. Phys. 28 (4), 653 (1989).

26. A. M. Glass, J. Appl. Phys. 40, 4699 (1981).

27. G. Burns and F. H. Dacol, Ferroelectrics 104, 25 (1990).

28. G. Burns, Phase Transitions 5, 261 (1985).

29. T. Cline, PhD Thesis, Pennsylvania State University (1979).

30. M. E. Lines and A. M. Glass, Principles and Applications of Ferroelectrics and related materials, Clarendon, Oxford (1977).

31. R. R. Neurgaonkar and W. K. Kory, J. Opt. Soc. Am. 3(B), 274 (1986).

32. E. J. Sharp, W. W. Clark III, M. Miller, G. L. Wood, B. Monson, and G. J. Salamo, Applied Optics 29 (6), 743 (1990).

33. M. H. Francombe, Acta. Cryst. 13, 131 (1960).

34. R. Guo, A. S. Bhalla, C. Randall, and L. E. Cross, J. Appl. Phys. 67 (10), 6405 (1990).

35. A. Schröder, J. Fisher, H. von Lohneysen, W. Bauhofer, and U. Steigenberger, J. Phys (Paris) Colloq (to be published).

36. A. Bell, J. of Physics: Condensed Matter (submitted).

37. V. Westphal, W. Kleemann, and M. D. Glinchuk, Phys. Rev. Letters (68 (6), 847 (1992).

MATERIALS STUDIES

APPENDIX 6

MICROSTRUCTURAL CHARACTERISTICS AND DIFFUSE PHASE TRANSITION BEHAVIOR OF LANTHANUM-MODIFIED LEAD TITANATE

G. A. ROSSETTI, JR†., W. CAO, AND C. A. RANDALL
Materials Research Laboratory, The Pennsylvania State University
University Park, Pennsylvania 16802
† Now with the Department of Geological and Geophysical Sciences and
Princeton Materials Institute, Princeton University, Princeton, New Jersey 08544

Abstract The introduction of structural disorder into perovskite ferroelectrics leads to the observation of diffuse phase transition behavior. In this paper, the microstructural characteristics and phase transition behavior of lanthanum-modified lead titanate are discussed. It is shown that the diffuse nature of the transition is connected with the appearance of ferroelectric domain structures exhibiting texture on the mesoscopic (≈ 10 nm) length scale. The theoretical implications of these results are briefly discussed.

INTRODUCTION

Diffuse phase transitions in perovskite ferroelectrics occur as a consequence of some level of structural disorder that breaks the translational invariance of the lattice. The type of diffuse transition observed depends both on the nature and scale of the structural disorder. Impurities, point defects, extended defects, incomplete or inhomogeneous cation ordering, macroscopic fluctuations in chemical composition, core/shell structures etc. can all lead to smearing of the ferroelectric phase transition. The physical origin of the smearing and the behavior of the ferroelectric properties in each particular case, however, may be very different. In chemically complex compounds and solid solutions, several types of structural disorder are often present simultaneously. To establish structure-property relations in these materials therefore requires characterization at all the relevant length scales, including the macroscopic (crystal symmetry, chemical homogeneity, core/shell structures), the microscopic (ferroelectric domain structures, extended defects), the mesoscopic (cation order domains, texture within ferroelectric domains), and the atomic (point defect chemistry, local environment).

For ferroelectrics such as lanthanum-modified lead zirconate-titanate (PLZT), the structural disorder arises as a consequence of the complex defect chemistry associated with the aliovalent A-site substitution of lanthanum[1]. Keizer, Lansink and Burggraaf[2] have shown that the nature of the ferroelectric transition in ceramic specimens of the end member $Pb_{1-\frac{3}{2}y}La_yTiO_3$ (PLT) changes smoothly from that expected in a sharp first-order phase change to that of a diffuse transition as

the lanthanum concentration is increased. Figure 1 shows that, when characterized by the exponent γ in the generalized Curie-Weiss law, the anomalous dielectric behavior onsets at y = 0.05 and becomes typical of diffuse transitions (i. e. γ = 2) when y > 0.23. Although the numerical values of γ depend somewhat on the lead elimination factor (α) as well as on the grain size, the general trend towards increasingly diffuse behavior with lanthanum substitution is intrinsic.

In order to better understand how structural disorder evolves and relates to the dielectric properties in PLT, we have recently undertaken transmission electron microscopy (TEM) and powder x-ray/neutron studies, the details of which are reported elsewhere[3-5]. In this paper, we draw on these results and speculate on some possible interconnections between the microstructure, dielectric properties, and the phase transition behavior.

RESULTS AND DISCUSSION

High resolution X-ray diffraction studies[4] of sol-gel derived powders have shown that the addition of lanthanum to lead titanate results in broadened diffraction profiles showing a marked profile asymmetry. The degree of asymmetry can be quantified by fitting the profiles to split Pearson distributions[6]. The split Pearson function gives two values for the full width at half maximum, β^L and β^H, which are characteristic of the peak shape on the low and high angle sides of the peak maximum, respectively. Figure 2 shows that both the peak asymmetry and the peak breadth renormalize as a function of lanthanum concentration. The asymmetry (β^H/β^L) changes markedly between y = 0 and y = 0.01, but then decreases and becomes constant for samples with y > 0.05. At the same time, the profile breadth decreases. Corresponding to the changes in the diffraction profiles, the crystal tetragonality (c/a) begins to deviate from the linear composition dependence as expected based on Vegard's law. These observations cannot be easily explained by macroscopic variations in chemical composition, nor by particle size effects.

Alternatively, recent TEM studies[3] (Figure 3) reveal that the development of sub-domain texture in PLT materials closely parallels the changes observed both in the X-ray studies and in the dielectric behavior. For samples with y < 0.05, no sub-domain texture is observed, and the transition behavior is sharp. For samples with y ≥ 0.05, sub-domain texture becomes apparent, and increases in degree with lanthanum concentration. As the sub-domain texture becomes more pronounced, the dielectric behavior near the transition becomes correspondingly more
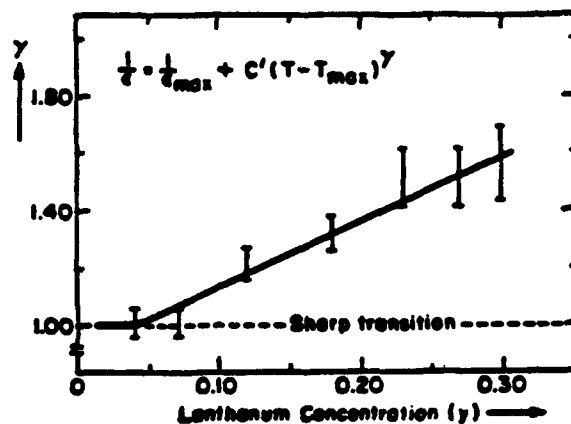
Figure 1. Composition dependence of the exponent γ in the generalized Curie-Weiss law for $Pb_{1-xy}La_yTiO_3$ (After Reference 2).

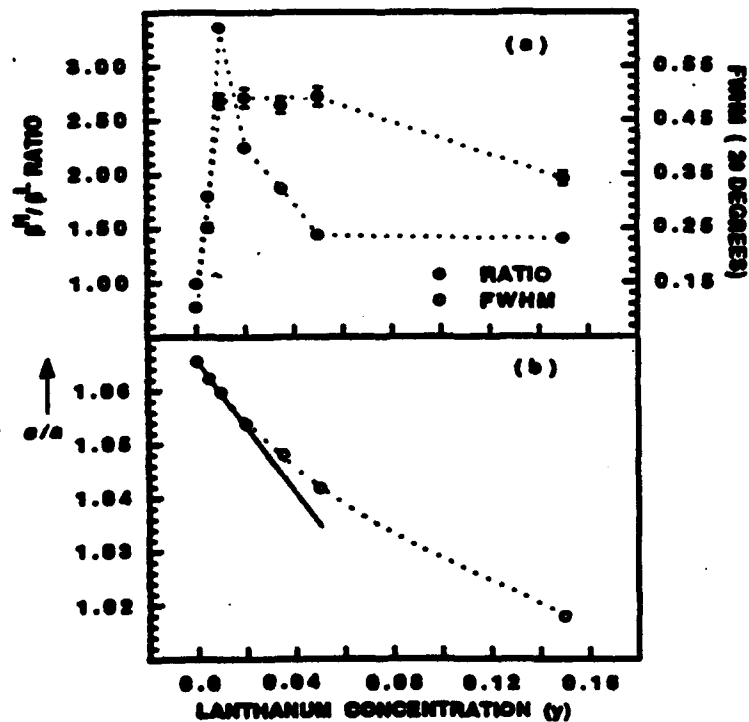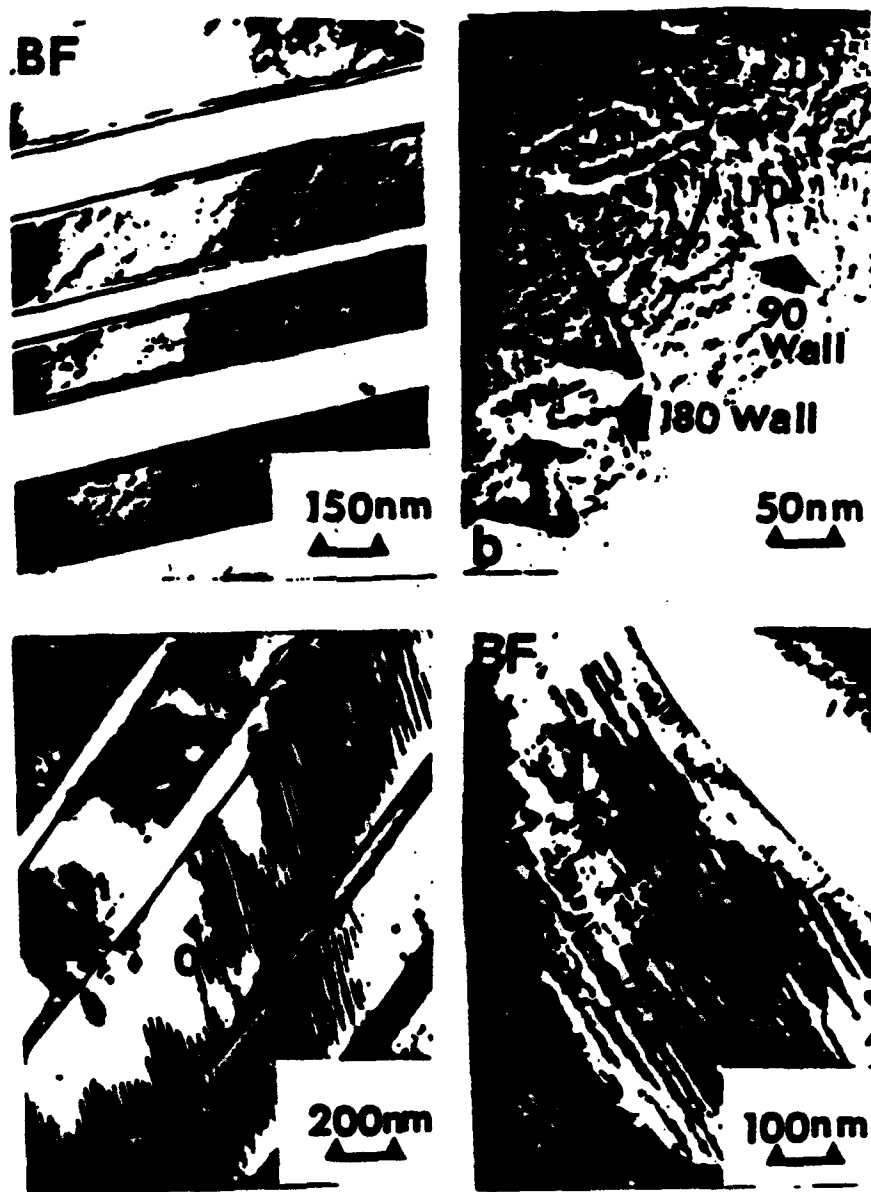**Figure 2.** Breadth and asymmetry of the 002 powder XRD profile (a) and crystal tetragonality (b) of $Pb_{1-xy}La_yTiO_3$.

Figure 3.   Transmission electron micrographs of $Pb_{1-xy}La_yTiO_3$: (a) y = 0.01 (b) y = 0.05 (c) y = 0.10 and (d) y = 0.25.

anomalous. For compositions with y > 0.25, the microstructure degenerates into a cross-hatched or tweed texture. For these compositions, the dielectric behavior is typical of that for diffuse phase transitions. Note that these textures disappear on heating above the transition temperature, and so cannot be identified with exsolution lamellae.

The tweed structures observed for the higher lanthanum concentrations would appear to be precursors for the mottled and poorly defined vestiges of sub-domain texture as observed for PLZT[7]. The Zr-rich PLZT compositions exhibit strongly frequency-dispersive diffuse transitions similar to those of the complex B-site perovskites such as $PbMg_{1/3}Nb_{2/3}O_3$ (PMN) and related compounds. In the later case, however, it is the cation order domains persisting on a ~10 nm length scale that lead to the breakdown of the ferroelectric domain structure[8-10]. The similarity in mesoscopic domain texture of the PLZT and PMN type materials[11-13] is intriguing, since at the atomic level, the origin of the structural disorder in these two materials is very different.

With regard to the nature of the phase transition in PLT, the first-order character also follows the changes in structural properties as revealed in the X-ray data. The development of a Landau-Devonshire[14] formulation for the phase transition in PLT requires the expansion coefficients to depend on spatial variables, which results in a distribution of transition temperature. As a macroscopic average, one expects that the first-order discontinuity of the transition will be drastically reduced as the transition becomes diffused. The Landau theory is valid, however, only when the sub-domain modulations are weak, otherwise the gradient related (Ginsburg) terms must be included. Using the methodology described previously[15], the coefficients in the Landau-Devonshire expansion were estimated for compositions with y < 0.05, where judging from Figure 3, this condition is approximately satisfied. As shown in Figure 4, the coefficient of the quartic term in the elastic Gibbs function (a_{11}^X) increases rapidly toward zero between y = 0 and y = 0.01 but then changes at a much lower rate. This increase reflects the apparent loss in the first-order character of the transition as the structure relaxes to the defects and the long range order is disrupted. The coefficient of the sixth-rank term also renormalizes, but to a much lesser extent. Large changes in the coefficient of the quartic term were also observed for PLZT compositions[16].

For the compositions with y > 0.05, the Ginsburg terms must be included in the formalism. The inclusion of the gradient energy can describe both the domains and their modulations. Periodic domain structures can be excited for a finite
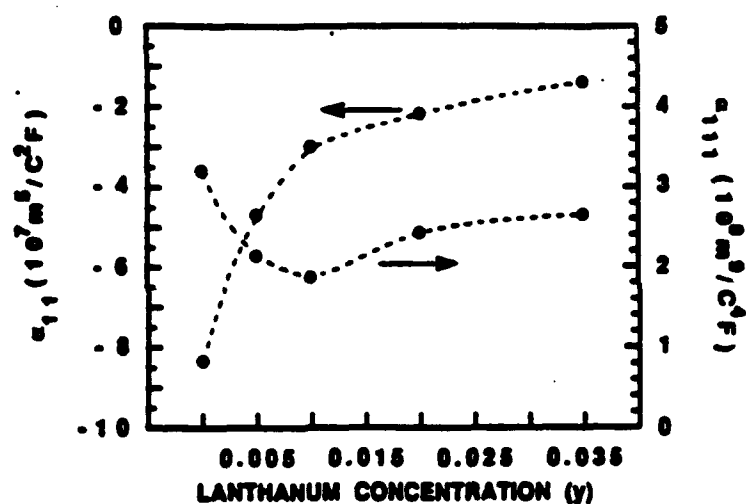
Figure 4.   Coefficients of the elastic Gibbs free energy density function of $Pb_{1-\frac{3}{2}y}La_yTiO_3$.
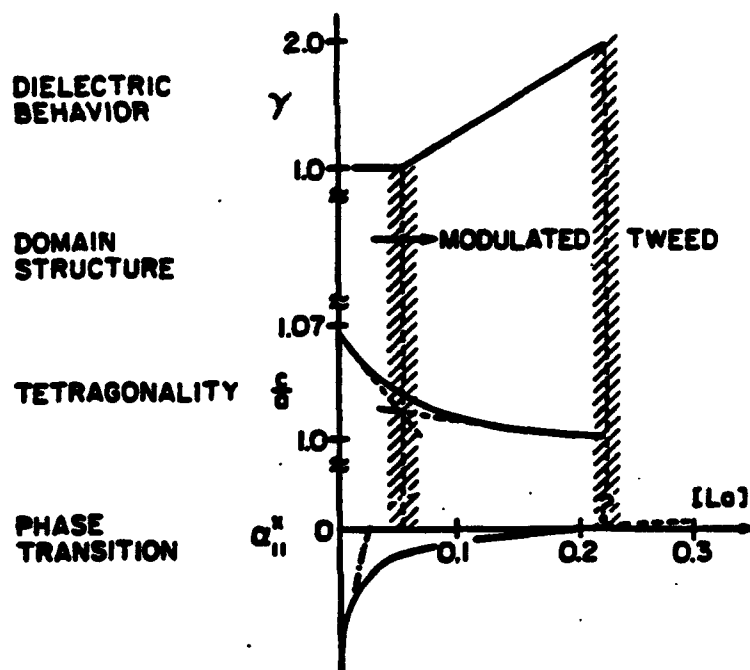

Figure 5.   Observed relationships between the first-order character of the transition, the crystal tetragonality, the sub-domain texture, and the dielectric properties of $Pb_{1-\frac{3}{2}y}La_yTiO_3$.

system due to the competition between nonlinearity and nonlocality. Modulated structures and tweed textures can be described in terms of crest riding periodons[17,18]. However, the modulated structures such as those in Figure 3c do not seem to follow the expected temperature variation pattern of the crest riding periodon excitations, which are unstable and can survive only in a finite temperature range near the transition. One possible explanation could involve an interaction of the defects with the periodons. These excitations might be stabilized by the lanthanum/vacancies if the defects are appropriately aligned. The alignment can be driven, on the other hand, by the field gradient created at the walls of the periodons. Consistent with this notion, the modulations have preferred orientations (although not perfect), and are nearly periodic, as shown in Figure 3. Further studies will be required to confirm this picture.

At the higher lanthanum concentrations (y > 0.25) the microstructure breaks down on still finer scales and more degenerate states are created. This will effectively increase the dielectric response of the system, as observed. For these materials, however, arguments based on the continuum theory as summarized above may not be used because the density representation (both in terms of energy and polarization) is no longer valid. Instead, discrete models must be developed.

The results described above can be represented schematically as shown in Figure 5, where the observed relationships between the first-order character of the transition, the crystal tetragonality, the sub-domain texture, and the dielectric properties are shown. Here it is worth mentioning that, in the Landau-Devonshire formalism, close inter-relationships exist between the curvature of the energy surface, the order of the transition, and the symmetry of the ferroelectric phase. In this connection, it is of interest to consider how the scenario depicted in Figure 5 may change as zirconium, which lowers the tetragonality of the system and further flattens the energy surface, is added to the system. Based on the above discussion, we might expect that lanthanum will become more effective at breaking down the domain structure as the rhombohedral side of the PLZT diagram is approached, leading to a large number of degenerate states and additional contributions to the dielectric response even at modest lanthanum concentrations.

SUMMARY

The breakdown of conventional ferroelectric phase transition behavior in lanthanum-modified lead titanate has been correlated with the appearance of

domain structures exhibiting texture on a nanometer scale. It was suggested that this type of mesoscopic sub-domain texture is a common feature of ferroelectrics showing diffuse/frequency dispersive transitions. The theoretical implications of the relationships existing between the curvature of the energy surface, the order of the transition, the symmetry of the ferroelectric phase, the development of the sub-domain texture, and the resulting dielectric properties were discussed.

ACKNOWLEDGEMENT

REFERENCES

1. K. H. Härdtl and D. Hennings, J. Am. Ceram. Soc., 55 230 (1972).
2. K. Keizer, G. J. Lansink, and A. J. Burggraaf, J. Phys. Chem Solids, 39 59 (1978).
3. C. A. Randall, G. A. Rossetti, Jr., and W. Cao, Ferroelectrics (in press).
4. G. A. Rossetti, Jr., L. E. Cross, and J. P. Cline, J. Phys: Cond. Mat., (submitted).
5. G. A. Rossetti, Jr., M. A. Rodriguez, A. Navrotsky, L. E. Cross, and R. E. Newnham, Acta Cryst. C. (submitted).
6. M. M. Hall, Jr., V. G. Veeraraghavan, H. Rubin, and P. G. Winchell, J. Appl. Cryst., 10 66 (1977).
7. C. A. Randall, D. J. Barber, and R. W. Whatmore, J. Microscopy, 145 275 (1987).
8. H. B. Krause, J. M. Cooley, and J. Wheatly, Acta Cryst., C35 1015 (1979).
9. C. A. Randall, D. J. Barber, and R. W. Whatmore, J. Mater. Sci., 22 935 (1987).
10. C. A. Randall and A. S. Bhalla, Jap. J. Appl. Phys., 29 327 (1990).
11. C. A. Randall, D. J. Barber, R. W. Whatmore, and P. Groves Ferroelectrics, 76 265 (1987).
12. A. D. Hilton, C. A. Randall, D. J. Barber, and R. W. Whatmore, Inst. Phys. Conference Series, No. 90, Chapter 9, 315 (1987).
13. A. D. Hilton, C. A. Randall, D. J. Barber, and T. R. Shrout, Ferroelectrics, 93 379 (1989).
14. A. F. Devonshire, Advances in Physics, 3 85 (1954).
15. G. A. Rossetti, Jr., Ferroelectrics, 133 103 (1992).
16. G. A. Rossetti, Jr., T. Nishimura, and L. E. Cross, J. Appl. Phys., 70 1630 (1991).
17. G. R. Barsch and J. A. Krumhansl, Met. Trans. A., 19A 761 (1988).
18. W. Cao (to be published).

APPENDIX 7

Distribution functions of coexisting phases in a complete solid solution system

Wenwu Cao and L. Eric Cross
Materials Research Laboratory, The Pennsylvania State University, University Park, Pennsylvania 16802

In the phase diagram of a binary system one often encounters a compositional region in which two phases coexist. A common practice is to use the Lever Rule to describe the distributions of the two coexisting phases. However, if the binary system is a complete solid solution system, the Lever Rule cannot be used. A new type of distribution has been derived for a solid solution system without solubility gap. Application of the theory to pure and modified lead-zirconate–lead-titanate (PZT) systems shows excellent agreement with the experimental data. Several disputed facts about PZT are also explained satisfactorily.

I. INTRODUCTION

A general phase diagram of a binary system A-B is given in Fig. 1(a). There is one liquid phase L and two solid solutions α and γ. A and B are completely miscible in the liquid phase, but in the solid phase there is a solubility gap in which the two solid solutions α and γ coexist. At temperature T_1, for any composition x inside the solubility gap, $g < x < h$, the molar percentages f_α and f_γ of the two coexisting phases are governed by the Lever Rule,

$$f_\alpha : f_\gamma = \overline{xh} : \overline{gx},$$

$$f_\alpha + f_\gamma = 1. \tag{1}$$

The two special points g and h on the isothermal tieline at $T = T_1$ represent the boundaries of the solubility gap. The corresponding free-energy versus composition plot is shown in Fig. 1(b). One can see that the two boundary compositions g and h are located at the common tangent points of the two free energies for the α and γ phases. For compositions falling inside this solubility gap, two-phase mixtures will be formed consisting of g and h compositions, with the ratio of the two phases obeying the Lever Rule [Eq. (1)].

Figure 1(c) is another type of phase diagram for an A-B binary compound. Looking at the subsolidus region we have three solid solutions, β, α, and γ. This is a complete solid solution system, viz., no miscibility gaps and no solubility gaps; however, there is a structural phase transition from β to either α or γ phase depending on the composition of the solid solution. The well-known lead zirconate titanate (PZT) and its derivatives are examples of this situation. For this system, the free energies of α and β phases are monotonic functions of composition. Because there are no chemical decompositions in the complete solid solution system, for simplicity we only consider the relative stability of the α and β phases. We know that in this system, the difference of the two low-temperature phases is characterized by the polarization which is the primary order parameter in the paraelectric-ferroelectric phase transition; hence, to analyze the relative stability we only need to know the free energy associated with the polarization. Using Landau–Devonshire type phenomenological theory,

the compositional dependence of the free energies associated with the polarization for the α and β phases may be drawn as in Fig. 1(d) at T_1.[1] One can see from Fig. 1(d) that the coexistence of the α and γ phases should be allowed only for one composition k, but not for a finite compositional region according to thermodynamics.

To some extent, Fig. 1(d) may be deceiving at first glance, because if the composition is taken as an independent variable, the transition from α to γ is obviously first order and the transition hysteresis with respect to the change of composition will result in a coexistence region. In fact, this is one of the explanations given for the coexistence region found in the PZT system.[2] Unfortunately, the composition cannot be changed in the subsolidus temperature region. Once a compound is formed at much higher temperature ($> 800\,°C$), the composition variable is frozen in the subsolidus region. The polarization related free energy for each phase at T_1 [Fig. 1(d)] is obtained independently for each composition from the corresponding prototype phase following the change of temperature. Therefore, in order to study this problem we must look at the temperature-induced phase transition from β to α and β to γ.

From Fig. 1(d) we can see that both free energies for the α and γ phases are monotonic functions of composition, and there is one crossover point k which is termed the morphotropic phase boundary (MPB). From energy minimization principles only one phase is stable in the low-temperature region for any given composition, which is to say that at T_c the β phase will be transformed into either the α or γ phase depending on the composition of the solid solution. However, when the transition temperature is reasonably high and the phase transition from β to α or γ is of second order, thermal energy could induce some amount of the second metastable phase at the transition, especially when the difference of the free energies of the two low-temperature phases is small, such as for those compositions near the MPB [see Fig. 1(d)]. It is our opinion that the phase coexistence observed in the PZT system near the MPB is the result of a frozen-in second metastable phase as elaborated below.

One must note that the phase mixing is completely different in the cases of Figs. 1(a) and 1(c). In the former
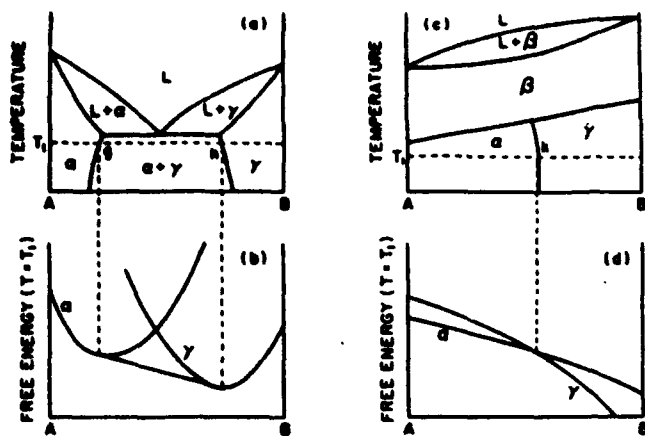
FIG. 1. Phase diagram for a binary A-B system. (a) Solid solutions α and γ coexist inside the solubility gap in the subsolidus region. (b) The free energies of α and γ phases vs composition at temperature T_1. The two tangent points correspond to the edge compositions of the solubility gap. (c) Phase diagram for a complete solid solution system. The nearly vertical line that divides the α and γ phase is the morphotropic phase boundary. (d) The change of the free energy related to the polarization with respect to composition at temperature T_1 for both the α and γ phases in the complete solid solution system described in (c).
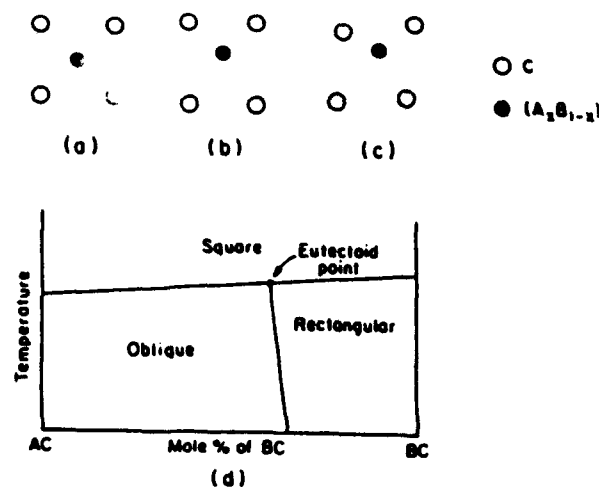
FIG. 2. Illustration of two-dimensional square-rectangular and square-oblique structural phase transitions in a complete solid solution AC-BC. (a), (b), and (c) are the lattice structures for the paraelectric square, ferroelectric rectangular, and ferroelectric oblique phases, respectively; (d) is the corresponding phase diagram.

we mix two phases of different structures and of different chemical compositions but in the latter we mix two different structures of the same chemical composition. Because of the different chemical compositions in the former case, the conservation of matter leads to the Lever Rule. But for the case in Fig. 1(c), the distribution functions cannot be obtained straightforwardly because the condition of identical chemical composition invalidates the arguments used to derive the Lever Rule.

A new approach has been proposed to calculate the partitioning of the rhombohedral and tetragonal phases at the MPB when the structural phase transition from β to α or γ is of second order.[3] Here we will try to extend that model to address the phase coexistence near the MPB in a complete solid solution system by incorporating classical statistics. This proposed theory is applicable to the PZT system because the paraelectric-ferroelectric phase transitions for PZT solid solutions of composition near the MPB are indeed second order.[4]

II. THEORY

For simplicity, we will study a statistical ensemble of independent particles, for example, a ceramic powder system or even (to first-order approximation) a ceramic system (an ensemble of grains) may be considered to be such ensembles. For each particle, we assume it is a single-phase system both before and after the phase transition. In what follows we will calculate the probabilities of one of the particles transforming from the high-temperature phase β into one of the low-temperature phases α or γ, and use these probability functions as the new distribution functions for the statistical ensemble with compositions near the MPB.

In order to visualize the concept let us look at a hypothesized 2D problem of a complete solid solution system AC-BC. The high-temperature phase is a nonferroelectric square phase as shown in Fig. 2(a) and the two low-temperature phases are rectangular and oblique ferroelectric phases as shown in Figs. 2(b) and 2(c), respectively. The phase diagram in the subsolidus region is given in Fig. 2(d). For convenience we call the starting point of the morphotropic phase boundary the "eutectoid point."

Assuming that the phase transition from the square phase to either the oblique or rectangular phase is second order near the eutectoid point, strong thermal fluctuations will occur near the transition temperature T_c. Sufficiently below T_c the system will be frozen into one of the low-temperature phases. In a way we are dealing with a "quenching" problem from the fluctuating state to a ferroelectric state. Hence, the probabilities of transforming from the square to the rectangular or oblique phases are predetermined in the fluctuating state. This situation is depicted in Fig. 3. The profile of the fluctuating state near T_c and the final low-temperature states are shown in Figs. 3(a) and 3(b), respectively, in the order parameter space. The
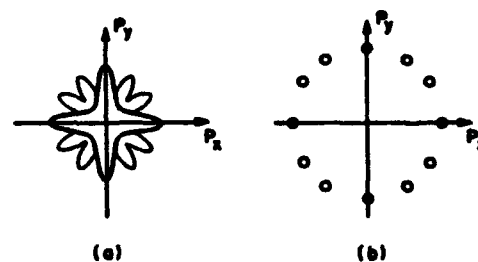

FIG. 3. (a) Thermal fluctuation profile at the eutectoid point in the order parameter space for the two-dimensional problem described in Fig. 2. (b) Degenerate low-temperature states for the morphotropic phase boundary composition: (●) rectangular phase; (○) oblique phase.

thicker line in Fig. 3(a) illustrates the profile for the case of square-rectangular transition [near the BC end of the composition region in Fig. 2(d)] and the thinner line is for the case of square-oblique transition [near the AC end of the composition region in Fig. 2(d)]. In the compositional region near the eutectoid point, the profile of the fluctuation will look like the outer rim of the pattern in Fig. 3(a).

There is a link between the situations described in Figs. 3(a) and 3(b), which becomes apparent if we assume that the thermal fluctuations have no orientational preference. In other words, although the magnitude of the fluctuation is regulated by the potential well, the orientation probability of thermally induced instant polarization P_{ist} should have no directional preference. Thus the probability of attaining a particular low-temperature state in Fig. 3(b) on cooling from the fluctuating state [Fig. 3(a)] is proportional to the effective angle that state corresponds to in the fluctuating state. A polygon may be constructed to calculate the effective angle of each low-temperature state in the 2D problem where each edge of the polygon subtends an effective angle for each of the low temperature states. An important task is to define the boundaries between these effective angles. A method for defining the boundary has been given when the low-temperature states are degenerate.[3] Considering the picture in Fig. 3(a), if P_{ist} is oriented inside a particular angular region while being frozen into the low-temperature phase, the final state should be one of the states in Fig. 3(b) whose polarization has the smallest angle with P_{ist}. Therefore, the probability of becoming one of the states in Fig. 3(b) on cooling from the fluctuating state is equal to a corresponding effective angle in Fig. 3(a) divided by 2π—the normalization constant.

This concept can be easily generalized to a three-dimensional case, for which the probability of attaining a low-temperature state when frozen from the fluctuating state is proportional to a corresponding effective solid angle divided by 4π. For the three-dimensional case, a polyhedron may be constructed in the order parameter space to calculate these effective solid angles; it has been named the "probability polyhedron.[3]"
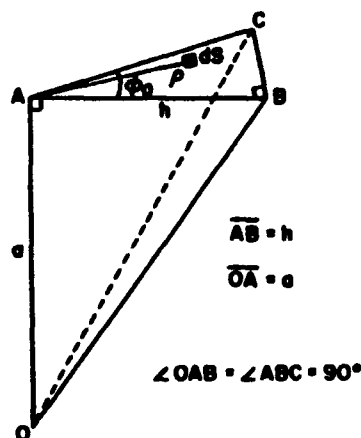
The solid angle calculations may be carried out on the surface of the polyhedron. Utilizing the relatively high symmetry of the problem, we only need to derive a general formula for the solid angle subtended by a right triangle surface as shown in Fig. 4; the solid angle is given by

$$\Omega_{OABC} = \iint_{\triangleleft ABC} \frac{a \, ds}{(\rho^2 + a^2)^{3/2}}, \tag{2}$$

where ds is the area element on the surface of $\triangleleft ABC$ and ρ is the distance of this area element from point A. The integration may be conveniently carried out using cylindrical coordinates

$$\Omega_{OABC} = a\phi_0 \int_0^h \frac{\rho \, d\rho}{(\rho^2 + a^2)^{3/2}}$$

$$+ a \int_h^{h/\cos \phi_0} \frac{\phi_0 - \arccos (h/\rho) \rho \, d\rho}{(a^2 + \rho^2)^{3/2}}$$

$$= \phi_0 - \frac{\pi}{4} - \frac{1}{2} \arcsin \left(\frac{1 - 2\cos^2 \phi_0 - (h/a)^2}{1 + (h/a)^2} \right). \tag{3}$$

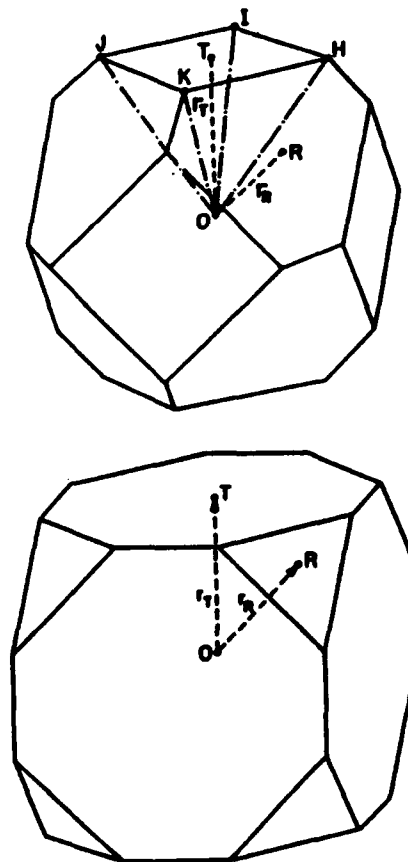For the study of the coexistence of nondegenerate

FIG. 5. Probability polyhedron for complete solid solution systems with coexisting rhombohedral and tetragonal phases, such as PZT, with the parameter δ in the ranges (a) $1 - \sqrt{3} < \delta < 1 - (2/\sqrt{3})$ and (b) $1 - (2/\sqrt{3}) < \delta < 1 - (1/\sqrt{3})$.

$$\overline{AB} = h$$

$$\overline{OA} = a$$

$$\angle OAB = \angle ABC = 90°$$

FIG. 4. Solid angle subtended by a right-angle surface $\triangleleft ABC$ with respect to the point O.

states, we use the following arguments to define the boundaries between different effective solid angles in the fluctuating states.

(i) At T_c the thermal energy is of the order of kT_c, so that there are probabilities for the non-lowest-energy states to be occupied; this probability is proportional to $\exp[-(G_i-G_L)/kT_c]$, where G_i and G_L are the free energies of the ith low-temperature state and the ground (lowest free energy) state, respectively. Here we have assumed that configurational tunneling near T_c is allowed to achieve global equilibrium, because the system is very "soft" near T_c.

(ii) The solid angle Ω_i subtended by a given surface area with respect to a fixed point in space is inversely proportional to the square of the distance r_i between this surface and that point.

Since the solid angle Ω_i is equivalent to the probability of attaining the ith low-temperature state, using the arguments (i) and (ii) above we may assume the following relationship between the distance variable r_i and the free energies:

$$r_i \propto \frac{1}{\sqrt{\Omega_i}} \propto \exp\left(\frac{G_i-G_L}{2kT_c}\right). \tag{4}$$

It can be proved that only one parameter δ is needed to calculate a binary system, such as the PZT system, where δ is the relative distance,

$$\delta = \frac{r_T-r_R}{r_T} = 1 - \exp\left(\frac{G_R-G_T}{2kT_c}\right). \tag{5}$$

G_R and G_T are the free energies of the rhombohedral and tetragonal phases, respectively.

The probability polyhedron for the PZT system is given in Figs. 5(a) and 5(b). One must note that the representative surfaces for the rhombohedral and tetragonal phases change their shape for $\delta > 1 - (2/\sqrt{3})$ and $\delta < 1 - (2/\sqrt{3})$. When $r_R > \sqrt{3} r_T$, the six representative surfaces for the tetragonal phase will meet each other to form a cube, which implies that only a tetragonal phase can be formed. Vice versa, when $r_R < (1/\sqrt{3}) r_T$ the representative surfaces of the rhombohedral phase will form a closed octahedron so that only a rhombohedral phase can be formed. This restricts the δ values in the following range:

$$1 - \sqrt{3} < \delta < 1 - (1/\sqrt{3}). \tag{6}$$

For δ values out of this range, the low-temperature phase will be single phase.

Using the formula Eq. (3) the distribution functions f_T and f_R in terms of this single parameter δ can be obtained for the polyhedron in Figs. 5(a) and 5(b):

$$f_T = \begin{cases} \dfrac{6}{\pi} \arcsin\left(\dfrac{\sqrt{3}[2(1-\delta)-\sqrt{3}]}{2(1-\delta)^2+[\sqrt{3}-(1-\delta)]^2}\right), & 1-\sqrt{3} < \delta < 1-\dfrac{2}{\sqrt{3}} \\[3mm] \dfrac{6}{\pi} \arcsin\left(\dfrac{[\sqrt{3}(1-\delta)-1]^2}{2+[\sqrt{3}(1-\delta)-1]^2}\right), & 1-\dfrac{2}{\sqrt{3}} < \delta < 1-\dfrac{1}{\sqrt{3}}, \end{cases} \tag{7}$$

$$f_R = 1 - f_T. \tag{8}$$

At the MPB we have $G_T = G_R$ or $\delta = 0$, so that the probability ratio for a particle of the cubic phase to transform into the rhombohedral and tetragonal phases becomes

$$\frac{f_R}{f_T} = \frac{\pi - 6\arcsin[(3-\sqrt{3})/6]}{6\arcsin[(3-\sqrt{3})/6]} \approx 1.45. \tag{9}$$

When we have an ensemble of the particles, such as a powder ceramic system, Eq. (9) represents the molar ratio of the two low-temperature phases at the MPB composition.[3]

III. COMPARISON WITH EXPERIMENTS

Because the difference of the two free-energy densities is small near the MPB we may write it as a series expansion of the composition about the MPB composition x_0,

$$g_R - g_T = \frac{1}{v}(G_R-G_T) = \sum_{n=1}^{\infty} a_n(x-x_0)^n, \tag{10}$$

where v is the volume of the individual element in a statistical ensemble and x_0 is the composition at which the free energies of the two low-temperature phases become equal. Looking at Fig. 1(d) one finds that Eq. (10) may be well represented by a linear function near x_0,

$$g_R - g_T = a_1(x-x_0). \tag{11}$$

Using this relation and Eqs. (5) and (6) we can derive the width of the coexistence region Δx,

$$\Delta x = (2kT_c/|a_1|v)\ln 3. \tag{12}$$

An important conclusion can be drawn from Eq. (12): The width and the boundary compositions of the coexistence region are not well defined in a complete solid solution system, they depend on the volume v of the statistical elements. This fact marks the physical difference between the phase coexistence inside a solubility gap and near the MPB of a complete solid solution system [see Figs. 1(a) and 1(c)]. A corollary from this conclusion is that the coexistence region will be infinitely sharp for a single-crystal system, but for a small-grain system the coexistence
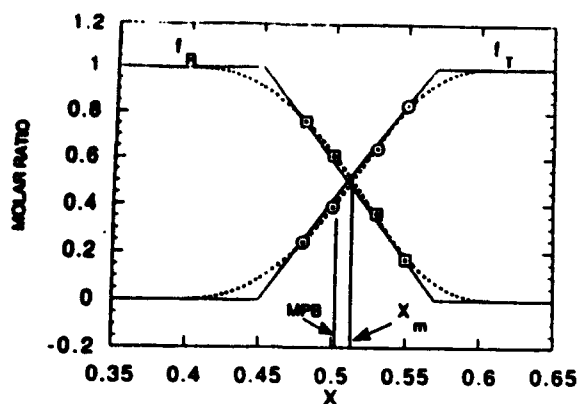
FIG. 6. Molar fractions f_R and f_T of the rhombohedral and tetragonal phases inside the coexistence compositional region for $0.1Pb_{0.9}K_{0.1}(Zn_{1/3}Nb_{2/3})O_{2.95}\cdot(0.9-x)PbZrO_3\cdot xPbTiO_3$ solid solution. The squares and circles are experimental data from Ref. 5; the solid curves were fitted using the Lever Rule, and the dotted curves were fitted using the current theory.
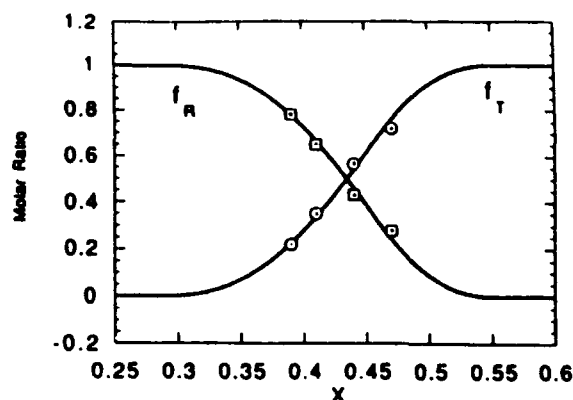

FIG. 7. Experimental data (the squares and circles) of Ari-Gur and Benguigui (Ref. 6) on the PZT system and the fitted curves using the current theory.

region will become considerably wider. For a fixed volume, if the free-energy difference of the two low-temperature phases changes drastically away from the MPB, i.e., $|\alpha_1|$ is large, there should be a very narrow coexistence region, otherwise the coexistence region could be wide.

Substituting Eq. (13) into Eq. (11) we can rewrite Eq. (5) in the following form:

$$\delta = 1 - \exp[(x-x_0)\ln 3/\Delta x]. \tag{13}$$

The parameters x_0 and Δx may be fitted from experimental data using Eqs. (13) and (7) [or Eq. (8)]. Two examples are given below to demonstrate the procedures.

It is known from experience that the coexistence region in the pure PZT system is very narrow because the grain growth is difficult to control. Therefore, due to the limitations of x-ray resolution it is difficult to obtain a reliable molar ratio of the rhombohedral and tetragonal phases from x-ray-diffraction measurements. However, when small amounts of dopants are added to the PZT system (within the limit of not destroying the solid solution characteristic), the coexistence region usually becomes wider and the x-ray-diffraction peaks become relatively easier to separate from each other.

We have found two sets of experimental data in the literature. The data points in Fig. 6 were measured by Hanh, Uchino, and Nomura[5] on the complete solid solution system $0.1Pb_{0.9}K_{0.1}(Zn_{1/3}Nb_{2/3})O_{2.95}\cdot(0.9-x)PbZrO_3\cdot xPbTiO_3$. (Note that the compositional variable x refers to the mole percent of $PbZrO_3$ in Ref. 5 but refers to the mole percent of $PbTiO_3$ in this article; all data points have been converted accordingly.) The squares and circles are the molar fractions of the rhombohedral and tetragonal phases, respectively. The authors of Ref. 5 have fitted their experimental data to the Lever Rule, which is shown in Fig. 6 as the solid curves. The two edge compositions are $x_1=0.45$ and $x_2=0.57$. Although it appears that the fitting is reasonably good for these limited data points, the kinks at x_1 and x_2 are in contradiction with the nature of a complete solid solution system. As men-

tioned above, the two edge compositions in the Lever Rule actually define a solubility gap, and one cannot explain the physical meaning of these two edge compositions for a complete solid solution system. The dotted curves are fitted using the theory presented in this article, and the two fitted parameters are $x_0=0.5027$ and $\Delta x=0.2066$. We can see that the fittings are surprisingly good. More important, the kinks have been smoothed out, which is more consistent with the nature of the complete solid solution systems.

In comparison the width of the coexisting region obtained from the current theory, $\Delta x=0.2066$, is wider than that given by the Lever Rule, $x_2-x_1=0.12$. Both theories agree reasonably well if the second phase has more than 20%, but they deviate severely from each other near the edges of the coexistence region. In practice, the long tails in our theory may be difficult to observe because of the limited resolution of conventional x-ray techniques. For this reason we give a useful relation to estimate the width parameter Δx,

$$\Delta x \approx 18.87\ (x_m - x_0), \tag{14}$$

where x_0 is the MPB composition at which $f_R:f_T \approx 60:40$, and x_m is the equal fraction composition at which $f_R:f_T = 50:50$. These two compositions can be easily obtained from experiments and are indicated in Fig. 6.

Unlike the Lever Rule, the distribution functions, Eqs. (7) and (8), are asymmetric with respect to the equal fraction composition x_m, and one may notice this point by looking at the dotted curves in Fig. 6. This asymmetric feature has been verified by experiments in other systems, for example, the experimental results of Ari-Gur and Benguigui[6] for the PZT solid solution system (Fig. 7). One can clearly see this asymmetry from their data. Although it seems that some errors might have occurred in their experiments because the MPB composition has been shifted further to the rhombohedral side (which might be caused by the presence of impurities in their chemicals), the data can still be well fitted using Eqs. (7) and (8). The two fitted parameters are $x_0=0.4212$ and $\Delta x=0.2554$.

IV. SUMMARY AND CONCLUSIONS

The distribution functions have been derived for the coexisting phases near the morphotropic phase boundary in a complete binary solid solution system. It is shown that the phase coexistence near the MPB in a complete solid solution is different from the phase coexistence inside a solubility gap. The latter has two special compositions x_1 and x_2 specifying the edges of a solubility gap, and the distribution inside the gap can be described by the Lever Rule. While for the former, only the MPB composition x_0 is well defined, the width of the coexisting region is inversely proportional to the volume of individual element in a statistical ensemble.

Explicitly, we can see the difference between the two theories through the following example. Assume we have a binary system AC-BC and assume they form solid solutions α and β for A- and B-rich compounds, respectively. Then, for any given composition x inside the coexistence region of α and β we have the two theories describe the following situations:

(a) Lever Rule:

$$x\mathrm{AC}+(1-x)\mathrm{BC}=f_\alpha\mathrm{A}_{x_1}\mathrm{B}_{1-x_1}\mathrm{C} \ (\alpha \ \text{structure})$$

$$+f_\beta\mathrm{A}_{x_2}\mathrm{B}_{1-x_2}\mathrm{C} \ (\beta \ \text{structure}),$$

(b) Present theory:

$$x\mathrm{AC}+(1-x)\mathrm{BC}=f_\alpha\mathrm{A}_x\mathrm{B}_{1-x}\mathrm{C} \ (\alpha \ \text{structure})$$

$$+f_\beta\mathrm{A}_x\mathrm{B}_{1-x}\mathrm{C} \ (\beta \ \text{structure}).$$

The Lever Rule specifies a solubility gap from x_1 to x_2, and the two coexisting phases have different chemical compositions as shown on the right-hand side (rhs) of the first equation, while the current theory deals with the structural phase mixing with the same chemical composition as indicated on the rhs of the second equation. It is our belief that the observed coexisting phases in a complete solid solution system actually consist of a second metastable structure that was frozen in at the paraelectric-ferroelectric phase transition.

Compared to the Lever Rule, the current theory does not give those kinks in the distribution functions, therefore it is more consistent with the nature of a complete solid solution system (no solubility gap). The distribution functions [Eqs. (7) and (8)] are asymmetric with respect to the middle point x_m, which is another major difference from the Lever Rule. Experimental results show that this asymmetry indeed exists (see Figs. 6 and 7). In addition to the surprisingly good agreement between the theory and the available experimental data, the current theory also provides a reasonable explanation to the controversy regarding the width of the coexistence region in the PZT system, which has been an issue of debate since the appearance of PZT. We conclude that a well-defined width cannot exist in a complete solid solution system because Δx is inversely proportional to the volume of the element in a given statistical ensemble, such as the grain size in a ceramic. Since the grain size depends strongly on the ceramic processing procedures, it is no surprise to see those reported experimental discrepancies regarding the width of the coexistence region.

[1] M. J. Haun, E. Furman, S. J. Jang, and L. E. Cross, Ferroelectrics 99, 63 (1989).
[2] V. A. Isupov, Sov. Phys. Solid State 12, 1084 (1970).
[3] W. Cao and L. E. Cross, Jpn. J. Appl. Phys. 31, 1399 (1992).
[4] M. J. Haun, E. Furman, H. A. McKinstry, and L. E. Cross, Ferroelectrics 99, 27 (1989).
[5] L. Hanh, K. Uchino, and S. Nomura, Jpn. J. Appl. Phys. 17, 637 (1978).
[6] P. Ari-Gur and L. Benguigui, Solid State Commun. 15, 1077 (1974).

3255   J. Appl. Phys., Vol. 73, No. 7, 1 April 1993

W. Cao and L. E. Cross   3255

APPENDIX 8

Polarization Gradient Coefficients and the Dispersion Surface of the Soft Mode in Perovskite Ferroelectrics

Wenwu Cao

Materials Research Laboratory, The Pennsylvania State University, University Park,

Pennsylvania 16802

Abstract

The gradient coefficients in the Landau-Ginzburg theory are crucial for quantitative description of domain walls in ferroelectrics. The magnitude of these gradient coefficients are a measure of nonlocal coupling strength of the polarization. In this paper, we intend to explain the physical meaning of these gradient coefficients in terms of lattice dynamics and give some relationships between these gradient coefficients and the dispersion surface of the soft mode. The implications for the study of over damped soft modes are also discussed.

I. Introduction

Many ferroelectric materials have perovskite structure with a cubic symmetry in the paraelectric phase. The symmetry of the low temperature ferroelectric phase can be tetragonal, rhombohedral or orthorhombic. Ferroelectric phases usually have more than one variants and these variants may coherently coexist within the symmetry frame of the parent phase, forming the so called twin structures. It is shown that these twin structures can be well described by Landau-Ginzburg (LG) type models.[1,2] All the expansion coefficients in the Landau theory correspond to certain macroscopic physical quantities and can be obtained experimentally. However, the physical meaning of the gradient coefficients, which regulate the domain wall formation and control the domain wall width in the twin structures, still needs to be specified.

A paraelectric-ferroelectric phase transition is characterized by a softening of a transverse optic mode at the Brillouin zone center due to the cancelation of the long range Coulomb forces and the short range repulsive forces.[3] The soft mode is stabilized above the phase transition temperature by the anharmonic interactions whose strength weakens as the temperature decreases. Using mean field theory, one can still formally retain the terminology of normal modes if the "soft mode" frequency is assigned to be temperature dependent.

Close to the phase transition temperature, the dominant contribution in the lattice Hamitonian is from the soft mode. Therefore, one may simply study the soft mode behavior to characterize the phase transition near T_c. For an inhomogeneous system, the spatial variation of the order parameter must be considered. This is done by adding an energy term induced by the order parameter gradients. Because the inclusion of both nonlinear and nonlocal terms in the energy expansion, one may expect to obtain large amplitude soliton-like solutions which can describe the domain walls (the transition region between coherent twin structures).[4,5,6] The physical meaning of these gradient coefficients can be seen from the study of small amplitude oscillations for which the nonlocal coupling can be treated as perturbations.[6,7] We will show in

2

this paper how these polarization gradients can be derived from a simplified lattice dynamical model.

Since polarization is the density of dipoles per unit volume, it is proportional to the magnitude of the associated optical mode. As will be shown in the third section of this paper that the lattice potential for a given optical mode can be written in terms of the polarization vector. Therefore, the Landau-Ginzburg potential can be directly used in the lattice dynamical calculations in the small representation of the soft mode.

II. Gradient Coefficients and Dispersion Surface of the Soft Mode

From soft mode theory, the potential energy for a cubic system may be expanded in terms of the eigenvector of the soft mode[3]

$$G = \frac{\kappa}{2} (u_1^2 + u_2^2 + u_3^2) \qquad (1)$$

where κ is related to the temperature dependent soft mode frequency, $\kappa \propto (T-T_c)$, and u_i ($i = 1,2,3$) are the components of the eigenvector of the soft mode. For the ferroelectric phase transition u is a relative displacement field.

If u is inhomogeneous, we must include the gradient energy in the energy expansion. For cubic symmetry the gradient energy may be written as follows,

$$G_g = \frac{\delta_{11}}{2} (u_{1,1}^2 + u_{2,2}^2 + u_{3,3}^2) + \delta_{12} (u_{1,1} u_{2,2} + u_{1,1} u_{3,3} + u_{2,2} u_{3,3})$$

$$+ \frac{\delta_{44}}{2} ((u_{1,2} + u_{2,1})^2 + (u_{1,3} + u_{3,1})^2 + (u_{2,3} + u_{3,2})^2) \qquad (2)$$

Assuming the effective mass for the mode is M then the equations of motion become

$$M \ddot{u}_1 + \kappa u_1 - \delta_{11} u_{1,11} - \delta_{12} (u_{2,21} + u_{3,31}) - \delta_{44} (u_{1,22} + u_{2,12} + u_{1,33} + u_{3,13}) = 0, \qquad (3a)$$

$$M \ddot{u}_2 + \kappa u_2 - \delta_{11} u_{2,22} - \delta_{12} (u_{1,12} + u_{3,32}) - \delta_{44} (u_{1,21} + u_{2,11} + u_{2,33} + u_{3,23}) = 0, \qquad (3b)$$

$$M \ddot{u}_3 + \kappa u_3 - \delta_{11} u_{3,33} - \delta_{12} (u_{1,13} + u_{2,23}) - \delta_{44} (u_{1,31} + u_{3,11} + u_{2,32} + u_{3,22}) = 0, \qquad (3c)$$

Eq.(3a-c) have plane wave solution of the form

$$u = U \exp [j (\omega t - k \cdot x)] \qquad (4)$$

3

Substituting eq. (4) into eqs. (3a-c) gives the eigenvalue problem

$$M\omega^2 U = \tilde{D}(k) U \qquad (5)$$

where $\tilde{D}(k)$ is the dynamical matrix

$$\tilde{D}(k) = \begin{pmatrix} \kappa + \delta_{11}k_1^2 + \delta_{44}(k_2^2 + k_3^2) & \delta_{12}\, k_1\, k_2 & \delta_{12}\, k_1\, k_3 \\ \delta_{12}\, k_1\, k_2 & \kappa + \delta_{11}k_2^2 + \delta_{44}(k_1^2 + k_3^2) & \delta_{12}\, k_2\, k_3 \\ \delta_{12}\, k_1\, k_3 & \delta_{12}\, k_2\, k_3 & \kappa + \delta_{11}k_3^2 + \delta_{44}(k_1^2 + k_2^2) \end{pmatrix} \qquad (6)$$

If the depolarization field is included, the equations of motion (3a-c) will contain one more term representing this contribution, which will split the longitudinal and transverse optical modes.[8,9] The depolarization field is given by

$$E(k) = - \frac{(P \cdot k)}{\varepsilon_0}\, \frac{k}{k^2} \qquad (7)$$

The additional contribution is a linear function of the polarization vector P which is proportional to the relative displacement field u. Adding eq. (7) to the r.h.s. of eq. (3a-c) leads to the dynamical matrix for a given k. In what follows, we will treat three k-values in the three principle directions of the k-space.

A. $k = [k, 0, 0]$.

Define $P_i = Z e u_i$, where Z is a constant which has a unit of inverse volume and e is the electron charge unit. The meanigng of Z will be clear from later derivations. For this k value, the dynamical matrix can be simplified to the following form

$$\tilde{D}(k) = \begin{pmatrix} \kappa + A + \delta_{11}k^2 & 0 & 0 \\ 0 & \kappa + \delta_{44}\, k^2 & 0 \\ 0 & 0 & \kappa + \delta_{44}\, k^2 \end{pmatrix} \qquad (8)$$

where A is a constant defined by

$$A = (1/\varepsilon_0)\,(Z e)^2 \qquad (9)$$

4

From Eq. (8) one can easily derive the dispersion relations for the longitudinal (ω_L) and transverse (ω_T) modes respectively:

$$\omega_L^2 = \frac{1}{M}(\kappa + A + \delta_{11} k^2) \qquad (10a)$$

$$\omega_T^2 = \frac{1}{M}(\kappa + \delta_{44} k^2) \qquad (10b)$$

B. $k = \frac{k}{\sqrt{2}} [1, 1, 0]$

The electrostatic force from the depolarization field is now given by

$$\frac{Z e (P_1 + P_2)}{2 \varepsilon_0} [1,1,0] = \frac{A (u_1 + u_2)}{2} [1, 1, 0] \qquad (11)$$

Therefore the dynamical matrix is

$$\tilde{D}(k) = \begin{pmatrix} \kappa + A/2 + (\delta_{11} + \delta_{44}) k^2/2 & A/2 + \delta_{12} k^2/2 & 0 \\ A/2 + (\delta_{12}/2) k^2 & \kappa + A/2 + (\delta_{11} + \delta_{44}) k^2/2 & 0 \\ 0 & 0 & \kappa + \delta_{44} k^2 \end{pmatrix} \qquad (12)$$

and the dispersion relations are

$$\omega_L^2 = \frac{1}{M}[\kappa + A + \frac{1}{2}(\delta_{11} + \delta_{12} + \delta_{44}) k^2] \qquad (13a)$$

$$\omega_{T_1}^2 = \frac{1}{M}[\kappa + \frac{1}{2}(\delta_{11} - \delta_{12} + \delta_{44}) k^2] \qquad (13b)$$

$$\omega_{T_2}^2 = \frac{1}{M}[\kappa + \delta_{44} k^2] \qquad (13c)$$

Here the two transverse modes are not degenerate.

C. $k = \frac{k}{\sqrt{3}} [1, 1, 1]$.

For this case the Coulomb force from the depolarization field is

$$\frac{Z e (P_1 + P_2 + P_3)}{3 \varepsilon_0} [1,1,1] = \frac{A (u_1 + u_2 + u_3)}{3} [1, 1, 1] \qquad (14)$$

5

and the dynamical matrix becomes

$$\widetilde{D}(k) = \begin{pmatrix} \kappa + A/3 + (\delta_{11}/3 + 2\,\delta_{44}/3)\,k^2 & A/3 + (\delta_{12}/3)\,k^2 & A/3 + (\delta_{12}/3)\,k^2 \\ A/3 + (\delta_{12}/3)\,k^2 & \kappa + A/3 + (\delta_{11}/3 + 2\,\delta_{44}/3)\,k^2 & A/3 + (\delta_{12}/3)\,k^2 \\ A/3 + (\delta_{12}/3)\,k^2 & A/3 + (\delta_{12}/3)\,k^2 & \kappa + A/3 + (\delta_{11}/3 + 2\,\delta_{44}/3)\,k^2 \end{pmatrix} \quad (15)$$

The dispersion relations are therefore given by

$$\omega_L^2 = \frac{1}{M}\left[\kappa + A + \frac{1}{3}(\delta_{11} + 2\,\delta_{12} + 2\,\delta_{44})\,k^2\right] \qquad (16a)$$

$$\omega_T^2 = \frac{1}{M}\left[\kappa + \frac{1}{3}(\delta_{11} - \delta_{12} + 2\,\delta_{44})\,k^2\right] \qquad (16b)$$

Note that the dispersion relations derived above are for the cubic phase near k=0 but not for the low temperature ferroelectric phase.

III. The Expansion Coefficients and Lattice Dynamics

Taking the limit $k \to 0$ in the dispersion relations derived above, one finds that the coefficient κ/M becomes the soft transverse mode frequency square,

$$\lim_{k \to 0} \omega_T^2 = \kappa/M \qquad (17)$$

The longitudinal mode will not become soft at $T = T_c$ because of the depolarization field contribution A,

$$\lim_{k \to 0} \omega_L^2 = \frac{1}{M}(\kappa + A) \qquad (18)$$

The simplest model to calculate these coefficients in terms of microscopic quantities is to study the k =0 mode for a biatomic system using rigid ion model, in which the soft mode represents the relative displacement field, the mass is the relative mass, and the polarization is equal to the ionic charge times the relative displacement then devided by the unit cell volume.

6

However, in the perovskite structure there are three different types of ions, hence, a more realistic model would be a three body system model. In what follows we will use a one dimensional rigid ion model for $BaTiO_3$ as an example to illustrate the relationship between the coefficients in Eq. (1) and the microscopic quantities.

According to the structural work of Shirane et al,[10] the soft optical mode in $BaTiO_3$ consists of the relative motion of Titanium, Barium and Oxygen (Fig. 1a). Because the center of mass and the center of charge for each type of ions coincide, we can effectively treat this system as a three-body system in the lattice dynamical calculations. For convenience the ion groups are labeled as follows (see Fig. 1b): Ba --- 1; Ti --- 2; and 3 O ---3.

The potential energy represents the $k = 0$ mode for this three-body system is

$$\Phi = \frac{\kappa_1}{2} (x_1 - x_2)^2 + \frac{\kappa_2}{2} (x_2 - x_3)^2 \qquad (19)$$

In order to derive the equations of motion one should also consider the Lorentz field, which leads to the following differential equations:

$$m_1 \ddot{x}_1 = - \kappa_1 (x_1 - x_2) + \frac{1}{3\varepsilon_0} q_1 P \qquad (20\,a)$$

$$m_2 \ddot{x}_2 = - \kappa_1 (x_2 - x_1) - \kappa_2 (x_2 - x_3) + \frac{1}{3\varepsilon_0} q_2 P \qquad (20\,b)$$

$$m_3 \ddot{x}_3 = - \kappa_2 (x_3 - x_2) + \frac{1}{3\varepsilon_0} q_3 P \qquad (20\,c)$$

$$q_1 + q_2 + q_3 = 0 \qquad (21)$$

$$P = (q_1 x_1 + q_2 x_2 + q_3 x_3) / a_0^3 \qquad (22)$$

where a_0 is the lattice constant, q_1, q_2, q_3 are the charges of the three ion groups, P is the polarization.

For convenience let us introduce two new variables

$$u = x_1 - x_3; \quad v = x_2 - x_3.$$

Using eqs. (21) and (22), and the new variables u and v the equations of motion (20a-c) can be simplified to become

7

$$\ddot{u} = a\,u + b\,v \qquad\qquad (23a)$$
$$\ddot{v} = c\,u + d\,v \qquad\qquad (23b)$$

where
$$a = -\frac{k_1}{m_1} + \frac{q_1}{3\,\varepsilon_0\,a_0^3}\left(\frac{q_1}{m_1} + \frac{q_1+q_2}{m_3}\right)$$
$$b = -\left(\frac{k_2}{m_3} - \frac{k_1}{m_1}\right) + \frac{q_2}{3\,\varepsilon_0\,a_0^3}\left(\frac{q_1}{m_1} + \frac{q_1+q_2}{m_3}\right)$$
$$c = \frac{k_1}{m_2} + \frac{q_1}{3\,\varepsilon_0\,a_0^3}\left(\frac{q_2}{m_2} + \frac{q_1+q_2}{m_3}\right)$$
$$d = -\left(\frac{k_1+k_2}{m_2} + \frac{k_2}{m_3}\right) + \frac{q_2}{3\,\varepsilon_0 a_0^3}\left(\frac{q_2}{m_2} + \frac{q_1+q_2}{m_3}\right)$$

Eqs (23a,b) have the harmonic oscillator solution

$$u = u_0\,\exp(j\omega t) \qquad\qquad (24)$$

$$v = v_0\,\exp(j\omega t) \qquad\qquad (25)$$

and the eigenfrequency ω is given by

$$\omega_\pm^2 = \frac{1}{2}\left[\,-a-d \pm \sqrt{(a+d)^2 - 4\,(ad-bc)}\,\right] \qquad\qquad (26)$$

In any given mode the relative displacement u and v are proportional to each other. For the coordinate system in Fig. 1, u and v always have the same sign. Assuming one of the modes, for example ω_-, becomes soft at lower temperatures due to the decrease of the coupling strength between different ions, then, their magnitudes have the following relationship:

$$v_0 = \frac{1}{2\,b}\left(d - a + \sqrt{(a+d)^2 - 4\,(ad-bc)}\,\right) u_0 \qquad\qquad (27)$$

From Eqs. (21) and (22) the polarization P is given by

$$P = (q_1\,u + q_2\,v)/a_0^3 = \left[\,q_1 + \frac{q_2}{2\,b}\left(d - a + \sqrt{(a+d)^2 - 4\,(ad-bc)}\,\right)\right] u\,/a_0^3 \qquad\qquad (28)$$

Therefore, in this mode

$$Z\,e = \left[\,q_1 + \frac{q_2}{2\,b}\left(d - a + \sqrt{(a+d)^2 - 4\,(ad-bc)}\,\right)\right]/a_0^3 \qquad\qquad (29)$$

The value of P can be obtained from pyroelectric measurements and u may be calculated from

X-ray diffractions of the low and high temperature phases, hence, Ze can also be obtained experimentally.

Since v and P are linearly proportional to u, we could simplify the problem by constructing a new single variable potential $G = (\kappa/2) u^2$ which gives rise to the following equation of motion.

$$\ddot{u} = a\, u + b\, v$$
$$= \frac{1}{2} [\, -(a+d) - \sqrt{(a+d)^2 - 4(ad-bc)} \,] \, u$$
$$= \frac{\kappa}{M} u \tag{30}$$

where κ has the dimension of force constant and M has the dimension of mass according to the definition of a, b, c and d. For a three dimensional system, the constructed potential which leads to Eq.(30) will have the same form as Eq. (1) according to symmetry. Because u is also proportional to the polarization P [eq. (28)], we may also write down the constructed potential in terms of the polarization vector P, which becomes the Landau potential for a ferroelectric system $G = (\alpha/2) P^2$, $\alpha = \kappa/ (Z\, e)^2$.

For longitudinal vibrations, we have to add the depolarization field $(- P/\varepsilon_0)$ to the equation of motion Eq.(20 a -c), which will add a positive contribution to the eigenfrequency preventing it to become soft like the transverse mode. Formally, the relationship between ω_L and ω_T may be written as

$$\omega_L^2 = \omega_T^2 + \frac{A}{M} \tag{30}$$

where A is a positive constant reflecting the contribution of the depolarization field.

IV. Summary and conclusions

It is shown that the polarization gradient coefficients in the Landau-Ginzburg theory can be directly related to the dispersion surface of the soft mode. Therefore, their physical meaning becomes apparent. The correspondence between the Landau theory and the lattice dynamic potential was illustrated through a simple one dimensional rigid ion model for BaTiO$_3$ at k=0. Since the polarization and the relative displacement field have a linear relationship, the polarization

9

coefficients in the Landau-Ginzburg theory may be calculated from the measured dispersion curves near the soft mode. For cubic symmetry there are only three independent gradient coefficients, the dispersion anisotropy of the soft mode can be determined through measurements along the three principal directions. These gradient coefficients in principle can be obtained through inelastic neutron scattering experiments. However, in many cases these dispersion curves are very difficult to measure because of the high transition temperature. To my knowledge, a complete set of the dispersion relations do not exist in the literatures for the known ferroelectric materials. One of the intentions of this paper is to re-emphasize the importance to measure these dispersion curves which can be used for the study of domain walls in ferroelectrics.

An interesting point should be also mentioned is the possibility of obtaining the dispersion surface of the soft mode through direct measurements on the domain wall profiles[11], because the gradient coefficients can be extracted from fitting the measured polarization profiles to the soliton-like solutions of nonlinear nonlocal continuous medium theory.[2-6] This could be very useful to study the dispersion surface of the over damped soft mode, such as in $BaTiO_3$, which can not be obtained through inelastic neutron scattering.

Reference

1. V. A. Zhirnov, Zh. Eksp. Teor. Fiz. 35, 1175 (1958) [Sov. Phys. JETP 35, 822 (19590]

2. W. Cao and L. E. Cross, Phys. Rev. B 44, 5 (1991).

3. W. Cochran, Advances in Phys., 9, 387 (1960).

4. J. A. Krumhansl and J. R. Schrieffer, Phys. Rev. B 11, 3535 (1975).

5. G. R. Barsch and J. A. Krumhansl, Phys. Rev. Lett., 11, 1069 (1984).

6. W. Cao and G. R. Barsch, Phys. Rev. B **41**, 4334 (1990).

7. K. Gesi, J. D. Axe, G. Shirane and A. Linz, Phys. Rev. B **5**, 1933 (1972).

8. G. Venkataraman, L. A. Feldkamp, and V. C. Sahni, in "Dynamics of Perfect Crystals" Dynamics" The MIT Press, Cambridge, Massachusetts, p166, (1975).

9. W. Cochran, in "The Dynamics of Atoms in Crystal" Edward Arnold, London,.p 83 (1973).

10. G. Shirane, R. Pepinsky, and D. C. Frazer, Acta Cryst., **9**, 131 (1956).

11. W. Cao and Clive Randall, Solid State Comm., **86**, 435 (1993).

Figure Captions

Figure 1. (a) Illustration of the ionic displacements in BaTiO$_3$ from ref. 10.

(b) One dimensional model for the soft mode.
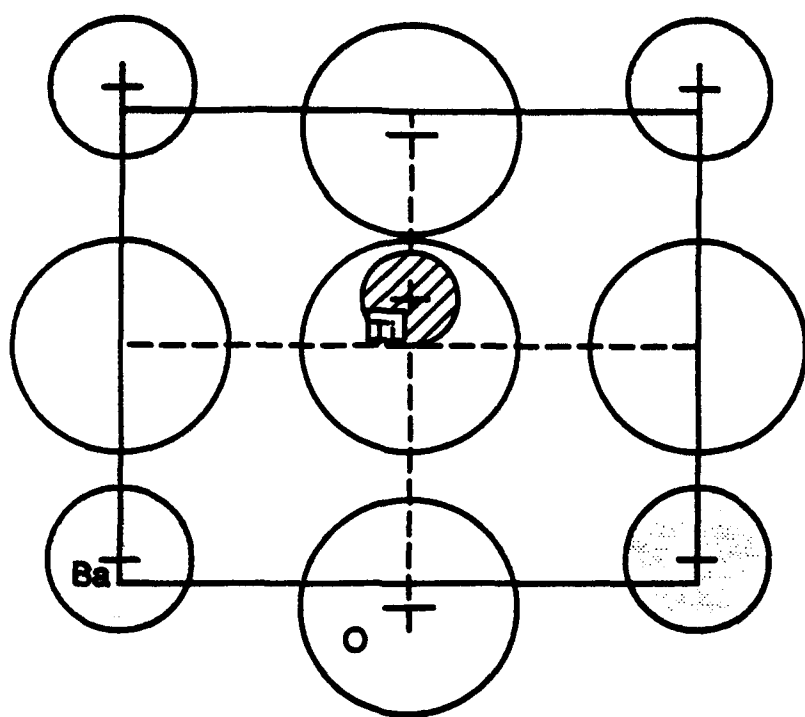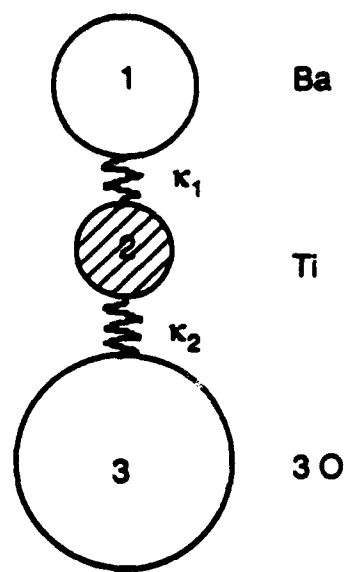
(a)   (b)

Figure 1.

APPENDIX 9

NONLINEAR AND NONLOCAL CONTINUUM THEORY ON DOMAIN WALLS IN FERROELECTRICS

WENWU CAO AND L. E. CROSS
Materials Research Laboratory, The Pennsylvania State University,
University Park, PA 16802

Abstract The domain structures in ferroelectrics can be described by a Landau-Ginzburg type theory with the twin and twin band (domain) structures being nonlinear and nonlocal excitations of the ferroelectric phase. The polarization gradients in the theory reflect the degree of nonlocal coupling along different crystallographic orientations. These gradient parameters can be obtained either from the dispersion surface of the soft mode or through fitting the polarization profile measured by the holographic electron microscopy.

INTRODUCTION

The understanding of domain structures is essential for the design and applications of ferroelectrics. It has been long recognized that the piezoelectric and dielectric properties of ferroelectric ceramics are mainly determined by the behavior of domain structures. The formation of domains in ferroelectrics is due to the existence of milti-variants in the ferroelectric phase. Atomic coherency is usually maintained across the domain boundaries, which make it possible to switch domain orientations from one to the other using external (either mechanical or electrical) fields. This switching gives rise to the so called extrinsic contributions to the materials properties. The formation of domain walls in ferroelectrics may be treated in terms of solitory wave excitations in a nonlinear and nonlocal system. Single kink-like and periodic solitory wave solutions for the twin and periodic domain structures can be derived using the continuum theory.[1-4] Since all the expansion coefficients in the Landau-Devonshire model can be expressed in terms of measurable macroscopic quantities, the continuum theory can give quantitative description of the domain wall properties, including the profile of polarization across the domain wall, domain wall width, energy stored in the muti-domain structure, and the stress build up at the domain wall region, once the polarization gradient coefficients are obtained.

THE MODEL

The Landau-Devonshire type phenomenological theory for ferroelectrics has been developed for the ferroelectric phase transition.[5,6,7] For a cubic system, such as perovskite ferroelectrics, the elastic Gibbs free energy can be expressed in the following form:

$$G = G_p + G_{el} + G_c \tag{1}$$

$$G_p = A (P_1^2 + P_2^2 + P_3^2) + B (P_1^4 + P_2^4 + P_3^4) + C (P_1^6 + P_2^6 + P_3^6)$$
$$+ D (P_1^2 P_2^2 + P_2^2 P_3^2 + P_1^2 P_3^2) + E (P_1^4 P_2^2 + P_1^2 P_2^4 + P_2^4 P_3^2 + P_2^2 P_3^4$$
$$+ P_3^2 P_1^4 + P_1^2 P_3^4) + H P_1^2 P_2^2 P_3^2 \tag{2}$$

$$G_{el} = -\frac{s_{11}}{2} (X_{11}^2 + X_{22}^2 + X_{33}^2) - s_{12} (X_{11}X_{22} + X_{22}X_{33} + X_{11}X_{33})$$
$$-\frac{s_{44}}{2} (X_{12}^2 + X_{13}^2 + X_{23}^2) \tag{3}$$

$$G_c = Q_{11} (X_{11} P_1^2 + X_{22} P_2^2 + X_{33} P_3^2) + Q_{12} [X_{11} (P_2^2 + P_3^2) + X_{22} (P_1^2 + P_3^2) + X_{33} (P_1^2 + P_2^2)] + Q_{44} (X_{12} P_1 P_2 + X_{13} P_1 P_3 + X_{23} P_2 P_3) \tag{4}$$

where A, B, C, D, E, H are the linear and nonlinear dielectric constants, s_{ij} are the elastic compliance coefficients, Q_{ij} are the electrostriction constants, P_i and X_{ij} are the components of polarization and stress, respectively. All the coefficients are assumed to be independent of temperature except A which is a linearly function of T,

$$A = \alpha (T - T_0) \tag{5}$$

In a homogeneous system, a paraelectric-ferroelectric phase transition occurs at Tc. Under stress free condition, the phase transition temperature Tc and the spontaneous polarization P_c at the transition can be derived by minimizing Eq. (1),

$$T_c = T_0 + \frac{B^2}{4 C \alpha} \tag{6}$$

$$P_c^2 = \frac{-B}{2 C} \cdot \tag{7}$$

One of the low temperature ferroelectric phases is the tetragonal phase. There are six energetically degenerate variants in the tetragonal phase: $(\pm P_s, 0, 0)$, $(0, \pm P_s, 0)$ and $(0, 0, \pm P_s)$, where P_s is the spontaneous polarization given by

$$P_s = \sqrt{\frac{-B + \sqrt{B^2 - 3 AC}}{3 C}} \tag{8}$$

These energetically degenerate variants can coexist in the ferroelectric phase to form the twin structures. Electron microscopy reveals that the ionic coherency is maintained across domain walls, but domain walls are not atomically sharp. Domain wall width is determined by the nonlocal coupling strength of the ferroelectric system.

Since the nonlinearity has been included in the model [see Eqs. (1)-(4)], if we add the contributions of nonlocal coupling, then from soliton theory, we may expect solitory wave excitations in the ferroelectric phase. These excitations are in deed found and they represent the ferroelectric domain walls.

For a perovskite system, the symmetry of the high temperature phase is cubic, therefore, the Gibbs energy representing the nonlocal coupling can be written as follows:[2]

$$G_g = \frac{1}{2} g_{11} (P_{1,1}^2 + P_{2,2}^2 + P_{3,3}^2) + g_{12} (P_{1,1} P_{2,2} + P_{1,1} P_{3,3} + P_{2,2} P_{3,3})$$
$$+ \frac{1}{2} g_{44} [(P_{1,2} + P_{2,1})^2 + (P_{1,3} + P_{3,1})^2 + (P_{2,3} + P_{3,2})^2] \qquad (9)$$

here the indices after the comma represent derivatives with respect to space variable along that axis. Upon the minimization of the total free energy of the system Eqs. (1) and (9), one can obtain the solutions for the domain walls.[2]

90° DOMAIN WALLS

There are two types of domain walls in the tetragonal ferroelectrics. One is the 180° domain wall which divides a twin domain with identical strain but opposite polarization, and the other is the 90° domain wall which divides two domains whose polarization and spontaneous strain are nearly 90° from each other. Solutions for the 180° domain walls can be easily obtained since the problem is one-dimensional.[2] Here we only solve the problem of 90° domain walls for which the problem can be rendered to quasi-one-dimensional.

From transmission electron microscopy studies, domain walls tend to broaden or bent near the surface, however, inside the sample they have well defined wall-like
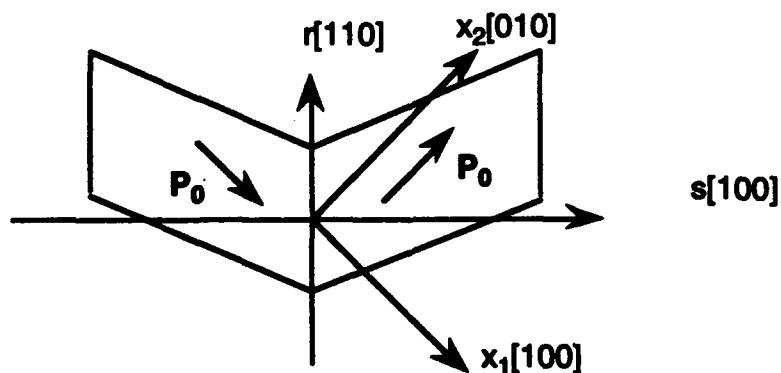

FIGURE 1. A tetragonal twin structure and the coordinate system used in this paper.

structure with translational symmetry parallel to the wall plane. Therefore, while dealing with a <110>-type domain walls in tetragonal ferroelectrics we can rotate the x_1, x_2 coordinates about the x_3 coordinate by 45° so that the properties of the domain walls only depend on one space variable (s-coordinate as indicated in Fig. 1) only.

In the new coordinate system the equilibrium conditions are governed by the following equations:[2]

$$\frac{\partial}{\partial x_j}[\frac{\partial G}{\partial P_{i,j}}] - \frac{\partial G}{\partial P_i} = 0 , \quad (i,j = s, r, 3)$$

(10)

$$X_{ij,j} = 0, \quad (i,j = s, r, 3)$$

(11)

and we also need the elastic compatibility relations

$$\varepsilon_{ikl}\, \varepsilon_{jmn}\, x_{ln,km} = 0 \quad (i,j,k,l,m,n = s, r, 3)$$

(12)

to insure the elastic continuity since in our model the domain walls are intrinsic excitations, no defects are created in the domain wall region. x_{ln} is the component of elastic strain tensor and ε_{ikl} is the Levi-Civita density.

Eqs (11) and (12) has three nontrivial solutions:

$$X_{r3} = 0$$

(13)

$$X_{rr}=\frac{1}{2\,(s_{11}s_{ss}-s_{12}^2)}\{[\, 2s_{12}Q_{12} -s_{11}(Q_{11}+Q_{12})]P_0^2 -[\, 2s_{12}Q_{12} -s_{11}(Q_{11}+Q_{12}-Q_{44})]P_s^2$$

$$-[2s_{12}Q_{12} -s_{11}(Q_{11}+Q_{12}+Q_{44})]P_r^2\}$$

(14)

$$X_{33}=\frac{1}{2(s_{11}s_{ss}-s_{12}^2)}\{[s_{12}(Q_{11}+Q_{12}) -2s_{ss}Q_{12}]P_0^2 -[\, s_{12}(Q_{11}+Q_{12}+Q_{44}) -2s_{ss}Q_{12}]P_r^2$$

$$-[s_{12}(Q_{11}+Q_{12}-Q_{44}) -2s_{ss}Q_{12}]\, P_s^2\}$$

(15)

where

$$s_{ss}=\frac{1}{2}(s_{11}+s_{12}+\frac{s_{44}}{2}).$$

It can be easily verified that the two stress components X_{rr} and X_{33} are nonzero only in the vicinity of the domain wall. These nonzero stress components near the domain wall region is the cause of the faster etching rate which makes the domain walls visible through chemical etching technique.

In order to see the general trend of the variation of polarization profile without specifying the coefficients to a particular system, we normalize the polarization and the space variable s into dimensionless forms by the following substitutions:

$$P_r=\sqrt{-\frac{B}{2C}}\quad f_r = P_c\, f_r \qquad\qquad P_s =\sqrt{-\frac{B}{2C}}\quad f_s = P_c\, f_s$$

(16a,b)

$$s = \gamma\, \xi, \qquad \gamma = (\frac{G_{ss}\, G_{rs}}{4\, A_c^2})^{1/4}$$

(17a,b)

where

$$G_{ss}=\frac{1}{2}(g_{11}+g_{12}+2g_{44}), \quad G_{rs}=\frac{1}{2}(g_{11}-g_{12}),$$

and define the dimensionless temperature as

$$\tau=\frac{T-T_0}{T_c-T_0} \tag{18}$$

then the equilibrium condition Eq. (10) can be written in the following form for a 90° twin structure,

$$a\,f_{s,\,\xi\xi}=\tau_s\,f_s+b_s f_s^3+c\,f_s f_r^2+df_s^5+(8-\frac{2}{3}d)\,f_s^3 f_r^2+(4-\frac{1}{3}d)\,f_s f_r^4 \tag{19}$$

$$\frac{1}{a}f_{r,\,\xi\xi}=\tau_r\,f_r+b_r f_r^3+c\,f_r f_s^2+df_r^5+(8-\frac{2}{3}d)\,f_r^3 f_s^2+(4-\frac{1}{3}d)\,f_r f_s^4 \tag{20}$$

where the coefficients are given by

$$a=\sqrt{\frac{G_{ss}}{G_{rs}}} \tag{21}$$

$$\tau_s=\tau-\frac{(1+\sqrt{1-\frac{3}{4}\tau})}{3(s_{11}s_{ss}-s_{12}^2)B}\{(Q_{11}+Q_{12}-Q_{44})[2s_{12}Q_{12}-s_{11}(Q_{11}+Q_{12})]$$
$$+2Q_{12}[s_{12}(Q_{11}+Q_{12})-2s_{ss}Q_{12}]\} \tag{22}$$

$$\tau_r=\tau-\frac{(1+\sqrt{1-\frac{3}{4}\tau})}{3(s_{11}s_{ss}-s_{12}^2)B}\{(Q_{11}+Q_{12}+Q_{44})[2s_{12}Q_{12}-s_{11}(Q_{11}+Q_{12})]$$
$$+2Q_{12}[s_{12}(Q_{11}+Q_{12})-2s_{ss}Q_{12}]\} \tag{23}$$

$$b_s=-2-\frac{D}{B}+\frac{1}{2B(s_{11}s_{ss}-s_{12}^2)}\{(Q_{11}+Q_{12}-Q_{44})[2s_{12}Q_{12}-s_{11}(Q_{11}+Q_{12}-Q_{44})]$$
$$+2Q_{12}[s_{12}(Q_{11}+Q_{12}-Q_{44})-2s_{ss}Q_{12}]\} \tag{24}$$

$$b_r=-2-\frac{D}{B}+\frac{1}{2B(s_{11}s_{ss}-s_{12}^2)}\{(Q_{11}+Q_{12}+Q_{44})[2s_{12}Q_{12}-s_{11}(Q_{11}+Q_{12}+Q_{44})]$$
$$+2Q_{12}[s_{12}(Q_{1.}+Q_{12}+Q_{44})-2s_{ss}Q_{12}]\} \tag{25}$$

$$c=-6+\frac{D}{B}+\frac{1}{2B(s_{11}s_{ss}-s_{12}^2)}\{(Q_{11}+Q_{12}-Q_{44})[2s_{12}Q_{12}-s_{11}(Q_{11}+Q_{12}+Q_{44})]$$
$$+2Q_{12}[s_{12}(Q_{11}+Q_{12}+Q_{44})-2s_{ss}Q_{12}]\} \tag{26}$$

$$d=\frac{3}{4}(1+\frac{E}{C}) \tag{27}$$

RESULTS AND DISCUSSIONS

Using the normalized equations, we can study the influence of different parameters to the polarization profile and obtain a conceptual understanding on the nature of the polarization variation in the domain wall region. Fig. 2 shows the variation of the polarization components with the parameter a across a 90° domain wall. One can see that the domain wall becomes wider as a increases. In real dimensions, because the scaling factor of the space variables, γ, is directly related to the product $G_{ss}*G_{rs}$ [see eq.(17)], domain wall becomes wider as the gradient coefficients become larger.
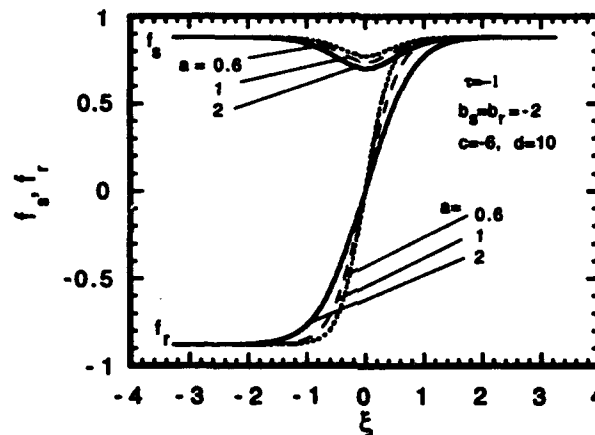
FIGURE 2. Variation of polarization components f_S and f_r induced by the change of parameter a across a 90° domain wall. The gradient parameter a determines the width of the domain wall.
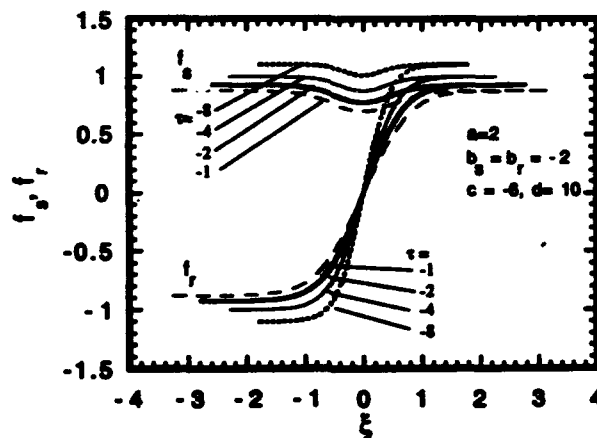
FIGURE 3. Variation of polarization components f_s and f_r with temperature τ across a 90° domain wall. The asymptotic values of the polarization components increase and the domain wall width decrease while lowering temperature.
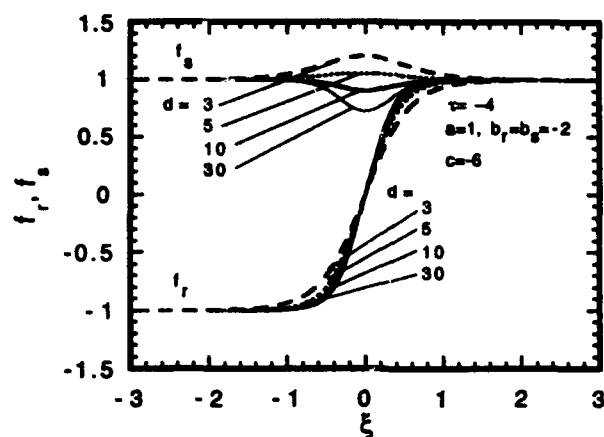
FIGURE 4. Variation of polarization components f_S and f_r induced by the change of parameter d across a 90° domain wall. The nonlinear parameter d influences the magnitude of the polarization variation in the domain wall region.
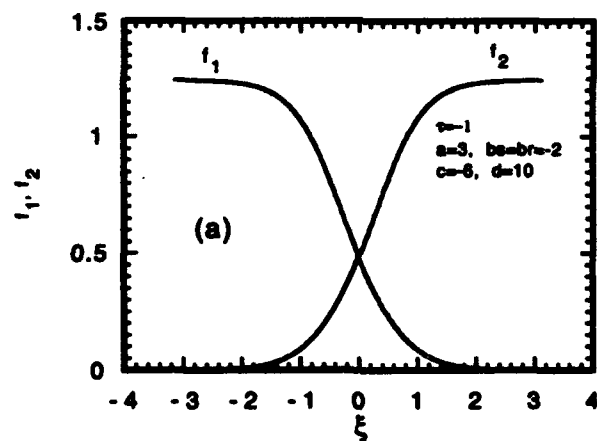

FIGURE 5. (a) Polarization components f_1 and f_2 across a 90° domain wall, and (b) Illustration of the variations of the polarization vector and the unite cell distortion across a 90° domain wall.

Fig. 3 shows the variation of the polarization with temperature τ. The asymptotic values of the magnitude of the polarization components increase and the domain wall thickness decreases as the temperature is lowered. The temperature dependence is strong near the transition and gradually becomes insensitive when the temperature is far below T_c. Fig. 4 shows the variation of the polarization components f_s and f_r induced by the change of parameter d. We can see that the magnitude of f_s is very sensitive to d while the domain wall thickness is relative insensitive to d. We can also calculate the polarization components f_1 and f_2 in the original coordinates. One example is given in Fig. 5 (a) for a set of chosen parameters. The corresponding unit cell distortion and the polarization variation across the domain wall are illustrated in Fig. 5(b). The polarization vector rotates gradually from one orientation into the other accompanied also by a change of the magnitude.

All properties of the domain walls can be quantitatively calculated using this model once the expansion coefficients are known. As we have mentioned above that the polarization gradient coefficients are most crucial for the study of domain walls, which may be derived from the measurements on the dispersion surface of the soft mode.[8,9] In general, inelastic neutron scattering to probe the soft mode may be difficult due to the relatively high transition temperature in many systems of interest and in some cases, the soft mode is over damped. An alternative way to obtain these coefficients would be to probe the polarization profile across the domain wall and then fitting the unknown coefficients using the differential equations (19) and (20). The recently emerged new technique, electron holography, may offer an option to this end.[10,11]

REFERENCES

1. V. A. Zhirnov, Zh. Eksp. Teor. Fiz. 35, 1175 (1958) [Sov. Phys. JETP 35, 822 (19590].
2. W. Cao and L. E. Cross, Phys. Rev. B 44, 5 (1991).
3. F. Falk, Z. Phys. B 51, 177 (1983).
4. G. R. Barsch and J. A. Krumhansl, Phys. Rev. Lett., 11, 1069 (1984).
5. A. F. Devonshire, Phil. Mag., 40, 1040 (1949); 42, 1065 (9151).
6. W. R. Bussem, L. E. Cross and A. K. Goswami; J. Amer. Ceram. Soc., 49, 33 (1966).
7. A. J, Bell and L. E. Cross, Ferroelectrics, 59 (1984).
8. W. Cao and G. R. Barsch, Phys. Rev. B 41, 4334 (1990).
9. K. Gesi, J. D. Axe, G. Shirane and A. Linz, Phys. Rev. B 5, 1933 (1972).
10. X. Zhang, T. Hashimoto and D. C. Joy, Appl. Phys. Lett. 60, 784 (1992).
11. W. Cao and C. A. Randall, Solid State Comm. 86, 435 (1993).

APPENDIX   10

THEORY ON THE FRINGE PATTERNS IN THE STUDY OF FERROELECTRIC DOMAIN WALLS USING ELECTRON HOLOGRAPHY

Wenwu Cao and Clive Randall
Materials Research Laboratory, The Pennsylvania State University
University Park, Pennsylvania 16802

The realization of electron holography provides a new powerful tool to probe the subtle and local changes of electric and magnetic fields inside a crystal structure through the phase variation of electron wave function. For a ferroelectric system the interference fringe patterns across a domain wall are very strongly affected by the presence of surface charge compensations. If the compensation is incomplete, a residue depolarization field will be present in the direction parallel to the electron beam, which can induce kink-like fringe bending. Earlier reported holographic images of ferroelectric domain walls revealed an asymmetry fringe bending. This behavior is explained through phase shifts induced by both the depolarization field and the strain field.

1 - Introduction

Electron holography provides us with a new methodology for the study of electric and magnetic field variations at the atomic scale.[1] In the past few years, the electron holography technique has demonstrated its power in the study of magnetic domain walls, p-n junctions, and fluxons in superconducting materials.[2-7] Recently, this method has been introduced into the study of ferroelectric materials, with particular interest to ferroelectric domain walls and defect dopants.[8] The kink-like phase change profile observed in the interference fringes qualitatively agree with the continuum theoretical descriptions of ferroelectric domain wall profiles.[9,10] However, quantitative agreement has not been obtained and the experimental results are not consistently reproducible. In this paper, a theoretical analysis is carried out, which intends to provide some basics for future studies on ferroelectric domain walls using electron holography.

Due to the existence of free charges, the study of polarization related electric field variations is much more complicated than the study of magnetic field variation using electron holography. The density of these free charges varies with the electric potential distribution and depends strongly on boundary conditions. The observed electron interference fringe patterns reflect the total electric potential distribution, therefore, in order to correlate them to the variation of polarization across a domain boundary one must separate different charge sources.

2 - Electron holography

The fundamental principle in electron holography is the interference of coherent high energy electrons. To a good approximation the transmission of high energy electrons through a thin foil sample can be treated as a one-dimensional problem. Define z to be the electron traveling direction, then the phase change in the electron wave function due to the existence of an electric potential $V(x_0, y_0, z)$ is given by

$$\phi(x_0, y_0) = \frac{2\pi}{\lambda} \int \left(\sqrt{\left(1 - \frac{V(x_0, y_0, z)}{\Sigma}\right)} - 1 \right) dz \tag{1}$$

where λ is the electron wave length, x_0 and y_0 define the point on the sample foil, Σ is the electron energy and $V(x_0, y_0, z)$ represents the electric potential produced by the object. When the electron energy, Σ, is much greater than the magnitude $|V(x_0, y_0, z)|_{max}$ of the potential barrier, the phase shift of the electron wave can be simplified as[11,12]

$$\phi(x_0, y_0) = \frac{\pi}{\lambda \Sigma} \int V(x_0, y_0, z) \, dz \tag{2}$$

Since the energy of the electron beam is very large, ~ 200 keV, Eq. (2) is usually sufficient to calculate the phase change.

The most important characteristic of a ferroelectric is a reversible spontaneous polarization. Generally, the spontaneous polarization results from a displacive or order-disorder phase transition. Without external electric fields, the macroscopic spontaneous polarization is developed in domains within the crystal, forming the so-called twin structures. There are two main types of twins. One has an inversion symmetry about the twin boundary but with equal strain in both variants. The second type is a twin of two variants with both different orientation of polarization and of spontaneous strain. The internal potential $V(x_0, y_0, z)$ in a domain depends on the polarization and the boundary conditions at the crystal surfaces.

3 - Theory

From electrodynamics we know that the macroscopic electric field E, polarization P, and the electric displacement D, are all interrelated by the following equation,

$$D = \epsilon_0 E + P \tag{3}$$

Generally speaking, polarization P depends on local electric field which is different from the macroscopic electric field E. A ferroelectric system has a number of additional considerations owing to the spontaneous polarization and boundary conditions. Two extreme cases are shown below to illustrate this situation. For simplicity we assume the spontaneous polarization, P_0, is perpendicular to the sample plane.

Case I. Complete charge compensation

The simplest case is when the sample surfaces are electroded and the two electrodes were short circuited during the development of the spontaneous polarization. For this system we have the condition E = 0, so that

$$D_0 = P_0 \tag{4}$$

Since $P_0 \cdot n$ is the surface "bound charge" density and $- D_0 \cdot n$ equals the surface "free charge" density, the polarization is completely compensated by the generated free charges. The system is in equilibrium and has a fully developed spontaneous polarization throughout the whole crystal. When the temperature is kept constant, there is no macroscopic electric field present either inside or outside of the ferroelectric crystal. Therefore, no fringe variations are expected.

Case II. Completely uncompensated polarization

The other simple but unrealistic case is the polarization being completely uncompensated, i.e., D = 0. Then there will be a very strong depolarization field being produced inside the sample,

$$E = - P_0 / \epsilon_0 \tag{5}$$

which is equal to the microscopic field. This field is too large to be sustained. For example, the polarization of BaTiO$_3$ is 18 μ C/m^2, from Eq.(5) the depolarization field can be as large as 2 x 10^8 V/cm. Under such a large field, either the polarization will be destroyed (which suppress the structural phase transition) or the system will obtain free charges (from the environment or within the crystal) to reduce the field level.

As free charges are readily available, a real system is more like Case I above, even when the sample is not being electroded. This is to say that the phase shift induced by the depolarization field difference across a domain boundary is being counterbalanced by the phase shift produced by the field of compensation charge. However,

charge compensation in a non-electroded sample is a relaxation process, the rate can be very slow as the equilibrium is approached. In addition, since most of the ferroelectrics are also improper ferroelastic, a small level of the depolarization field could be sustained through elastic distortion of the structure. In other words, the system is sometimes not fully compensated, at least in a finite time period. This situation can also happen in an already compensated system through the change of temperature (pyroelectric effect) or mechanical stress (piezoelectric effect).

The depolarization field in the partially compensated system can be expressed as

$$E = - (P_0 - D)/\epsilon_0 = - (1-\eta) P_0 / \epsilon_0 \tag{6}$$

Here we have defined a compensation factor $\eta = D/P_0$ (in our problem the vectors D and P_0 are in the same direction) which is less or equal to unity, $0 < \eta \leq 1$. The compensation factor η depends strongly on temperature, stress, and also on time. Since the net field in Eq. (6) is non-zero if $\eta < 1$, and proportional to the polarization, one may use holographic electron microscopy to study the variation of polarization inside a twin domain structure, through the residue field and the associated phase shift. The basic requirement is that η changes slowly with time.

The associated spontaneous polarization profiles can be determined using Landau-Ginsburg theory. As an example, in a 180° twin structure with the polarization in the z-direction (the electron beam direction), the profile can be described by[10]

$$P_{(x)} = \frac{P_0 \sinh (x/\xi)}{\sqrt{A + \sinh^2 (x/\xi)}} \tag{7}$$

where x is the space variable in the domain wall normal direction and ξ is the characteristic width of the domain wall; the parameter A is a constant which reflects the sharpness of the first order transition. For a second order phase transition A = 1 and Eq. (9) reduces to a hyperbolic tangent function[9]

$$P = P_0 \tanh (x/\xi) \tag{8}$$

From Eqs. (2), (6), and (7) or (8), one can calculate the phase profile across a domain wall:

$$\Delta\phi(x_0) = \frac{(1-\eta) \pi t^2}{\lambda \Sigma} P_z(x_0) \tag{9}$$

Here x_0 defines the coordinate on the sample surface and the phase reference is chosen at the domain wall center. Since phase variations are proportional to the polarization, the fringe patterns should be kink-like as observed in BaTiO$_3$.[8] For later convenience, we define these kink-like patterns as type I fringes for domain walls, which is antisymmetric.
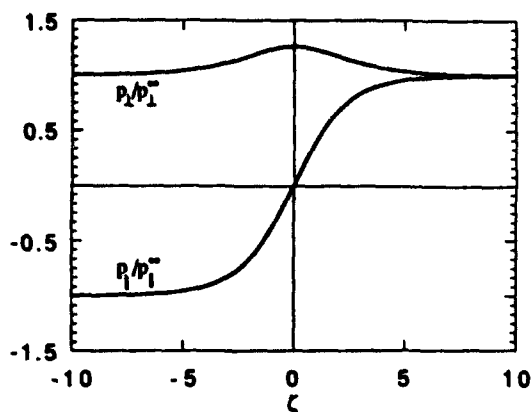
Most ferroelectrics are also improper

Fig. 1. The polarization profiles for the polarization components perpenticular and parallel to the domain wall in a 90° twin structure.

Fig. 2. Variation of the total phase shift profile with respect to the ratio $\alpha = |\Delta\phi_0|/|\Delta\phi_\infty|$ of contributions from Type I and Type II.

ferroelastics, i.e., the strain is the secondary order parameter and coupled to the polarizations; hence, it also changes in the domain wall region. The relationship b.tween the spontaneous polarization P and the spontaneous strain $\tilde{S}$ can be written as:

$$S_{ij} = Q_{ijkl} P_k P_l \quad (i,j,k,l = 1,2,3) \quad (10)$$

where Q_{ijkl} is the electrostriction constant. The non-zero strain components are defined by the crystal symmetry and boundary conditions. For the 180° ferroelectric twin discussed above the strain variation in the domain wall region is[10,13]

$$\Delta S_{ij} = Q_{ij33} (P_\infty^2 - P^2(x)) \quad (11)$$

Due to the symmetric nature of Eq.(11), the phase profile reflecting the strain variation will be symmetric about the center of the domain wall. We define the hump-like symmetric fringes as type II fringes for domain walls. Additional contribution to the type II fringes may come from the polarization component perpendicular to the domain wall, which is non-zero for all non-180°
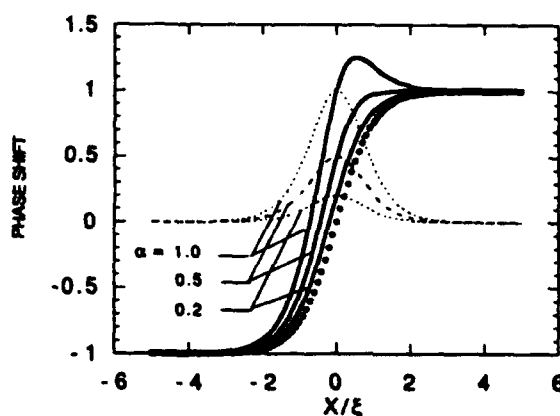
domain walls. The profile of this component is hump-like as illustrated in Fig. 1. Also, because the strong polarization gradient at the domain wall region, charge defects and vacancies tend to be trapped by the domain walls, these point charge defects can also contribute to the type II fringes as summarized in Table I.

In general, the fringe patterns observed across a ferroelectric domain wall will be a mixture of type I and type II, so that the resultant fringe patterns will be non-symmetric. For example, assuming the polarization is given by Eq. (8), then the resultant normalized fringe profile is illustrated in Fig. 2. The circles in Fig. 2 represent type I profile and the dashed lines represent type II profile, $\alpha = |\Delta\phi_0|/|\Delta\phi_\infty|$ is the ratio of the maximum phase shifts of type II versus type I. One can see that the resultant phase shift becomes more and more asymmetric as α increases from 0 to 1, and the total profile moves to the left. This asymmetric feature is obviously seen in the results reported in ref. 8 for BaTiO$_3$ (see the data points in Fig. 3). According to the above analysis, we propose the fringes to be fitted in the following equation:

Table I

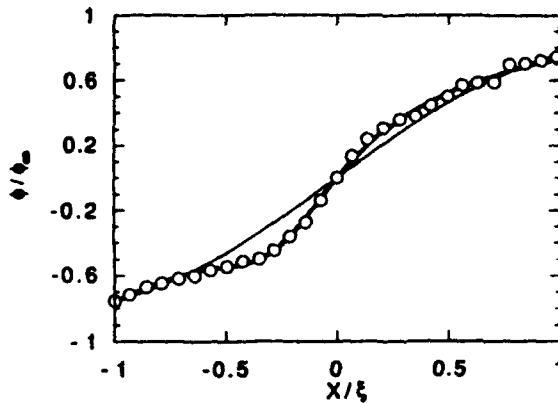|	Shape	Symmetry	Source of Contribution
Type I		Antisymmetric	Polarization parallel to domain wall
Type II		Symmetric	Polarization perpendicular to domain wall; point charge defects; strain variation across the domain wall

Fig. 3. Comparison of the theory with the experimental data of ref. 8. The circles are the experimental data, the thin line is the fitting to a simple hyperbolic tangent and the thick line was obtained using Eq. (12).

Fig. 5. Calculated fringes across a domain wall for different a assuming $|\Delta\phi_0| = \pi/2$.

$$\Delta\phi(x)/|\Delta\phi_-| = \tanh\left(\frac{x-x_d}{\xi}\right) + \alpha\left(1 - \tanh^2\left(\frac{x-x_d}{\xi_s}\right)\right) + \beta \tag{12}$$

where x_d and β are respectively the horizontal and vertical deviations of the domain wall center from the reference center used in the experiment. A different characteristic length ξ_s for the type II fringe is introduced, which may not be the same as ξ. Fig. 3 shows the comparison between the fitting of ref. 8 (thin line) and the fitting using Eq. (12) [thick line]. One can see that the current fitting is quite satisfactory with the following fitting parameters: $x_d = -0.285\ \xi$; $\alpha = -0.323$; $\xi_s = 0.31\ \xi$ and $\beta = -0.1285$. Here we like to emphasize that the functional form for the first order phase transition in $BaTiO_3$ would be more appropriate to use eq. (7) instead of eq. (8) if the constant A can be determined.
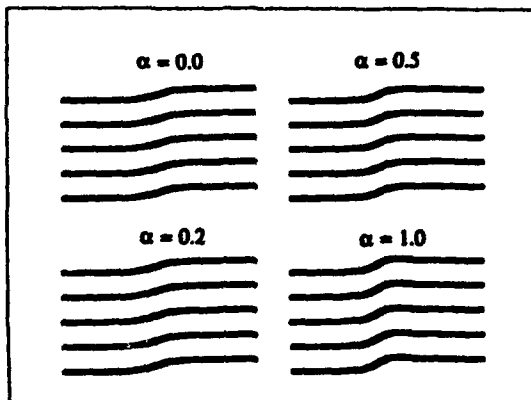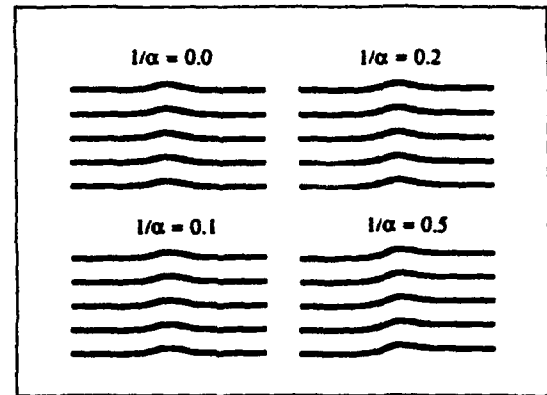
Figures 4 and 5 show some of the expected fringe patterns across a ferroelectric domain wall using the current analysis. The fringes in Fig. 4 were calculated by assuming $|\Delta\phi_-| = \pi/2$ while the fringes in Fig. 5 were calculated by assuming $|\Delta\phi_0| = \pi/2$. One can see the nature of the fringes changes from type I to type II as the parameter α increases from 0 to ∞.

4 - Conclusions

As the electron holography technique is very sensitive to the local electric potential variations, the incompletely compensated depolarization field in domain wall regions can be measured. The fringe patterns can be directly correlated to the space profile of polarization variation in a twin structure. The sample should not be electroded and the electron energy must be very high. For a compensated sample, one may vary the temperature to destroy the charge balance and make the domain wall visible through the electron phase shift. In general, the fringe bending observed is a mixture of type I and type II, one must separate the two types of contributions in order to extract useful information from electron holography. Eqs. (9) and (12) can be used to fit the fringe patterns across a 180° and a non-180° domain wall, respectively.

Fig. 4. Calculated fringes across a domain wall for different a assuming $|\Delta\phi_-| = \pi/2$.

References

1. A. Tonomura, Rev. Mod. Phys., **59**, 639 (1987).

2. S. Frabboni, G. Matteucci, and G. Pozzi, Phy. Rev. Lett., **55**, 2196 (1985).

3. A. Tonomura, T. Matsuda, J. Endo, J. Arii, and K. Mihama, Phys. Rev. Lett., **44**, 1430 (1980).

4. A. Fukuhara, K. Shinagawa, A. Tonomura, and H. Fujiwara, Phys. Rev. B, **27**, 1839 (1983).

5. A. Tonomura, T. Matsuda, R. Suzuki, A. Fukuhara, N. Osakabe, H. Umezaki, J. Endo, K. Shinagawa, Y. Sugita, and H. Fujiwara, Phys. Rev. Lett., **48**, 1443 (1982).

6. A. Tonomura, N. Osakabe, T. Matsuda, K. Kawasaki, R. Suzuki, J. Endo, S. Yano and H. Yamada, Phys. Rev. Lett., **56**, 792 (1986).

7. M. Tsuyoshi, A Tonomura, R. Suzuki, J. Endo, N. Osakabe, H. Umezaki, H. Tanabe, Y. Sugita and H. Fujiwara, J. Appl. Phys., **53**, 5444 (1982).

8. X. Zhang, T. Hashimoto and D. C. Joy, Appl. Phys. Lett., **60**, 784 (1992).

9. V. A. Zhirnov, Sov. Phys. JETP, **35**, 822 (1959).

10. W. Cao and L. E. Cross, Phy. Rev. B, **44**, 5, (1991).

11. G. F. Missiroli, G. Pozzi, and U. Valdrè, J. Phys. E, **14**, 549 (1981).

12. M. Yanzi, Optik, **68**, 319 (1984).

13. W. Cao and G. R. Barsch, Phys. Rev. B, **41**, 4334 (1990).

APPENDIX 11

Direct evaluation of domain-wall and intrinsic contributions to the dielectric and piezoelectric response and their temperature dependence on lead zirconate-titanate ceramics

Q. M. Zhang, H. Wang, N. Kim, and L. E. Cross
Materials Research Laboratory, The Pennsylvania State University, University Park, Pennsylvania 16802

By making use of the fact that domain-wall motions do not produce volumetric changes, an experimental method is introduced to directly and quantitatively determine the domain-wall and intrinsic contributions to the piezoelectric and dielectric responses of a ferroelectric material. Utilizing this method, the contributions from the domain walls and intrinsic part as well as their temperature dependence for lead zirconate-titanate (PZT) 52/48 and PZT-500 ceramics are evaluated. The data show that at temperatures below 300 K, the large change in the dielectric and piezoelectric constants with temperature is due to the change in the domain-wall activities in the materials. The results confirm that most of the dielectric and piezoelectric responses at room temperature for the materials studied is from the domain-wall contributions. The data also indicate that in PZT-500, both 180° wall and non-180° walls are possibly active under a weak external driving field.

I. INTRODUCTION

For most ferroelectric materials, the existence of domain structures or domain walls makes a significant influence on the material properties. For example, in lead zirconate-titanate (PZT) solid solution system, the material properties can be modified over a wide range by using different dopants or by different processing conditions.[1] Such changes in the material properties are believed to be the result of changes in the domain-wall response in the materials.[2,3] From the Landau–Devonshire phenomenological theory, it has been proposed that for PZT at compositions near the morphotropic phase boundary, the domain-wall contribution accounts for more than half of the room-temperature dielectric and piezoelectric responses.[4]

In the literature, the material properties from a single-domain material are denoted as the intrinsic properties (or volume contribution) of the material, while the contributions from the other parts of the material, mainly from domain walls, are lumped as extrinsic properties of the material. Under this convention, the dielectric constant ϵ, piezoelectric constant d, and elastic compliance s, can be written as a summation of two terms,[5]

$$\epsilon = \epsilon_{ex} + \epsilon_{in},$$

$$d = d_{ex} + d_{in},$$

$$s = s_{ex} + s_{in},$$

(1)

where the subscripts ex and in denote the extrinsic and intrinsic contributions, respectively.

To understand how domain structures and domain-wall motions are influenced by different processing conditions and dopants so that the material properties can be better tailored, one needs to quantitatively describe the changes of ϵ_{ex}, ϵ_{in}, d_{ex}, d_{in}, s_{ex}, s_{in} with the processing conditions and dopants. That is, to distinguish the intrinsic and extrinsic contributions from the experimental data which usually contain both parts. Currently, two methods are commonly used in separating the extrinsic properties and intrinsic properties in ceramics: One is based on the frequency dispersion characteristics of the dielectric constant and the other is based on the properties measured at near 0 K temperature.[3,6-8] Since dielectric dispersion only describes the dielectric property of a material, it cannot provide information on the piezoelectric responses from different parts and the difference between 180° domain-wall response and non-180° domain-wall response. While the results derived from the second method are only related to the material properties at near 0 K and may not be directly related to the material properties at higher temperatures.

In this article, we introduce a new experimental methodology which can directly and quantitatively determine the domain-wall and intrinsic contributions to the material properties and their temperature dependence. Using this method, the piezoelectric and dielectric responses from both the intrinsic and domain-wall contributions were investigated for both doped and pure PZT ceramics near the morphotropic phase boundary in the temperature range from 10 to 300 K. The basic principle of this method is that in contrast to the intrinsic response where any polarization change will be accompanied by a change in the unit-cell volume, the polarization change induced by domain-wall motion will not cause volume changes. As a consequence, the domain-wall motion will not contribute to the hydrostatic response of a material and the change in the piezoelectric hydrostatic coefficient d_h will not be related to the response from domain walls; therefore, d_h provides a very sensitive means to separate the intrinsic and extrinsic material responses. By combining these results with the data measured near 0 K, we can get the temperature dependence of the extrinsic response and intrinsic response of

these PZT samples. In addition, making use of both dielectric and piezoelectric responses, one is able to gain information on the change of domain-wall responses of 180° type and non-180° type as the processing conditions or dopants are varied.

II. EXPERIMENTS

The piezoelectric constants d_{33} and d_{31}, dielectric constant ϵ_{33}, and remanent polarization P_r were characterized for pure PZT at the composition near the morphotropic phase boundary (PZT 52/48), and a soft PZT in the temperature range from 10 to 300 K. The PZT 52/48 ceramic samples were made through the standard solid-state processing.[9] The samples were poled at an electric field of 50 kV/cm and a temperature of 375 K for 5 min. All the samples were aged for more than 1 week at room temperature before any measurement. The soft PZT ceramic samples (PZT-500) were purchased from Piezo Kinetics, Inc. (Bellefonte, PA 16823) and were poled by the manufacturer.

The piezoelectric constants d_{33} and d_{31} were acquired through the resonance technique using a HP impedance analyzer (HP 4194A) for bar-shaped samples and the resonance frequencies were around 150 kHz. These constants were also measured at room temperature by a laser dilatometer.[10] The results from the two measurements were in good agreement. The temperature regulation for the resonance experiment was provided by a helium closed-cycle refrigerator (APD Cryogenics, Model HC-2).

The dielectric constant measurement was carried out using a HP multifrequency RLC meter (HP 4274A) and the temperature dependence of the remanent polarization P_r was obtained by combining the data acquired using the Byer–Roundy technique and from polarization hysteresis loop measurements. Since the ferroelectric-paraelectric transition temperature (Curie temperature) for these samples is far above the upper operation temperature for the setup which is at 500 K, the Byer–Roundy technique cannot provide the absolute value of the remanent polarization of the samples. To establish the absolute scale of the remanent polarization, the polarization hysteresis loop was measured at room temperature using a modified Sayer–Tower circuit. A homemade temperature chamber was used to regulate the temperature for the polarization measurement. The temperature range of the measurement was from 100 to 470 K for PZT-500 and 100 to 340 K for PZT 52/48. In all experiments, the sample thickness was about 1 mm and the sample area was about 5×5 mm^2. The electrodes were made by sputtering gold on both surfaces of the samples.

III. RESULTS AND DISCUSSION

A. Temperature dependence of the piezoelectric constants

Shown in Figs. 1(a) and 1(b) is the temperature dependence of the piezoelectric constants d_{33} and d_{31} for PZT 52/48 and PZT-500 samples, respectively. For PZT 52/48,
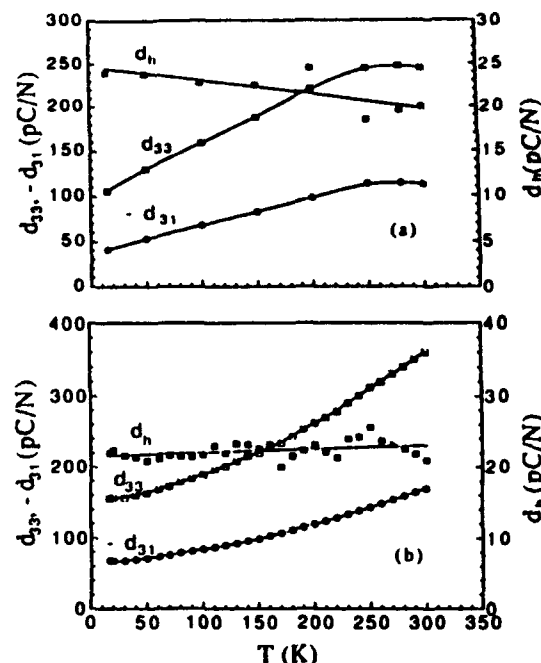

FIG. 1. The temperature dependence of piezoelectric constants d_{33}, d_{31}, and d_h for (a) PZT 52/48 and (b) PZT-500 ceramics.

as the temperature increases from 10 K to room temperature (300 K), d_{33} increases about two and a half times (from about 105 to 245 pC/N). In the same temperature range, $-d_{31}$ has about a threefold increase (from about 40 to 114 pC/N). From the relation $d_h = d_{33} + 2d_{31}$, d_h can be determined in the same temperature range and clearly, unlike d_{33} and d_{31}, d_h does not increase with temperature. Instead, from low temperature to room temperature, d_h exhibits a slight decrease from about 24 to 20 pC/N, which is shown in Fig. 1(a). The data for d_h in Fig. 1(a) also shows larger scattering than those of d_{33} and d_{31}. This is understandable since both d_{33} and d_{31} are much larger than d_h, any small data scattering in d_{33} and d_{31} will induce a relative large scattering in d_h when it is obtained by the difference between d_{31} and d_{33}. In spite of that, the data clearly shows that d_h has a much smaller temperature variation compared with both d_{33} and d_{31}.

Similarly, for PZT-500, in the temperature range from 15 K to room temperature, d_{33} increases from about 132 to 360 pC/N and $-d_{31}$ from 54 to 170 pC/N, while d_h stays almost a constant around 23 pC/N in the same temperature range, as shown in Fig. 2. By relating this behavior to the discussions above, one can immediately draw the conclusion that in both pure and doped PZT ceramics, the large change in the piezoelectric activity (d_{33} and d_{31}) in this temperature range is caused by the extrinsic contribution, most likely by the non-180° domain-wall motions.

B. Temperature dependence of the dielectric constant and remanent polarization

In Fig. 2, the temperature dependence of ϵ_{33} for both PZT 52/48 and PZT-500 is plotted from 15 to 300 K. For
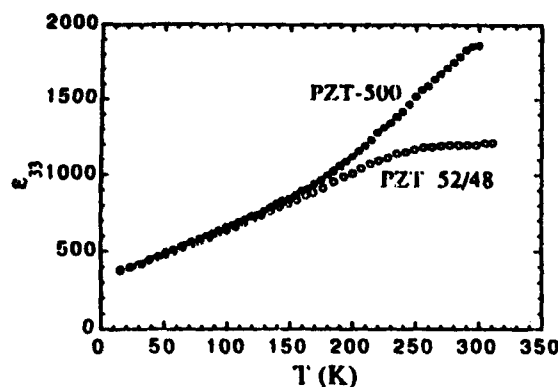
J. Appl. Phys., Vol. 75, No. 1, 1 January 1994

Zhang et al.   455

FIG. 2. The dielectric constant ϵ_{33} for PZT-500 (●) and PZT 52/48 (○) poled samples measured at 1 kHz.
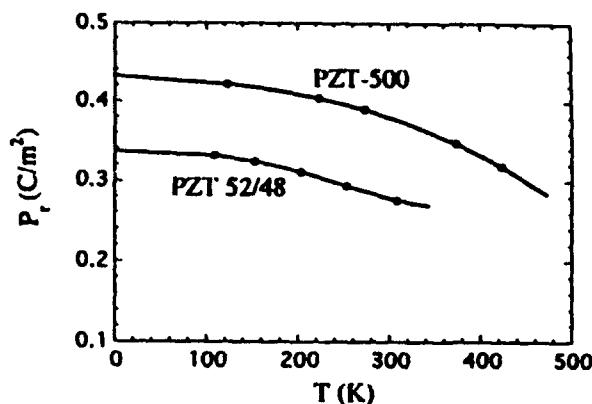

FIG. 3. The remanent polarization for PZT-500 and PZT 52/48 as a function of temperature. The curves at temperatures below 100 K are calculated from the fitting to the higher-temperature data.

PZT 52/48, except for a broad anomaly at a temperature near 260 K, ϵ_{33} shows a large increase, from about 370 at 15 K to near 1200 at room temperature, which is a more than threefold increase. For PZT-500, ϵ_{33} is 375 at 15 K and increases to 1800 at room temperature. Therefore, the dielectric constants of the two PZT materials are almost the same at temperatures near 0 K. This is consistent with an earlier experimental result in which all the dielectric constants measured from PZTs with different dopants converged to a common value as the temperature approached to 0 K.[3] In contrast, at a temperature near 0 K, the piezoelectric constants for the two materials are not the same, which is probably caused by different degree of poling and different distribution of polarization about the poling direction in the materials. As is shown later, the remanent polarization of PZT-500 is higher than that of PZT 52/48. Apparently, dopants in PZT-500 facilitate the domain-wall movement and increase the degree of poling.

The piezoelectric response in a single-domain material can be viewed as polarization-biased electrostriction. Hence, the intrinsic piezoelectric and dielectric response are related through the electrostrictive coefficient Q_{ij} and the remanent polarization P_r.[11]

$$d_{33} = 2\epsilon_{33}\epsilon_0 Q_{11} P_r, \tag{2a}$$

$$d_{31} = 2\epsilon_{33}\epsilon_0 Q_{12} P_r, \tag{2b}$$

and

$$d_h = 2\epsilon_{33}\epsilon_0 Q_h P_r, \tag{2c}$$

where ϵ_0 is the vacuum permittivity. These relations are derived from single-domain materials and should be valid for ceramics where the quantities in Eq. (2) are the averaged ones. Although the piezoelectric constants d_{ij} vary widely as the composition or temperature changes, the polarization-related electrostrictive coefficients Q_{ij} hardly change with composition and temperature in PZT ceramics.[4] Therefore, once the temperature dependence of P_r is determined, the temperature dependence of the intrinsic dielectric response can be evaluated through Eq. (2c). Similarly, d_{33} and d_{31} from the intrinsic contribution can also be determined from Eqs. (2a) and (2b).

For the two PZTs, the remanent polarization P_r as a function of temperature is shown in Fig. 3. Since the lowest temperature measured for the P_r was at 100 K, the data were fitted using a polynomial and the low-temperature (0 K) P_r was extrapolated from the fitting. As can be seen from Fig. 3, the P_r is a smooth function of temperature and from the theoretical consideration, one does not expect any irregular changes in P_r as the temperature is lowered, which justifies the extrapolation.[4,11] At temperatures near and above room temperature, there is a small irregular change in the P_r for PZT 52/48. This is likely caused by the internal stress field in the material, which increasingly realigns the domain as the temperature is raised. Hence, for PZT 52/48 the higher-temperature data are not plotted here.

C. Discussion

From the results presented in Secs. III A, and III B, the temperature dependence of the piezoelectric and dielectric constants from both the intrinsic and domain-wall contributions can be determined. Assuming at 0 K, d_{ij} and ϵ_{33} are from the intrinsic contribution, Q_{11}, Q_{12} and Q_h for the PZT ceramics are calculated using Eq. (2), and the results (listed in Table I) are close to those of an earlier experimental result.[4] In the calculation, the data of d_{ij} and ϵ_{33} at 0 K are extrapolated from the higher-temperature data and are very close to those measured at 15 K. Making use of Eq. (2), the temperature dependence of the dielectric constant ϵ_{33} and piezoelectric constants d_{33} and d_{31} from the intrinsic contribution are calculated and they are shown in Figs. 4 and 5 for the dielectric constant and the piezoelectric constants, respectively. In all these calculations we as-

TABLE I. The electrostrictive coefficients for PZT-500 and PZT 52/48 ceramics used in this experiment.

	Q_h $(m^4 C^2)$	Q_{11} $(m^4 C^4)$	Q_{12} $(m^4 C^4)$
PZT-500	0.0091	0.0505	−0.0207
PZT 52/48	0.012	0.046	−0.017

hat the electrostrictive coefficients Q_{ij} were inde-
of temperature. Clearly, in the temperature range
there is very little increase in the intrinsic dielec-
vity. For PZT 52/48, it stays at about 350 in this
iture range and for PZT-500, it increases slightly
nperature from 350 at 0 K to 430 at 300 K. This is
int with the experimental results from Bottger and
id from Kersten and Schmidt[6] on PZT ceramics, in
the low-frequency dielectric constant ϵ_{33} showed a
hange with temperature, while at frequencies above
lectric relaxation peak (near 1 GHz) ϵ_{33} was nearly
tant of about 400 at temperatures below 300 K for
i2/48. Since the dielectric relaxation at frequency
GHz is believed to be due to the relaxation from
n walls, at frequencies above that one expects that
imain-wall contribution will die out and the major
bution to the dielectric response will only be the in-
: part. In addition, ϵ_{33} value of about 400 is almost
me as what we observed here at temperatures near 0
ierefore, in spite of different techniques used, the two
f measurements yield almost the identical results. Be-
that, the dielectric constants measured from single-
il samples of PZT also stayed almost constant at low
eratures.[12]

.he results presented here provide direct evidence that
om temperature, domain walls make major contribu-
. to the dielectric and piezoelectric responses of PZT
irials. This is consistent with the theoretical prediction
g Landau–Devonshire theory.[4] At room temperature
intrinsic dielectric and piezoelectric contributions are
than 25% and about 37% of the total responses for
:-500, and 30% and ⅓ for PZT 52/48.

In PZT, there exist two groups of domain walls: 180°
wall and non-180° wall. A major difference between these
two groups of walls is that 180° walls are not ferroelastic
active, while non-180° walls are ferroelastic active. As a
result, 180° wall motion will affect only the dielectric prop-
erty and non-180° wall will affect both dielectric and piezo-
electric properties. Hence, when one discusses domain-wall
contributions to the material responses, it is important to
know which kind of wall is active under weak driving field
because by enhancing only the non-180° wall activity one
can greatly improve the electromechanical coupling factor
of the material, and on the other hand, by enhancing only
the 180° wall activity, the dielectric response of the mate-
rial can be improved significantly without introducing
large dielectric losses, which are mostly caused by non-180°
wall motions.[13] Currently, it seems to be widely believed
that for PZT and other ferroelectrics with perovskite struc-
ture, under weak external driving fields, the major part of
the domain-wall response is from non-180° walls and 180°
walls are almost idle. The reason is that 180° wall width is
much narrower (probably on the order of one unit cell) in
comparison with non-180° walls,[14,15] which implies that
there is a much steeper potential well for 180° walls; there-
fore, a weak external field may not be able to induce sub-
stantial changes in the 180° wall structure. Experimentally,
there was no direct evidence to prove or disprove this;
however, the results presented here may not be consistent
with the idea that 180° walls in PZT ceramics are idle.
From the results presented above, at room temperature,
the extrinsic contribution to the dielectric constant is larger
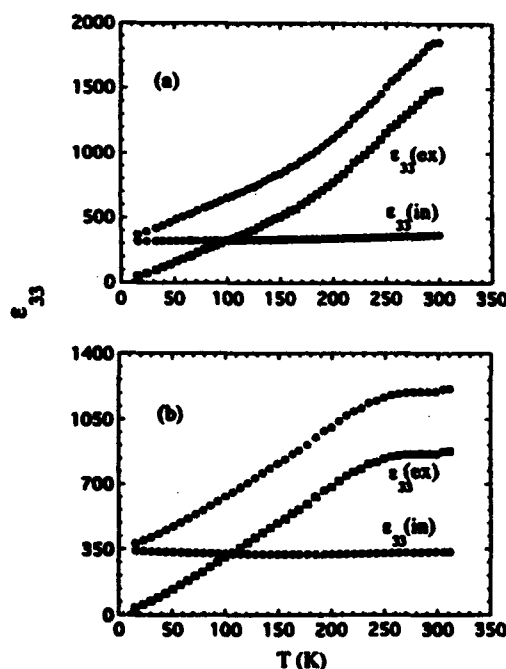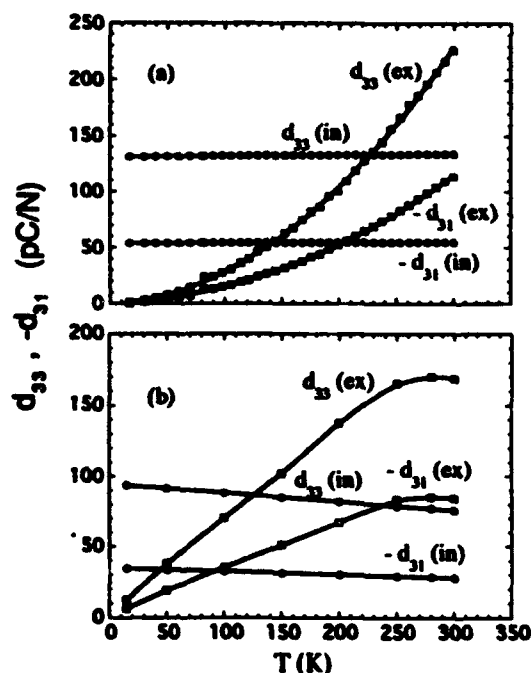than that to the piezoelectric constant for PZT-500, while

FIG. 4. The calculated intrinsic (O) and extrinsic (■) dielectric con-
stant for (a) PZT-500 and (b) PZT 52/48. For the comparison, the total
dielectric constant (●) measured is also presented.

FIG. 5. The calculated intrinsic and extrinsic piezoelectric constants
for (a) PZT-500, and (b) PZT 52/48: open circles are intrinsic d_{31},
solid circles intrinsic d_{33}, open squares extrinsic d_{31}, and solid squares
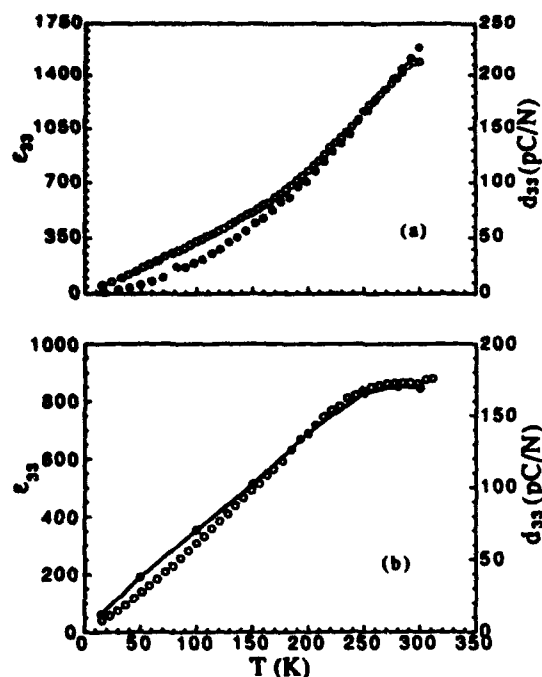extrinsic d_{33}.

FIG. 6. The calculated extrinsic piezoelectric and dielectric constants for (a) PZT-500 and (b) PZT 52/48; solid circles are extrinsic d_{33}, open circles extrinsic ϵ_{33}.

for PZT 52/48 they are almost the same (the ratio d_{33}^{ex}/d_{33} and $\epsilon_{33}^{ex}/\epsilon_{33}$). That is, increased domain-wall activities in PZT-500 raise the dielectric constant more than the piezoelectric constant. The large increase in d_{ex} is apparently due to the increased activity in non-180° walls in PZT-500; however, the disproportionate increase in ϵ_{ex} may reflect the fact that there are substantial increases in the 180° wall activity, too. In addition, as illustrated in Fig. 6, the extrinsic piezoelectric and dielectric contributions show a similar temperature dependence for both PZT-500 and PZT 52/48; however the ratio of d_{ex} to ϵ_{ex} (d_{ex}/ϵ_{ex}) for the two materials is quite different. At room temperature, this ratio is 0.2 pC/N for PZT 52/48 and less than 0.15 pC/N for PZT-500. In other words, on average, corresponding to the same polarization change, the domain-wall motions will produce much less piezoelectric response in PZT-500 than in PZT 52/48 even though the poling level in PZT-500 is higher. From the analysis by Haun,[4] Arlt, Dederichs, and Herbiet,[16] Zhang et al.[17] and the earlier experimental results, which showed that as the poling level increases this ratio should increase if there are only non-180° domain walls active, the phenomenon observed here strongly suggests that there is a substantial increase in 180° wall activity in PZT-500, which raises the dielectric constant of the material while keeping the piezoelectric constant unchanged; therefore, both the non-180° wall and 180° wall should be active in PZT-500.

We would like to emphasize that the notion introduced here that the domain-wall motions do not contribute to the volume change may not be applicable when the wall motions are related to the polarization switch, which may introduce significant local stress and result in some volume change. This kind of volume change may provide informa-

tion on the local stress distribution and themselve detailed studies. In addition, for ceramic materia exist pores which could change the local stress pa cause volume changes as the wall moves. How well-fabricated materials, this probability is very s should not significantly alter the conclusions pre this article. The consistency between the results earlier experimental results confirms this point.

IV. SUMMARY

In this article, we presented a new exp method, based on the notion that domain-wall induced by weak external fields will not contrib hydrostatic piezoelectric response, to directly ev intrinsic and domain-wall contributions in a pie ceramic sample. Using this method, the domain intrinsic contributions to the piezoelectric and responses and their temperature dependence 52/48 and PZT-500 ceramics are evaluated di quantitatively. The data show that at temperatt 300 K the large change in the dielectric and pi properties with temperature is from the domain tribution. The results confirm that most of diel piezoelectric responses at room temperature for rials studied are from the domain-wall contribt data also show that in PZT-500, both 180° wal 180° wall are most likely active under weak ext ing fields.

The experimental methods presented in this be extended to a wide range of materials and temperature range to study how various extern ters change the extrinsic and intrinsic contrit their temperature-dependence behavior. In c with the analysis similar to that employed b co-workers[16] and the information of the polar tribution in a material, one can quantitatively how the 180° wall and non-180° wall activitie one varies various conditions.

[1] B. Jaffe, W. J. Cook, and H. Jaffe, *Piezoelectric Ceram.* London, 1971).
[2] G. Arlt, Ferroelectrics 104, 217 (1990).
[3] X. L. Zhang, Z. X. Chen, L. E. Cross, and W. A. Schulz 18, 968 (1983).
[4] M. J. Haun, Ph.D. thesis, The Pennsylvania State Uni
[5] R. Herbiet, U. Robels, H. Dederichs, and G. Arlt, F 107 (1989).
[6] O. Kersten and G. Schmidt, Ferroelectrics 67, 191 (1!
[7] U. Bottger and G. Arlt, Ferroelectrics 127, 95 (1992)
[8] W. Kleemann and H. Schremmer, Phys. Rev. B 41

hul Kim, Ph.D. thesis, The Pennsylvania State University, 1993.
. Zhang, S. J. Jang, and L. E. Cross, J. Appl. Phys. 65, 2807
).
Devonshire, Philos. Mag. 42 1065 (1951).
uzuki, K. Sakata, and M. Wada, Ferroelectrics 8, 501 (1974).
It and H. Dederichs, Ferroelectrics 29, 47 (1980).

[14] F. Jona and G. Shirane, *Ferroelectric Crystals* (Dover, New York, 1993).
[15] Wenwu Cao and L. E. Cross, Phys. Rev. B 44, 5 (1991).
[16] G. Arlt, H. Dederichs, and R. Herbiet, Ferroelectronics 74, 37 (1987).
[17] Q. M. Zhang, W. Y. Pan, S. J. Jang, and L. E. Cross, J. Appl. Phys. 64, 6445 (1988).

APPENDIX 12

DOMAIN SWITCHING AND MICROCRACKING DURING POLING OF LEAD ZIRCONATE TITANATE CERAMICS

E. C. SUBBARAO,† V. SRIKANTH, W. CAO and L. E. CROSS

*Materials Research Laboratory, The Pennsylvania State University,
University Park, PA 16802-4800 USA*

The application of a DC electric field (poling) to a ferroelectric lead zirconate titanate (PZT) ceramic aligns domains in the field direction. The non 180°-domain switches involve mechanical deformations, which are detected as acoustic emission signals. Concurrent with AE signals, electrical current pulses arise from domain reorientations. When the poling field is large and domain switches are extensive, the resulting deformations, under the constraint of neighboring domains or grains, may exceed the elastic limit and cause microcracking. The onset and propagation of microcracking during poling of PZT is signalled by the appearance of continuous AE signals, unaccompanied by current pulses, in contrast to intermittent AE signals accompanied by corresponding current pulses during domain switching. The onset and extent of microcracking established by this method is confirmed by scanning electron micrographs and decrease in the value of piezoelectric coefficient (d_{33}) and mechanical quality factor (Q_M). The amplitude of AE signals due to domain switches are spread widely, while that of AE signals caused by microcracking occur in a narrow range around 50 db.

Keywords: Acoustic emission, PZT, domain switching, microcracking

INTRODUCTION

The polar direction of ferroelectric crystals can be changed by an applied electric field. Due to the existence of many variants in the low temperature ferroelectric phase, a ceramic (polycrystalline) sample contains many randomly oriented regions of uniform polarization, called domains, upon transforming from the high temperature non-ferroelectric (paraelectric) phase, thus eliminating net polarization.[1] For many practical applications such as a piezoelectric device, the ceramic must be poled (i.e., subjected to a DC electric field) to align the polar axes as fully as possible in the field direction so that the ceramic acquires a net (non-zero) polarization. The fact that only partial alignment of domains is possible in a ceramic is reflected in the rounded D-E hysteresis loop compared to a square loop of a ferroelectric single crystal, and in a spontaneous polarization (P_s) value of about 8 $\mu C/cm^2$ for a ceramic versus 26 $\mu C/cm^2$ for a single crystal of $BaTiO_3$.[1]

Associated with the spontaneous polarization (P_s), there is a spontaneous strain (e_s), which is proportional to P_s^2. This strain is a consequence of the fact that the polar axis is elongated compared to other crystallographic axes. When the ferroelectric domain switches by 180°, there is no strain change and hence does not affect its neighbors. On the other hand, domain reorientations by 90° cause max-

imum strain change, leading to intergranular stresses (Figure 1). Thus, domain switching during the poling process proceeds to minimize the total energy and accommodate the elastic deformation. For example, only 12% of the domains switch by 90° upon application of an electric field to ceramic $BaTiO_3$ and half of them revert back on removal of the field.[2,3] This constraint by surrounding grains does not affect domain switches by 180°, since no strain is involved in this case.

Extensive studies on $BaTiO_3$ single crystals have shown [4-7] that the domain switching is a nucleation and growth process. It starts with a wedge shaped domain of the new polarization state, proceed with a fast forward growth rate and slow sidewise growth rate, finally the wedge taking the shape of a stripe a ross the grain or crystal. Ultimately the two 180° domain walls move sidewise to widen the new polar region to complete the switching process.

Lead zirconate titanate (PZT) is a solid solution of ferroelectric lead titanate ($PbTiO_3$) and antiferroelectric lead zirconate ($PbZrO_3$). A composition at 48% $PbTiO_3$—52% $PbZrO_3$ exhibits a morphotropic phase boundary (MPB), separating a tetragonal $PbTiO_3$-rich and a rhombohedral $PbZrO_3$-rich ferroelectric phases. Many properties (dielectric constant, piezoelectric coefficients, etc.) peak at this
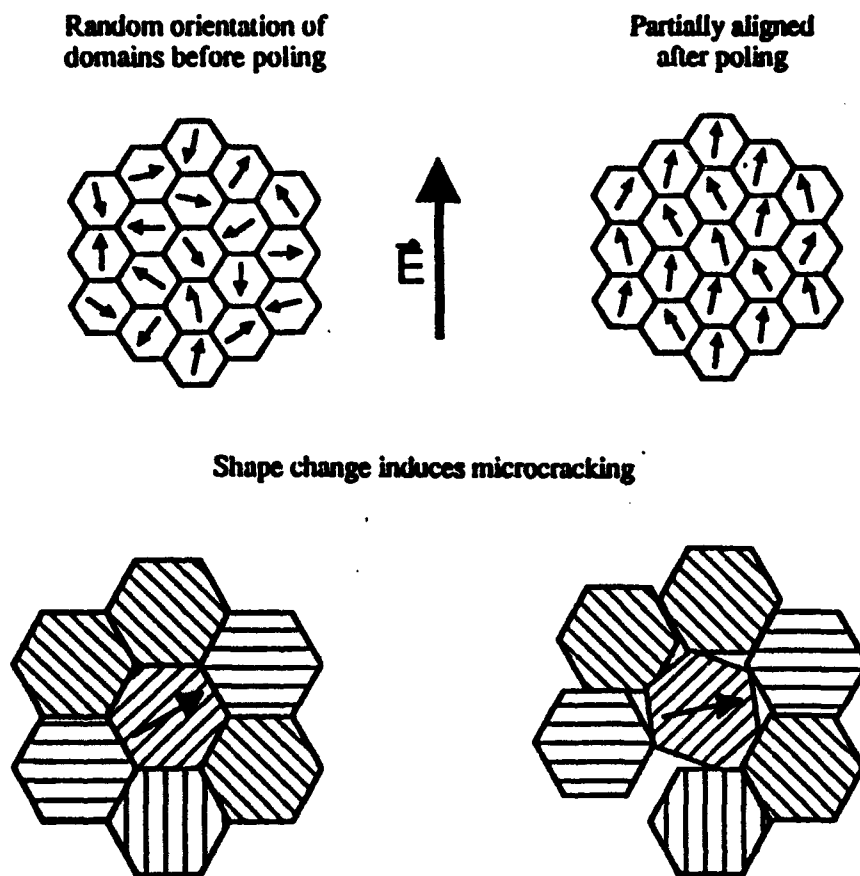

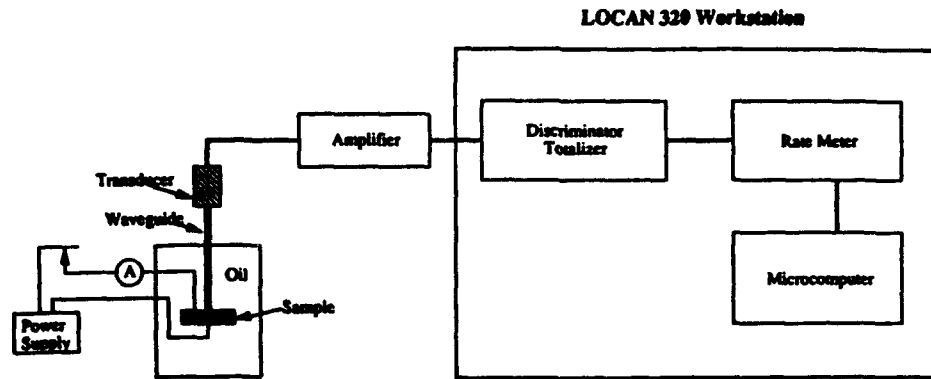FIGURE 1   Schematic of domain structure of a ferroelectric ceramic before and after poling.

FIGURE 2   Schematic of experimental arrangement used for simultaneous detection of acoustic emission and current pulses during poling of a ferroelectric ceramic.
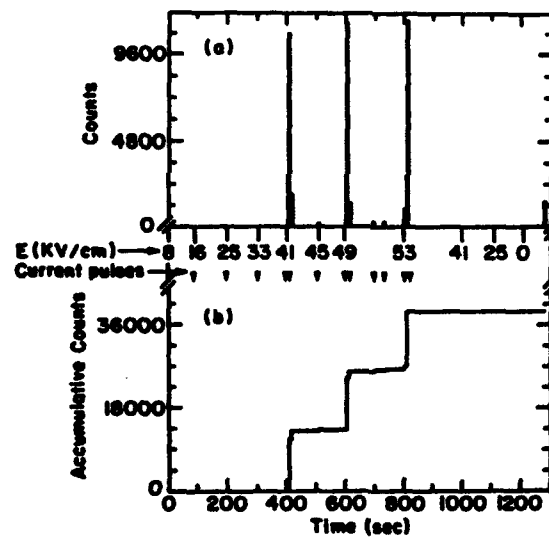

FIGURE 3   Acoustic emission count rate (a) and total AE counts (b) as a PZT ceramic (sample C) is poled to successively higher fields. The current pulses were observed at times indicated by triangles in this and succeeding figures (4 and 5).

TABLE I

Microcracking and electrical properties of poled PZT

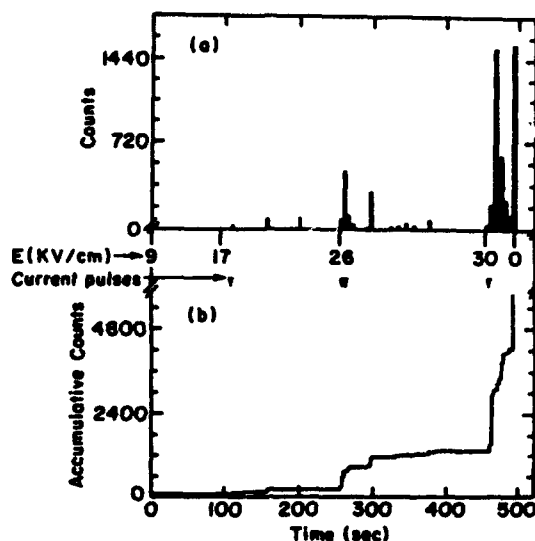| Sample	Extent of Poling and Microcracking	d_{33} (10^{-12} C/N)	Q_M
C	Poled but no onset of microcracking	333	89
SS	Poled till microcracking barely starts	350	65
B	Poled till microcracking starts	200	49
E	Poled till extensive microcracking occurred	119	

FIGURE 4   Similar data as in Figure 3 but for another sample B, poled till microcracking just starts.

composition, presumably due to the increase in the number of energetically degenerate states which makes the switching of domains easier under the influence of an electric field.[8] The higher Curie temperature (360°C vs 120°C), remanent polarization (47 vs 8 μC/cm^2) and piezoelectric coefficients make PZT far superior to BaTiO$_3$ for piezoelectric applications. In fact, PZT is the leading electromechanical transducer material for over a quarter century and therefore is chosen for the present study.

The effect of electric field on the extent of domain reorientations in PZT is somewhat different in the tetragonal and rhombohedral phase regions. In tetragonal PZT, it is estimated that 66⅓% of all dipoles instead of the initial 16⅔% become aligned within the sextant around the poling direction.[9] On the other hand, dipoles switch by 71°, 109° and 180° in the rhombohedral phase. For PZT modified by Nb^{5+} ion addition, it is suggested that 74% of the dipoles are present in the octant around the policy direction.[8] The larger P_s value and the higher degree of domain orientation in PZT make the remanent polarization of PZT substantially higher than that of BaTiO$_3$. The improvement in planar coupling coefficient (k_p) of PZT as a function of poling conditions (field, time and temperature) has been studied by Chiang *et al.*[10]

As already pointed out, the non-180° domain switches involve strain changes and hence demand the coordination of neighbor domains. The microdeformations arising from the domain wall movements, though small in magnitude, are detectable by sensitive acoustic emission methods.[11,12] The poling effects on acoustic velocity and attenuation in poled and unpoled PZT ceramics were studied as a function of temperature and frequency.[14] Application of a large electric field (or mechanical stress) can lead to microcracking, due to internal stresses.[15] Electrically induced microcracking in PZT has been shown to be dependent on grain size and tetragonality[10,14,16–19] and is detected by microscopy[20] and dielectric measurements. The external parameters influencing the extent of microcracking are the poling conditions (field, time and temperature).[19,21] Microcracking results in a deterio-
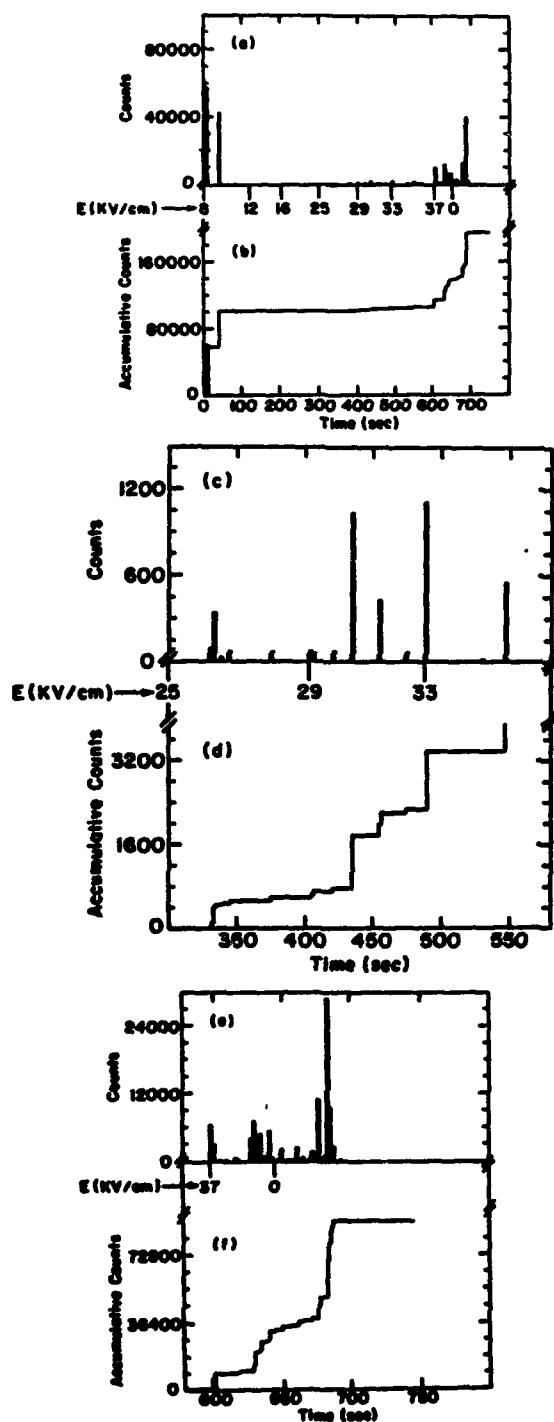
FIGURE 5 Same as in Figure 3 for sample SS but the electric field is maintained even after the onset of continuous AE counts, signifying beginning of microcracking. The regime just before [Figures (c) and (d)] and just after [Figures (e) and (f)] the onset of microcracking is shown in detail.
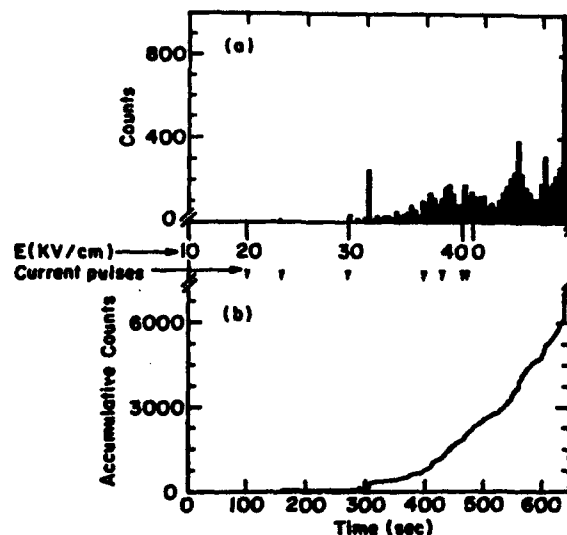
FIGURE 6 Same as in Figure 5 for sample *E* but the electric field is retained for extensive micro-cracking to occur, as indicated by continuous AE counts.

ration of electrical and mechanical properties of the ceramic[21-23] and hence should be minimized if not eliminated. Uchino *et al.* have studied AE signals in piezoelectric and electrostrictive actuators subjected to bipolar and unipolar electric fields and also after repeated cycles of thermal shocking.[24] They found that the unipolar field does not lead to acoustic emission, unless the samples have suffered mechanical damage as by thermal shocking.

The acoustic emission technique has recently been applied to the study of domain switching, as well as the occurrence and recombination of microcracks in ferroelectric $PbTiO_3$ ceramics as it is heated and cooled.[25]

From the above discussion it is clear that poling is a critical process for achieving optimum piezoelectric properties of a ferroelectric ceramic. The domain reorientations which give rise to enhanced piezoelectric behavior also give rise to mechanical stresses, which can lead to microcracking, if the induced stresses exceed the elastic limit of the material. Therefore poling should be carried out to obtain maximum domain reorientation, but without the onset of the microcracking process, provided there is a simple, reliable means to distinguish the two deformation processes.

The purpose of the present study is to delineate the microdeformations accompanying domain switching from those due to microcracking during poling of PZT ceramics, as a contribution toward a better understanding and optimization of the poling process. Simultaneous detection of acoustic emission and electrical current pulses were employed in the study and the results are substantiated by scanning electron micrographs and electrical property measurements.

EXPERIMENTAL

Ceramic lead zirconate titanate (PZT) composition (52% $PbZrO_3$, 48% $PbTiO_3$) at the morphotropic phase boundary (MPB) was prepared by conventional method.
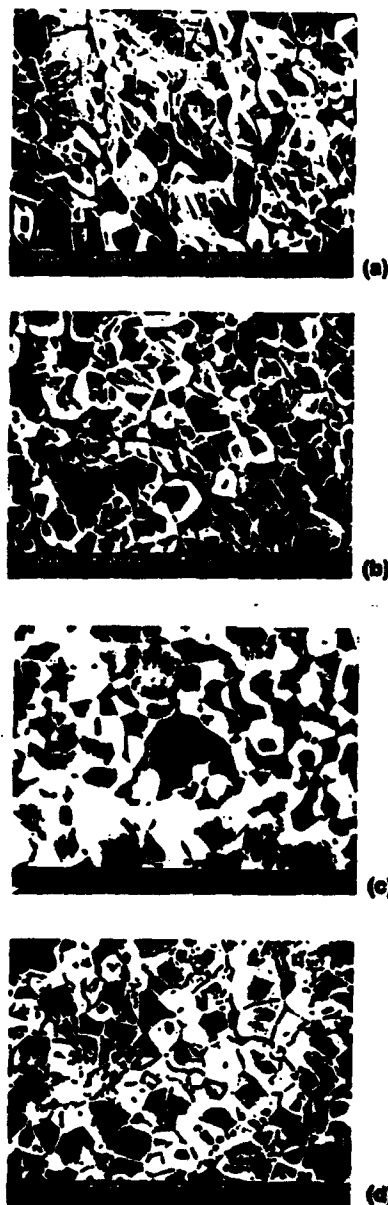
FIGURE 7   Scanning electron micrographs of PZT ceramic (a) as sintered; (b) poled, but not microcracked (sample C); (c) poled till microcracking started (sample B); (d) poled and extensively microcracked (sample E).

Stoichiometric proportions of reagent grade oxides (PbO from Hammond Lead Products, Potterstown, Pennsylvania, ZrO_2 from Harshaw Chemical Co., Cleveland, Ohio, and TiO_2 from J. T. Baker Chemical Co., Phillipsburg, New Jersey) were mixed in a polyethylene bottle for 12 hours using ethyl alcohol as wetting agent and ½" diameter zirconia balls as grinding media. Excess lead oxide (0.5 wt%)
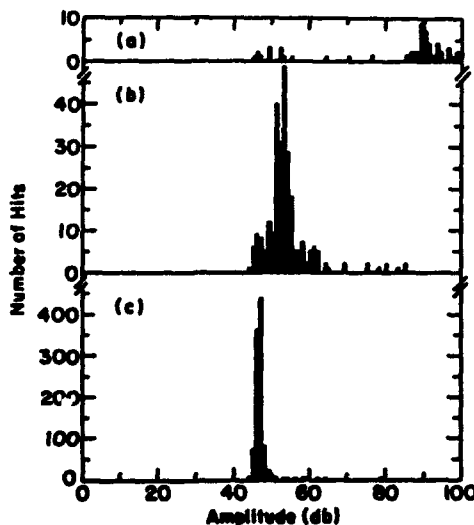
FIGURE 8   Number of AE hits vs amplitude for samples with (a) only domain reorientations (sample C), (b) both domain reorientations and initial microcracking (sample B) and (c) extensive micro-cracking (sample E). Note the scale change for (c) from (a) and (b).

was added to compensate for lead loss during calcination. The milled powder was dried at 80°C for 24 hours and calcined at 900°C for 24 hours. X-ray diffraction examination confirmed the formation of the perovskite phase. After mixing with 2% polyvinyl alcohol binder, the powder was pressed into pellets at 105 MPa. The binder was removed by heating at 350°C for three hours and 550°C for three hours. The pellets were sintered at 1250°C for five hours in closed crucibles in PbO atmosphere, at a rate of 5°C/min during heating and 3°C/min during cooling.

Sintered PZT ceramic discs were polished to obtain two parallel faces, which were then electroded with sputtered gold. The electroded disc is located in a suitable holder and immersed in a silicone oil bath at 50°C. High DC field is applied in a stepwise fashion from a power supply (Tred COR-A-TROL), while an alumina rod serving as a wave guide rests on the ceramic disc. A transducer is mounted at the other end of the wave guide. Acoustic emission signals are collected, filtered and analyzed by appropriate electronic circuitry and displayed as counts or count rate as a function of time (Locan 320 System from Physical Acoustics Corp.). The schematic of the experimental arrangement is shown in Figure 2. A microammeter is placed in the voltage input lead of the poling circuit, to detect current pulses arising from domain switching, superimposed on leakage current.

After various stages of poling, the samples were examined for piezoelectric coefficient, d_{33}, using a Berlincourt d_{33} meter, for mechanical quality factor, Q_M, using IRE standard method, and for microstructure and microcracks from scanning electron micrographs.

RESULTS AND DISCUSSION

A PZT ceramic sample (C) was poled in successive steps of increasing DC field at intervals of 100 sec, while acoustic emission signals and current pulses were recorded

(Figure 3). No AE signals were detected until a poling field of 41 kv/cm was applied (though a few current pulses were observed as soon as poling field $\geq$ 16 kv/cm was applied). The current pulses (2–12 mA) were superimposed on a steady leakage current of 0.5 to 3 mA. It can be seen that a substantial number of AE signals occur as soon as the poling field is increased, though a smaller number of AE counts were recorded at irregular time intervals during the application of a fixed poling field, in agreement with earlier reports.[12] Everytime AE counts occurred, there were accompanying current pulses. Evidently both the AE and current pulses arise from domain reorientations. After 800 sec, the field was reduced in steps to zero at 1200 sec. While no AE counts were detected till the applied field was dropped to zero, AE counts were indeed recorded nearly 60 sec after removal of the field and these AE events may reflect domain reversals. The piezoelectric coefficient, d_{33}, of this sample was 333 $\pm$ 7 $\times$ 10^{-12} C/N. The scanning electron micrograph of this sample [Figure 7(b)] is similar to that of a virgin sample [Figure 7(a)] and does not show clear microcracking, though grain boundaries become more obvious. The sample has a mechanical quality factory (Q_M) of 89 (Table I).

An example of a sample (B) which was subjected to a stepwise increase of the poling field till microcracking just starts, as evidenced by continuous AE counts instead of intermittent AE signals, is shown in Figure 4. The field was quickly reduced to zero soon after the appearance of continuous AE counts. While current pulses were observed corresponding to the intermittent AE signals, no current pulses were observed during the continuous occurrence of AE counts. The d_{33} value of this sample is lower at ~200 $\times$ 10^{-12} C/N and the scanning electron micrograph does not show any significant microcracking [Figure 7(c)].

These results were confirmed with another PZT ceramic sample (SS) which shows a large number of AE counts as soon as a poling field of 8 kv/cm is applied (poling temperature 50°C), but no further AE counts till the field applied was 25 kv/cm at 300 sec (Figure 5). There were intermittent AE signals as the poling field was increased stepwise from 25 kv/cm to about 37 kv/cm at 600 sec [Figures 5(c) and (d)]. In this regime AE counts were invariably accompanied by current pulses up to 60 mA. As soon as continuous AE counts started appearing at about 620 sec, the poling field was turned off. The AE counts continued which may indicate domain reversals [Figures 5(e) and (f)]. Since the microcracking process was quickly interrupted, the d_{33} was nearly unaffected (350).

The stepwise poling of another sample (E) was continued beyond the occurrence of intermittent AE signals accompanied by associated current pulses (of up to ~40 mA) to the regime where AE counts occur continuously but no current pulses are detected (Figure 6). We believe that the onset of continuous AE counts must signify the beginning of microcracking due to excessive mechanical stresses generated by extensive domain switching. The poling field was reduced to zero at 480 sec but AE counts persisted for sometime (at least up to 640 sec) suggesting further microcracking or propagation of cracks till adequate stress relief is attained. Due to the extensive microcracking, the d_{33} value (119 $\times$ 10^{-12} C/N) and Q_M were severely affected (Table I). The scanning electron micrograph of this sample [Figure 7(d)] shows extensive intergranular cracking.

The threshold amplitude for the AE experiments was set at 45 db. The distribution of the magnitude of the detected AE signals for three samples is given in

Figure 8. It can be seen that the number of hits increases and the amplitude spread decreases as the extent of microcracking changes from none to minor to extensive. When acoustic emission signals arise from domain reorientations, their amplitude reflects a wide range of accompanying microdeformations, depending upon the original domain orientations and the magnitude of the poling field [Figure 8(a)]. On the other hand, the initiation and propagation of microcracking is driven by stress concentrations in the ceramic and the corresponding AE signals occur in a narrow amplitude range [Figure 8(c)]. The case where domain reorientations and initial microcracking occur simultaneously represents an intermediate situation [Figure 8(b)]. This is in agreement with the observation of Pan and Cao,[13] who state that the AE signal amplitude is maximal at the polarization switching and minimal when the poling is established. Iwasaki and Izumi[11] also find that the peak of AE counts occurs at lower amplitude range and the spread of amplitude narrow as the poling field is increased.

CONCLUSIONS

Application of a DC field to ferroelectric ceramics (poling) causes domain reorientations in the field direction. All but the 180° domain switches involve dimensional changes leading to mechanical stresses due to the constraint of the neighboring grains in a ceramic. When the stresses exceed the bonding strength between grains, the ceramic suffers microcracking, resulting in deterioration of electrical (d_{33}, k_p, e, etc.) and mechanical (Q_M, strength, etc.) properties. The present study established that concurrent AE counts and current pulses are observed when domain switches take place during poling. The onset and progress of microcracking is signalled by continuous AE counts but no accompanying current pulses. The delineation of domain switching from microcracking by this approach is corroborated by changes in electrical and mechanical properties and scanning electron micrographs and constitutes a simple, reliable, non-destructive in-situ means to control the poling process to achieve optimum piezoelectric properties in a ferroelectric ceramic.

REFERENCES

1. F. Jona and G. Shirane, *Ferroelectric Crystals*, McMillan, New York (1962).
2. E. C. Subbarao, M. C. McQuarrie and W. R. Buessem, *J. Appl. Phys.*, 28, 1194 (1957).
3. H. G. Baerwald, *Phys. Rev.*, 105, 480 (1957).
4. R. C. Miller and A. Savage, *Phys. Rev.*, 112, 755 (1958).
5. W. J. Merz, *J. Appl. Phys.*, 27, 938 (1956).
6. E. A. Little, *Phys. Rev.*, 98, 978 (1955).
7. R. C. Bradt and G. S. Ansell, *J. Am. Ceram. Soc.*, 52, 192 (1969).
8. B. Jaffe, W. R. Cook, Jr. and H. Jaffe, *Piezoelectric Ceramics*, Academic Press, New York (1971).
9. D. Berlincourt and H. H. A. Krueger, *J. Appl. Phys.*, 30, 1804 (1959).
10. S. S. Chiang, R. M. Fulrath and J. A. Pask, *J. Am. Ceram. Soc.*, 64, C-141 (1981).

11. H. Iwasaki and M. Izumi, *Ferroelectrics*, **37**, 563 (1981).
12. C. S. Wang, X. X. Yi, G. C. Xu, X. G. Zhu and J. P. Zhou, *Appl. Acoustics*, p. 39 (1984) in Chinese.
13. W. Pan and H. Cao, *Ferroelectrics*, **129**, 119 (1992).
14. C. K. Jen, C. J. Chung, G. Shapiro, J. R. Monchalin, P. Langlois and J. F. Bussiere, *J. Am. Ceram. Soc.*, **70**, C-256 (1987).
15. R. C. Pohanka, R. W. Rice and B. E. Walker, Jr., *J. Am. Ceram. Soc.*, **59**, 71 (1976).
16. H. T. Chung, B. C. Shin and H. G. Kim, *J. Am. Ceram. Soc.*, **72**, 327 (1989).
17. C. I. Cheon, S. J. Kin and H. G. Kim, *Ferroelectrics*, **115**, 35 (1991).
18. F. Kroupa, K. Nejezchleb, J. Rataj and I. Saxl, *Ferroelectrics*, **100**, 281 (1989).
19. B. C. Shin and H. G. Kim, *Ferroelectrics*, **100**, 209 (1989).
20. F. Kroupa, K. Nejezechleb and I. Saxl, *Ferroelectrics*, **88**, 123 (1988).
21. H. T. Chung and H. G. Kim, *Ferroelectrics*, **76**, 327 (1987).
22. K. Nejezchleb, F. Kroupa, M. Boudys and J. Zelenka, *Ferroelectrics* **81**, 339 (1988).
23. S. W. Freiman, *Proc. Sixth IEEE Intl. Symp. on Applications of Ferroelectrics*, Lehigh Univ., Bethlehem, p. 367 (1986).
24. K. Uchino, T. Hirose and A. M. Varaprasad, *Japan J. Appl. Phys.*, **26**, Suppl. 26-2, 167 (1987).
25. V. Srikanth and E. C. Subbarao, *Acta. Metall. Mater.*, **40**, 1091 (1992).